Event-by-Event Temperature Fluctuation In Heavy Ion Collisions at Large Hadron Collider energies in ALICE Experiment

By

Sumit Basu

Enrollment No. PHYS04201004002

Variable Energy Cyclotron Centre, Kolkata

A thesis submitted to

The Board of Studies in Physical Sciences

In partial fulfillment of requirements for the Degree of

DOCTOR OF PHILOSOPHY

of

HOMI BHABHA NATIONAL INSTITUTE
Bhabha Atomic Research Centre
Mumbai-400085, India

December, 2016

Homi Bhabha National Institute[1]

Recommendations of the Viva Voce Committee

As members of the Viva Voce Committee, we certify that we have read the dissertation prepared by **Sumit Basu** entitled "***Event-by-Event temperature fluctuations in high energy collisions at the LHC energies in the ALICE experiment***" and recommend that it may be accepted as fulfilling the thesis requirement for the award of Degree of Doctor of Philosophy.

Chairman – Asis K. Chaudhuri **Date: 21/3/2017**

Guide / Convener – Tapan K. Nayak **Date: 21/3/2017**

Co-guide - <Name> (if any) **Date:**

21.3.17

Examiner – Prasanta K. Panigrahi **Date: 21/3/2017**

Member 1- Sourav Sarkar **Date: 21/3/2017**

Member 2- Basanta K. Nandi **Date: 21/3/2017**

Final approval and acceptance of this thesis is contingent upon the candidate's submission of the final copies of the thesis to HBNI.

We hereby certify that I/we have read this thesis prepared under my/our direction and recommend that it may be accepted as fulfilling the thesis requirement.

Date: 21/3/2017

Place:

Guide: (Tapan K. Nayak)

[1] This page is to be included only for final submission after successful completion of viva voce.

STATEMENT BY AUTHOR

Sumit Basu

DECLARATION

I, hereby declare that the investigation presented in the thesis has been carried out by me. The work is original and has not been submitted earlier as a whole or in part for a degree/diploma at this or any other Institution/University.

Sumit Basu

List of Publications arising from the thesis

In peer-reviewed Journal

1. ”Specific Heat of Matter Formed in Relativistic Nuclear Collisions”
   Sumit Basu, Sandeep Chatterjee, Rupa Chatterjee, Basanta K. Nandi, Tapan K. Nayak.
   Phys. Rev. C 94, 034909, (2016)
   DOI:10.1103/PhysRevC.94.034909.

2. “Beam energy dependence of Elliptic and Triangular flow with the AMPT model”
   Dronika Solanki, Paul Sorensen, **Sumit Basu**, Rashmi Raniwala, Tapan Kumar Nayak.
   Phys. Lett. B 720, 352 (2013).
   DOI:10.1016/j.physletb.2013.02.028

3. ”Beam energy dependence of pseudorapidity distributions of charged particles produced in heavy-ion collisions at RHIC and LHC energies”
   Sumit Basu, Tapan K Nayak, Kaustuv Datta.
   Phys. Rev. C 93, 064902, (2016)
   DOI:10.1103/PhysRevC.93.064902

4. “Characterization of relativistic heavy-ion collisions through temperature fluctuations”
   Sumit Basu, Rupa Chatterjee, Basanta K. Nandi, Tapan K. Nayak.
   arXiv:1504.04502. Communicated to **EPJC(2015)**.

5. “Maps of the Little Bangs Through Energy Density and Temperature Fluctuations”
   Sumit Basu, Rupa Chatterjee, Basanta K. Nandi, Tapan K. Nayak.
   arXiv:1405.3969 (2014).

Conferences and Symposia

1. “Higher Harmonic Flow in Heavy Ion Collisions at Different Beam Energies ”
   Sumit Basu, Dronika Solanki, Rashmi Raniwala, Tapan Kumar Nayak, Proceedings of the DAE Symp. on Nucl. Phys. 59 (2014).

2. “Beam energy and centrality dependence of multiplicity fluctuations in heavy ion collisions”
   Maitreyee Mukherjee, **Sumit Basu**, Subikash Choudhury,Tapan Nayak.
   Published **Journal of Physics: Conference Series (JPCS)**. 668 (2016) 012043.
   DOI:10.1088/1742-6596/668/1/012043

3. “Temperature Fluctuations: A New Insight to Heavy Ion Collisions”
   Sumit Basu, Rupa Chatterjee, Basanta K. Nandi, Tapan K. Nayak.
   Accepted for publication in **Proceedings of science (PoS)** 2016.

4. “Temperature Fluctuations in Little Bang : Hydro dynamical Approach”
   Sumit Basu, Rupa Chatterjee, Tapan Kumar Nayak, Proceedings of the DAE-BRNS Symp. on Nucl. Phys. 60 (2015)

5. “Beam energy and centrality dependence of multiplicity fluctuations in heavy ion collisions”
   Maitreyee Mukherjee, **Sumit Basu**, Subikash Choudhury,Tapan Nayak, Proceedings of the DAE-BRNS Symp. on Nucl. Phys. 60 (2015).

6. “Temperature and Multiplicity Fluctuations as a New Tool of Characterization for Heavy Ion Collisions at LHC energy”
   Sumit Basu, Rupa Chatterjee, Basanta K. Nandi, Tapan K. Nayak.
   Published in Springer Proceedings in Physics book series, **Springer Proc.Phys. 174 (2016)** 189-194. DOI: 10.1007/978-3-319-25619-1_30.

7. “Beam Energy Scan of Specific Heat through Temperature Fluctuations”
   Sumit Basu, Sandeep Chatterjee, Rupa Chatterjee, Basanta K. Nandi, Tapan K. Nayak.
   Published **Journal of Physics: Conference Series (JPCS)**. 668 (2016) 012043.
   DOI:10.1088/1742-6596/668/1/012118.

List of ALICE Collaboration Paper

All ALICE Collaboration papers from Mar 2012 till now. Here are the full list of **my ALICE Collaboration papers** (https://inspirehep.net/search?ln=enp=find+a+basu+and+cn+alicejrec=1sf=earliestdate).

Among them following papers are either closely related to the thesis topic or some of the significant work done on these papers.

1. “Event−by−event mean pT fluctuations in pp and Pb−Pb collisions at the LHC”
   ALICE Collaboration, Jul 21, 2014. 15 pp.
   Published in Eur.Phys.J. C74 (2014) 10, 3077
   DOI: 10.1140/epjc/s10052-014-3077-y
   e-Print: arXiv:1407.5530 [nucl-ex]

2. “Multiplicity dependence of the average transverse momentum in pp, p−Pb, and Pb−Pb collisions at the LHC ”

ALICE Collaboration,
Jul 3, 2013. 10 pp.
Published in Phys.Lett. B727 (2013) 371-380
DOI: 10.1016/j.physletb.2013.10.054
e-Print: arXiv:1307.1094 [nucl-ex]

3. "Centrality dependence of π, K, p production in Pb$-$Pb collisions at $\sqrt{S}_{NN} = 2.76$ TeV"
ALICE Collaboration,
Mar 4, 2013. 23 pp.
Published in Phys.Rev. C88 (2013) 044910 DOI: 10.1103/PhysRevC.88.044910
e-Print: arXiv:1303.0737 [hep-ex]

4. "Energy Dependence of the Transverse Momentum Distributions of Charged Particles in pp Collisions Measured by ALICE"
ALICE Collaboration, Jul 3, 2013. 18 pp.
Published in Eur.Phys.J. C73 (2013) 12, 2662
DOI: 10.1140/epjc/s10052-013-2662-9
e-Print: arXiv:1307.1093 [nucl-ex]

5. "Transverse momentum dependence of inclusive primary charged-particle production in p$-$Pb collisions at $\sqrt{S}_{NN} = 5.02$ TeV"
ALICE Collaboration,
May 12, 2014. 10 pp.
Published in Eur.Phys.J. C74 (2014) 9, 3054
DOI: 10.1140/epjc/s10052-014-3054-5
e-Print: arXiv:1405.2737 [nucl-ex]

6. "Centrality dependence of particle production in p$-$Pb collisions at $\sqrt{S}_{NN} = 5.02$ TeV"
ALICE Collaboration,
Dec 21, 2014. 46 pp.
CERN-PH-EP-2014-281
e-Print: arXiv:1412.6828 [nucl-ex]

7. "Production of charged pions, kaons and protons at large transverse momenta in pp and Pb?Pb collisions at $\sqrt{S}_{NN} = 2.76$ TeV"
ALICE Collaboration,
Jan 6, 2014. 11 pp.
Published in Phys.Lett. B736 (2014) 196-207
DOI: 10.1016/j.physletb.2014.07.011
e-Print: arXiv:1401.1250 [nucl-ex]

8. "Centrality dependence of the pseudorapidity density distribution for charged particles in Pb$-$Pb collisions at $\sqrt{S}_{NN} = 2.76$ TeV"
ALICE Collaboration,
Apr 1, 2013. 13 pp.
Published in Phys.Lett. B726 (2013) 610-622

DOI: 10.1016/j.physletb.2013.09.022
e-Print: arXiv:1304.0347 [nucl-ex]

9. "Multiplicity Dependence of Pion, Kaon, Proton and Lambda Production in p−Pb Collisions at $\sqrt{S}_{NN} = 5.02$ TeV" **ALICE Collaboration,**
Jul 25, 2013. 14 pp.
Published in Phys.Lett. B728 (2014) 25-38
DOI: 10.1016/j.physletb.2013.11.020
e-Print: arXiv:1307.6796 [nucl-ex]

10. "Inclusive photon production at forward rapidities in proton-proton collisions at $\sqrt{S}_{NN} =$ 0.9, 2.76 and 7 TeV " **ALICE Collaboration,**
Nov 18, 2014. 24 pp.
CERN-PH-EP-2014-280
e-Print: arXiv:1411.4981 [nucl-ex]

DEDICATION

I dedicate my thesis to my God-like parents (Samar Basu & Siuli Basu) and loving wife Sana (Banashri Basu Sinha). Without their constant, selfless support and sacrifices this thesis would not be completed.
I also dedicate this thesis to Dr. Atri Deshamukhya and Prof. Tapan K Nayak (Thesis Supervisor), the two best teachers of my life.

ACKNOWLEDGMENTS

I would like to express my gratitude to my supervisor, Prof. Tapan Kumar Nayak for his continuous support, encouragement, enthusiasm, and guidance during my PhD work. I would like to thank Prof. Subhasish Chattopadhyay for enourmous support and valuable discussions.

I would also like to thank my doctoral committee members Prof. Asis Chowdhury, Sourav Sarkar and Prof. Basanta K. Nandi for their valuable advices. I would like to thank Dr. Y.P. Viyogi, Prof. Bedangadas Mohanty, Dr. Premomoy Ghosh, Dr. Zubayer Ahmed and Dr. Anand Dubey, Dr. Partha Pratim Bhaduri of Experimental High Energy Physics and Application Group, VECC, for inspiring me. I convey my gratitude to Dr. Prithwish Tribedy for his support and help. I am thankful to the staffs of the Photon Multiplicity Detector (PMD) laboratory in VECC to help me to understand the functions of the detectors as well as to help in detector testing, etc. I sincerely thank Mr. Vikas Singhal for constant help in matters related to computing and grid at VECC. I am thankful to my seniors Sidharth Bhai, Sudipan Da, Nihar Bhai, Nasim Da and Subhas Da for helping me with advices and suggestions. I would like to thank all my friends Balaram, Subikash, Arindam, Rajesh, Maitreye, Vishal and Rihan for making my journey enjoyable.

I am fortunate to have discussions on several topics, especially on my analysis work, with Dr. Jurgen Schukraft (Former Spokesperson of ALICE), Dr. Federico Antinori (Physics Coordinator), Dr. Alexander Phillip Kalweit (PWGLF Convenor), Dr. Roberto Preghenella, Dr. Alice Ohlson (Convenor of the Physics Analysis Group (PAG) in ALICE), Dr. Michael Weber and Dr. Panos Christakoglou (Convenors of Physics Working Group (Correlations and Fluctuations) in ALICE) during my stay in CERN. I would like to thank the ALICE-India Collaboration members and all my friends from ALICE-India. A thankful note to Dr. Sandeep Chatterjee, Dr. Rupa Chatterjee, Dr. Satyajit jena, Dr. Nirbhay Behara and Dr. Prabhat R Pujahari for helping me in understanding the subject in variuos stages during the journey. I would also liketo thank my jouniors Arghya, Debojit, Somnath, Noor, Ashik, Nachiketa for their constant support.

I express my gratitude to my parents and my wife for their unconditional support throughout my PhD work and encouragement in the completion of my thesis.

Sumit Basu

Contents

Synopsis

The major goal of colliding heavy-ions at the Relativistic Heavy Ion Collider (RHIC) at Brookhaven National Laboratory and the Large Hadron Collider (LHC) at CERN is to study matter at extreme conditions of temperature and energy densities, where quarks and gluons, rather than mesons and baryons, define the relevant degrees of freedom. This new phase of matter, the Quark-Gluon Plasma (QGP), is governed by the principles of Quantum Chromodynamics (QCD) and is the result of a deconfined phase transition from the normal nuclear matter. Experiments at RHIC and LHC are on the quest to unearth the nature of the QCD phase transition and to get a glimpse of how matter behaves at extreme conditions. How the entropy is produced? what is the nature of phase transitions? How the hadronizations occur? What are the properties of the medium? Answer to all of the above questions are lies in the theory of fluctuations and correlation. Also study of fluctuations of various quantities provides a powerful means of observing QCD phase transition (which is associated with a discontinuity of free energies of the system), as in QCD phase transition associated with a QGP and hadronic phase change. So, any fluctuation observables have a high value near the phase boundary. The most conclusive piece of evidence for the Big Bang is the existence of an isotropic radiation bath that permeates the entire Universe known as the "cosmic microwave background" (CMB). The COBE DMR (Differential microwave radiator) results showed tiny variations ($<$ 10-5K) in the Cosmic Background Radiation temperature (fluctuations at the part in 100,000 level). This reflects small density fluctuations in the early Universe before matter and light parted company. After decoupling, the density fluctuations grow under gravity to form the seeds for galaxies and clusters. The nature of these fluctuations agrees with current theories of the formation of structure in the Universe. Heavy-ion collisions at ultra-relativistic energies create matter at extreme conditions of energy density and temperature, similar to the ones that existed within a few microseconds after the Big Bang. The fireball produced in the collision goes through a rapid evolution from an early partonic phase of deconfined quark-gluon plasma (QGP) to a hadronic phase and ultimately freezing out after a few tens of fm. Temperature fluctuations have been discussed in the literature as a means of characterizing the evolving system. The fluctuations may have two distinct origins, first, quantum fluctuations that are initial state fluctuations, and second, thermodynamical fluctuations. We discuss a method of extracting the thermodynamic temperature from the mean transverse momentum of pions, by using controllable parameters such as centrality of the system, and range of the transverse momenta. Event-by-event fluctuations in global temperature over a large phase space provide the specific heat of the system. We present Beam Energy Scan of sp. heat from data, AMPT and HRG model prediction. For Pb-Pb collisions at the Large Hadron Collider (LHC) energies, because of the production of a large number of particles in every event, it is possible to divide the phase space into small bins and obtain local temperature for each bin. Event-by-event fluctuations in local temperature can be obtained by following a novel procedure of making fluctuation map of each event.

The origin of the local fluctuations has been studied with the help of event-by-event hydrodynamic calculations, which shows that the system exhibits fiercely large fluctuations at early times after the collision, which diminishes with the elapse of time. Any observation of non-zero local fluctuations may imply that a part of the early fluctuations might have survived till freeze-out. We discuss the hydrodynamic calculations and a feasibility study at LHC using AMPT simulated data.

These temperature fluctuations are the imprints of very small irregularities, which through time have grown to become the galaxies and clusters of galaxies, which we see today. Similarly, same temperature fluctuation can also be studied in heavy-ion physics at TeV energy scale in ALICE experiment as for both a very large number of events and very large multiplicity at each event.

From the slope of the p_T spectrum of identified particles for every event fit with different functions such as exponential, Levy, Tsallis, Boltzmann Gibbs Blast Wave etc. The slope parameter is obtained for each event and can be studied by plotting it for a large number of events and get a distribution. Also this study can be done for a specified phase space (η-ϕ) or (y-ϕ).

These phase transitions are governed by a set of thermodynamic parameters, like, temperature (T), pressure, entropy, and energy density (E), and can be further characterized by their response functions, such as, specific heat, compressibility, and susceptibility. In thermodynamics, the heat capacity (C) is defined in terms of the ratio of the event-by-event fluctuations of the energy of a part of a finite system in thermal equilibrium to the energy $\langle \Delta E^2 \rangle = T^2 C(T)$. This can be applied for a locally thermalized system produced during the evolution of heavy-ion collisions. But for a system at freeze-out, specific heat can expressed in terms of the event-by-event fluctuations in temperature of the system where volume is fixed: $\frac{1}{C} = \frac{(\langle T^2 \rangle - \langle T \rangle^2)}{\langle T \rangle^2}$. We define the specific heat as the heat capacity per pion multiplicity within the available phase space or the experimentally available window in rapidity and azimuth. For a system in equilibrium, the mean values of temperature and energy density are related by an equation of state. However, the fluctuations in energy and temperature have quite different behavior. Energy being an extensive quantity, its fluctuations have a component arising from the volume fluctuations, and not directly suited for obtaining the heat capacity. From there the specific heat for heavy-ion collisions at SPS, RHIC beam energy scan energies and for LHC energy. Experimental results from NA49, STAR, PHENIX, PHOBOS and ALICE are combined to obtain the specific heat as a function of beam energy. The results are compared to results from AMPT event generator, HRG model and lattice calculations. We also present local hot spot search at LHC energy for better understanding the collision dynamics.

I have been involved in the detailed analysis work for more than two years, analyzing data sets of Pb+Pb collisions at $\sqrt{s}_{NN}$= 2760 GeV for the data taken in a period of two years (Run 10 and 11). In addition, I have a plan to analyse the analyzed data for Pb+Pb collisions with different centrality in order to understand the system size dependence. In the analysis process, detail QA for the event-by-event fluctuation studies has been performed to remove fluctuations originating from the experimental background. For this I used TPC and TOF detectors. The ALICE detector consists of a central part, which measures event-by-event hadrons, electrons and photons, and of a forward spectrometer to measure muons. The central part, which covers polar angles from 45 to 135 ($\eta < 0.9$) over the full azimuth, is embedded in the large L3 solenoidal magnet. The central barrel consists of: an Inner Tracking System (ITS) of high-resolution silicon detectors; a cylindrical Time-Projection Chamber (TPC), a Transition Radiation Detector (TRD) and a Time-Of-Flight (TOF) detector. The particle identification with TPC only and TPC+TOF combined gives reasonably well control over the mis-identification and purity effect. In order to have p_T and slope parameter for different particle to perform Temperature Fluctuation and subsequently the specific heat of the matter produced in the collision of LHC energy, a detailed study of spectral shape analysis and event-by-event correlation measurement is performed. The systematic study and result finding are on board and still going on. The photon multiplicity detector (PMD) and the forward multiplicity detector (FMD) measure photon multiplicity and charged particle multiplicities, in the forward region. Comparison to the amount of fluctuation in the central to forward region may shed more light on the properties of matter created in high energy heavy-ion collisions. For identified spectra we use TPC$-$TOF detector combined and measure the event$-$by$-$event basis fluctuations with the mean p_T and slope of the spectra. Similar method has been employed to find out the fluctuations within the event by making a grid in y-ϕ within the limited phase space.

In addition of the main research work, the following detailed studies have been performed as a part thesis work:

1. Transverse Momentum spectra for identified particles with p_T correlations: Several experiments involves with the basic observables like transverse momentum. Although it has very rich physics goal. During the detailed research work, we try to relate the p_T correlation with it. It has been observed that different experiments uses different observables for this study. A inter-relation and comparative study has been made on this basis. A system size and en-

ergy dependence helps a lot for characterizing and understanding the evolving fire ball. Also a centrality scan may address the effect of mini jets and degree of hadronizations.

2. Spectra−fitting functions and associated physics.

Different spectra fitting functions are available for addressing the different physics aspects. Mainly these are used for calculated the particle yield, temperature and flow. Combined blast wave are used for decoupling the radial boost from the kinematic freeze-out temperature in heavy ion collisions where as Tsallis are used for non−extinsive type spectra or non thermalized spectra. An extensive study has been made for both the data and different event generators.

3. Theoretical baseline studies using Hydro, HRG and AMPT.

To understand various sources of fluctuation related to heavy ion collision, various model simulations have been performed for the Temperature fluctuations. Those models are HIJING, AMPT and Event by event Hydro. These models are based upon certain known physics processes like, jet-interaction, transport phenomena, coalescence mechanism, thermal equilibrium etc., which are blind to the CP phenomena. These models may sever as baseline studies for the Temperature fluctuation analysis and other baseline studies.

4. Higher harmonic anisotropic flow.

A beam energy scan from RHIC to LHC energies of anisotropic flow had been performed. The detailed study of elliptic, triangular and other higher harmonic flow are done in models and compared with different published results. These study are very important to understand for NCQ scaling, quark coalescence and other phenomena to fixing the initial conditions and also the shear viscosity of the system.

5. Multiplicity fluctuations.

Detailed study of total charge multiplicity, η distributions and its fluctuations had been studied for having the nature of the evolution of these observable with the centrality and collision beam energy. It could also help to predict the same for the intermediate or higher energy. The event−by−event basis study of net charge, particle ratio, net baryon is related to some susceptibility as these are the conserved quantities. from there one can achieve the corresponding observable which are directly comparable with the Lattice QCD results.

6. Photon Multiplicity Detector (PMD).

Hardware and software associated with PMD is one part of my dissertation. High voltage testing, detector building is performed for part of the full detectors. The modules which had been prepare and tested now taking data in ALICE experiments at CERN. The detailed QA test for these detector data set has been performed for gain calculations and other characteristics.

List of Figures

List of Tables

Chapter 1

INTRODUCTION

The title of my thesis is "Event-by-Event Temperature Fluctuation In Heavy Ion Collisions at Large Hadron Collider energies in ALICE Experiment". So, I will try to give a brief introduction first about heavy ion collisions, its outcome and the signatures which confirms the various properties of the system produced while two nuclei colliding each other at ultra-relativistic energies. Second what is the connection and importance of studying the fluctuations in temperature in this context. The rest chapters will follow up the detail discussion how this can be done from various theoretical models, what would be expected at particular ALICE experiment energy, the detector setup, how the data have been analyzed and the outcome. Before entering to the main topic I would like to be philosophical while discussing the history that how the journey begins.

1.1 Prelude for Heavy Ion Collisions:

In experimental high energy physics of heavy ions, we use particle accelerators to collide heavy ions such as Lead or Gold nuclei, instead of colliding single protons or electrons, to study the properties of Quark-Gloun Plasma (QGP). By doing so, we produce a much more violent collision where a large number of particles are created and a considerable amount of energy is deposited in a volume bigger than the size of a single proton.

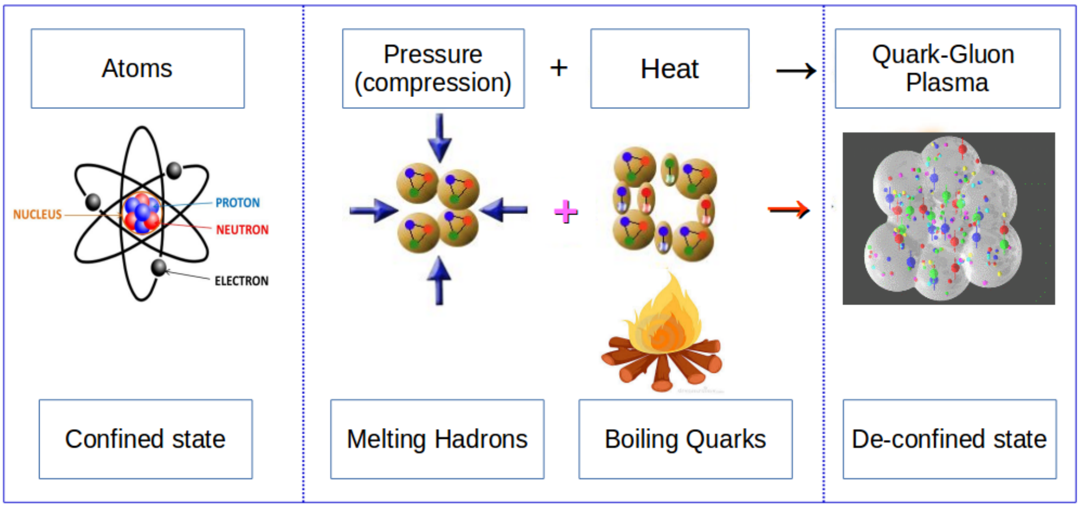

Figure 1.1: schematic diagram of producing Quark-Gluon Plasma(QGP) by heat and compression.

As a result, a highly excited state of matter is created and this state can have different characteristics from regular hadronic matter. It is postulated that if the energy density is high enough, the formed system will be in a de-confined state where quarks and gluons are no longer confined into hadrons and thus exhibits partonic degrees of freedom (1; 2). Here, the main theory that explains the interaction of matter in these extreme conditions is the theory of Quantum CromoDynamics (QCD), by studying the system formed in these relativistic heavy ion collisions, we can explore the QCD phase diagram and understand the characteristics of the different phases of matter.

In particular, QCD predicts that at extreme conditions, in high temperature or high baryoninc density, a new phase of matter known as the Quark-Gluon Plasma (QGP) would be formed, where partonic degrees of freedom could be observed in a volume larger that the size of a single hadron (3; 4). To set the scale on phase diagriam we conside to extreme cases: On one extreme of the QCD phase diagram, where density is high and temperature is low, the reduction of the coupling constant at small distances would make the quarks and gluons behave as free partons, thus forming a deconfined state of partons. This kind of matter could exist at the center of very dense astrophysical objects such as neutron stars (5). On the other extreme, of very

high temperature when the energy density exceeds some typical hadronic value, ($1GeV/fm^3$), matter would also go through a phase transition and form a deconfined state of quarks and gluons. Lattice QCD calculations (6) predicts a phase transition to a quark-gluon plasma at a temperature of approximately T$\approx$ 150-160 MeV, which is equivalent to $\approx 10^{12}$ K. This extreme condition is believed to be similar to the early stages of the evolution of our universe just after the Big-Bang, thus, studying the characteristics of the QGP and how it evolves allows us probe the different stages of our universe expansion.
In QCD a new quantum number, carried by quarks and gluons, is introduced. It is called color charge and particles carrying it interact strongly. This means that gluons mediate the strong force between quarks and they interact strongly themselves. This is not the case for e.g., photons that mediate the electromagnetic force without self-interactions. QCD is a non-Abelian gauge theory, which means that the strong interaction shows almost no resemblance to e.g., the electromagnetic interactions.

Of course, since the colliding system consists hundreds of nucleons in heavy ion collisions at the same time and in each reaction thousands of different particles are produced, the observation and analysis of these events require some work. Moreover, most of the particles that we measure are from the final stages of the system evolution, after it has gone though the phase transition back into ordinary matter and suffered multiple scatterings, so these particles do not carry direct information from the partonic phase. But exactly because of this challenging task imposed by the complexity of a heavy ion collision and the subsequent dynamical evolution of the system formed, opens further possibilities for new physics topics to be studied in these collisions and also the study of heavy ion collisions is a rich environment where many different models and theories can be tested, like hydrodynamical models (8; 9; 16), statistical thermodynamic models (17) are also used to study the global characteristics of the system formed, while phenomenological models such as coalescence models (10; 11; 12; 13; 14), microscopic transport models (21) are also used to study specific experimental observables.

Experiments in Heavy Ion Physics are carried out using accelerator and collider facilities available at laboratories throughout the world notably the Relativistic Heavy Ion Collider (RHIC) at Brookhaven National Laboratory (BNL), USA and the Super Proton Synchrotron (SPS) and the Large Hadron Collider (LHC), CERN, Switzerland.

1.2 Sandard Model Particle Physics & QCD

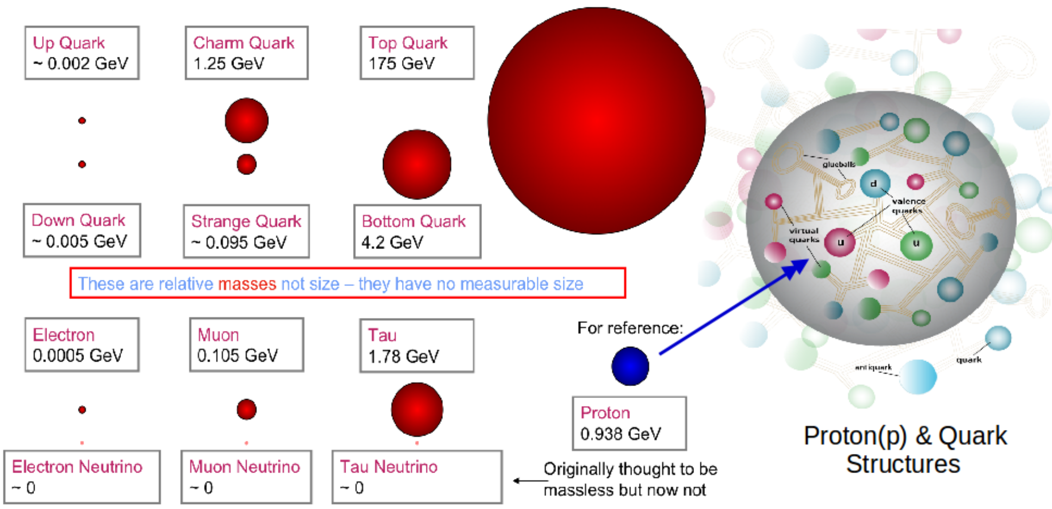

Figure 1.2: Structures of fundamenal particles and relative mass-size.

The fundamenal particles and their inerplay could be summarizes with help of the Standard Model of particle physics which introduces the basic particles, forces, and the rules of their combinations and interactions.

According to the Standard Model all matter consists of either leptons or quarks 1 . Table 1.1 summarizes the particles of the Standard Model. For a graphical overview of the interactions of these particles see Figure 1.1. All particles in the Standard Model have antiparticles with the same mass but with opposite electrical charge and color charge (see section 1.1.1 below). Antiparticles are denoted with a bar, so that an anti up quark is labelled $\bar{u}$, anti down quark is labelled as $\bar{d}$. Leptons have only been observed as free particles whereas quarks have not. In the present Universe the only quarks observed are the u and d quarks which are found in

Table 1.1: The fundamental particles, forces and their basic properties.

Quarks	Mass (GeV)	Charge	Leptons	Mass (GeV)	Charge	Carriers	Force
up (u)	0.003	2/3	electron (e)	0.00051111	-1	gluon (g)	strong
down (d)	0.006	-1/3	e- neutrino (ν_e)	$< 10^{-8}$	0	photon (γ)	electromagnetic
charm (c)	1.3	2/3	muon (μ)	0.106	-1	Z^0	weak
strange(s) (s)	0.1	-1/3	μ neutrino (ν_μ)	>0.0002	0	$W^\pm$	weak
top(t) (t)	175	2/3	tau (τ)	1.7771	-1	H	weak
bottom (b)	4.3	-1/3	τ neutrino (ν_τ)	<0.02	0	graviton ?	gravity

the neutrons (udd) and protons (uud). In general, composite particles built from quarks are called hadrons; hadrons containing two quarks are called mesons and hadrons composed of three quarks are called baryons. Thus, the neutron and the proton are baryons. The conservation of certain quantum numbers (electrical charge, spin, isospin etc.)

QCD calculations predict the existence of a high density medium composed of deconfined quarks and gluons at high temperature (22; 23). As early as 1951 a conjecture was put forward that the finite size of hadrons implied some critical compression above which matter could not exist in hadronic form (24). To describe the QGP and the phase transition a statistical approach is often used. The QGP is assumed to be a thermally equilibrated fluid or gas of quarks and gluons. If the baryonic chemical potential is set to zero (ie. no net-baryons: B = $\bar{B}$ where B is the number of baryons) the partition functions for fermions and bosons in relativistic gases are (25):

$$(TlnZ)_f = \frac{g_f V}{12}(\frac{7\pi^2}{30}T^4 + \mu^2 T^2 + \frac{1}{2\pi^2}\mu^4) \tag{1.1}$$

$$(TlnZ)_b = \frac{g_b V \pi^2}{90}T^4 \tag{1.2}$$

Here g_f and g_b are the degrees of freedom of fermions and bosons, respectively. Assuming that the equation of state is that of an ideal gas, p = $\epsilon/3$, and that the hadronic phase is composed only of pions, the following equations are obtained for the energy densities of the hadronic and QGP phases, respectively:

$$\frac{\epsilon_h}{T^4} = \frac{\pi^2}{10} \tag{1.3}$$

$$\frac{\epsilon_{QGP}}{T^4} = (32 + 21N_f)\frac{\pi^2}{60} \tag{1.4}$$

Evidently the QGP phase is characterised by a huge increase in the number of degrees of freedom caused by the asymptotically free quarks and gluons. No matter the value of the number of flavors, N_f , it is clear from Equation (1.3) that the energy density of the QGP phase is much higher compared to the hadronic phase. The case $N_f = 3$ (u,d,s) is known as the Stefan-Boltzmann limit. It is possible to solve the QCD equations in lQCD to obtain the behaviour of the matter near the critical temperature of the phase transition, T_c . The value of T_c is believed to be $T_c \sim 150 - 160$ MeV. The associated critical energy density is estimated to be around $\epsilon_c \sim 1GeV/fm^3$. Figure 1.6 shows the result of a lQCD calcution for ϵ/T^4 around T_c . The increase in energy density discussed above for the ideal gas case. The most realistic case shown in Figure 1.6 is the 2+1? case which has been calculated for 2 light quark flavors (u,d) and one heavy quark (s). The shape of the curve in Figure 1.6 is related to the nature of the phase transition.Results of a recent calculation of ε/T^4 are shown in Fig. 1.3, for 2- and 3-flavours QCD with light quarks and for 2 light plus 1 heavier (strange) quark (indicated by the stars) (26). The latter case is likely to be the closest to the physically realized quark mass spectrum. The number of flavours and the masses of the quarks constitute the main uncertainties in the determination of the critical temperature and critical energy density. The critical temperature is estimated to be $T_c = (155 \pm 10)MeV$ and the critical energy density $\varepsilon_c \simeq (6 \pm 2)\, T_c^4 \simeq$ (0.3-1.3)GeV/fm^3. Most of the uncertainty on ε_c arises from the 10% uncertainty on T_c. Although the transition is not a first order one (which would be characterized by a discontinuity of ε at $T = T_c$), a large

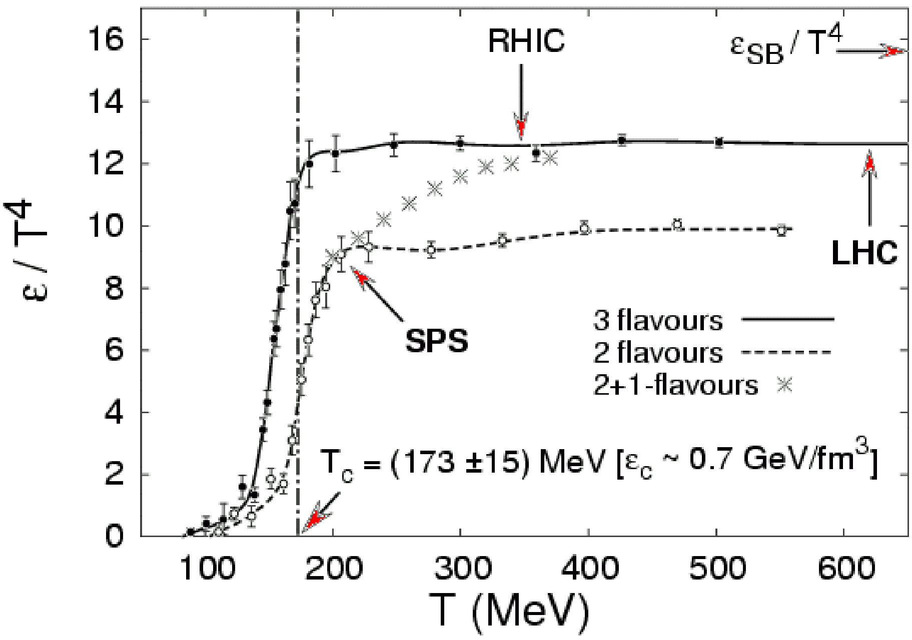

Figure 1.3: The energy density in lattice QCD with 2 and 3 light quarks and with 2 light plus 1 heavier (strange) quarks (26). The calculation uses $\mu_B = 0$.

'jump' of $\Delta\varepsilon/T_c^4 \simeq 8$ in the energy density is observed in a temperature interval of only about 40 Mev (for the 2-flavours calculation). Considering that the energy density of an equilibrated ideal gas of particles with $n_{\rm dof}$ degrees of freedom is

$$\varepsilon = n_{\rm dof}\,\frac{\pi^2}{30}\,T^4, \tag{1.5}$$

the dramatic increase of ε/T^4 can be interpreted as due to the change of $n_{\rm dof}$ from 3 in the pion gas phase to 37 (with 2 flavours) in the deconfined phase, where the additional colour and quark flavour degrees of freedom are available. In a pion gas the degrees of freedom are only the 3 values of the isospin for π^+, π^0, π^-. In a QGP with 2 quark flavours the degrees of freedom are $n_g + 7/8\,(n_q + n_{\bar{q}}) = N_g(8)\,N_{\rm pol}(2) + 7/8\, \times 2 \times N_{\rm flav}(2)\,N_{\rm col}(3)\,N_{\rm spin}(2) = 37$. The factor 7/8 accounts for the difference between Bose-Einstein (gluons) and Fermi-Dirac (quarks) statistics.

1.3 QCD Phase diagram

Physical systems can be made to undergo phase transitions by varying parameters such as the temperature (T) or a chemical potential (μ) of the system. Systems whose underlying interactions are strong interactions, are not different. In the theory of strong interactions, Quantum Chromodynamics (QCD), there are distinct conserved quantities. For a grand canonical ensemble of strongly interacting particles, the conserved baryon, electric charge and strangeness numbers are associated with the corresponding chemical potentials μ_B, μ_Q, and μ_S, respectively. So for a system with strong interactions one can lay out the phase diagram with axes being T, μ_B, μ_Q, and μ_S.

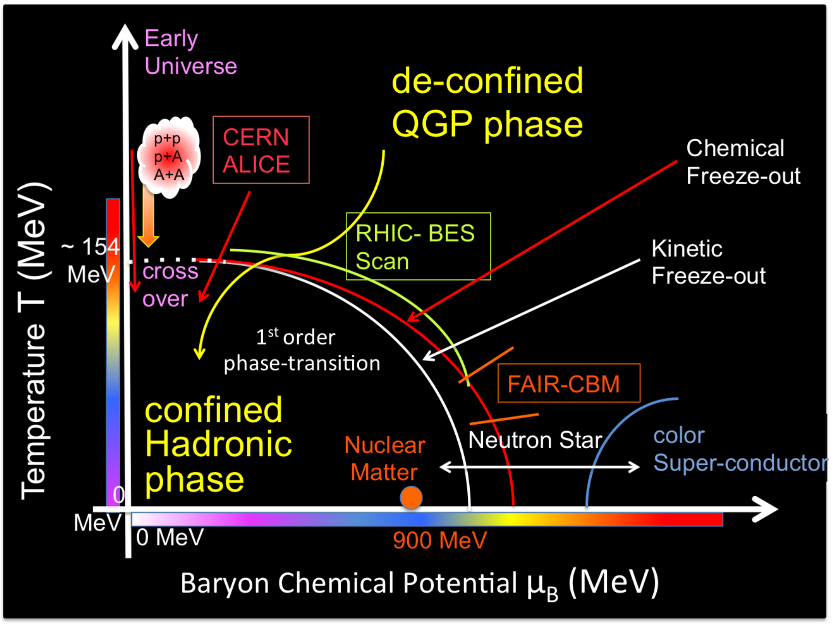

Figure 1.4: schematic diagram of QCD phase transitions in T-μ_B plane

Experimentally such a system of strong interactions can be created by colliding two nuclei at high energy. However, in such a system one can only vary to an appreciable extent T and μ_B (values of μ_Q, and μ_S are small (28)). This can be done by varying the center of mass energies ($\sqrt{s_{\rm NN}}$) of the collision of the two heavy nuclei (29; 30). Hence through relativistic heavy-ion collisions we can explore a two dimensional phase diagram, T versus μ_B, of strong interactions (31).

Such a phase diagram has several distinct phase structures. Some of which are: (a) high temperature and/or density phase of deconfined quarks and gluons (QGP), (b) low temperature and/or density phase of hadrons, (c) nature of quark-hadron transition is crossover for the small μ_B part of the phase diagram and first order for the rest (large μ_B) of the phase diagram, and (d) end point of the first order phase transition line (called the critical point (CP)).

The possible existence of a phase of highly compressed, asymptotically free partonic matter in the theoretical framework of the quark and gluon fields was proposed as early as 1975 (32) Here it is speculated that such a state might have an density as high as $\rho = 6.10^{16}\ g/cm^3$. In 1974 it was proposed at the conference at Bear Mountain (33) that collisions of heavy ions could be used to probe this medium as well as the properties of the vacuum. This meeting is often mentioned 3 as the starting point of experimental heavy ion physics. Figure 1.3 shows a conceptual sketch of the creation of QGP by compression. As the compression increases the hadrons cease to exist individually which leads to the formation of a QGP. In heavy ion collisions this compression is of course extremely violent and the lifetime of the created state very short (of the order of $1fm/c = 10^{-23}$ s or even shorter).

1.4 Evolution of QGP & Freeze-out Hypersurfaces

The expansion of the system happens at (almost) the speed of light in beam direction, and at about half the speed of light in the transverse direction. This phase can successfully be described by relativistic hydrodynamics assuming local thermodynamic equi- librium. The acceleration in radial direction is called radial flow. During this expansion also the initial spatial asymmetry transforms into a momentum anisotropy leading to a azimuthal modulation of particle production. This modulation can be decomposed into a Fourier series with respect to the reaction plane. The 2nd order asymmetry depends on the impact parameter of the collision, higher order asymmetries are caused by fluctuations.

During the expansion of the fireball the energy density (an thus also the temperature) decreases and when it falls below T_c the free partons hadronize forming a hadron gas. At this time the energy density has dropped to about $1GeV/fm^3$. Even below T_c this hadron gas is still very dense with a mean free path of the hadrons much smaller than the system size and can be described by hydrodynamics as well. The hadron gas continues to expand and cool and eventually the rate of inelastic collisions becomes small. At this stage, the **chemical freeze-out**, the hadron abundances become fixed. The hadronic stage with inelastic collisions could also be very short with hadron abundances fixed already at the phase transition. From the measured yields of particles with different mass the temperature of the chemical freeze-out can be deduced. The **kinetic freeze-out** occurs when also the elastic collisions stop, at this time the particle mo- menta are fixed. This marks the transition from a fluid description to free streaming particles. The bulk particle spectra follow a thermal (exponential) distribution in the local rest frame re- flecting the freeze-out temperature. Measured identified particle spectra can be well described if a blue-shift from a common radial velocity is folded into the exponential spectra leading to the so-called blast wave parameterization. The hydrodynamical description of the central rapidity region in heavy ion collisions. The description relies on four important assumptions on collisions between nuclei with nucleon number. There are two important famous descriptions from The Bjorken and Landau. In this section, particle ratios are used in the context of a thermal equilibrium model (34; 35; 36; 37) to extract chemical freeze-out properties. The extracted blast-wave model fit parameters are investigated to learn about the kinetic freeze-out properties. The systematics of the chemical and kinetic freeze-out properties extracted from data within the model frameworks are studied, and implications of these results in terms of the system created in heavy-ion collisions are discussed.

1.4.1 Chemical Freeze-out Properties

In the chemical equilibrium model, particle abundance in a thermal system of volume V is governed by only a few parameters,

$$N_i/V = \frac{g_i}{(2\pi)^3}\gamma_S^{S_i}\int \frac{1}{\exp\left(\frac{E_i-\mu_B B_i-\mu_S S_i}{ch}\right)\pm 1}d^3p \tag{1.6}$$

where N_i is the abundance of particle species i, g_i is the spin degeneracy, B_i and S_i are the baryon number and strangeness number, respectively, E_i is the particle energy, and the integral is over the whole momentum space. The model parameters are the chemical freeze-out temperature (the temperature of the system), T_{ch}, the baryon and strangeness chemical potentials, μ_B and μ_S, respectively, and the ad-hoc strangeness suppression factor, γ_S.

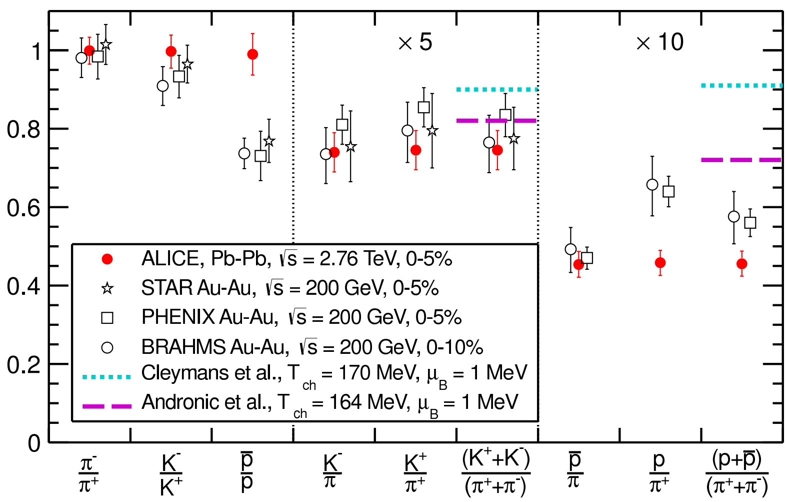

Figure 1.5: The tharmal model fit for particle ratios to Pb-Pb, pp and Au+Au collisions; fit results are taken from Ref. (46).

The measured particle abundance ratios are fit by the chemical equilibrium model. The ratios included in the fit are: π^-/π^+, K^-/K^+, $\bar{p}/p$, K^-/π^-, $\bar{p}/\pi^-$. The fit is performed for each collision system and each multiplicity or centrality class. Figure 1.5 shows the extracted T_{ch} for Pb-Pb, pp and Au+Au results from Ref. (46) .

The strangeness chemical potential is small and close to zero. It is mainly reflected in the K/π and K^-/K^+ ratios, the K^-/K^+ ratio is correlated with the $\bar{p}/p$ ratio by a universal curve. In the chemical equilibrium picture without considering resonance decays, these ratios are simply equal to $K^-/K^+ = \exp[(-2\mu_B/3 + 2\mu_S)/T_{ch}]$ and $\bar{p}/p = \exp(-2\mu_B/T_{ch})$, respectively. Weak decays and resonance decays complicate the situation, but the effects of decays are small for the K^-/K^+ and $\bar{p}/p$ ratios. A power-law fit to all data points in Fig. 1.6 yields $K^-/K^+ \propto (\bar{p}/p)^{0.21}$. This gives $\mu_S/\mu_B \approx 0.12$ in the chemical equilibrium picture. Analyses of chemical freeze-out parameters in heavy-ion collisions at other energies indicate a similar relationship (45). The strong correlation between μ_S and μ_B should not come as a surprise, as the (anti)hyperons couple these two parameters naturally. However, the same relationship holding for different energies is not expected a priori.

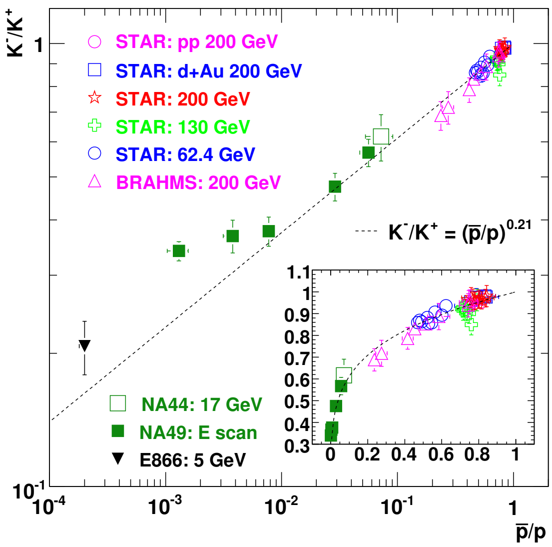

Figure 1.6: K^-/K^+ to $\bar{p}/p$ plot for 200GeV Au+Au collision.

The extracted chemical freeze-out temperature is shown in Fig. 1.5. A striking feature is that the chemical freeze-out temperature is independent of collision system or centrality. In each system investigated the extracted chemical freeze-out temperature is $T_{ch} \approx 156$ MeV which is close to the Lattice QCD calculation of the cross-over temperature between the deconfined phase and the hadronic phase for three flavors (154 ± 8 MeV) (26). On the other hand, the initial conditions in Au+Au collisions of different centralities (and at different energies) are very different. In other words, systems starting off with different initial conditions always evolve toward a 'universal' condition at chemical freeze-out, independent of the initial conditions (46). The proximity of the fit T_{ch} and the predicted phase-transition temperature strongly suggests that chemical freeze-out happens at the phase-transition boundary, or hadronization. Indeed, hadronization should be universal.

1.4.2 Kinetic Freeze-out Properties

The measured p_{T}spectral shape flattens significantly with increasing particle mass in central Au+Au collisions. This suggests the presence of a collective transverse radial flow field, although other physics mechanisms such as (semi-)hard scatterings also contribute. As shown in Figs. 1.7 the spectra are well described by the hydrodynamics-motivated blast-wave model (38; 39; 40; 41; 42; 43; 44). The blast-wave model makes the simple assumption that particles are locally thermalized at a kinetic freeze-out temperature and are moving with a common collective transverse radial flow velocity field. The common flow velocity field results in a larger transverse momentum of heavier particles, leading to the change in the observed spectral shape with increasing particle mass.

Assuming a hard-sphere uniform density particle source with a kinetic freeze-out temperature T_{kin} and a transverse radial flow velocity β, the particle transverse momentum spectral shape is given by (38)

$$\frac{dN}{p_T dp_T} \propto \int_0^R r dr m_T I_0 \left(\frac{p_T \sinh\rho}{T_{kin}}\right) K_1 \left(\frac{m_T \cosh\rho}{T_{kin}}\right) \tag{1.7}$$

where $\rho = \tanh^{-1}\beta$, and I_0 and K_1 are the modified Bessel functions. We use a flow velocity profile of the form

$$\beta = \beta_S \left(r/R\right)^n \ , \tag{1.8}$$

where β_S is the surface velocity and r/R is the relative radial position in the thermal source. The choice of the value of R bears no effect in the model.

Six particle spectra ($\pi^{\pm}$, $K^{\pm}$, p and $\bar{p}$) of a given centrality bin are fit simultaneously with the blast-wave model. The free parameters are: the kinetic freeze-out temperature, T_{kin}, the average transverse flow velocity, $\langle\beta\rangle = \frac{2}{2+n}\beta_S$, and the exponent of the assumed flow velocity profile, n. The low momentum part of the pion spectra ($p_T < 0.5$ GeV/c) are excluded from the fit, due to significant contributions from resonance decays.

The blast-wave fit results for Au+Au collisions are listed in Figs. 1.7. The χ^2/NDF is smaller than unity because the point-to-point systematic errors, which are included in the fit and dominate over statistical ones, are estimated on the conservative side and might not be completely random. If the χ^2/NDF is scaled such that the minimum is unity, then somewhat smaller statistical errors on the fit parameters are obtained.

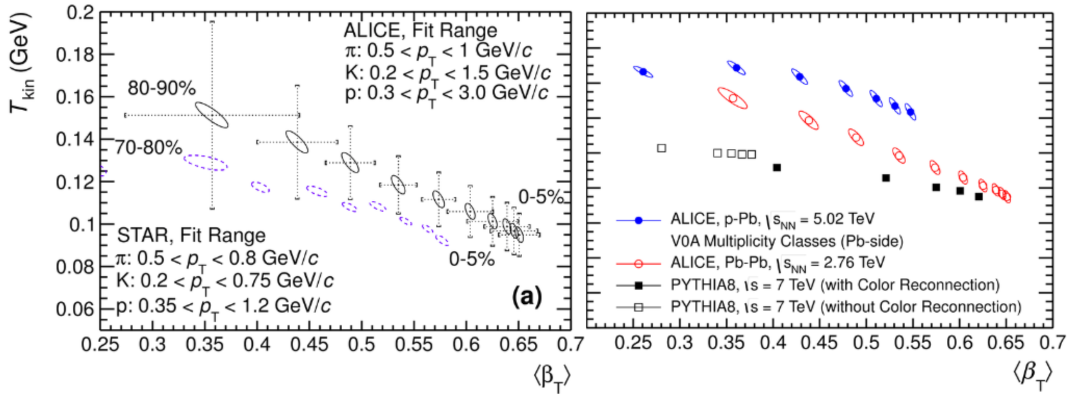

Figure 1.7: T_{kin} and $\langle\beta\rangle$ extracted from simultaneous Blast Wave fitting of A+A, p+A and p+p collisions.

Figure 1.7 shows the extracted average transverse radial flow velocity $\langle\beta\rangle$ as a function of the event multiplicity. The $\langle\beta\rangle$ increases dramatically with increasing centrality in A+A collisions. The effect of the $\langle\beta\rangle$ increase on the transverse spectra is significantly stronger than the counter effect of the T_{kin} drop. The combination of the π, K, p and $\bar{p}$ spectra favor an increase of $\langle\beta\rangle$ with centrality rather than a similar increase in T_{kin}. The spectra are found to be less sensitive to the kinetic freeze-out temperature than the flow velocity.

The model is found to give a fairly good description of the measured $\pi^{\pm}$, $K^{\pm}$, p and $\bar{p}$ spectra. Surprisingly, the fit average flow velocities from pp and d+Au collisions are not small, and certainly not zero as one would naively expect. This should not be taken as a proof that there is collective flow in pp and d+Au collisions, because hard scatterings and jet production, generating relatively more high-p_T hadrons, can mimic collective flow and give rise to the extracted finite $\langle\beta\rangle$ (47). In d+Au collisions, there is an additional effect of initial state scattering, which broadens the transverse momentum of the colliding constituents and hence the produced hadrons in the final state. Meanwhile, statistical global energy and momentum conservation can deplete large momentum particles shown in recent studies (48), and the effect can be large in low multiplicity collisions. In the same framework, large initial energy fluctuation available for mid-rapidity particle production tends to harden the transverse spectrum (50; 53). The interplay, as well as the relevance of statistical global energy and momentum conservation in high energy collisions, needs further quantitative studies.

In A+A collisions the contribution from hard (and semi-hard) scatterings is larger than in pp collisions because hard scatterings scale with the number of binary nucleon-nucleon collisions while soft processes scale with the number of participant nucleons. From the two-component model study, the hard-scattering contribution in pp collisions at 200 GeV is 13%, while in the top 5% central Au+Au collisions it is 46%, a factor of 3.5 times that in pp. From the blast-wave model with a linear flow velocity profile, the increase in average $\langle p_{\mathrm{T}}\rangle$ *or* $\langle \mathrm{m_T}\rangle$ due to radial flow velocity $\langle\beta\rangle$ is approximately proportional to $\langle\beta\rangle^3$. Assuming the apparent finite flow velocity extracted from pp data, $\langle\beta\rangle_{pp} = 0.24 \pm 0.08$, is solely due to the energy excess of produced particles from hard processes over soft processes, and assuming the particle production from hard processes is identical in pp and central A+A collisions, then the hard processes in central Au+Au collisions would generate an apparent flow velocity of $3.5^{1/3}\langle\beta\rangle_{pp} = 0.36$. However, the extracted flow velocity from the blast-wave model for central A+A collisions is significantly larger, $\langle\beta\rangle_{\mathrm{AA}} = 0.59 \pm 0.05$. One may take the additional excess in central Au+Au collisions as the effect of collective transverse radial flow, and estimate the collective flow velocity in central Au+Au collisions by $\langle\beta\rangle_{\text{flow}} \sim \sqrt[3]{\langle\beta\rangle^3_{\text{AA}} - 3.5\langle\beta\rangle^3_{pp}} = 0.54 \pm 0.08$. According to Kharzeev-Nardi two-component model likely overestimates the fraction of the hard component in pp collisions. However, using the hard-component fraction obtained from Ref. (47), with the same assumptions as stated above, the estimate of the collective flow velocity in central Au+Au collisions is not significantly altered. We note, however, that the preceding estimate is simplistic. The full understanding of the effects on transverse spectra from radial flow, (semi-)hard scatterings, interactions between (semi-)hard scatterings and the medium (49; 51; 52), and the interplay between these effects will need rigorous study. It should be understood that the extracted values of the radial flow velocity in this thesis is under the framework of the Blast-wave model.

1.5 Some jargons

The field of the relativistic heavy ion physics is saturated with jargon, a minefield for the uninitiated. Before we embark on the rest of this dissertation, here is a brief description of some of the commonly used terms:

- **Center of mass energy:** a.k.a. $\sqrt{s}$, this is the Lorentz invariant quantity:

$$s = (p_1 + p_2)_\mu (p_1 + p_2)^\mu \tag{1.9}$$

For nuclei with energy E_i and 3-momentum $\mathbf{p_i}$, it reduces to:

$$\sqrt{s} = \sqrt{m_1^2 + 2E_1E_2 - 2\mathbf{p_1} \cdot \mathbf{p_2} + \mathbf{m_2^2}} \tag{1.10}$$

For instance at RHIC (Run 2 and 3), the center-of-mass energy per nucleon is $\sqrt{s_{NN}} = 200$ GeV.

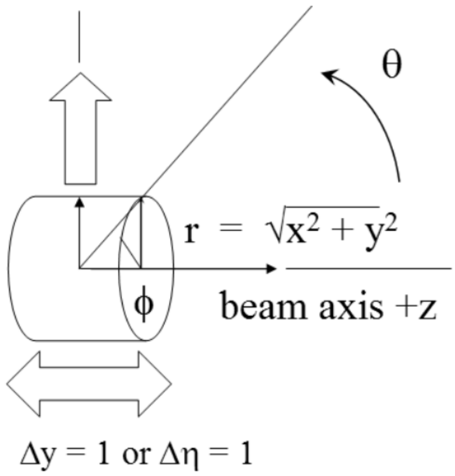

Figure 1.8: Beam axis, transverse momentum p_T and rapidity y.

- **Tranverse momentum p_T:** this is simply the projection of a particle's momentum perpendicular to the collision axis: z (see Figure 1.8).

$$p_T = p \sin\theta \tag{1.11}$$

where θ is the polar angle along the z-axis. A common variable derived from this is the transverse energy (or mass) $m_T = \sqrt{p_T^2 + m_0^2}$.

- **Rapidity y:** this defines the longitudinal motion scale for a particle of mass m_0 moving along z-axis (see Figure 1.8):

$$y = \frac{1}{2}\log\left(\frac{E+p_z}{E-p_z}\right) \tag{1.12}$$

Since there is cylindrical symmetry around the collision axis, this allows us to describe the 4-momentum of particle in terms of its transverse momentum p_T, rapidity y and the transverse energy m_T as:

$$p^\mu = (m_T \cosh y, p_T \cos\phi_0, m_T \sinh y) \tag{1.13}$$

- **Pseudorapidity η:** derived from rapidity (Eq. 1.12), this variable is used when the particle in question is unidentified i.e., m_0 is not known:

$$\eta = -\log\left(\tan\frac{\theta}{2}\right) \tag{1.14}$$

Where θ is the angle w.r.t. the beam axis. η is often used to describe geometrical acceptances of detectors.

- **Invariant yield:** the invariant differential cross section of a particle is the probability of obtaining d^3N particles in the phase space volume dp^3/E in a given number of events N_{event}:

$$\frac{1}{N_{event}}E\frac{d^3N}{dp^3} = \frac{d^3N}{N_{event}p_T dp_T dy} \tag{1.15}$$

In cylindrical coordinates $dp^3 = dp_x dp_y dp_z$ reduces to $p_T dp_T d\phi m_t \cosh y dy$. Due to azimuthal symmetry we get a factor of $1/2\pi$, resulting in the form:

$$\frac{1}{N_{event}}E\frac{d^2N}{dp^2} = \frac{d^2N}{2\pi N_{event}p_T dp_T dy} \tag{1.16}$$

Using $dN/p_T dp_T = dN/m_T dm_T$, we get our final form:

$$\frac{1}{N_{event}}E\frac{d^2N}{dp^2} = \frac{d^2N}{2\pi N_{event}m_T dm_T dy} \tag{1.17}$$

- **Centrality:** when the two nuclei collide, there can be range of impact parameters. Events with a small impact parameter are known as central events whereas events with a large impact parameter are called peripheral (see Figure 1.9), and the variation in impact parameters is called centrality.

- **Minimum Bias:** this is the collection of events containing all possible ranges of impact

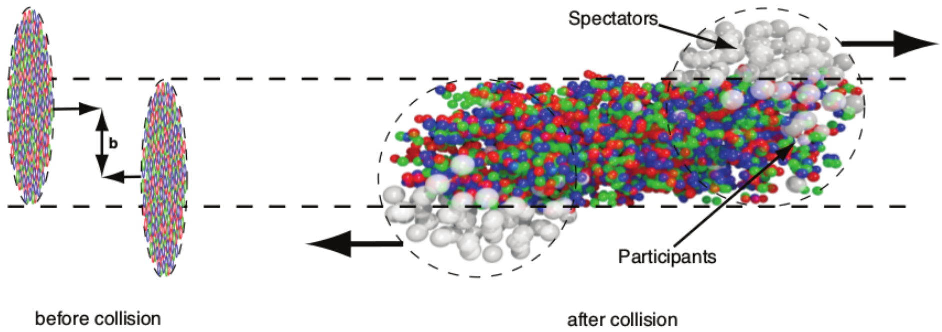

Figure 1.9: Centrality is related to impact parameter: large impact parameter events are called peripheral and small impact parameter events are called central.

parameters. This is important so that our data does not have any bias due to events that might be triggered by specific signals e.g. presence of a high p_T particle.

1.6 Signatures of Quark Gluon Plasma (QGP)

RHIC and LHC aims to provide facilities for studying physics of dense and hot hadronic matter in ultra relativistic heavy ion collisions. The main goal is to study the quark gluon plasma. Furthermore, the detailed characteristics of the phase transitions and QCD bulk matter involving elementary quantum fields will be extracted. It is extremely interesting to establish the equation of state and understand the phase diagram of strongly interacting matter. Moreover ALICE will allow to explore and test QCD in its natural scale (Λ QCD) including problems of confinement and chiral symmetry breaking. There is no direct way to check the existence of quark-gluon plasma. Due to the multi-particle interactions, the dynamics of nuclear collision is so complicated, that any conclusions related to the properties of QGP from indirect signals. Moreover, a unique signal that would confirm QGP formation wheather exist or not, and we have to rely on accumulated observations of the collision. I will discuss some of the general signatures of the search for the QGP from the early days before the start of the RHIC accelerator (STAR,PHENIX and PHOBOS) what was learned at RHIC and what is expected to be measured at the LHC in ALICE experiment.

- Particle production and Multiplicity densities
- Strangeness enhancement
- Flow
- Perfect liquid (η/s)
- High p_T hadron suppression
- Quarkonia suppression
- Direct photons and Lepton pairs
- Hanbury Brown-Twiss (HBT)
- p_T and Temperature fluctuations

1.6.1 Particle production and Multiplicity densities:

The interactions between heavy ions are complex and for their interpretation the knowledge of the initial conditions of the fireball at the instant after the collision is essential. The multiplicity, that is, the total number of particles produced in a collision, tells us a lot about how the quarks and gluons of the incoming nuclei transform into particles (pions, kaons etc) observed in the detectors; also about the energy density reached within the collision and the temperature of the fireball.

The most trivial, but very important day-one observable is particle multiplicity and its rapidity density. Since it is associated with the energy density, it is also connected with most of the other observables. The number of generated particles is correlated with the distance between centres of the colliding nuclei (impact parameter).

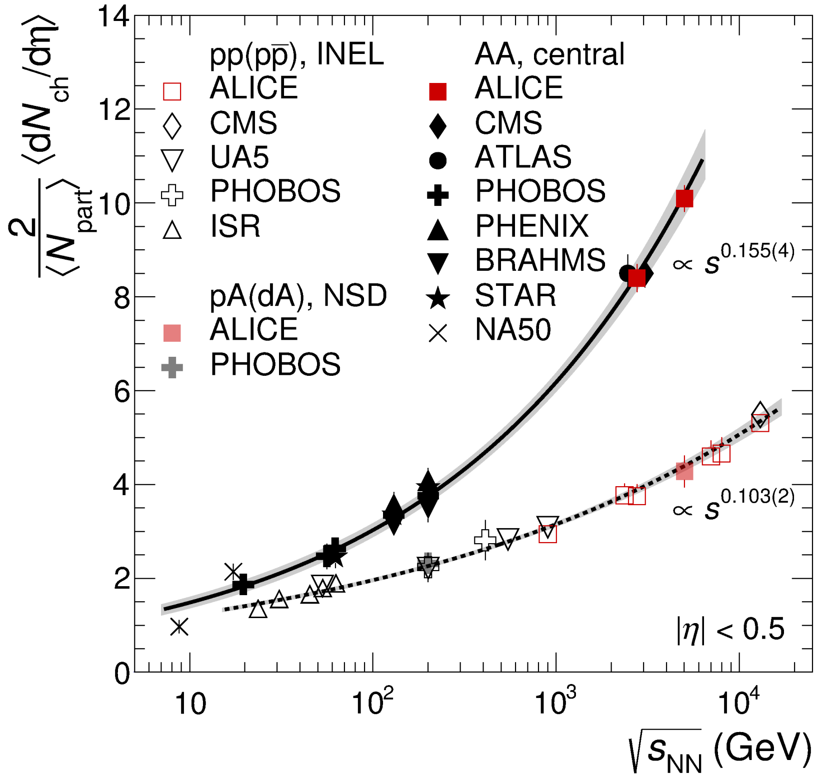

Figure 1.10: Charged particle multiplicity per colliding nucleon pair as a function of the collision energy.

Head-on (central) collisions (small impact parameter), when the largest number of incoming protons and neutrons participate in the collision, generate most particles. The charged particle multiplicity per colliding nucleon pair measured by ALICE for the most central collisions is double that measured at RHIC, where the collision energy is factor 14 lower, fig.1. This shows that the system created at LHC has much higher energy density and is at least 30% hotter that at RHIC. Fig. 2 shows the charged particle multiplicity as a function of the number of participants. The charecteristics property of the $A-A$ data, measured at different $\sqrt{S_{NN}}$ upto 5.02 TeV (79; 80) which is calculated from the observed as $\propto\ s^{0.155}$ dependence of the results in the most central collisions and signaficantly differ from The proton–proton result at the same energies ($\sqrt{S}$) (78) with the $\propto\ s^{0.103}$ dependence.

1.6.2 Strangeness enhancement

Production of strangeness in pp collisions is very regular over wide range of collision energies with an almost constant ratio between newly produced s and u quarks. Similarly, in the scenario in which QGP is not created strangeness production is suppressed comparing to production of up and down quarks, because s quarks are heavier. The suppression increases for particles which have more (anti)strange quarks.
One cannot assume that under all conditions the yield of strange quarks is in thermal equilibrium. In general, the quark-flavor composition of the plasma varies during its ultra short lifetime as new flavors of quarks such as strangeness are cooked up inside. The up and down quarks from which normal matter is made are easily produced as quark-antiquark pairs in the hot fireball because they have small masses. On the other hand the next lightest quark flavor, strange quarks, will reach its high quark-gluon plasma thermal abundance only on the most violent collisions generating high temperatures and that at the end of the cooking process. If QGP is formed the strange quark content is rapidly saturated with $s\bar{s}$ pair creation due to gg or $q\bar{q}$ interactions. Thus, strange, antistrange and multistrange hadrons appear in the final state, which are not observed in a purely hadronic scenario and cannot be explained in any other way than by the existence of QGP. Furthermore enhanced strangeness cannot be destroyed by interactions during freeze-out and expansion [63, 64].

The main measurement in strangeness enhancement determination is the K/π ratio, which can be obtained with small uncertainty due to the high multiplicities of these particles. It also provides informa- tion about time-scale of strangeness equilibration. Thus k/π and p/π fluctuations nature contrasting each other is a one of the most important signature in QGP formation and finding its various properties, Ordinary matter around us is made of protons and neutrons, which in turn are composed of up (u) and down (d) quarks. The next quark that can be liberated from the sea of quark-anti-quark pairs that populate the vacuum is the strange quark (s-quark). It is heavier than u and d, yet close enough in mass to undergo production and modification processes in similar manner. That, and the relative abundance of the strange

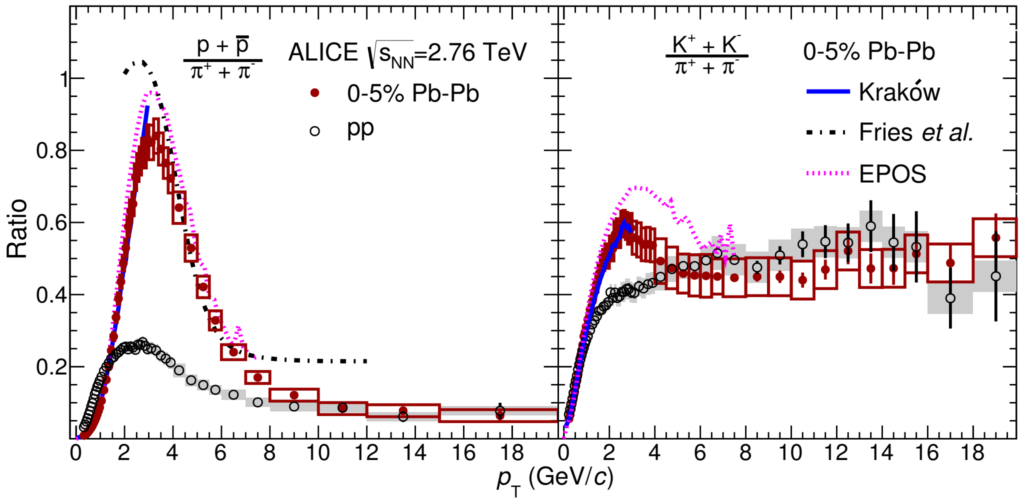

Figure 1.11: Particle ratios as a function of p_T measured in p-p collision and the most central, 0-5%, Pb-Pb (A-A) collisions.

quark in high-energy interactions, make the s-quark a very useful study tool for proton-proton and heavy nucleus collisions. Strange particles, K-mesons (Kaons, made up of a strange and a non-strange quark pair), Λ (uds), Ξ (dss) and Ω (sss) baryons have an appreciable lifetime before they decay into ordinary matter. These decays have a characteristic geometrical configuration, which allows an effective reconstruction of strange particles. An enhancement in the production of particles with strange quarks has long been thought to be a signature of extra degrees of freedom available in the QGP. Indeed, this enhancement has been seen at lower energies as well: the larger the volume of the collision, the more the number of Λ (uds), Ξ (dss) and Ω (sss) baryons increases with respect to the baseline (a pp or a Be-Be collision). This is also observed at 2.76 TeV Pb-Pb collisions.

1.6.3 Flow

Collective flow is an important consequence of the Quark Gluon Plasma formation, hence an interesting observable used for the study of the quark gluon plasma: it provides information on the equation of state and the transport properties of matter created in heavy-ion collisions. Since

QGP is by definition a thermalised system of quark and gluons, it has an associated thermal pressure. The fireball is surrounded by the vacuum, this creates a pressure gradient which leads to a collective expansion of the system. The collective motion is interpreted by hydrodynamics. Collective flow is an important tool to test the assumption of the equilibrium of the system.

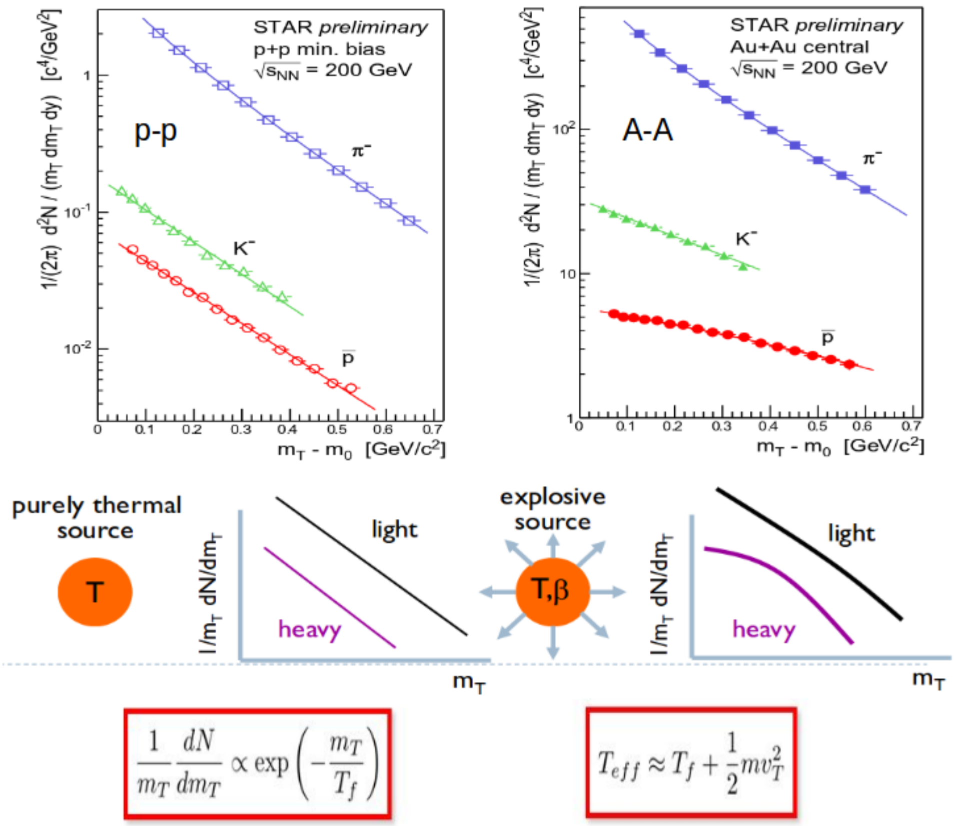

Figure 1.12: Pion, kaon and antiproton spectra from 200 A GeV minimum bias p-p collisions (left) and central Au-Au collisions (right) , measured by the STAR experiment. Note the similar slopes for kaons and antiprotons in p-p collisions and their dramatically different slopes at low transverse kinetic energy in central Au-Au collisions (81)

Radial Flow:

The collective expansion of the nuclear fireball results in a flattening of the p_T spectra with respect to hadron-hadron collisions. Particle spectra in central Au-Au and minimum bias p-p collisions at $\sqrt{S_{NN}}$ = 200 GeV are reported in

Figure 1.12. In p-p collisions π, K and p have a common slope, indicating a no medium formation, whereas in A-A collsion although the kinetic temperature (T_{kin}) is same but due to radial boost multiplied with different mass make the slope different for different particles. The inverse slope of these spectra reflects a blueshifted freeze-out temperature, given by the collective expansion of the system.

Higher Harmonic flow:

The anisotropic flow in heavy ion collisions at ultra-relativistic energies is expected to provide information about the early stages of the evolution of the system. It may also provide information about the reaction dynamics and fluctuations at the initial stage of the collision. The anisotropic flow arises when the spatial anisotropy at the early times after the collision gets converted in to momentum anisotropy.

Heavy-ions are extended object and the system created in central nucleus-nucleus collisions is different from the one created in peripheral collisions. For non central collisions, the overlapping region is almond shaped, the pressure gradient is different along the minor axes of the system is larger than the minor axes in the transverse plane. These anisotropic pressure gradients give rise to azimuthal anisotropic patterns in the momentum distribution of particles in the final state. As a consequence of the interaction among the medium constituents, hydrodynamic evolution of the fireball will translate the initial geometric eccentricity into final state momentum anisotropy.

To quantify such effect, one may perform the Fourier decomposition for the transverse momentum distribution of final state particles,

$$\frac{dN}{dydp_T d\psi} \propto 1 + 2\sum_n v_n(p_T, y)\cos\left[n(\psi - \Psi_n(p_T, y))\right] \ , \tag{1.18}$$

where v_n and Ψ_n are the magnitude and orientation angle (event plane) of the n-th order anisotropic flow vector $\mathbf{v}_n = v_n e^{in\Psi_n}$. Note that v_n and Ψ_n are defined for a single collision,

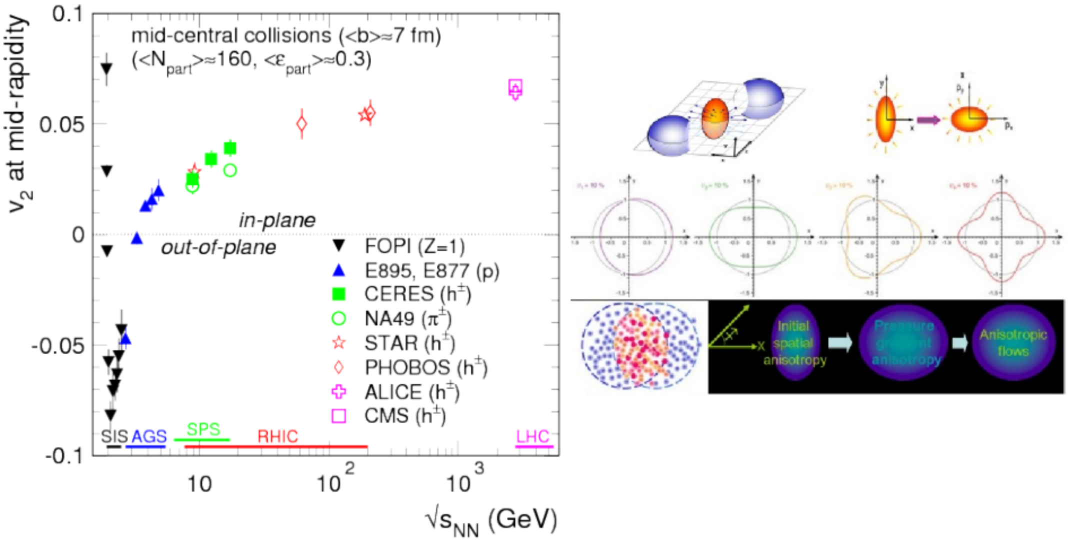

Figure 1.13: Beam Energy Scan of integrated elliptic flow ($v2\{4\}$) for the 20-30% central A-A collisions (**?**).

and can be p_T (and y) dependent or integrated. The anisotropic flow may be obtained from the final state momentum distribution as follows:

$$\mathbf{v}_n = v_n e^{in\Psi_n} = \langle e^{in\psi} \rangle \tag{1.19}$$

1.6.4 A perfect liquid at the LHC

An interesting observable used for the study of the quark gluon plasma is flow: it provides information on the equation of state and the transport properties of matter created in heavy-ion collisions. Multiple interactions between the constituents of the created matter and initial asymmetries in the spatial geometry of non-central collisions result in an azimuthal anisotropy in particle production. The measured azimuthal distribution of particles in momentum space can be decomposed into Fourier coefficients. The second Fourier coefficient of this azimuthal asymmetry is known as elliptic flow. Its magnitude depends strongly on the friction in the created matter, characterized be the ratio η/s, where η is the shear viscosity and s the entropy. For a less denser fluid such as water the value of η/s is small. For a thick fluid η/s has large values.

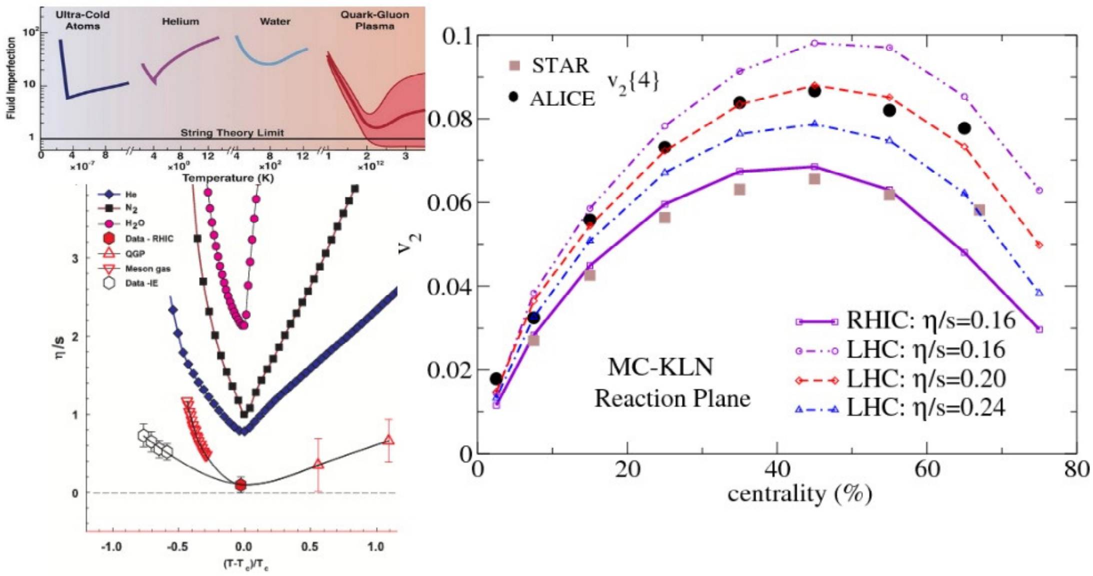

Figure 1.14: QGP is near Perfect liquid??? (85; 86)

Measurements of the elliptic flow at RHIC had revealed that the hot matter created in heavy ion collisions flows like a fluid with little friction, with η/s close to the lower limit for a perfect fluid. At LHC this observation was confirmed, with values of the elliptic flow higher by 30% with respect to those at RHIC. Fig. 1.14 shows the anisotropic flow coefficients v_n as a function of centrality in Au-Au collisions at 200 AGeV at RHIC (left panel) and in Pb-Pb collisions at 2.76 AGeV at the LHC (right panel). The theoretical results are from (3+1)-dimensional viscous hydrodynamics model calculations.(85). The data at RHIC from STAR (87) and LHC are from ALICE (86). The best descriptions to the experimental data give the average value of η/s to be 0.16 at RHIC and 0.20 at the LHC. This means that on average the QGP medium produced at the LHC is less strongly coupled than that at RHIC. Since the temperature of the medium is higher at the LHC, this suggests that there is a strong temperature dependence for η/s. The precise determination of the temperature-dependent specific shear viscosity $\eta/s(T)$ is one of the essential tasks in the current study of heavy-ion collisions.

1.6.5 High p_T hadron suppression

When the fast partons (quarks and gluons) produced from heavy ion collisions propagate through the dense medium of the fireball, they lose energy via gluon radiation or elastic scattering. The amount of radiated energy depends on the density of the medium and distance travelled by the parton in the medium, as well as the flavour of the parton. These partons become observable as jets of hadrons when they hadronize and the energy loss becomes evident in a phenomenon known as jet quenching. Instead of two jets going back-to-back and having similar energies, a striking imbalance is observed, one jet being almost absorbed by the medium as shown in the figure.

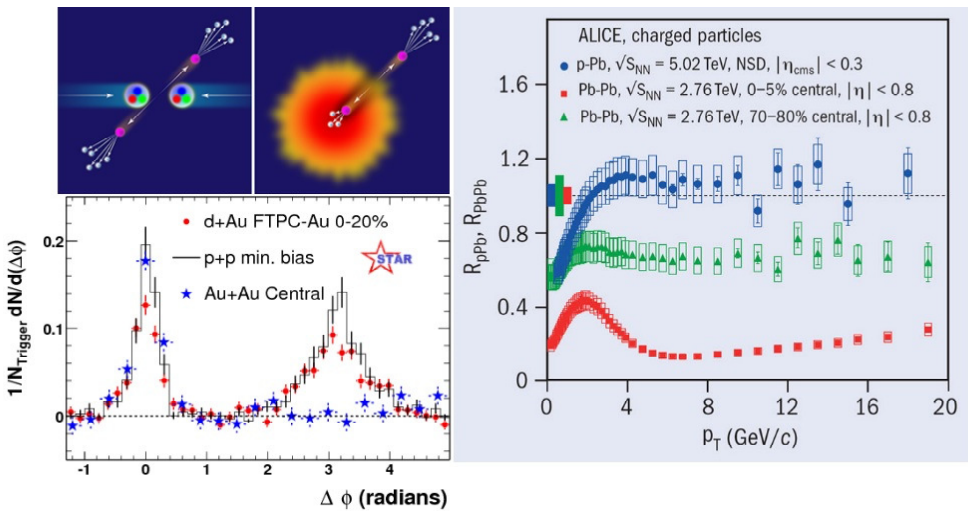

Figure 1.15: The suppression of the strongly interacting particles in A-A collisions compared to p-p or p-A collisions is evident. left: STAR measurement of the hadron yield at $\eta = 0$ when triggering on a jet at $\eta = 0$. right: ALICE measurement of R_{CP} with At high p_T, the effect of the medium is evident (91)

If the medium created in a heavy ion collision is truly strongly interacting it should affect jets propagating through it if these jets are able to interact strongly. Due to various low p_T collective effects such as color screening or Cronin enhancement this effect should be most pronounced at high p_T . To quantify this effect the heavy ion yields are compared to the scaled yields of p+p collisions at the same energy. This is expressed through the nuclear modification factor. The

R_{AA} is defined as

$$R_{AA} = \frac{d^2N_{AA}/dp_T d\eta}{< T_{AA} > d^2\sigma_{pp}/dp_T d\eta}, \tag{1.20}$$

where $d^2N_{AA}/dp_T d\eta$ represents the differential particle yield in nucleus-nucleus collisions and $d^2\sigma_{pp}/dp_T d\eta$ is the cross-section in proton-proton collisions. In the above expression, nuclear overlap function $< T_{AA} >$ is obtained from Glauber model and is proportional to the number of binary collisions ($< N_{coll} >$). At high p_T, and in the absence of medium effects, R_{AA} is expected to be unity. In the region of low transverse momentum,the soft scatterings are the dominant processes, and so R_{AA} deviates from unity.

The R_{CP} is thus defined as,

$$R_{CP} = \frac{< N_{coll}^{peri} > d^2N_{cent}/dp_T d\eta}{< N_{coll}^{cent} > .d^2N_{peri}/dp_T d\eta}, \tag{1.21}$$

where $< N_{coll}^{cent} >$ and $< N_{coll}^{peri} >$ are the average number of binary collisions in central and peripheral $Au - Au$ collisions, respectively. Nuclear medium effects are expected to be much stronger in central relative to peripheral collisions, which makes R_{CP} an important physical quantity to study these effects.

1.6.6 Quarkonia suppression

Heavy-flavour particles are recognized as effective probes of the highly excited system (medium) formed in nucleus-nucleus collisions; they are expected to be sensitive to its energy density, through the mechanism of in-medium energy loss. Because of the QCD nature of parton energy-loss, quarks are predicted to lose less energy than gluons (which have a higher colour charge); in addition, the so-called "dead-cone" effect and other mechanisms are expected to reduce the energy loss of heavy partons with respect to light ones. Therefore, there a pattern of gradually decreasing R_{AA} suppression should emerge when going from the mostly gluon-originated light-flavour hadrons (e.g. pions) to the heavier D and B mesons:

R_{AA} (π) < R_{AA} (D) < R_{AA} (B)

The measurement and comparison of these different probes provides a unique test of the colour-charge and mass dependence of parton energy-loss. The J/Ψ is composed of a heavy quark-antiquark pair with the two objects orbiting at a relative distance of about 0.5 fm, held together by the strong colour interaction. However, if such a state were to be placed inside a QGP, it turns out that its binding could be screened by the huge number of colour charges (quarks and gluons) that make up the QGP freely roaming around it. This causes the binding of the quark and antiquark in the J/Ψ to become weaker so that ultimately the pair disintegrates and the J/Ψ melted i.e. it is "suppressed". Theory has shown that the probability of dissociation depends on the temperature of the QGP, so that the observation of a suppression of the J/Ψ can be seen as a way to place a "thermometer" in the medium itself.

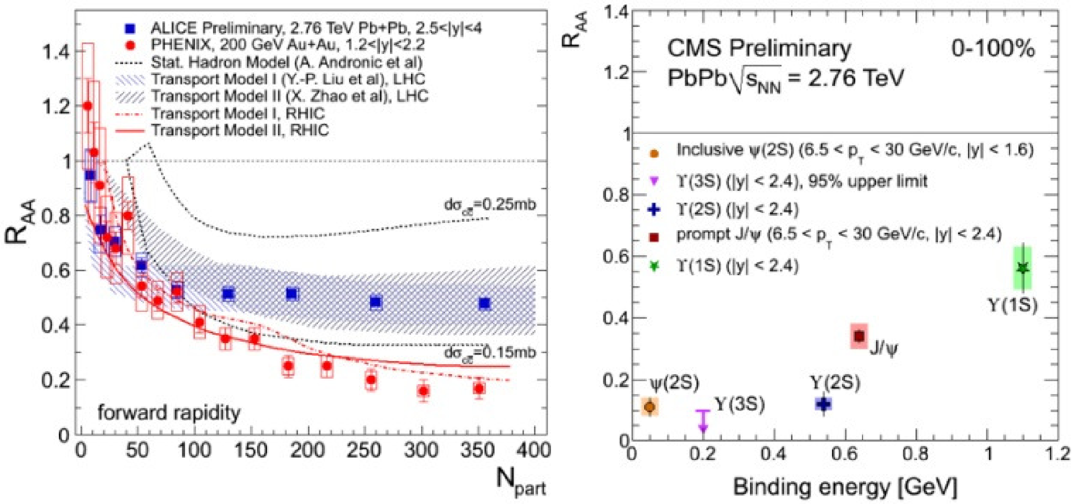

Figure 1.16: J/Ψ suppression (66)

As predicted by the theory, a suppression of the J/Ψ yield was observed with respect to what would be expected from a mere superposition of production from elementary nucleon?nucleon collisions. However, the experiments also made some puzzling observations. In particular, the size of the suppression (about 60-70% for central, i.e. head-on nucleus-nucleus collisions) was found to be approximately the same at the SPS and RHIC, despite the jump in the centre-of-mass energy of more than one order of magnitude, which would suggest higher QGP temperatures at RHIC. Ingenious explanations were suggested but a clear-cut explanation of this puzzle proved impossible.

At the LHC,extremely interesting scenario are expected. In particular, a much higher number of charm-anticharm pairs are produced in the nuclear interaction, thanks to the unprecedented centre-of-mass energies. As a consequence, even a suppression of the J/Ψ yield in the hot QGP phase could be more than by a statistical combination of charm-anticharm pairs happening when the system, after expansion and cooling, finally crosses the temperature boundary between the QGP and a hot gas of particles. If the density of heavy quark pairs is large enough, this regeneration process may even lead to an enhancement of the J/Ψ yield.

1.6.7 Direct photons and measurement of the QGP temperature:

One of the fancy-classic signals expected for a quark-gluon plasma (QGP) is the radiation of "thermal photons", with a spectrum reflecting the temperature of the system. Direct photons are defined as photons not coming from decays of hadrons, so photons from initial hard parton-scatterings (prompt photons and photons produced in the fragmentation of jets). With a mean-free path much larger than nuclear scales, these photons leave the reaction zone created in a nucleus-nucleus collision unscathed. So, unlike hadrons, they provide a direct means to examine the early hot phase of the collision. However, thermal photons are produced throughout the entire evolution of the reaction and also after the transition of the QGP to a hot gas of hadrons. In the PbPb collisions at the LHC, thermal photons are expected to be a significant source of photons at low energies (transverse momenta, pT, less than around 5 GeV/c). The experimental challenge in detecting them comes from the huge background of photons from hadron decays, predominantly from the two-photon decays of neutral pions and mesons.

For p_T greater than around 4 GeV/c, the measured spectrum agrees with that for photons from initial hard scattering obtained in a next-to-leading-order perturbative QCD calculation. For lower pT, however, the spectrum has an exponential shape and lies significantly above the

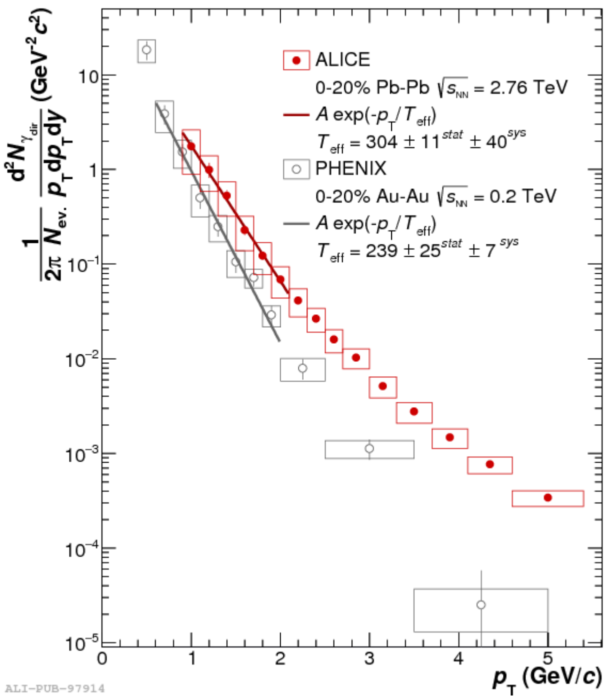

Figure 1.17: Prompt photon measurements in RHIC and LHC (77)

expectation for hard scattering, as the figure shows. The inverse slope parameter measured by ALICE, T = 304 ± 40 MeV, is larger than the value observed in Au-Au collisions at $\sqrt{S_{NN}}$ = 0.2 TeV at Brookhaven's Relativistic Heavy-Ion Collider (RHIC), T = 239 ± 25 MeV. InTypical hydrodynamic models, this parameter corresponds to an effective temperature averaged over the time evolution of the reaction. The measured values suggest initial temperatures well above the critical temperature of 150-160 MeV at which the transition between ordinary hadronic matter and the QGP occurs. Photons are not sensitive to the colour charge of the QGP, they escape from the collision zone without interacting in the medium and carry pristine information about their parent quarks and gluons, this features made prompt photon studies as a unique-one.

1.6.8 Temperature flucutuations:

Due to collisions of heavy ions, fluctuations and their dependence on the parameters of the collision contains more information than the corresponding moments of one-particle inclusive distributions. Some of these questions have been addressed in (55; 56) where it was pointed out that, temperature fluctuations are related to heat capacity via

$$\frac{\langle(\Delta T)^2\rangle}{T^2} = \frac{1}{C_V(T)}, \tag{1.22}$$

and so can tell us about *thermodynamic* properties of the matter at freeze-out. As common picture of phase transition is in T-μ plane, one can also think this in (56) relate fluctuations in the occupation of certain momentum bins with $\partial\mu/\partial N$ and the average quantum density in phase space. Additionally, Mrówczyński has discussed the study of the compressibility of hadronic matter at freeze-out via the event-by-event fluctuations of the particle number (57) and Gaździcki(58) and Mrówczyński(59) have considered event-by-event fluctuations of the kaon to pion ratio as measured by NA49(54). Thermodynamic relations like (1.22) suggest the following strategy. Measure the mean transverse momentum fluctuations on event-by-event basis. Since the inclusive average of the transverse momentum ofparticles from an ensemble of events reflects the temperature of the ensemble, one can use p_T, the mean transverse momentum in a single event as a proxy for the temperature of a single event, and so use (1.22) to obtain C_V.

For a system in equilibrium, the mean values of T and E are directly related by an equation of state $E(T)$; their fluctuations, however, have quite different behavior as a function of C_V, and therefore behave differently when C_V diverges at a critical point. So, is the centrality and energy dependence of the event-by-event fluctuations of Temperature and p_T could use to study phase diagram and also tells something about the thermodynamic behavior of the matter produced at heavy ion collision ? or from energy dependence in C_V from ΔT could sense the critical point as C_V diverges at critical point. In this thesis, I discuss in detailed how temperature fluctuation could be a important tool for signature of QGP, signal extraction strategy, relation to the thermodynamic variables and analysis in next chapters.

Bibliography

[1] D.J. Gross and F. Wilczek, Phys. Rev. Lett. 30 (1973) 1343 ; H.D. Politzer, Phys. Rev. Lett. 30 (1973) 1346.

[2] J.C. Collins and M.J. Perry, Phys. Rev. Lett. 34 (1975) 1353.

[3] D.H. Rischke review for Prog. Part. Nucl. Phys. 52 (2004) 197-296 (nucl-th/0305030v2).

[4] E.V.Shuryak, Phys. Rep. 61 (1980) 71.

[5] J.C.Collins and M.J.Perry, Phys. Rev. Lett 34 (1975) 1353.

[6] F. Karsch, in: Lecture Notes in Physics, vol. 583, Springer, Berlin, 2002, p.209; F. Karsch, K. Redlich and A. Tawk, Phys.Lett. B571 (2003) 67-74, (hep-ph/0306208v2); Karsch F 2002 Nucl. Phys. A698 199

[7] Huovinen P, et al. *Phys. Lett.* B503:58 (2001)
Kolb PF, *AIP Conf. Proc.* 698:694 (2004)

[8] Kolb PF, Heinz UW. 2004. In *Quark Gluon Plasma 3*. ed. RC Hwa, XN Wang, 634. Singapore: World Scientific. preprint *arXiv:nucl-th/0305084*

[9] Hirano T, Nara Y. *Phys. Rev. C* 69:034908 (2004)

[10] Voloshin SA. *Nucl. Phys.* A715:379 (2003)

[11] Hwa RC, Yang CB. *Phys. Rev. C* 67:064902 (2003)

[12] Fries RJ, Muller B, Nonaka C, Bass SA. *Phys. Rev. Lett.* 90:202303 (2003)

[13] Greco V, Ko CM, Levai P. *Phys. Rev. Lett.* 90:202302 (2003)

[14] Molnar D, Voloshin SA. *Phys. Rev. Lett.* 91:092301 (2003)

[15] M. Gyulassy, (nucl-th/0403032); M. Gyulassy and L. McLerran, Nucl. Phys. A 750 (2005) 30.

[16] P.F.Kolb, U.Heintz, in: R.C.Hwa, X.N. Wang (Eds.), World Scientific, Singapore, 2003, (nucl-th/0305084).

[17] P. Braun-Munzinger, K. Redlich, J. Stachel, in: R.C. Hwa, X.N. Wang (Eds.), Quark Gluon Plasma 3, World Scientific, Singapore, 2003 (nucl-th/0304013).

[18] Agakishiev H, et al., STAR Collaboration, Nature 473, (2011) 353-356.

[19] B.I. Abelev, et al., STAR Collaboration, SCIENCE 328 (5974): 58-62.

[20] Thermus, A thermal Model Package for Root, S. Wheaton and J. Cleymans (hep-ph/0407174).

[21] S.A. Bass, A. Dumitru, M. Bleicher, L. Bravina, E. Zabrodin, H. Stöcker, and W. Greiner, Phys. Rev. C **60** (1999) 021902; and S.A. Bass, private communication.

[22] M. Kliemant, R. Sahoo, T. Schuster, and R. Stock, Global Properties of Nucleus-Nucleus Colli- sions, Lect.Notes Phys., vol. 785, pp. 23103, 2010.

[23] H. Satz, Colour deconfinement in nuclear collisions, Rept. Prog. Phys., vol. 63, p. 1511, 2000.

[24] I. Y. Pomeranchuk, On the theory of multiple particle production in a single collision, Dokl. Akad. Nauk Ser. Fiz., vol. 78, pp. 889891, 1951.

[25] A. Andronic and P. Braun-Munzinger, Ultrarelativistic nucleus nucleus collisions and the quark- gluon plasma, Lect. Notes Phys., vol. 652, pp. 3568, 2004.

[26] F. Karsch, Lattice QCD at high temperature and density, Lect. Notes Phys., vol. 583, pp. 209249, 2002.

[27] J. Adams et al., STAR collaboration, Nuclear Physics, A 757 (2005) 102; I. Arsene et. al., BRAHMS collaboration, Nuclear Physics, A 757 (2005) 1; B.B.Back et. al., PHOBOS collaboration, Nuclear Physics, A 757 (2005) 28; K. Adcox et. al., PHENIX collaboration, Nuclear Physics, A 757 (2005) 184.

[28] B. I. Abelev *et al.* [STAR Collaboration], Phys. Rev. C **79**, 034909 (2009).

[29] J. Cleymans, H. Oeschler, K. Redlich and S. Wheaton, Phys. Rev. C **73**, 034905 (2006).

[30] P. Braun-Munzinger and J. Stachel, Nature **448**, 302 (2007).

[31] K. Rajagopal and F. Wilczek, In *Shifman, M. (ed.): At the frontier of particle physics, vol. 3* 2061-2151 [hep-ph/0011333].

[32] J. C. Collins and M. J. Perry, Superdense Matter: Neutrons Or Asymptotically Free Quarks?, Phys. Rev. Lett., vol. 34, p. 1353, 1975.

[33] G. Baym, RHIC: From dreams to beams in two decades, Nucl. Phys., vol. A698, pp. XXIII XXXII, 2002.

[34] P. Braun-Munzinger, J. Stachel, J.P. Wessels, N. Xu, Thermal Equilibration and Expansion in Nucleus-Nucleus Collisions at the AGS Phys. Lett. B344431995 th/9410026

[35] P. Braun-Munzinger, J. Stachel, J.P. Wessels, N. Xu, Thermal and Hadrochemical Equilibration in Nucleus-Nucleus Collisions at the SPS Phys. Lett. B36511996 nucl-th/9508020

[36] P. Braun-Munzinger, I. Heppe and J. Stachel, Chemical Equilibration in Pb + Pb Collisions at the SPS Phys. Lett. B465151999 th/9903010

[37] N. Xu and M. Kaneta, Hadron Freeze-Out Conditions in High Energy Nuclear Collisions Nucl. Phys.A6983062002

[38] E. Schnedermann, J. Sollfrank, and U. Heinz, Thermal Phenomenology of Hadrons from 200-A/GeV S+S Collisions Phys. Rev. C4824621993

[39] D. Teaney, J. Lauret, and E.V. Shuryak, A Hydrodynamic Description of Heavy Ion Collisions at the SPS and RHIC nucl-th/0110037

[40] D. Teaney, J. Lauret, and E.V. Shuryak, Flow at the SPS and RHIC as a Quark Gluon Plasma Signature Phys. Rev. Lett.8647832001

[41] P. Kolb , Centrality Dependence of Multiplicity, Transverse Energy, and Elliptic Flow from Hydrodynamics Nucl. Phys.A6961972001

[42] P. Huovinen , Radial and Elliptic Flow at RHIC: Further Predictions Phys. Lett. B503582001

[43] U. Heinz and P. Kolb, Early Thermalization at RHIC Nucl. Phys.A7022692002

[44] F. Retiere and M.A. Lisa, Observable Implications of Geometrical and Dynamical Aspects of Freeze Out in Heavy Ion Collisions Phys. Rev. C700449072004 nucl-th/0312024

[45] L.A. Stiles and M. Murray, Limiting Fragmentation of Chemical Potentials in Heavy Ion Collisions nucl-ex/0601039

[46] B. Abelev et al. [ALICE Collaboration], Phys.Rev. Lett.109, 252301 (2012).

[47] J. Adams STAR The Multiplicity dependence of inclusive p(t) spectra from p-p collisions at s**(1/2) = 200-GeV Phys. Rev. D740320062006 nucl-ex/0606028.

[48] Z. Chajecki and M. Lisa, Conservation Laws and the Multiplicity Evolution of Spectra at the Relativistic Heavy Ion Collider 0807.3569

[49] J. Adams STAR Distributions of charged hadrons associated with high transverse momentum particles in pp and Au + Au collisions at s(NN)**(1/2) = 200-GeV Phys. Rev. Lett.951523012005

[50] G. Wilk and Z. Wlodarczyk, On the interpretation of nonextensive parameter q in Tsallis statistics and Levy distributions Phys. Rev. Lett.8427702000

[51] J. Adams STAR Minijet deformation and charge-independent angular correlations on momentum subspace (eta, phi) in Au-Au collisions at s(NN)**(1/2) = 130-GeV Phys. Rev. C730649072006

[52] J. Adams STAR Transverse-momentum pt correlations on (eta,phi) from mean-pt fluctuations in Au-Au collisions at 200 GeV J. Phys. G32L372006

[53] J. Adams STAR K*(892) Resonance Production in Au + Au and p + p Collisions at s(NN)**(1/2) = 200-GeV at STAR Phys. Rev. C710649022005 nucl-ex/0412019

[54] NA49 Collaboration, paper to be submitted. G. Roland, private communication. Talk by G. Roland at Trento Workshop on Event-by-Event Physics in Relativistic Heavy Ion Collisions, October 1998. See also G. Roland for the NA49 Collaboration, Proceedings of Quark Matter '97, Nucl. Phys. **A638** (1998) 91c and talk by G. Roland, Proceedings of the Hirschegg Workshop on QCD Phase Transitions, January 1997, p. 309.

[55] L. Stodolsky, Phys. Rev. Lett. **75** (1995) 1044.

[56] E. V. Shuryak, Phys. Lett. **B423** (1998) 9.

[57] St. Mrówczyński, Phys. Lett. **B430** (1998) 9.

[58] M. Gaździcki, nucl-th/9712050.

[59] St. Mrówczyński, nucl-th/9901078.

[60] W. Czyz, L.C. Maximon, Ann. Phys. 52 (1969) 59; R.J. Glauber Lectures in Theoretical Physics, vol. 1 Inter-Science Publishers, New York, 1958.

[61] nucl-ex/1012.1004 and also published as K. Aamodt, et al., ALICE Collaboration, Phys. Lett. B 696 (2011) 30 (nucl-ex/1012.1004)

[62] D. Gross, "Asymptotic freedom and QCD: A historical perspective", Nucl.Phys.Proc.Suppl. 135 (2004) 193?211.

[63] F. Karsch and E. Laermann, arXiv:hep-lat/0305025, (2003).

[64] C. Adler et al. (STAR Collaboration), Phys. Rev. Lett. 87, 182301 (2001).

[65] L. Adamczyk et al. (STAR Collaboration),Phys. Rev. Lett. 116, 062301 (2016).

[66] B. Abelev et al.(ALICE Collaboration), Phys. Rev. Lett. 109, 072301 (2012).

[67] P. Kovtun, D. T. Son and A. O. Starinets, Phys. Rev. Lett. 94, 111601 (2005).

[68] D. d?Enterria, ?Jet quenching?, Landolt-Boernstein, Springer-Verlag Vol. 1-23A (2010) 99, arXiv:0902.2011.

[69] S. Chatrchyan et al. (CMS Collaboration), Phys. Rev. C 84, 024906 (2011).

[70] B. Alver et al., Phys. Rev. C 77, 014906 (2008).

[71] A. Dainese, C. Loizides, and G. Paic, Eur. Phys. J. C 38, 461 (2005) .

[72] I. Vitev and M. Gyulassy, Phys. Rev. Lett. 89, 252301 (2002).

[73] I. Vitev, J. Phys. G30, S791 (2004) .

[74] T. Renk et al.,Phys. Rev. C 84, 014906 (2011).

[75] C. Adler et al (STAR Collaboration),Phys. Rev. Lett. 90, 082302 (2003).

[76] L. Adamczyk et al. (STAR Collaboration), Phys. Rev. Lett. 112, 122301 (2014).

[77] K. Aamodt et al. (ALICE Collaboration), Phys. Lett. B 754 (2016) 235-248.

[78] B. B. Abelev et al. (ALICE Collaboration) Phys. Lett. B 753 (2016) 319-329.

[79] J. Adam et al. (ALICE Collaboration), Phys. Lett. B 754 (2016) 373-385

[80] J. Adam et al. (ALICE Collaboration), Phys. Rev. Lett. 116 (2016) 222302.

[81] U. W. Heinz. Concepts of Heavy-Ion Physics. arXiv:hep-ph/0407360, 2004.

[82] S. Chatrchyan et al (CMS Collaboration), JHEP 03 022, (2015).

[83] S. S. Adler et al. (PHENIX Collaboration), Phys. Rev. Lett. 91, 172301 (2003).

[84] B. I. Abelev et al. (STAR Collaboration), Phys. Rev. Lett. 97, 152301 (2006).

[85] B. Schenke, S. Jeon and C. Gale, *Phys.Rev.Lett.* **106** (2011) 042301, arXiv:1009.3244.

[86] J. Adam et al. (ALICE Collaboration), arXiv:1606.06057.

[87] STAR Collaboration Collaboration (Y. Pandit), *Nucl.Phys.* **A904-905** (2013) 357c, arXiv:1210.5315.

[88] J. Adam et. al (STAR Collaboration), Phys. Rev. Lett. 92, (2004) 052302.

[89] J. Adam et. al (STAR Collaboration), Phys. Lett. B 612, 181 (2005).

[90] B.I. Abelev et, al (STAR Collaboration), Phys. Rev. C 79, 064903 (2009).

[91] J. Adam et. al (ALICE Collaboration), JHEP 9 (2012) 112.

Chapter 2

Correlations & Fluctuations

In this chapter I am discussing the general criteria of phase transition (1; 2), critical phenomena (3). The importance of fluctuation and correaliton in context of phase transition has also been discussed (4; 5). Lastly, the $p_T - p_T$ correaliton (5; 6; 7; 8; 9; 10; 11; 13; 14) and extraction of dynamical fluctuation in terms of temperature fluctuation (15; 16; 17; 18; 19) will be discussed.

2.1 Continuous Phase Transition or Critical Phenomena

Critical phenomena are the characteristic features that accompany the second order phase transition at a critical point. The critical point is reached by tuning thermodynamic parameters (for example temperature T or pressure P or both). A critical phenomenon is seen as T(P) approaches the critical point $T_C(P_C)$.In order to understand the characteristic features appearing at the critical point, one must study the macroscopic properties of the system at the critical point. In principle, all macroscopic properties can be obtained from the free energy or the partition function of a given system. However, since the critical phenomena, a second order phase transition or a continuous phase transitions, involve discontinuities in the response functions (which are second derivatives of the free energy function) at the critical point there must be singularities in the free energy at the critical point. On the other hand, the canonical partition function of a finite number of particles is always analytic. The critical phenomena then can only be associated with infinitely many particles, i.e. in the "thermodynamic limit", and to their cooperative behaviour. The study of critical phenomena is thus essentially related to finding the origin of various singularities in the free energy and characterizing them.

Let us consider more carefully the two classic examples of second order phase transition involving condensation of gas into liquid and transformation of paramagnet to ferromagnet. In the liquid-gas or fluid system the thermodynamic parameters are (P,V,T) and in magnetic system the corresponding thermodynamic parameters are (H,M,T).One may note the correspondence between the thermodynamic parameters of fluid and magnetic systems as:$V \rightarrow -M \& P \rightarrow H$. In the case of fluid, instead of volume V we will be considering the density as a parameter. The equations of states in these systems are then given by $f(P, \rho, T) = 0$ and f(H,M,T)=0 respectively. A second order phase transition is a qualitative change in the system behaviour at a sharply defined parameter value, the critical point, when the parameter changes continuously. The critical points are usually denoted by (P_C, ρ_C, T_C) and (H_C, M_C, T_C). Commonly, phase transitions are studied varying the temperature T of the system and a phase transition occurs at $T = T_C$.We will be describing the features at the critical point by considering different phase diagrams such as P-T,H-T; P-ρ,H-M;ρ-T,M-T of the full three dimensional phase space of (P,ρ,T) or (H,M,T).

2.2 Morphology, fluctuation and correlation

The isotherms, P-ρ or H-M curves in the respective phase diagrams (Fig.4) develop curvature as the system approaches the critical temperature T_C from above. The curvature in the isotherms is the manifestation of the long range correlation of the molecules in the fluid or spins in magnets. At high temperature, the gas molecules move randomly or the magnetic moments flip their orientation randomly. Due to the presence of interactions small droplets or domains of correlated spins appear as the temperature decreases. These droplets grow in size as T decreases closer to T_C. At T=T_C,droplets or domains of correlated spins of all possible sizes appear in the system. Lateral dimension of these droplets become of the order of the wavelength of ordinary light. Upon shining light on the fluid at T=T_C , a strong scattering is observed and the fluid appears as milky white. The phenomenon is known as critical opalescence . Similarly in magnetic systems, domains of correlated spins of all possible sizes appear in the system and a huge neutron scattering cross section is observed at T=T_C.As T $\rightarrow$ T_C , there appears droplet or domain of correlated spins of the order of system size. One may define a length scale called correlation length which is the lateral dimension of the droplets or domains of correlated spins. Therefore, the correlation length diverges as T $\rightarrow$ T_C.One should note that the system does not correspond to a ordered state at T_C and a completely ordered state is achieved only at T=0 .

As the system approaches T_C ,there are long wave-length fluctuations in density in fluid or in the orientation of magnetic moments in the magnetic system. These fluctuations occur at every scale. If ξ is the largest scale of fluctuation and a is the lattice spacing, then the system appears to be self-similar on all length scales x for $a < x < \xi$. At T=T_C, ξ is infinite and the system becomes truly scale invariant. The correlation between the spins (or molecules) is measured in terms of fluctuations of spins (or density) away from their mean values:

$$G(s_i, s_j) =< (s_i- < s_i >)(s_j- < s_j >) >= r^{-(d-2+\eta)}e^{-r/\xi} \tag{2.1}$$

where r is the distance between s_i&s_j, ξ is the correlation length and η is some exponent. At the criticality, ξ diverges to infinity and $G(\vec{r})$ decays as a power law.

Close to a critical point, the large spatial correlations which develop in the system are associated with long temporal correlations as well. At the critical point, the relaxation time and characteristic time scales diverge as determined by the conservation laws. This is known as the critical slowing down . A relaxation function $\phi(t)$ may decay exponentially at long times as $\phi(t)$:$e^{-t/\eta}$ where τ is the relaxation time.τ diverges at the critical point and the dynamic critical behavior can be expressed in terms of the power law as $\tau \propto \xi^Z$, where z is called the dynamic critical exponent.

2.3 Fluctuation and response functions:

Apart from macroscopic thermodynamics quantities, statistical mechanics can also provide information about microscopic quantities such as fluctuations and correlation. Even if the system is in thermal equilibrium (constant T) or mechanical equilibrium (constant P) or chemical equilibrium (constant μ), the energy E, magnetization M, number of particles M may vary indefinitely and only the average values remain constant. It would be interesting to check that the thermodynamics response functions such as specific heat C_V, isothermal compressibility κ_T or or isothermal susceptibility χ_T are directly proportional to the fluctuation in energy, density or magnetization respectively.
The fluctuation in energy is defined as

$$< (\Delta E)^2 >=< (E- < E >)^2 >=< E^2 > - < E >^2 \tag{2.2}$$

By calculating $< E^2 >$, it can be shown that
$< (\Delta E)^2 >= -\frac{\partial < E >}{\partial \beta} = \kappa_B T^2 C_V$
or

$$C_V = \frac{1}{\kappa_B T^2}(< E^2 > - < E >^2). \tag{2.3}$$

Thus the specific heat is nothing but fluctuation in energy.

The fluctuation in number of particles N is defined as

$$< (\Delta N)^2 >=< (N- < N >)^2 >=< N^2 > - < N >^2= \kappa_B T \frac{\partial < N >}{\partial \mu} = \frac{< N >^2 \kappa_B T}{V} \kappa_T \tag{2.4}$$

where κ_T is the isothermal compressibility. The isothermal compressibility is then proportional to density fluctuation.If κ_T^0 =V/($< N > K_B T$) , one has

$$\frac{\kappa_T}{\kappa_T^0} = \frac{< (N- < N >)^2 >}{< N >} \tag{2.5}$$

Similarly, the isothermal susceptibility is proportional to the fluctuation in magnetization

$$\chi = \frac{\kappa_B T}{N}(< M^2 > - < M >^2) \tag{2.6}$$

These are system-independent general results. Generally these fluctuations are negligibly small at normal conditions. At room temperature, the rms energy fluctuation for 1 kg of water is : 4.2×10^{-8} J $[T(K_B C_V)^{1/2}]$,whereas to change the water temperature by degree the energy needed is $10^{11} \times C_V$ .Since the heat capacity grows linearly with the system size, the relative energy fluctuation goes to zero at the thermodynamic limit.
The above relation shows that the responses C_V, κ_T, χ_T are linearly proportional to the fluctuation in respective thermodynamic quantities - this is known as linear response theorem .

2.4 Correlation in terms of fluctuation and response:

So far, the response functions are obtained as the thermal-average of corresponding macroscopic variables from the knowledge of the probability distribution of the microstates of the system. It can also be obtained in terms of microscopic variables like spin or particle density at a point. A quantitative way of doing it is through defining two point correlation functions, how the spins or particle densities at different points are related. Below we will establish a relationship between correlation, fluctuation and responses of the system for fluid and magnetic systems.
Fluid: Density at any point $\vec{r}$ is given by the Dirac delta function $\delta(\vec{r})$ as

$$\rho(\vec{r}) = \frac{< N >}{V} = \sum_{i=1}^{N} \delta(r - r_i). \tag{2.7}$$

A density-density correlation function is the correlation of the fluctuation of the densities from its average values at $\vec{r}$ and $\vec{r}$ and can be defined as

$$G(\vec{r},\vec{r'}) =< (\rho(\vec{r})- < \rho(\vec{r}) >)(\rho(\vec{r'})- < \rho(\vec{r'}) >) >=< \rho(\vec{r}) > - < \rho(\vec{r'}) >= \rho \tag{2.8}$$

$$\tag{2.9}$$

the average density of the system, the correaliton function can be written as

$$G(\vec{r},\vec{r'}) =< \rho(\vec{r})\rho(\vec{r'}) > -\rho^2 \tag{2.10}$$

As $|\vec{r} - \vec{r'}| \to \infty$,the probability of finding a particle at $\vec{r'}$ becomes independent of what is happening at $\vec{r}$ i.e., the densities become uncorrelated. Hence, $G(\vec{r},\vec{r'}) \to 0$ as $|\vec{r} - \vec{r'}| \to \infty$. However, at a short distance, the correlation function $G(\vec{r})$ depends on r as

$$G(\vec{r}) \approx r^{-\tau}e^{-r/\xi} \tag{2.11}$$

where τ is an exponent and ξ is called the correlation length.

On the other hand, the particle number fluctuation can be written as

$$< (N- < N >)^2 >=< \int d^3\vec{r}(\rho(\vec{r})- < \rho(\vec{r}) >)\int d^3\vec{r'}(\rho(\vec{r'})- < \rho(\vec{r'}) >) >= \int\int G(\vec{r},\vec{r'})d \tag{2.12}$$

OR,

$$< (N- < N >)^2 >= \int d^3\vec{r}\int d^3\vec{r'}G(\vec{r}-\vec{r'}) = V\int d^3\vec{r''}G(\vec{r''}) where, \vec{r''} = \vec{r} - \vec{r'} \tag{2.13}$$

and then the isothermal compressibility can be expressed in terms of the density-density correlation function as

$$\frac{\kappa_T}{\kappa_T^0} = \frac{< (N- < N >)^2 >}{< N >} = V/N\int d^3\vec{r''}G(\vec{r''}) \tag{2.14}$$

Thus, the density fluctuation, isothermal compressibility and the density-density correlation function are all interrelated quantities.

2.5 Critical exponents

It was demonstrated in the previous section that different thermodynamic quantities become singular as $T \to T_C$. They exhibit either branch point singularity or diverging singularity. The order parameter continuously goes to zero as $T \to T_C$ and exhibits a branch point singularity since it becomes a double valued function. The response functions and correlation length diverge and exhibit diverging singularity. Long range order appears in density-density or spin-spin correlation and it decays with power law. The singular behaviour of thermodynamic quantities around the critical temperature can be described by power series. The leading singularity of the power series in the limit $T \to T_C$ are characterized by certain exponents called critical exponents. The power series for different thermodynamic quantities and the associated critical exponents will be described below.

The power series describing the thermodynamic quantities in the critical regime are usually expressed in terms of the reduced temperature t=(T-T_C)/T_C .In terms of the reduced temperature, the power series of different thermodynamic quantities and the associated critical exponents are given below.

The order parameter, density difference $\Delta\rho$ in fluid and spontaneous magnetization M in ferromagnets, below T_C are given as

$$\Delta\rho = A(-t)^{\beta}[1 + A_1(-t)_1^{\beta} + ...]\&M = A(-t)^{\beta}[1 + A_1(-t)_1^{\beta} + ...] \tag{2.15}$$

respectively with $\beta_1 > 0$. Note that below T_C, t is negative. The exponent β describes the leading singularity of these quantities and is called the critical exponent of the order parameter.The specific heats at constant volume V or constant magnetic field H below and above are given as,

$$C_V = B(-t)^{-\alpha}[1 + b(-t)_1^{\alpha} + ...], C_H = B(-t)^{-\alpha}[1 + b(-t)_1^{\alpha} + ...] \tag{2.16}$$

for $T < T_C$

$$C_V = B(t)^{-\alpha}[1 + b(t)_1^{\alpha} + ...], C_H = B(t)^{-\alpha}[1 + b(t)_1^{\alpha} + ...]T > T_C \tag{2.17}$$

where α' and α are the specific heat exponents below and above T_C.
The isothermal compressibility κ_T and isothermal susceptibility ξ_T below and above T_C are given by

$$\kappa_T = C(-t)^{-\gamma'}[1 + c(-t)_1^{\gamma} + ...], \chi_T = C(-t)^{-\gamma}[1 + c(-t)_1^{\alpha} + ...]T < T_C \tag{2.18}$$

$$\kappa_T = C(t)^{-\gamma'}[1 + c(t)_1^{\gamma} + ...], \chi_T = C(t)^{-\gamma}[1 + c(t)_1^{\alpha} + ...]T > T_C \tag{2.19}$$

where γ' and γ are the compressibility or susceptibility exponents below and above T_C .

2.6 Two gaussian

Given two normal random variables X and Y

$$X \approx N(\mu_X, \sigma_X^2) \quad \& \quad Y \approx N(\mu_Y, \sigma_Y^2) \tag{2.20}$$

that are correlated such that

$$\rho = \frac{\sigma_{XY}}{\sigma_X \sigma_Y} \tag{2.21}$$

Where,

$$\rho \triangleq corr(X,Y) \quad \& \quad \sigma_{XY} \triangleq cov(X,Y) \tag{2.22}$$

we endeavor to show that

$$Z \triangleq X - Y \approx N(\mu_X - \mu_Y, \sigma_X^2 + \sigma_Y^2 - 2\sigma XY) \tag{2.23}$$

To solve this problem, we appeal to the bivariate normal probability density function. The proof that follows will make significant use of variables and lemmas to condense notation. Amazingly, the distribution of a difference of two normally distributed variates X and Y with means and variances

$$P_{X-Y}(u) = \int_{-\infty}^{\infty}\int_{-\infty}^{\infty} \frac{e^{-x^2/(2\sigma_x^2)}}{\sigma_x\sqrt{2\pi}} \frac{e^{-y^2/(2\sigma_y^2)}}{\sigma_y\sqrt{2\pi}} \delta((x-y)-u)dxdy$$

$$= \frac{e^{-[u-(\mu_x-\mu_y)]^2/[2(\sigma_x^2+\sigma_y^2)]}}{\sqrt{2\pi(\sigma_x^2+\sigma_y^2)}} \tag{2.24}$$

where $\delta(x)$ is a delta function, which is another normal distribution having mean

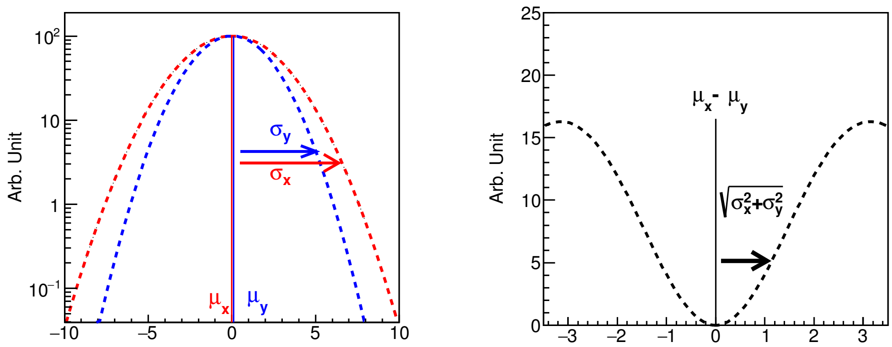

Figure 2.1: Difference of two gaussian funtions representations

$$\mu_{X-Y} = \mu_x - \mu_y \tag{2.25}$$

and variance

$$\sigma^2_{X-Y} = \sigma^2_x + \sigma^2_y \tag{2.26}$$

2.7 Correlation & Fluctuation in terms of p_T & Temperature

Two particle p_t correlation is described by,

$$< \Delta p_{t,i} \Delta p_{t,j} >= \frac{1}{N_{event}} \sum_{k=1}^{N_{event}} \frac{C_k}{N_k(N_k - 1)} \tag{2.27}$$

Where, C_k is the two particle p_t covariance for kth event, defined as, $C_k = \sum_{i=1}^{N_k} \sum_{j=1,inotj}^{N_k} (p_{t,i} - << p_t >>)(p_{t,j} - << p_t >>)$ and N_k is the no. of tracks in kth event and $<< p_t >>$ is the overall event average of mean $p_t = \frac{1}{N_{event}} \sum_{k=1}^{N_{event}} < p_t >_k$

Now, C_k can be written as

$$C_k = \sum_{i=1}^{N_k} \sum_{j=1}^{N_k} (p_{t,i} - << p_t >>)(p_{t,j} - << p_t >>) \sum_{i=j=1}^{N_k} (p_{t,i} - << p_t >>)(p_{t,j} - << p_t >>) \tag{2.28}$$

Where, First term = ${N_k}^2$

$$\frac{1}{N_k} \sum_{i=1}^{N_k} (p_{t,i} - << p_t >>) \frac{1}{N_k} \sum_{j=1}^{N_k} (p_{t,j} - << p_t >>)$$

$$= {N_k}^2 (< p_t > - << p_t >>)(< p_t > - << p_t >>)$$

$$= {N_k}^2 [< p_t >^2 - 2 < p_t >< < p_t >> + << p_t >>^2]$$

And, Second term= $\sum_{i=1}^{N_k} (p_{t,i} - << p_t >>)^2$

$= \sum_{i=1}^{N_k}({p_{t,i}}^2 - 2p_{t,i} << p_t >> + << p_t >>^2)$

$= \sum_{i=1}^{N_k} {p_{t,i}}^2 - 2N_k << p_t >>< p_t > + << p_t >>^2 N_k$

So, $C_k = {N_k}^2 < p_t >^2 - \sum_{i=1}^{N_k} {p_{t,i}}^2 + N_k << p_t >>^2 (N_k - 1) - 2N_k < p_t >< < p_t >> (N_k - 1)$

So,

$$\frac{C_k}{N_k(N_k-1)} = << p_t >>^2 - 2 < p_t >< < p_t >> + \frac{{N_k}^2}{N_k(N_k-1)} < {p_t}^2 - \frac{1}{N_k(N_k)} \sum_{i=1}^{N_k} {p_{t,i}}^2$$

$= (< p_t > - << p_t >>)^2 + \frac{1}{N_k - 1} < p_t >^2 - \frac{1}{N_k(N_k-1)} \sum_{i=1}^{N_k} {p_{t,i}}^2$

$= (< p_t > - << p_t >>)^2 + \frac{1}{N_k - 1} (< p_t >^2 - < {p_t}^2 >)$

$= (< p_t > - << p_t >>)^2 - \frac{{\sigma_{pt}}^2}{N_k - 1}$

So,

$$< \Delta p_{t,i} \Delta p_{t,j} >=< < p_t >^2 > - << p_t >>^2 - \frac{1}{N_{event}} \sum_{k=1}^{N_{event}} \frac{{\sigma_p}^2}{N_k - 1}$$

$= \sigma_{stat}^2 + \sigma^2{}_{dyn} - {\sigma_p}^2 \frac{1}{<N>} = \sigma^2{}_{stat} + \sigma^2{}_{dyn} - {\sigma_{stat}}^2 = \sigma^2{}_{dyn} (2.29)$

which denotes the fluctuation in p_t. Thus,

$(< p_t > - << p_t >>) \ \propto (\Delta \langle T_{dyn} \rangle)^2$

Bibliography

[1] F. Karsch, E. Laermann and A. Peikert, Phys. Lett. B 478, 447 (2000).

[2] S. Hands, Contemp. Phys. 42, 209 (2001).

[3] D. Gross, ?Asymptotic freedom and QCD: A historical perspective?, Nucl.Phys.Proc.Suppl. 135 (2004) 193?211.

[4] F. Karsch and E. Laermann, arXiv:hep-lat/0305025, (2003).

[5] early proceedings of the CLASHEP schools: J. Schukraft (2001,2003) Brazil and Mexico, U.A.Wiedemann (2007) Chile, G. Herrera Corral (2009) Colombia.

[6] S. Jeon and V. Koch, "Event by event fluctuations," `arXiv:hep-ph/0304012 [hep-ph]`.

[7] S. Mrowczynski, "Plasma instability at the initial stage of ultrarelativistic heavy ion collisions," *Phys.Lett.* **B314** (1993) 118–121.

[8] L. Stodolsky, "Temperature fluctuations in multiparticle production," *Phys.Rev.Lett.* **75** (1995) 1044–1045.

[9] E. V. Shuryak, "Event per event analysis of heavy ion collisions and thermodynamical fluctuations," *Phys.Lett.* **B423** (1998) 9–14, `arXiv:hep-ph/9704456 [hep-ph]`.

[10] M. A. Stephanov, K. Rajagopal, and E. V. Shuryak, "Signatures of the tricritical point in QCD," *Phys.Rev.Lett.* **81** (1998) 4816–4819, `arXiv:hep-ph/9806219 [hep-ph]`.

[11] M. A. Stephanov, K. Rajagopal, and E. V. Shuryak, "Event-by-event fluctuations in heavy ion collisions and the QCD critical point," *Phys.Rev.* **D60** (1999) 114028, `arXiv:hep-ph/9903292 [hep-ph]`.

[12] H. Heiselberg, "Event-by-event physics in relativistic heavy ion collisions," *Phys.Rept.* **351** (2001) 161–194, `arXiv:nucl-th/0003046 [nucl-th]`.

[13] A. Dumitru and R. D. Pisarski, "Event-by-event fluctuations from decay of a Polyakov loop condensate," *Phys.Lett.* **B504** (2001) 282–290, `arXiv:hep-ph/0010083 [hep-ph]`.

[14] Z. Fodor and S. Katz, "Critical point of QCD at finite T and mu, lattice results for physical quark masses," *JHEP* **0404** (2004) 050, `arXiv:hep-lat/0402006 [hep-lat]`.

[15] **NA49** Collaboration, H. Appelshäuser *et al.*, "Event-by-event fluctuations of average transverse momentum in central Pb + Pb collisions at 158 GeV per nucleon," *Phys.Lett.* **B459** (1999) 679–686, `arXiv:hep-ex/9904014 [hep-ex]`.

[16] **CERES** Collaboration, D. Adamová *et al.*, "Event by event fluctuations of the mean transverse momentum in 40, 80 and 158 A GeV / c Pb - Au collisions," *Nucl.Phys.* **A727** (2003) 97–119, `arXiv:nucl-ex/0305002 [nucl-ex]`.

[17] **NA49** Collaboration, T. Anticic *et al.*, "Transverse momentum fluctuations in nuclear collisions at 158-A GeV," *Phys.Rev.* **C70** (2004) 034902, `arXiv:hep-ex/0311009 [hep-ex]`.

[18] **CERES** Collaboration, D. Adamová *et al.*, "Scale-dependence of transverse momentum correlations in Pb-Au collisions at 158A GeV/c," *Nucl.Phys.* **A811** (2008) 179–196, `arXiv:0803.2407 [nucl-ex]`.

[19] **NA49** Collaboration, T. Anticic *et al.*, "Energy dependence of transverse momentum fluctuations in Pb+Pb collisions at the CERN Super Proton Synchrotron (SPS) at 20A to 158A GeV," *Phys.Rev.* **C79** (2009) 044904, `arXiv:0810.5580 [nucl-ex]`.

[20] **PHENIX** Collaboration, K. Adcox *et al.*, “Event-by-event fluctuations in mean p(T) and mean e(T) in $\sqrt{s_{NN}} = 130$ GeV Au+Au collisions,” *Phys.Rev.* **C66** (2002) 024901, arXiv:nucl-ex/0203015 [nucl-ex].

[21] **PHENIX** Collaboration, S. Adler *et al.*, “Measurement of nonrandom event by event fluctuations of average transverse momentum in $\sqrt{s_{NN}} = 200$ GeV Au+Au and p+p collisions,” *Phys.Rev.Lett.* **93** (2004) 092301,

[22] **STAR** Collaboration, J. Adams *et al.*, “Event by event mean-p(t) fluctuations in Au - Au collisions at $\sqrt{s_{NN}} = 130$ GeV,” *Phys.Rev.* **C71** (2005) 064906, arXiv:nucl-ex/0308033 [nucl-ex].

[23] **STAR** Collaboration, J. Adams *et al.*, “Incident energy dependence of pt correlations at RHIC,” *Phys.Rev.* **C72** (2005) 044902, arXiv:nucl-ex/0504031 [nucl-ex].

Chapter 3

Motivation of Temperature Fluctuations

In this chapter, I have discussed about the temperature fluctuations in heavy ions, its extraction strategies. Also, the difference between the inter-event(within the event) and intra-event(event-by-event) fluctuations and its importance will be discussed. The various factors, which might effect the study of temperature fluctuations and the extraction of thermodynamic quantity from it are also raised.

3.1 Event-by-Event Temperature Fluctuation in Heavy Ions

Heavy-ion collisions at ultra-relativistic energies create matter at extreme conditions of energy density (ϵ) and temperature (T), similar to the ones that existed within a few microseconds after the Big Bang (1). The fireball produced in the collision goes through a rapid evolution from an early partonic phase of deconfined quark-gluon plasma (QGP) to a hadronic phase and ultimately freezing out after a few tens of fm. The major goals of colliding heavy-ions at the Relativistic Heavy Ion Collider (RHIC) and at the Large Hadron Collider (LHC) are to study the nature of the phase transition and understand the QGP matter in detail. With the production of large number of particles in each of the collisions, it has become possible to extract thermodynamic quantities on an event-by-event basis, rather than averaging over a sample of events. Event-by-event fluctuations of ϵ, T, mean transverse momentum, particle multiplicity, particle ratios, etc., as well as fluctuations of conserved quantities within finite detector acceptances have been proposed to provide dynamical information regarding the evolving system (2; 5; 6; 7; 7; 8; 8; 9; 10; 11; 12).

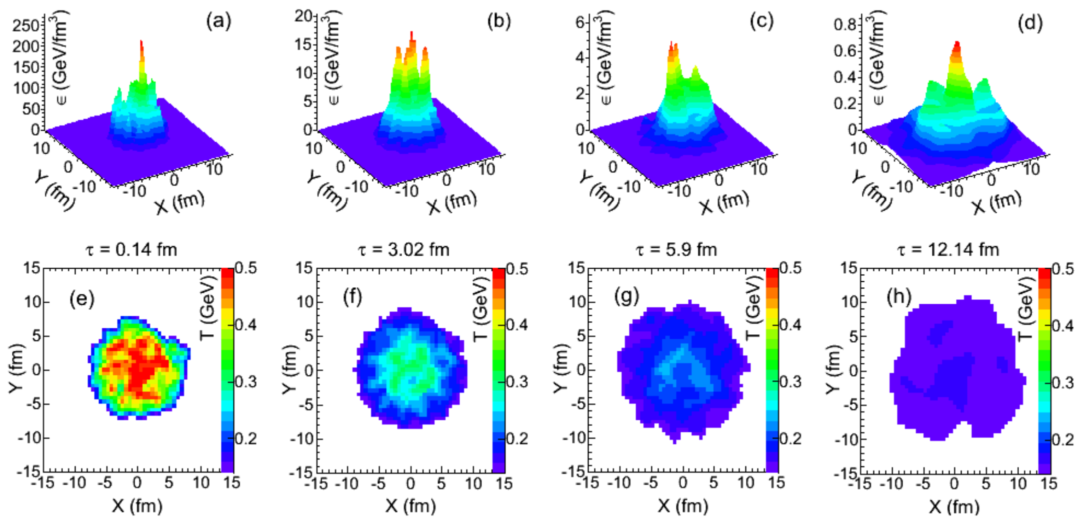

Figure 3.1: (Color online). Distributions of energy density (upper panles) and temperature (lower panels) in the transverse (X-Y) plane at four proper times (τ) obtained from hydrodynamic calculations for a single central Pb-Pb event at $\sqrt{s_{\rm NN}}$ =2.76 TeV.

Temperature fluctuations have been studied on an event-by-event basis by estimating global temperature of the event, and local temperatures in small phase space bins within the event. Determination of temperature and its fluctuation for heavy-ion collisions have been possible because of large number of particles emitted in each event (13**?**), which is essential to keep the statistical uncertainties of the measurements within a reasonable limit. Global event to event temperature fluctuations provide the heat capacity ($c_{\rm v}$), which is an important thermodynamic quantity in characterizing the system. Lattice QCD calculations predict a strong temperature dependence of the heat capacity, the nature of which depends on the order of the phase transition (5; 15). This study sheds light on the nature of phase transition at the LHC energy. Fluctuations of initial energy density and temperature may survive till the freeze-out and manifest themselves in the measured temperature fluctuations. In fact, initial fluctuating conditions have been found to be necessary for explaining observed elliptic flow in central collisions and substantial triangular flow of charged particles (16). The initial state fluctuations may have their imprint on the bin to bin local fluctuations within an event. Event-by-event hydrodynamic calculations provide a strong theoretical basis for studying the global and local temperature fluctuations.

3.2 Global Temperature Fluctuations: Event-by-event

The thermodynamic state of the QCD matter can be specified by the temperature T and the chemical potentials μ_B, μ_S and μ_Q corresponding to the conserved charges of QCD, namely baryon number (B), strangeness (S), and electric charge (Q), respectively. Phase transitions are associated with the transformation of thermodynamic quantities such as pressure, entropy and energy density, as well as a set of response functions, like, specific heat, compressibility and susceptibility with change in T, μ_B, μ_Q and μ_S. In this section, we discuss the specific heat (c_v) of the system produced in heavy-ion collisions at relativistic energies and its behaviour as a function of collision energy.

Specific heat is a thermodynamic quantity characterizing the equation of state of the system. For a system undergoing phase transition, c_v is expected to go through a sudden change around the transition point. Temperature fluctuation of the system provides a measure of c_v. Hadron Resonance Gas (HRG) model analysis of the particle yields indicate the formation of a thermal source for the produced particles in heavy-ion collisions (4; 5). The production of large number of particles in each collision at the RHIC and LHC energies makes it even possible to study several quantities on an event-by-event basis (4; 5; 6; 7; 8; 9) and hence measure their event to event fluctuations. Thus, with the measurement of T on an event-by-event basis, it is possible to extract the c_v of the hot and dense strongly interacting matter produced in heavy-ion collisions.

Assuming complete thermal equilibrium up to the surface of last scattering which is the kinetic freezeout surface, c_{v} is then expected to reveal the thermodynamic state of the matter at the moment of kinetic freezeout.

Lattice QCD calculations (10; 15; 16) provide estimations of c_{v} for a wide range of temperatures. In Ref. (15), continuum limits of c_{v} have been calculated in quenched QCD at temperatures of $2T_c$ and $3T_c$, where T_c is the transition temperature. It is found that c_{v} differs significantly from that of the ideal gas. Recent lattice calculations using (2+1)-flavor QCD with almost physical quark masses give the results of c_{v} for a temperature range of 130 to 400 MeV (15). The low temperature (hadron phase) results agree well with HRG.

The specific heat has its origin in the event-by-event temperature fluctuations, which manifests through the fluctuations in the transverse momenta (p_{T}) (4; 5; 11; 12; 13; 17; 18; 19; 20; 21). Event-by-event fluctuations of $\langle p_{\mathrm{T}} \rangle$ have been reported by experiments at the CERN Super Proton Synchrotron (SPS) (22; 23; 24; 25) and beam energy scan at RHIC (26; 27; 28; 29).

The values of c_{v} extracted from the experimental results have large errors (21; 23; 24; 30). The p_{T} fluctuation data from Ref. (22) yielded the value of c_{v} to be 60 ± 100 at $T = 180$ MeV for SPS energies. The statistical fluctuations arising from the finite multiplicity distributions of charged particles may significantly affect the extracted thermodynamic fluctuations (17). In the present work, this is taken care of by subtracting the widths of the results of mixed events from the real data. Since radial flow affects the estimation of temperature, its effect has also been considered. Finally, the values of c_{v} have been calculated as a function of beam energy from published experimental data and compared to lattice and HRG calculations. Further predictions have been made for the LHC energies.

The heat capacity C of a system is defined as (37):

$$C = \left(\frac{\partial E}{\partial T}\right)_V \tag{3.1}$$

where T, V and E are temperature, volume and energy of the system, respectively. Equivalently,

C of a system in thermal equlibrium to a bath at T can be computed from the event-by-event fluctuations of E:

$$C = \frac{(\langle E^2 \rangle - \langle E \rangle^2)}{\langle T \rangle^2}. \tag{3.2}$$

For a system in equilibrium, the event-by-event temperature fluctuation is controlled by the heat capacity:

$$P(T) \sim \exp[-\frac{C}{2}\frac{(\Delta T)^2}{\langle T \rangle^2}], \tag{3.3}$$

where $\langle T \rangle$ is the mean temperature and $\Delta T = T - \langle T \rangle$ is the variance in temperature. This yields the expression for C (4; 5; 6; 11; 37):

$$\frac{1}{C} = \frac{(\langle T^2 \rangle - \langle T \rangle^2)}{\langle T \rangle^2}. \tag{3.4}$$

Heat capacity thus can be estimated from the fluctuations in energy or temperature. For a system in equilibrium, the mean values of T and E are related by an equation of state. However, the fluctuations in energy and temperature have very different behaviour. Energy being an extensive quantity, its fluctuation has a volume dependent component. So energy is not suited for obtaining the heat capacity. On the other hand, temperature fluctuations provide a good major for estimating the c_{v} (4; 5; 6; 37).

The temperature of the system can be obtained from the transverse momentum (p_{T}) spectra of the emitted particles. An exponential Boltzmann-type fit to the p_{T} spectra gives a measure of the temperature:

$$F(p_{\mathrm{T}}) = \frac{1}{p_{\mathrm{T}}}\frac{dN}{dp_{\mathrm{T}}} \approx A e^{-p_{\mathrm{T}}/T_{\mathrm{eff}}}, \tag{3.5}$$

where A is a normalization factor and T_{eff} is the apparent or effective temperature of the system (11). For obtaining the event-by-event fluctuation, the temperature needs to be estimated in every event. The fitting is possible only for central heavy-ion collisions at the LHC energies when the number of particles is at least one thousand in every event. Even in this case, the error associated with the fitting will be relatively large. This can be overcome by making a connection of mean transverse momentum ($\langle p_{\mathrm{T}} \rangle$) of particles in every event with the temperature. Since the calculation of the mean value is more stable, this method of temperature estimation can also be used for collisions at RHIC energies. The $\langle p_{\mathrm{T}} \rangle$ can be written as (29):

$$
\begin{aligned}
\langle p_{\mathrm{T}} \rangle &= \frac{\int_0^\infty p_{\mathrm{T}}^2 F(p_{\mathrm{T}}) dp_{\mathrm{T}}}{\int_0^\infty p_{\mathrm{T}} F(p_{\mathrm{T}}) dp_{\mathrm{T}}} && (3.6) \\
&= \frac{2T_{\mathrm{eff}}^2 + 2m_0 T_{\mathrm{eff}} + m_0^2}{m_0 + T_{\mathrm{eff}}}, && (3.7)
\end{aligned}
$$

where m_0 is the rest mass of the particle. Note that the integration for p_{T} is from 0 to ∞. But in reality the p_{T} window is finite. For a range of p_{T} within a to b, we obtain:

$$
\begin{aligned}
\langle p_{\mathrm{T}} \rangle &= \frac{\int_a^b p_{\mathrm{T}}^2 F(p_{\mathrm{T}}) dp_{\mathrm{T}}}{\int_a^b p_{\mathrm{T}} F(p_{\mathrm{T}}) dp_{\mathrm{T}}} && (3.8) \\
&= 2T_{\mathrm{eff}} + && (3.9) \\
&\quad \frac{a^2 e^{-a/T_{\mathrm{eff}}} - b^2 e^{-b/T_{\mathrm{eff}}}}{(a + T_{\mathrm{eff}}) e^{-a/T_{\mathrm{eff}}} - (b + T_{\mathrm{eff}}) e^{-b/T_{\mathrm{eff}}}}. && (3.10)
\end{aligned}
$$

This equation links the value of $\langle p_{\mathrm{T}} \rangle$ within a specified range of p_{T} to T_{eff}.

In order to validate the relation between p_{T} to T_{eff}, we have generated a large number of events using the AMPT model (32) for Pb+Pb collisions at $\sqrt{s_{\mathrm{NN}}} = 2.76$ TeV. The goal is to compare the values of T_{eff} obtained from event-by-event p_{T} distribution and from $\langle p_{\mathrm{T}} \rangle$ distributions. For top central (top 5% cross section) collisions, p_{T} distribution of pions has been constructed for each event within a rapidity range of -1.0 to 1.0. The distribution is fitted to an exponential function and the inverse slope parameter (T_{eff}) is extracted within fit range, $0.15 < p_{\mathrm{T}} < 2.0$ GeV. Fig. 3.2 shows the extracted event-by-event T_{eff} distribution (as solid circles). For the same set of events, the values of $\langle p_{\mathrm{T}} \rangle$ has been calculated within the same η and p_{T} ranges for each event. From the value of $\langle p_{\mathrm{T}} \rangle$ for each event, the T_{eff} is calculated using

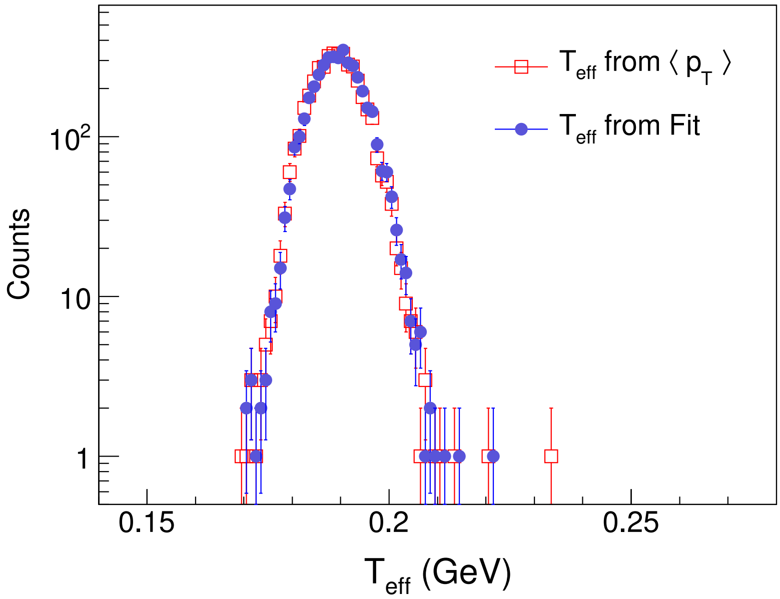

Figure 3.2: Event-by-event T_{eff} distributions of pions for central Pb+Pb collisions at $\sqrt{s_{\mathrm{NN}}}$= 2.76 TeV from the AMPT model within rapidity range of -1.0 to 1.0 and $0.15 < p_{\mathrm{T}} <$ 2.0 GeV. T_{eff} distributions, obtained by fitting the p_{T} distribution of each event and from the $\langle p_{\mathrm{T}} \rangle$ for are presented.

eqn. (4.3). Resulting T_{eff} distribution has been plotted as open squares in Fig. 3.2. Both the T_{eff} distributions are observed to be same. This validates the relationship of $\langle p_{\mathrm{T}} \rangle$ and T_{eff} as given in eqn. (4.3).

We note that the extracted temperature, T_{eff}, is a combination of kinetic freeze-out temperature (T_{kin}) and transverse flow velocity (β_{T}) of the system:

$$T_{\mathrm{eff}} = T_{\mathrm{kin}} + f(\beta_{\mathrm{T}}). \tag{3.11}$$

For pion, $f(\beta_{\mathrm{T}}) \approx m_0 \langle \beta_{\mathrm{T}} \rangle^2$. The event-by-event fluctuations of β_{T} needs to be taken into account for calculating the fluctuation in kinetic temperature (19; 38; 39; 40). Fluctuation in β_{T} dominates over the fluctuation in T_{kin} for small systems (e.g. pp) (41), asymmetric (e.g., pPb) (19) and non-central collisions. For central Au+Au collisions at $\sqrt{s_{\mathrm{NN}}}$ = 200 GeV (44), $\beta_{\mathrm{T}} = 0.59 \pm 0.051$ and for central Pb+Pb collisions at $\sqrt{s_{\mathrm{NN}}}$ = 2.76 TeV (45), $\beta_{\mathrm{T}} = 0.651 \pm 0.02$, which translate to $T_{\rm kin}$ as 0.095 ± 0.010 GeV and 0.09 ± 0.005 GeV, respectively by using blast-wave fit (42). For the present work, we consider 10% fluctuation in $\beta_{\rm T}$ and calculate its effect on specific heat. C is calculated using the equation,

$$\begin{aligned} \frac{1}{C} &= \frac{(\langle T_{\rm kin}^2\rangle - \langle T_{\rm kin}\rangle^2)}{\langle T_{\rm kin}\rangle^2} \approx \frac{(\langle T_{\rm eff}^2\rangle - \langle T_{\rm eff}\rangle^2)}{\langle T_{\rm kin}\rangle^2} \\ &= \frac{(\Delta T_{\rm eff})^2}{\langle T_{\rm kin}\rangle^2}. \end{aligned} \tag{3.12}$$

The values of $\langle T_{\rm kin}\rangle$ are obtained from the blast-wave fits to the $p_{\rm T}$ distributions of identified particles. With this, we obtain the specific heat as the heat capacity per number of particles (N) as ($c_{\rm v} = C/N$) within the system.

Let us put the specific heat calculated in the present scenario (heat capacity per particle) in perspective with quantities normally quoted in theoretical calculations. For an ideal gas of particles of mass m and degeneracy factor g at temperature T, zero chemical potential and volume V, the number of particles $N(T,V)$ can be expressed using Boltzmann statistics:

$$\begin{aligned} N &= g\int \frac{d^3x d^3p}{h^3}\exp[-\frac{\sqrt{p^2+m^2}}{T}] = \\ g\int d^3x \int \frac{d^3p}{h^3}\exp[-\frac{\sqrt{p^2+m^2}}{T}] & \\ &= g\frac{VT^3}{(2\pi)^3}\int d^3q \exp[-\sqrt{q^2+(m/T)^2}] \\ &= g\frac{VT^3}{(2\pi)^3}\alpha, \end{aligned}$$

where $q = p/T$, $\alpha = \int d^3q \exp[-\sqrt{q^2 + (\frac{m}{T})^2}]$ and we have taken $\hbar = h/(2\pi) = 1$. The energy $E(T,V)$ is given by:

$$E = g\int \frac{d^3x d^3p}{h^3}\sqrt{p^2+m^2}\exp[-\frac{\sqrt{p^2+m^2}}{T}]. \tag{3.13}$$

The heat capacity (from eqn. 4.2) can be written as,

$$C = g\int d^3x \int \frac{d^3p}{h^3}\left(\frac{p^2+m^2}{T^2}\right)\exp[-\frac{\sqrt{p^2+m^2}}{T}]$$

$$g\frac{VT^3}{(2\pi)^3}\int d^3q(q^2+(\frac{m}{T})^2)\exp[-\sqrt{q^2+(\frac{m}{T})^2}] = g\frac{VT^3}{(2\pi)^3}\beta.$$

$\beta = \int d^3q(q^2+(\frac{m}{T})^2)\exp[-\sqrt{q^2+(\frac{m}{T})^2}]$ is a dimensionless quantity. The specific heat is the heat capacity per unit phase space volume,

$$c_{\rm v} = C/\Delta, \tag{3.14}$$

where Δ is an estimate of the phase space volume. In lattice calculations one extracts the dimensionless quantity $C/(VT^3)$ and investigate its temperature dependence (15), so in these calculations $\Delta = VT^3$. However, in experiments it is simpler to measure the dimensionless quantity C/N where N is the charged particle multiplicity, and thus $\Delta = N$, where N is taken as pseudorapidity (η) density of charged particles at mid rapidity ($dN_{\rm ch}/d\eta$ at $\eta = 0$). We compare the experimental results to other model calculations for C/N as in Ref. (11), where a parton and hadron cascade model, PACIAE has been used to compute C/N. We also compare with HRG where it is straightforward to obtain both, $C/(VT^3)$ and C/N.

In experiments, the widths of the $T_{\rm eff}$ distributions are strongly affected by statistical fluctuations, which need to be subtracted as the heat capacity is related only to the dynamical part of the fluctuation. The width contains two components:

$$(\Delta T_{\rm eff})^2 = (\Delta T_{\rm eff}^{dyn})^2 + (\Delta T_{\rm eff}^{stat})^2. \tag{3.15}$$

$\Delta T_{\rm eff}^{dyn}$ values are obtained by subtracting the widths of the $T_{\rm eff}$ distributions for mixed events from the real data. With this, eqn. 3.12 is expressed as:

$$\frac{1}{C} = \frac{(\Delta T_{\rm eff}^{dyn})^2}{\langle T_{\rm kin}\rangle^2}. \tag{3.16}$$

The heat capacity C is calculated from eqn. 4.6 by using the values of T_{kin} from Fig. 4.8. Knowing the heat capacity, the specific heat, c_{v} is obtained by dividing C by number of charged particles in the system. Since the experimental results presented here are at mid-rapidity, we have divided the value of C by charged particle multiplicity at mid-rapidity (49; 50) to obtain the specific heat.

3.3 Local Temperature Fluctuations: Within the event

Local fluctuations in energy density arise because of the internal structures of the colliding nuclei. These initial fluctuations manifest into local temperature fluctuations of the fireball at different stages of the collision.

Local temperature fluctuations, which provide the amount of non-uniformity within a single event, are studied by dividing the available phase space into several y–ϕ bins, and estimating the bin temperature (T_{bin}). It helps to find local hotspots created during the initial energy density, whether those have survived or died out. The bin temperatures are obtained using the similar prescription as above. The $\langle m_{\mathrm{T}} \rangle$ of pions are calculated within the y–ϕ bin and $m_0 \leq m_{\mathrm{T}} \leq 1.5$ GeV, and T_{bin} is evaluated by using eqn. (3.3). The number of y–ϕ bins has been chosen by taking into account the number of pions in each bin so that fluctuations in the number of pions do not affect the estimation of m_{T}. The amount of local fluctuation may vary depending on the number of y bins, which needs to be evaluated.

For a given event, local temperature fluctuation in a given y–ϕ bin is expressed as:

$$F_{\mathrm{bin}} = (T_{\mathrm{bin}} - T_{\mathrm{eff}})/T_{\mathrm{eff}}. \tag{3.17}$$

For each event, a fluctuation map in y–ϕ phase space is constructed by plotting the corresponding values of F_{bin}. Fig. 3.3 shows the the temperature fluctuation map for a typical event in 6×6 bins in y–ϕ, where the fluctuations are represented by different colour pallets. This map gives a quantitative view of the local temperature fluctuation in the available phase space for an event.

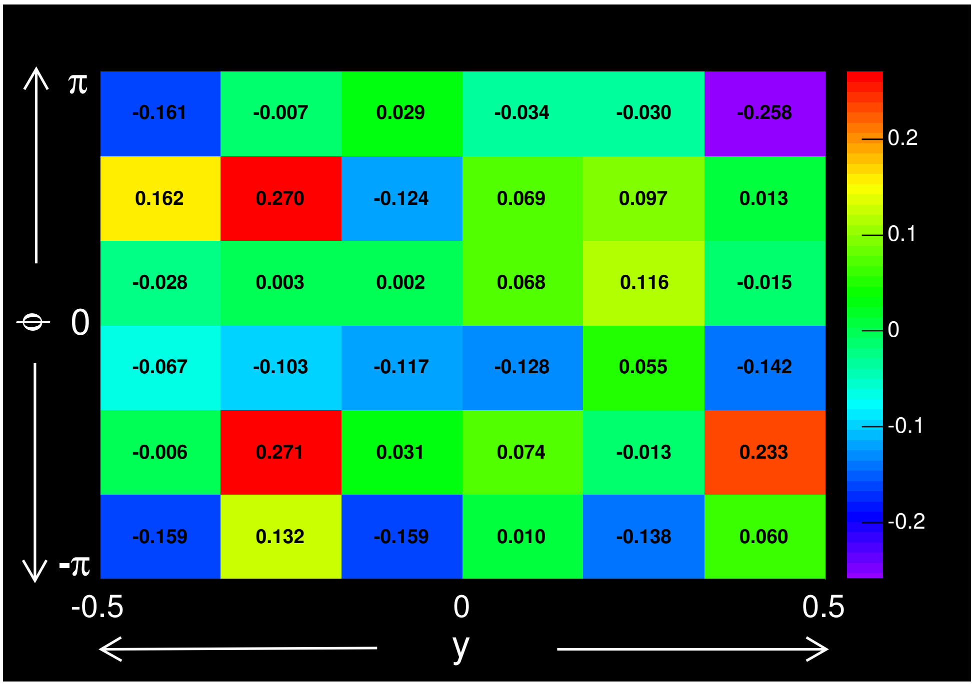

Figure 3.3: (Color online). Temperature fluctuation map in y–ϕ bins for central Pb-Pb collisions at $\sqrt{s_{\rm NN}}$ = 2.76 TeV using the AMPT model. For each y–ϕ bin, fluctuation is expressed as $(T_{\rm bin} - T_{\rm eff})/T_{\rm eff}$, the deviation of the bin temperature to the event temperature. The colour palettes indicate the magnitude of fluctuations.

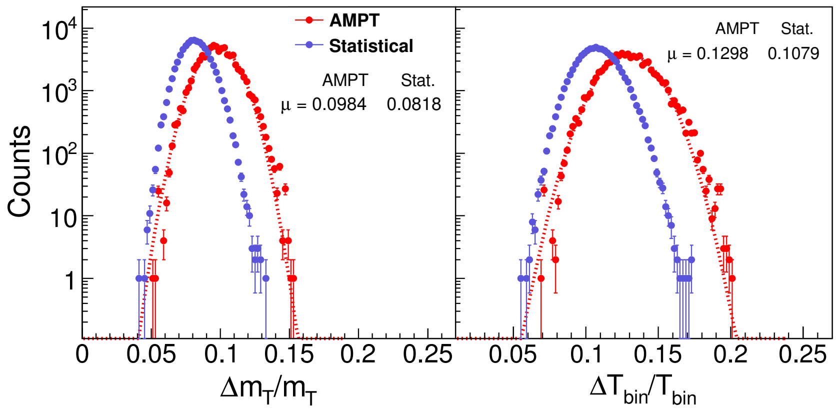

Figure 3.4: (Color online). Event-by-event local temperature fluctuations, obtained from 6×6 y–ϕ bins in central rapidity and full azimuth for central Pb-Pb collisions at $\sqrt{s_{\rm NN}} = 2.76$ TeV using the AMPT event generator.

The map shows several hot (red) as well as cold (blue) zones, and zones with average (green) fluctuation throughout the phase space. It is to be seen whether the hot and cold zones have their origin from the extreme regions of phase space that existed during the early stages of the reaction.

For a single event, the amount of local temperature fluctuation is quantified by the ratio of RMS to the mean of the $T_{\rm bin}$ distribution. Local fluctuations in $\langle m_{\rm T} \rangle$ and corresponding temperature for each event have been evaluated and their event-by-event distributions are plotted in Fig. 3.4. The left and right panels of the figure show the distributions from $\langle m_{\rm T} \rangle$ and $T_{\rm bin}$, respectively. Mean value of the local temperature fluctuation for the event sample is 12.98% for 6×6 bins in central rapidity. Statistical component of the local fluctuations has been extracted from the "synthetic" events as discussed earlier. The mean value corresponding to the statistical component of the local temperature fluctuation has been estimated to be 10.79% as shown in Fig. 3.4. The average dynamical local fluctuation, extracted after subtracting the statistical component, for AMPT events is 7.2%. The non-zero value of local temperature fluctuation may imply that these might have the contributions from the early state fluctuations.

Extraction of temperature fluctuations from experimental data maybe affected by some of the effects. Event plane orientation is one such effects, which needs to be taken care of, especially for non-central events. For the present study using AMPT, the events are event plane oriented. Fourier decomposition of the momentum distributions in the transverse plane yields a ϕ–independent, axially symmetric radial flow component and a ϕ–dependent part containing the anisotropic flow coefficients. For most central collisions, radial flow remains similar for all the events and the anisotropic flow components do not affect the slope of the m_{T} distribution. Final state effects, such as resonance decay, and hadronic rescattering tend to make the m_{T} spectra softer, and so choice of the m_{T} window has to be made in order to minimize such effects. Although present analysis uses charged pions, species dependence of temperature fluctuations may provide extra information regarding their freeze-out hyper surfaces as the particle production mechanisms of mesons, baryons and strange particles are different. This study may shed light on whether the origin of the temperature fluctuations are solely due to initial state fluctuations or includes final state effect. Viscosity tends to dilute the fluctuations. The SM version of AMPT includes the effect of viscosity ($\eta/s \sim 0.15$ at T=436 MeV (30; 34)). Further analysis using a viscous hydrodynamic models will be more realistic for this study.

Local temperature fluctuation map for each event, as shown in Fig. 3.3, has a striking similarity to the fluctuation map of the cosmic microwave background radiation (CMBR) (38). Fluctuation analysis of CMBR fluctuation map confirms the Big Bang evolution, inflation and provides information regarding the early Universe. The study of higher order moments using the maps may give access to various thermodynamic parameters at the early stages of the evolving system. Similarly, the fluctuation maps of heavy-ion collisions may form the basis of power spectrum analysis (39; 40; 41). Access to large number of events in heavy-ion collisions compared to single event analysis in CMBR may have definite advantage which can be utilized to our advantage in order to gain access to conditions that prevailed at the primordial state.

3.4 Discussions

Event-by-event temperature fluctuations over full phase space as well as local phase space bins have been proposed to characterize the hot and dense system produced in heavy-ion collisions at ultra-relativistic energies. The global temperature fluctuations provide the heat capacity as well as specific heat of the system, whereas the observation of local fluctuations would imply the presence of fluctuations at early stages of the collision. Relativistic hydrodynamic calculations have been used to understand the evolution of ϵ and T fluctuations. It shows that the system exhibits fiercely large fluctuations at early times, which diminishes with the elapse of time.

The feasibility of studying temperature fluctuations in Pb-Pb collisions at $\sqrt{s_{\rm NN}}$=2.76 TeV has been demonstrated by using simulated events from the AMPT model. Temperatures are extracted from $\langle m_{\rm T} \rangle$ of charged pions. The global fluctuation in the event temperature has been extracted and used to calculate the heat capacity. At the LHC, the phase transition is expected to be a cross over. Thus the transition may not take place at a unique point in the phase diagram due to the evolution of entropy fluctuation created at the initial state, which reflects into energy density and temperature fluctuations. Thus, the estimation of the heat capacity helps in understanding the nature of the phase transition. The variation of c_v as a function of center-of-mass beam energy for Au+Au collisions at RHIC may provide an effective tool for locating the QCD critical point (29; 30). At LHC energies, it is possible to extract local temperatures over small phase space bins in central rapidity. Extraction of Local temperature fluctuation complements the global event temperature fluctuation as the origin of local fluctuations may be of primordial in nature. For the AMPT, local temperature fluctuations over small phase bins within each event have been extracted. The amount of local fluctuation is used for n$\times$n bins in central rapidity. The observation of the non-zero local fluctuation may imply that a part of the initial fluctuations might have survived till freeze-out. The present study of global and local temperature fluctuations in conjunction with theoretical model calculations open up new avenues for characterizing the heavy-ion collisions.

Bibliography

[1] U. Heinz, J. Phys.: Conf. Ser. **455**, 012044 (2013).

[2] L. Stodolsky, Phys. Rev. Lett. **75**, 1044 (1995).

[3] M.A. Stephanov, K. Rajagopal and E. V. Shuryak, Phys. Rev. Lett. **81**, 4816 (1998).

[4] E.V. Shuryak, Phys. Lett. **B 423**, 9 (1998).

[5] M.A. Stephanov, K. Rajagopal and E. V. Shuryak, Phys. Rev. **D 60**, 114028 (1999).

[6] G. Wilk and Z. Wlodarczyk, Phys. Rev. Lett. **84**, 2770 (2000).

[7] G. Wilk and Z. Wlodarczyk, Eur. Phys. Jour. **A 48**, 161 (2012).

[8] T.K. Nayak, Jour. Phys. **G 32** S187 (2006).

[9] S. Jeon and V. Koch, arXiv:hep-ph/0304012v1 (2003).

[10] R. V. Gavai and Sourendu Gupta, Phys. Rev. **D 73**, 014004 (2006).

[11] S. Borsanyi *et al.*, JHEP **1201** 138 (2012).

[12] S. Ejiri, F. Karsch, K. Redlich, Phys. Lett. **B 633** 275 (2006).

[13] K. Aamodt *et al.*, (ALICE Collaboration), Phys. Rev. Lett. **105**, 252301 (2010).

[14] E. Abbas *et al.*, (ALICE Collaboration), Phys.Lett. **B 726** 610 (2013).

[15] R. Gavai, S. Gupta and S. Mukherjee, Phys. Rev. **D 71**, 074013 (2005).

[16] H. Holopainen, H. Niemi, and K. Eskola, Phys. Rev. **C 83**, 034901 (2011).

[17] H. Song, arXiv:1401.0079v1 [nucl-th].

[18] S. Floerchinger, U.A. Wiedemann, Phys. Rev. **C 88**, 044906 (2013).

[19] M. Laine and Y. Schroder, Phys. Rev. **D 73**, 085009 (2006).

[20] R. Paatelainen *et al.*, Phys. Rev. **C 87**, 044904 (2013).

[21] R. Chatterjee *et al.*, Phys. Rev. **C 83**, 054908 (2011).

[22] A. Toia (ALICE Collaboration), Jour. Phys. **G 38**, 124007 (2011).

[23] J. I. Kapusta, B. Muller, and M. Stephanov, Phys.Rev. **C 85**, 054906 (2012)

[24] R. Korus *et al.*, Phys. Rev. **C 64**, 054908 (2001).

[25] S. Mrowczynski, Phys. Lett. **B 430**, 9 (1998).

[26] S.A. Voloshin, V. Koch, and H.G. Ritter, Phys. Rev. **C 60** 024901 (1999).

[27] T. Alber *et al.* (NA49 Collaboration) Phys. Rev. Lett. **75** 3814 (1995).

[28] L. Adamczyk *et al.* (STAR Collaboration) Phys. Rev. **C 87**, 064902 (2013).

[29] M.M. Aggarwal *et al.* (STAR Collaboration) arXiv:1007.2613 [nucl-ex] (2010).

[30] R.V. Gavai, arXiv:1404.6615 [hep-ph] (2014).

[31] Z.-W. Lin, C.M. Ko, B.-A. Li, B. Zhang, S. Pal, Phys. Rev. **C 72**, 064901 (2005).

[32] J.K. Nayak and J. Alam, Phys. Rev. **C 80**, 064906 (2009).

[33] B. Abelev *et al.* (ALICE Collaboration), Phys. Rev. **C 88**, 044910 (2013).

[34] S. Pal and M. Bleicher, Phys. Lett. **B 709**, 82 (2012).

[35] J. Xu and C.M. Ko, Phys. Rev. **C 83**, 034904 (2011).

[36] J. Xu and C.M. Ko, Phys. Rev. **C 84**, 014903 (2011).

[37] D. Solanki, *et al.*, Phys. Lett. **B 720**, 352 (2013).

[38] E. Komatsu and C. L. Bennett (WMAP science team) Prog. Theor. Exp. Phys., 06B102 (2014).

[39] A.P. Mishra *et al.*, Phys. Rev. **C 77**, 064902 (2008); *ibid.*, Phys. Rev. **C 81**, 034903 (2010).

[40] A. Mocsy and P. Sorensen, Nucl. Phys. **A 855**, 241 (2011).

[41] P. Naselsky *et al.* Phys. Rev. **C 86**, 024916 (2012).

[42] Ben-Hao Sa *et al.* Phys. Rev. **C 75**, 054912 (2007).

Chapter 4

Base-Line Study of Temperature Fluctuation

In this chapter I will discuss different model predictions about specific heat from temperature fluctuations, theory predictions (9; 10; 33), lattice calculations (15), results from event generators motivated via microscopic transport models (32), results from earlier experiments and calculation from previous data (27; 28; 29). The methodology followed to extraction of specific heat result are same as previous chapter. This chapter also provide a strong base-line analysis and towards feasibility checking and expectations for future studies.

The major goal of colliding heavy-ions at the Relativistic Heavy Ion Collider (RHIC) at Brookhaven National Laboratory and the Large Hadron Collider (LHC) at CERN is to study matter at extreme conditions of temperature and energy densities, where quarks and gluons, rather than mesons and baryons, define the relevant degrees of freedom (1). This new phase of matter, the Quark-Gluon Plasma (QGP), is governed by the principles of Quantum Chromodynamics (QCD) and is the result of a phase transition from the normal nuclear matter (1; 2). Experiments at RHIC and LHC are on the quest to unearth the nature of the QCD phase transition and to get a glimpse of how matter behaves at extreme conditions.

4.1 Toy Model Study:

In this section, I develove a toy model to study the feasibility of studying temperature fluctuations. This is a very naive model, based on Maxwell-Boltzmann statistics, i.e the randomly generated particle spectra distributed as

$$F(p_{\mathrm{T}}) = \frac{1}{p_{\mathrm{T}}}\frac{dN}{dp_{\mathrm{T}}} \approx Ae^{-p_{\mathrm{T}}/T_{\mathrm{eff}}}, \tag{4.1}$$

Now, investigating one more step that wheather due limited number of particle produced each collision this temperature or inverse slope, depends on particle number. For this we use a data driven method, that $\frac{dN_{ch}}{d\eta}$ at midrapidity varies with $\sqrt{S_{NN}}$ as $\propto s^{0.155}$. Also, like the real scenario, the particle number fluctuations due to impact parameter fluctuation, a 10% fluctuation on multiplicities are considered initially. But it can be further, investigated starting from no or 0% fluctuation to a 20% fluctuation how temperature fluctuation get affected. The schematic diagram of the processes are shown in Fig 4.1.

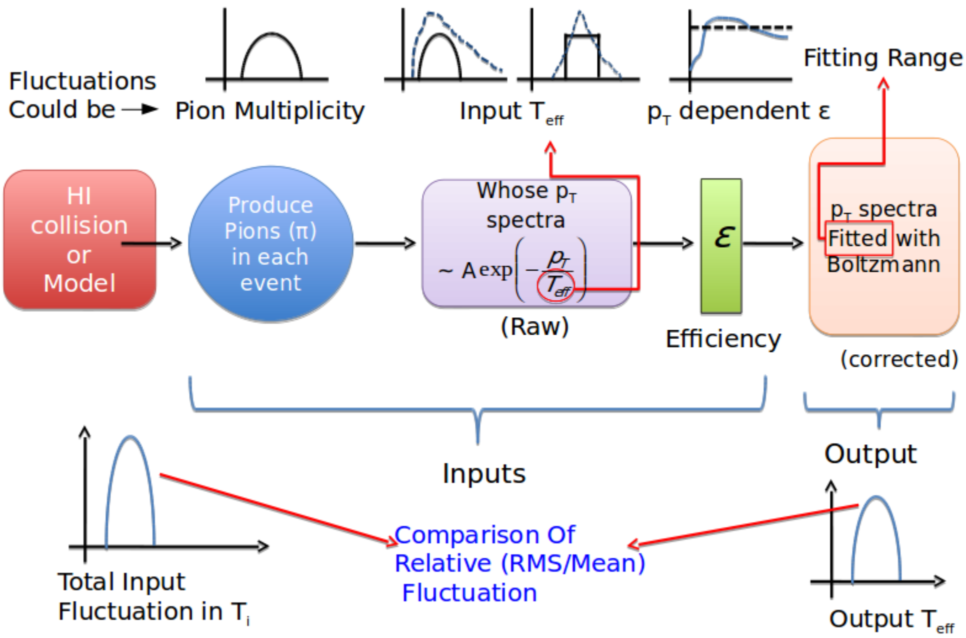

Figure 4.1: Schematic diagram of the Toy Model of event-by-event Mean p_T & T_{eff} of pions.

Now, another source of fluctuation is again consider about the probability distribution like gaussian type or NBD type and similarly fluctuations of their parameters. Next coming to the physics part, assuming fluctuations in inverse slope part by varying different % of fluctuations on T_{eff}.

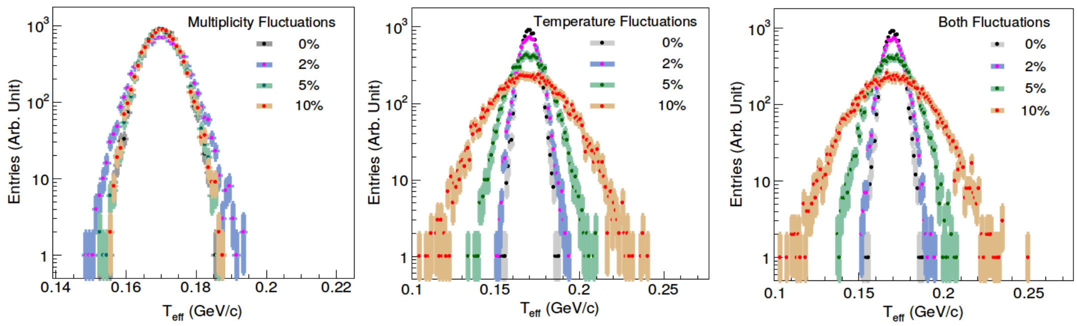

Figure 4.2: Fluctuation of output $T_{\rm eff}$ from toy model due to (a) only multiplicity, (b) only temperature and (c) both multiplicity and temperature fluctuations.

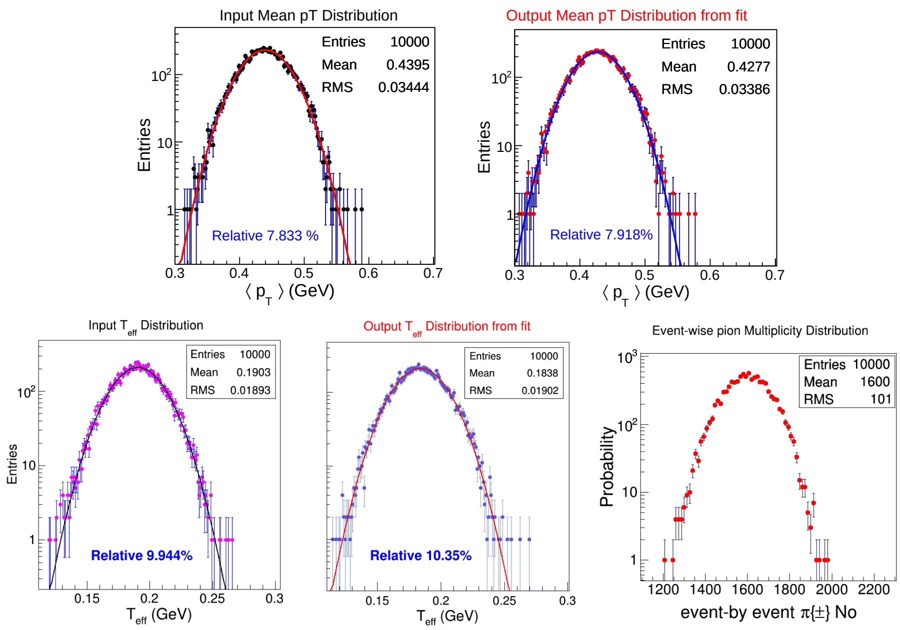

Figure 4.3: Comparing the relative fluctuation of input and output $\langle p_{\rm T} \rangle$ and $T_{\rm eff}$ from toy model various factors.

Again, as in experiment final spectra normally corrected from a p_T dependent detector effeciency correlations. here we employ a data driven realistic p_T dependent efficiency factor and scalled it accordingly. I also study the variation of different efficiency shape.

Finnally, with this generated efficiency corrected pseudo-spectra temperature extraction is done via both the ways (a) Mean p_T and (b) by fitting with Boltzmann. In both the cases fluctuation aries due to the choice of p_T window. Now, all this input fluctuations which are known and user controlled are being translated and can be compared with the final form of fluctuation. By doing this one can have some idea how their fluctuation strength evolved, is there any dilution of flucuation or enhancement by these processes. These steps can be redone via more realistic particle production approach considering Boltzmann-Gibbs Blast wave type of prticle production.

To investigate with this toy model, first we fixed the temperature and varying the fluctuation % in multiplicity in an event-by-event basis around a fixed multiplicity for a perticular centrality and fixed energy. Later, repeated the steps with fixed multiplicity and varying % of fluctuation in temperature. Then I consider, fluctuation in both multiplicity and temperature as shown in Fig 4.2. Here one can conclude multiplicity fluctuation has minimal effects on temperature fluctuation above a certain average multiplicity ~ 50. investigating further, the propagation of fluctuation by comparing both $\langle p_{\mathrm{T}} \rangle$ and $T_{\mathrm{eff}}$from input and output considering all the processes like realistic p_{T} dependent efficiency correction, multiplicity fluctuation and choice of fitting range are shown in Fig 4.3.

4.2 Hydrodynamical Model Expectations:

Fluctuations of any observable of a system have two distinct origins, first, quantum fluctuations which are initial state fluctuations occurring at fast time scales and second, classical thermodynamical fluctuations which occur after elapse of sufficient time after the collision (23; 37). Initial state fluctuations arise because of internal structures of the colliding nuclei, and fluctuation in initial energy densities, and appear as event-by-event fluctuations in the energy density or temperature. Thermodynamic fluctuations have multiple sources, such as local thermal fluctuations of energy density, and event-by-event variation in the freeze-out conditions. Local fluctuations in energy density arise because of the internal structures of the colliding nuclei. These initial fluctuations manifest into local temperature fluctuations of the fireball at different stages of the collision. Relativistic hydrodynamic calculations which take such effects into account reveal large local fluctuations in ϵ and T in small phase space bins at early stages of the collision (1; 16; 17; 18). The local fluctuations have been quantified throughout the evolution by simulating central (0–5% of the total cross section) Pb-Pb events at $\sqrt{s_{\rm NN}} = 2.76$ TeV by the use of a (2+1)-dimensional event-by-event ideal hydrodynamical framework (16) with lattice-based equation of state (60). The formation time of the plasma is taken to be 0.14 fm (20; 21). A wounded nucleon (WN) profile is considered where the initial entropy density is distributed using a 2-dimensional Gaussian distribution function,

$$s(X,Y) = \frac{K}{2\pi\sigma^2} \sum_{i=1}^{N_{\rm WN}} \exp\Big(- \frac{(X-X_i)^2 + (Y-Y_i)^2}{2\sigma^2}\Big). \tag{4.2}$$

Here X_i, Y_i are the transverse coordinates of the $i^{\rm th}$ nucleon and K is an overall normalization constant. The size of the density fluctuations is determined by the free parameter σ, which is taken to be 0.4 fm (16). The transition temperature from the QGP to the hadronic phase is chosen to be 170 MeV and the kinetic freeze-out temperature is taken as 160 MeV. The results for ϵ and T at different times (τ) are analyzed for each collision in X-Y phase space bins in the transverse plane (each bin is chosen to be 0.6 fm$\times$0.6 fm).

Time evolutions of the distributions of ϵ and T have been presented for four values of τ in Fig. 3.1 for a single event. The upper panels (a-d) of the figure show three dimensional view of ϵ, whereas the lower panels (e-h) show corresponding values of T in the transverse plane. At early times, sharp and pronounced peaks in ϵ and hotspots in T are observed. Large bin-to-bin fluctuations observed in ϵ and T indicate that the system formed immediately after collision is quite inhomogeneous in phase space. As time elapses, the system cools, expands, and the bin-to-bin variations in ϵ and T smoothen out.

Observations from Fig. 3.1 have been quantified in terms of the mean energy density ($\langle\epsilon\rangle$),

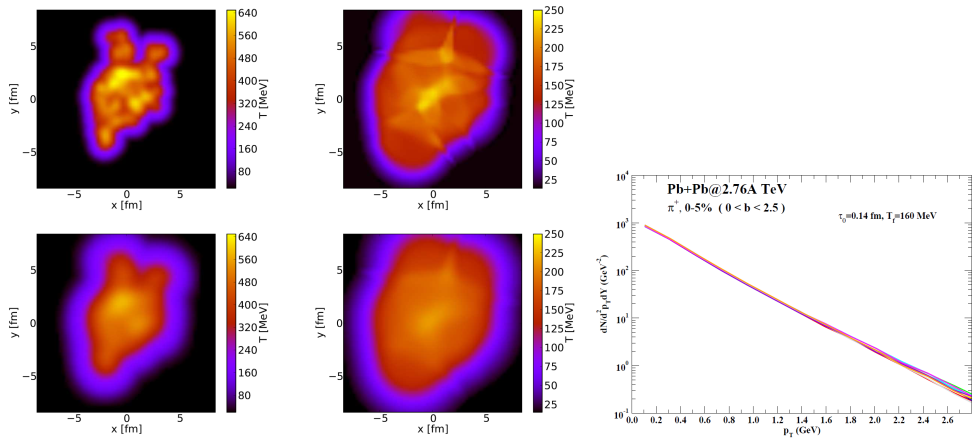

Figure 4.4: Evolution of temperature in the X-Y plane with different time-snap and produced final spectra shape from hydrodynamic calculation.

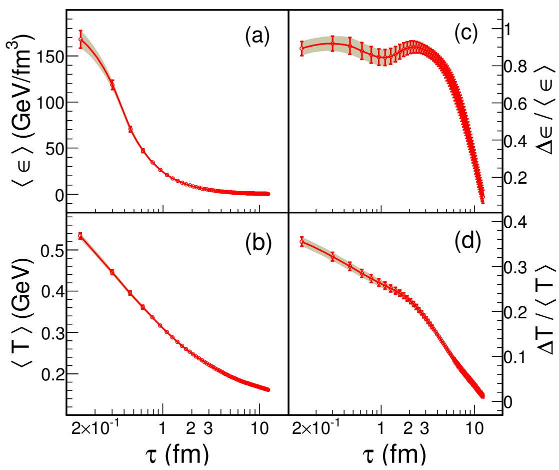

Figure 4.5: Evolution of mean energy density and temperature and their relative fluctuations in the X-Y plane with elapsed time from hydrodynamic calculation.

mean temperature ($\langle T\rangle$) over the X-Y bins, and the bin-to-bin fluctuations of ϵ and T as a function of τ. The time evolution of $\langle\epsilon\rangle$, $\langle T\rangle$, and their fluctuations are presented in Fig. 1.2, where τ is plotted in logarithmic scale for zooming in on the early times.

The shaded regions represent the extent of event-by-event variations, taken from a sample of five hundred events. It is observed that $\langle\epsilon\rangle$ falls sharply from $\sim$168 GeV/fm^3 at $\tau = 0.14$ fm to a value of ~20 GeV/fm^3 at $\tau = 1$ fm, and then falls slowly till freeze-out. The initial ϵ is close to the experimental result, estimated by the ALICE collaboration (13; 22). The fall of $\langle T \rangle$ with τ is smooth, which goes down from ~530 MeV at $\tau = 0.14$ fm to ~300 MeV at $\tau = 1$ fm. At the freeze-out, as expected, $\langle T \rangle$ is close to 160 MeV.

The bin-to-bin fluctuations, $\Delta\epsilon/\langle\epsilon\rangle$ and $\Delta T/\langle T \rangle$, are presented in the right panels of Fig. 1.2, where $\Delta\epsilon$ and ΔT are the root mean square (RMS) deviations of the two quantities over the bins. Averaging is taken over the X-Y bins in every event. The shaded regions in the figure, represent the extent of event-by-event variations for a large number of events. At early times, the fluctuations are observed to be very large (~90% and ~35% for ϵ and T, respectively), which indicate the violent nature of the matter created in the collision. Interestingly, although $\langle\epsilon\rangle$ decreases quite fast, the fluctuation in ϵ remains almost constant up to τ~2.5 fm, and then decreases rapidly. Around the same τ, the fluctuation in T shows a kink, beyond which the fluctuation decreases even faster. During the hydrodynamic evolution, there may be a characteristic change in the behaviour of the system at this time, which needs to be understood. Nevertheless, it is clear that a detailed insight to the evolution of fluctuations is possible by studying local temperature fluctuations.

4.3 HRG and AMPT Expectations:

Starting from the discussion in last chapter, the relation of $\langle p_{\rm T} \rangle$ within a range of a to b, is given by:

$$\langle p_{\rm T} \rangle = 2T_{\rm eff} + \frac{a^2 e^{-a/T_{\rm eff}} - b^2 e^{-b/T_{\rm eff}}}{(a + T_{\rm eff})e^{-a/T_{\rm eff}} - (b + T_{\rm eff})e^{-b/T_{\rm eff}}}. \tag{4.3}$$

This equation links the value of $\langle p_{\rm T} \rangle$ within a specified range of $p_{\rm T}$ to $T_{\rm eff}$.

In order to validate the relation between $p_{\rm T}$ to $T_{\rm eff}$, we have generated a large number of events using the AMPT model (32) and URQMD model for A+A collisions at different energies. The goal is to compare the values of $T_{\rm eff}$ obtained from event-by-event $p_{\rm T}$ distribution and from

$\langle p_T \rangle$ distributions. For top central (top 5% cross section) collisions, p_T distribution of pions has been constructed for each event within a rapidity range of -1.0 to 1.0. The distribution is fitted to an exponential function and the inverse slope parameter ($T_{\rm eff}$) is extracted within fit range, $0.15 < p_T < 2.0$ GeV. Fig. 4.11 shows the extracted event-by-event $T_{\rm eff}$ distribution (as solid circles). For the same set of events, the values of $\langle p_T \rangle$ has been calculated within the same η and p_T ranges for each event. From the value of $\langle p_T \rangle$ for each event, the $T_{\rm eff}$ is calculated using eqn. (4.3). Resulting $T_{\rm eff}$ distribution has been plotted as open squares in Fig. 4.11. Both the $T_{\rm eff}$ distributions are observed to be same. This validates the relationship of $\langle p_T \rangle$ and $T_{\rm eff}$ as given in eqn. (4.3).

For pion, $f(\beta_T) \approx m_0 \langle \beta_T \rangle^2$. The event-by-event fluctuations of β_T needs to be taken into account for calculating the fluctuation in kinetic temperature (19; 38; 39; 40). Fluctuation in β_T dominates over the fluctuation in $T_{\rm kin}$ for small systems (e.g. pp) (41), asymmetric (e.g., pPb) (19) and non-central collisions. For central Au+Au collisions at $\sqrt{s_{\rm NN}} = 200$ GeV (44), $\beta_T = 0.59 \pm 0.051$ and for central Pb+Pb collisions at $\sqrt{s_{\rm NN}} = 2.76$ TeV (45), $\beta_T = 0.651 \pm 0.02$, which translate to $T_{\rm kin}$ as 0.095 ± 0.010 GeV and 0.09 ± 0.005 GeV, respectively by using blast-wave fit (42). For the present work, we consider 10% fluctuation in β_T and calculate its effect on specific heat. C is calculated using the equation, Let us put the specific heat calculated in the present scenario (heat capacity per particle) in perspective with quantities normally quoted in theoretical calculations. For an ideal gas of particles of mass m and degeneracy factor g at temperature T, zero chemical potential and volume V, the number of particles $N(T, V)$ can be expressed using Boltzmann statistics. We compare the experimental results to other model calculations for C/N as in Ref. (11), where a parton and hadron cascade model, PACIAE has been used to compute C/N. We also compare with HRG where it is straightforward to obtain both, $C/(VT^3)$ and C/N as discussed in previous chapter.

The values of $T_{\rm kin}$ have been reported by experiments at RHIC and LHC, as the final state particles give the information about $T_{\rm kin}$ from the particle spectra (43). These are obtained by making combined fits to the identified particle spectra using the Boltzmann-Gibbs blast-wave

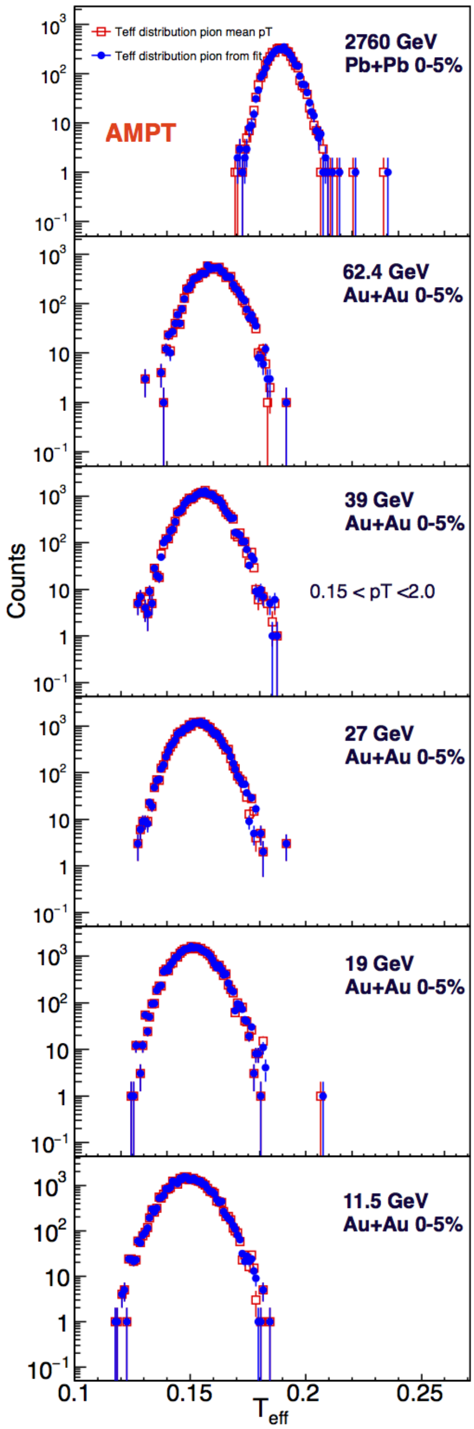

Figure 4.6: Checking of eqn. (4.3) for 5% most central A+A collisions at $\sqrt{s_{\mathrm{NN}}}$ = 7.7 and 2760 GeV (29) with AMPT event generator.

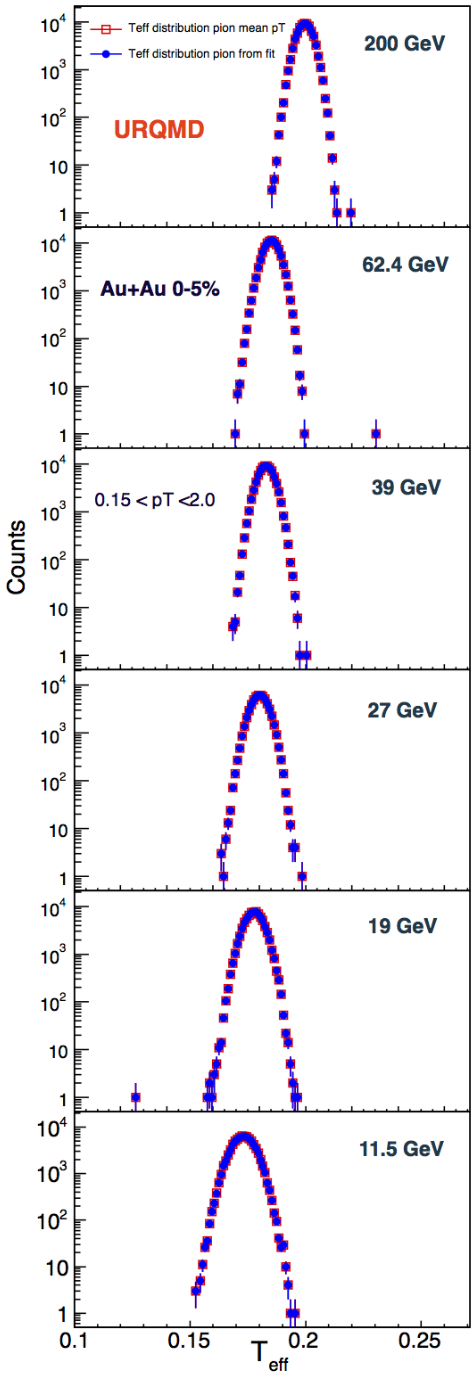

Figure 4.7: Further checking of eqn. (4.3) for 5% most central A+A collisions at $\sqrt{s_{\mathrm{NN}}} = 7.7$ and 200 GeV (29) with UrQMD models event generator.

Table 4.1: AMPT model data to calculate excitation fuction of specific heat

System	$\sqrt{S_{NN}}$ (GeV)	T_{eff} (GeV)	ΔT_{eff} (GeV)	$\frac{dN_{ch}}{d\eta}\|_{\eta=0}$
Au+Au	7	0.1672	0.00971	270.1±22.96
	11	0.1705	0.008479	331.5±26.34
	19	0.1725	0.007607	399.7±30.62
	27	0.1739	0.007457	437.4±34.56
	39	0.176	0.007337	486.1±37.17
	62.4	0.1797	0.006943	530.1±42.58
	200	0.2009	0.006007	741.8±66.93
Pb+Pb	2760	0.2048	0.004594	1520±192.7

model. Figure 4.8 gives the T_{kin} values for different beam energies and collision systems (29; 44; 45). In addition, chemical freeze-out temperatures (T_{ch}), extracted from the identified particle yield by using thermal model calculations (46; 47), are also shown in the figure. We find that the difference between T_{ch} and T_{kin} increases with the increase of beam energy. Lattice calculations indicate that c_{v} is a monotonically increasing function of T at zero μ_B. Thus we expect that the difference between the c_{v} extracted at the chemical and kinetic freezeout surfaces should also increase with beam energy following the trends of T_{ch} and T_{kin}. We calculate c_{v} from HRG model for two scenarios. In the first case, we compute at the chemical freezeout surface using the extracted T_{ch} as well as μ_B. However, in the experiment one can only determine the c_{v} at the kinetic freezeout surface where the momentum exchange freezes. The thermal conditions at the kinetic freezeout surface are much different from that at the chemical freezeout surface. Hence the fireball is expected to have different c_{v} at the two surfaces. In the second case, we try to estimate c_{v} at the kinetic freezeout surface using $T_{\text{kin}}$and zero hadron chemical potentials.

A better estimate of c_{v} could be made with realistic hadron chemical potentials taking into account the conservation of hadron number from the chemical to the kinetic freezeout surfaces. For both scenarios, we calculate $C/(VT^3)$ and C/N for a wide range of beam energy, from $\sqrt{s_{\text{NN}}}$ = 1.91 GeV to 2.76 TeV. The results of c_{v} are shown in the Fig. 4.9. It is observed

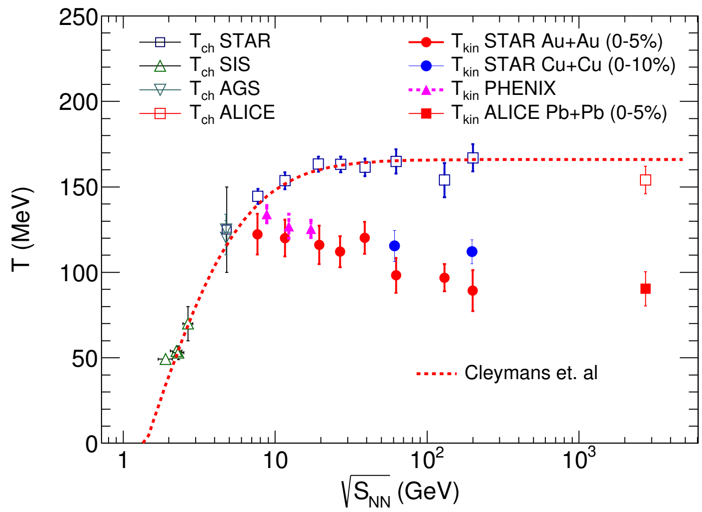

Figure 4.8: Chemical and kinetic freeze-out temperatures for central Au+Au (44) and Cu+Cu (29) collisions at RHIC energies, and Pb+Pb collisions at $\sqrt{s_{\rm NN}} = 2.76$ TeV (45). Thermal model calculation (46) to $T_{\rm ch}$ is also shown.

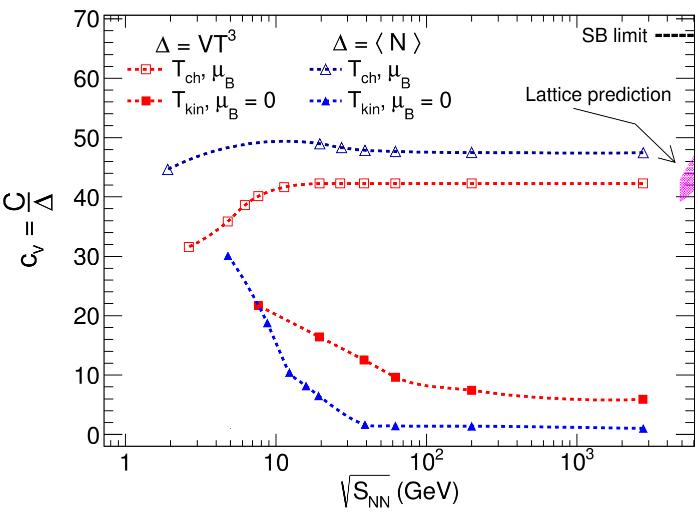

Figure 4.9: Specific heat, $c_{\rm v}$ as a function of collision energy from the HRG model for two temperature settings, $T_{\rm ch}$ with finite $\mu_{\rm B}$, and $T_{\rm kin}$, and two phase space volumes, $\Delta = VT^3$ and $\langle N \rangle$. Lattice calculation for $c_{\rm v}$ at $T = 154 \pm 9$ MeV (15) and Stefan-Boltzmann limit are indicated in the figure.

Table 4.2: Experimental data to calculate excitation fuction of specific heat

Experiment	$\sqrt{s_{NN}}$ (GeV)	T_{kin} (GeV)	ΔT_{kin} (GeV)	T_{ch} (GeV)	ΔT_{ch} (GeV)	T_{eff}	ΔT_{eff}	$\frac{dN_{ch}}{d\eta}\|_{\eta=0}$
NA49 Pb+Pb (Fixed Target)	6.27	0.117	0.004	0.134	0.005	0.117	0.0264	29±6
	7.62	0.132	0.004	0.142	0.004	0.132	0.0275	38±6
	8.77	0.123	0.003	0.146	0.004	0.123	0.0232	44±15
	8.80	0.134	0.005	0.143	0.005	0.123	0.0232	44±15
	12.30	0.127	0.007	0.153	0.005	0.123	0.0232	61±9
	17.30	0.125	0.005	0.168	0.005	0.126	0.0189	77±10
STAR Au+Au (collider)	62	0.098	0.010	0.154	0.009	0.248	0.008	472
	130	0.096	0.008	0.154	0.0097	0.257	0.00894	587
	200	0.089	0.012	0.159	0.0058	0.268	0.00815	691
STAR Cu+Cu (collider)	62.4	0.115	0.009	0.256	0.0175	0.132		
	200	0.112	0.007	0.268	0.0161	0.190		
EB66 (F.T.)	4.80	0.127	0.010	0.125	0.003			

that the trend of c_{v} as a function of $\sqrt{s_{\mathrm{NN}}}$ is similar to the nature followed by chemical and kinetic freeze-out temperatures. The value of C/N corresponding to T_{kin} shows a sharp drop with increase of energy, and beyond $\sqrt{s_{\mathrm{NN}}} = 62.4$ GeV, the rate of decrease is very slow.

Recent lattice calculations for c_{v} have been reported (15) as a function of temperature. The lattice results are at zero baryonic potential, hence only relevant at the LHC and higher energies. The value of c_{v} as indicated in the Fig. 4.9 is for $T = 154 \pm 9$ MeV, corresponding to the QCD transition temperature. It is seen that at the transition temperature and below, HRG results of $C/(VT^3)$ agree well with lattice calculations (15). The Steffan-Boltzmann non-interacting gas limit ($c_{\mathrm{v}} \approx 66$) is also shown in the figure.

4.4 Fluctuations of $\langle p_{\mathrm{T}} \rangle$ and T_{eff} from Published data:

Experimental data for $\langle p_{\mathrm{T}} \rangle$ distributions have been reported by experiments at SPS and RHIC (22; 23; 24; 25; 26; 27; 28). In the left panel of Fig. 4.10 we present the $\langle p_{\mathrm{T}} \rangle$ distributions from the STAR experiment (27; 28) for the 5% most central Au+Au collisions at $\sqrt{s_{\mathrm{NN}}} = 20$, 62.4, 130 and 200 GeV. The results are shown for charged particle tracks within $|\eta| < 1$ and

$0.15 < p_{\mathrm{T}} < 2.0$ GeV. The solid points are the event-by-event $\langle p_{\mathrm{T}} \rangle$ distributions from the experimental data, whereas the open circles are the corresponding results for mixed events. The mixed events are created by randomly selecting charged particles from different events. The mixed event distributions contain all the systematic effects arising from the detector effects, such as efficiency and acceptance, as well as include statistical fluctuations. The non-statistical or dynamical fluctuations in $\langle p_{\mathrm{T}} \rangle$ can be extracted by subtracting the width of the mixed event distribution from that of the real data.

It has been observed that the $\langle p_{\mathrm{T}} \rangle$ distributions are nicely described by using the gamma (Γ) distribution (27; 28; 31):

$$f(x) = \frac{x^{\alpha-1} e^{-x/\beta}}{\Gamma(\alpha)\beta^{\alpha}}. \tag{4.4}$$

Here x represents the $\langle p_{\mathrm{T}} \rangle$. The mean ($\mu$) and standard deviation (σ) of the distribution are related to the fit parameters (α and β) by $\mu = \alpha\beta$ and $\sigma = \sqrt{\alpha\beta^2}$. Both the real and mixed event $\langle p_{\mathrm{T}} \rangle$ distributions are fitted with the Γ function and the fits are shown by the solid and dashed lines, respectively, in the left panels of Fig. 4.10. The fitted distributions are used to generate a large number of $\langle p_{\mathrm{T}} \rangle$ values for which corresponding T_{eff} values are calculated from eqn. 4.3. The resulting histograms represent event-by-event T_{eff} distributions, which are shown in the right panels of Fig. 4.10 for both real data and mixed events. These distributions are also fitted by the Γ function as shown by the solid and dashed lines for data and mixed events, respectively. Table 8.1 lists the fit parameters for event-by-event T_{eff} distributions for data and mixed events.

The system size dependence of $\langle p_{\mathrm{T}} \rangle$ and T_{eff} distributions have been studied with the STAR experimental data of top 10% central Cu+Cu collisions at $\sqrt{s_{\mathrm{NN}}} = 62.4$ and 200 GeV (29). The results are presented in in Fig. 4.11. Corresponding Γ distribution fit parameters to the event-by-event T_{eff} distributions for top 10% central collisions are tabulated in Table 8.2.

From these two figures and the given tables for $\langle p_{\mathrm{T}} \rangle$ and T_{eff} distributions for Au+Au and

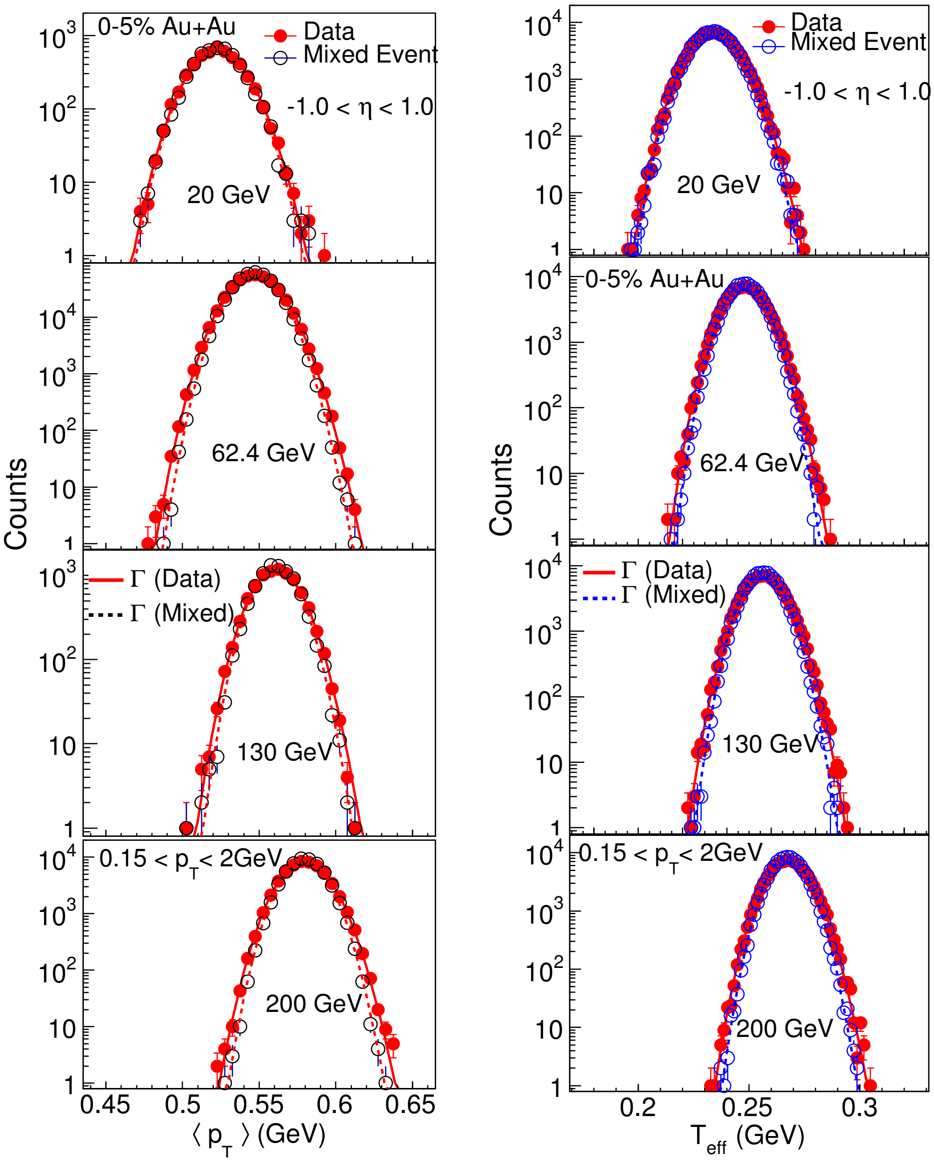

Figure 4.10: Left panels show event-by-event mean transverse momentum distributions for 5% most central Au+Au collisions at $\sqrt{s_{\mathrm{NN}}}$ = 20, 62.4, 130 and 200 GeV within $|\eta| < 1$ and $0.15 < p_{\mathrm{T}} < 2.0$ GeV (28). Distributions for mixed events are superimposed on the data. The solid and dashed lines show the fits with Γ functions. The right panels show the extracted T_{eff} distributions for each incident energy.

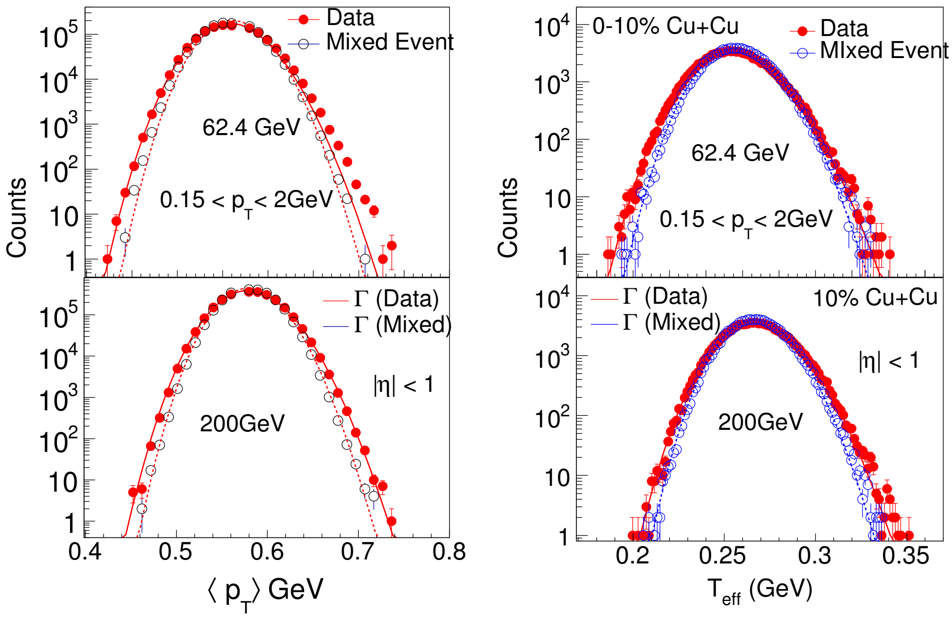

Figure 4.11: Similar distributions as in Fig. 4.10 for 10% most central Cu+Cu collisions at $\sqrt{s_{\mathrm{NN}}} = 62.4$ and 200 GeV (29).

Table 4.3: The event-by-event T_{eff} distributions for central (top 5%) Au+Au collisions are fitted by the gamma function. Table gives fhe fit parameters, α and β along with mean (μ) and standard deviation (σ).

$\sqrt{s_{\mathrm{NN}}}$ (GeV)	Case	α	β (GeV)	μ (GeV)	σ (GeV)
20	data	658.53	3.556×10^{-4}	0.2341	0.00912
20	mixed	724.56	3.229×10^{-4}	0.2339	0.00869
62.4	data	860.20	2.885×10^{-4}	0.2482	0.00846
62.4	mixed	1043.67	2.378×10^{-4}	0.2481	0.00768
130	data	920.25	2.789×10^{-4}	0.2566	0.00846
130	mixed	1140.12	2.249×10^{-4}	0.2564	0.00759
200	data	1078.23	2.483×10^{-4}	0.2677	0.00815
200	mixed	1387.56	1.927×10^{-4}	0.2674	0.00718

Table 4.4: The event-by-event T_{eff} distributions for central (top 10%) Cu+Cu collisions are fitted by the gamma function. Table gives th fit parameters, α and β along with mean (μ) and standard deviation (σ).

$\sqrt{s_{\text{NN}}}$ (GeV)	Case	α	β (GeV)	μ (GeV)	σ (GeV)
62.4	data	211.88	12.040×10^{-4}	0.2550	0.0175
62.4	mixed	271.94	9.455×10^{-4}	0.2571	0.0156
200	data	277.08	9.687×10^{-4}	0.2684	0.0161
200	mixed	370.71	7.278×10^{-4}	0.2698	0.0140

Cu+Cu collisions at RHIC energies, we can infer that: (a) the mean values of the event-by-event $\langle p_{\text{T}}\rangle$ and T_{eff} consistently increase with the increase of beam energy, (b) the widths of the distributions decrease with the increase of beam energy. In addition, the widths for Cu+Cu system are observed to be larger compared to the corresponding widths of the Au+Au system. This may be because of the smaller system size for Cu+Cu compared to Au+Au system.

Experimental data for event-by-event $\langle p_{\text{T}}\rangle$ distributions are not available for Pb+Pb collisions at LHC energies (48). The string melting mode of AMPT model is used to generate central (top 5%) Pb+Pb collisions at $\sqrt{s_{\text{NN}}} = 2.76$ TeV. The $\langle p_{\text{T}}\rangle$ and T_{eff} distributions are constructed from these generated events as shown in Fig 1. This distribution will be used to extract specific heat at the LHC energy.

4.5 Specific heat from experimental data

The widths of the T_{eff} distributions are strongly affected by statistical fluctuations, which need to be subtracted as the heat capacity is related only to the dynamical part of the fluctuation. The width contains two components:

$$(\Delta T_{\text{eff}})^2 = (\Delta T_{\text{eff}}^{dyn})^2 + (\Delta T_{\text{eff}}^{stat})^2. \tag{4.5}$$

$\Delta T_{\rm eff}^{dyn}$ values are obtained by subtracting the widths of the $T_{\rm eff}$ distributions for mixed events from the real data. With this, eqn. 3.12 is expressed as:

$$\frac{1}{C} = \frac{(\Delta T_{\rm eff}^{dyn})^2}{\langle T_{\rm kin}\rangle^2}. \tag{4.6}$$

The heat capacity C is calculated from eqn. 4.6 by using the values of $T_{\rm kin}$ from Fig. 4.8. Knowing the heat capacity, the specific heat, $c_{\rm v}$ is obtained by dividing C by number of charged particles in the system. Since the experimental results presented here are at mid-rapidity, we have divided the value of C by charged particle multiplicity at mid-rapidity (49; 50) to obtain the specific heat. This is presented in Fig. 4.9 for Au+Au and Cu+Cu collisions at RHIC energies. The estimated C/N for the LHC energy from the AMPT model using Fig. 3.2 is also shown in the figure. The errors in the data points are estimated mainly from the following sources:

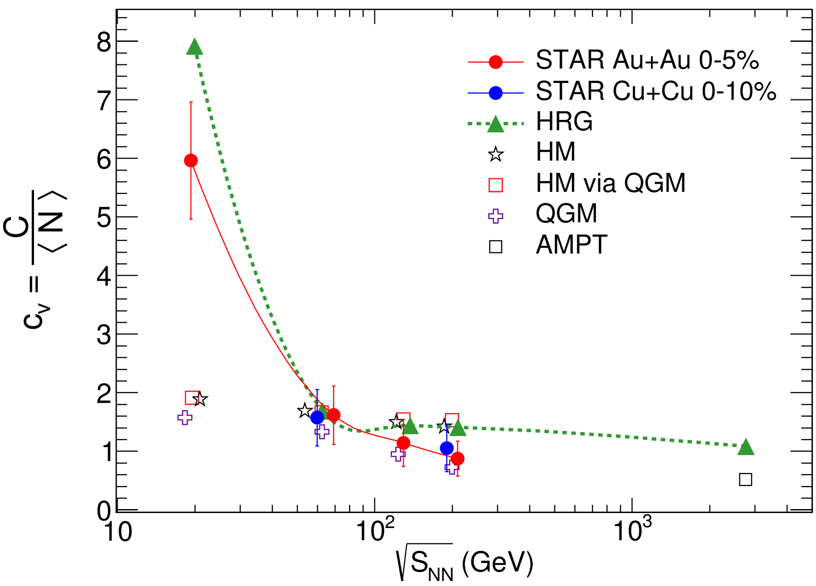

Figure 4.12: Specific heat, $c_{\rm v}$ as a function of collision energy for central Au+Au and Cu+Cu collisions at RHIC energies. Result from AMPT model is given for the LHC energy at $\sqrt{s_{\rm NN}}$ = 2.76 TeV. HRG calculations at $T_{\rm kin}$ are shown in the figure. Model calculations for three different scenarios from Ref. (11) are superimposed on the experimental results.

(a) error in extraction of $T_{\rm kin}$ using the blast-wave fits, (b) error in charge particle multiplicity density, and (c) error in $\langle p_{\mathrm{T}} \rangle$ as reported in the experimental data. The error in T_{kin} takes into account the spread in the value of (β_{T}). It is observed that C/N has a sharp drop from $\sqrt{s_{\mathrm{NN}}} = 20$ GeV to 62.4 GeV, beyond which the decrease is rather slow up to the LHC energy.

HRG calculations for C/N with T_{kin} are superimposed in Fig. 4.12. These results follow the experimental data points quite well. In Ref. (11), specific heat for central (top 5%) Au+Au collisions at RHIC energies are discussed using a parton and hadron cascade model, called PACIAE. The results of the model calculations are presented for three cases: hadronic matter in the final state (HM), quark-gluon matter in the partonic initial state (QGM), and hadronic matter via quark-gluon matter (HM via QGM). These results for Au+Au collisions are also presented in Fig. 4.12. The results of these models miss the experimental data point at $\sqrt{s_{\mathrm{NN}}} = 20$ GeV, but can explain the data at higher energies.

4.6 Discussion

In an earlier publication by R. Korus *et al.* (Ref. (21)), the experimental data of p_{T} correlations from the NA49 experiment (22; 23; 24) for Pb+Pb collision at laboratory energy of 158 GeV had used to calculate specific heat, which yielded a value of 60 ± 100. The large error bars of these results made the reported results insignificant. One of the possible reasons for the large errors is the low particle multiplicity which gives a significant hindrance to the calculation of dynamic temperature fluctuations (17). At the SPS energies, $\langle p_{\mathrm{T}} \rangle$ distributions have been reported by NA49 collaboration for laboratory energies of 20, 30, 40 80 and 158 GeV (22; 23; 24) and the CERES collaboration at 40, 80 and 158 GeV (25). In both of the data sets, the $\langle p_{\mathrm{T}} \rangle$ distributions for real data and mixed event are indistinguishable. These are also prominent in the ratio plots of real and mixed events as shown in Ref. (25). Thus the extraction of dynamic fluctuation in temperature and so the specific heat is not possible. In the present work, we have probed much higher energy collisions, where the charged particle multiplicities in each event are large, allowing for the extraction of the dynamical part of the temperature fluctuation by overcoming the statistical fluctuations.

The results of specific heat for Cu+Cu collisions are close to that of Au+Au collisions. This shows that although a large change of volume happens in going from Cu+Cu to Au+Au systems, the two systems are not very different thermodynamically.

4.7 Summary and Outlook

We have studied the excitation energy dependence of specific heat of hadronic matter formed in heavy-ion collisions corresponding to RHIC and LHC energies. In the present work, dynamical component of the temperature fluctuation is calculated from $\langle p_{\rm T}\rangle$ distributions. From this, the specific heat is obtained as heat capacity per charge particle. We employ the HRG model to calculate heat capacity from the variation of energy of the system with temperature. Results of the HRG calculations are close to the data. With increase of collision energy, $c_{\rm v}$ shows a sharp drop from low energy till $\sqrt{s_{\rm NN}}$ = 62.4 GeV, beyond which the rate of decrease is very slow. In this regard, we look forward to results of RHIC beam energy scan program (BES), where the collision energy and centrality dependences of $c_{\rm v}$ are expected to provide important signatures for the onset of the QGP phase transition. We propose a finer scan of beam energies for the BES-II program, specifically from 14 GeV to 62.4 GeV. Studies of heat capacity at high baryon density and lower temperatures accessible at Facility for Antiproton and Ion Research (FAIR) would be of high interest, unless it is critically challenged by statistical fluctuations. Predictions for $c_{\rm v}$ at the LHC at $\sqrt{s_{\rm NN}}$ = 2.76 TeV are made using different models. It will be interesting to obtain $c_{\rm v}$ at the highest LHC energy of $\sqrt{s_{\rm NN}}$ = 5.02 TeV in order to make a direct comparison to lattice calculations. In literature, it has been also proposed to calculate thermal conductivity from transverse energy ($E_{\rm T}$) fluctuations, which can be explored in future studies. The excitation energy dependence of $c_{\rm v}$ provides important information regarding the thermodynamic properties, such as, heat conductivity, speed of sound ($c_{\rm s}^2$), compressibility ($k_{\rm T}$), etc., which may reveal better understandings of the matter formed in relativistic nuclear collisions.

Bibliography

[1] Y. Aoki, G. Endrodi, Z. Fodor, S.D. Katz, K.K. Szabo, Nature **443**, 675 (2006).

[2] J.W. Harris, B. Muller, Ann. Rev. Nucl. Part. Sci. **46**, 71 (1996).

[3] P. Braun-Munzinger and J. Stachel, Nature **448**, 302 (2007).

[4] L. Stodolsky, Phys. Rev. Lett. **75**, 1044 (1995).

[5] E.V. Shuryak, Phys. Lett. B **423**, 9 (1998).

[6] M.A. Stephanov, K. Rajagopal and E. V. Shuryak, Phys. Rev. Lett. **81**, 4816 (1998).

[7] M.A. Stephanov, K. Rajagopal and E. Shuryak, Phys. Rev. **D 60**, 114028 (1999).

[8] M. Stephanov, Phys. Rev. **D 65**, 096008 (2002).

[9] H. Heiselberg, Phys. Rep. **351**, 161 (2001).

[10] S. Chatterjee, R.M. Godbole and S. Gupta, Phys. Rev. **C 81** 044907 (2010).

[11] B-H Sa, X-M Li, S-Y Hu, S-P Li, J. Feng, and D-M Zhou, Phys. Rev. **75**, 054912 (2007).

[12] X-M Li *et al.* Int. Jor. of Mod. Phys. **E 16** 1906 (2007).

[13] Aram Mekjian, Phys. Rev. **C 73**, 014901 (2006).

[14] R.V. Gavai, S. Gupta and S. Mukherjee, Phys. Rev. **D 71** 074013 (2005).

[15] A. Bazavov *et al.* Phys. Rev. **D 90** 094503 (2014).

[16] Yoshitaka Hatta and Kenji Fukushima, arXiv:hep-ph/0311267.

[17] S. A. Voloshin, V. Koch, and H. G. Ritter, Phys. Rev. **C 60** 024901 (1999).

[18] W. Broniowski, B. Hiller, W. Florkowski, and P. Bozek, Phys. Lett. **B 635**, 290 (2006).

[19] P. Bozek and W. Broniowski, Phys. Rev. **C 85** 044910 (2012).

[20] M. Bleicher *et al.*, Nucl. Phys. **A368**, 391c (1998).

[21] R. Korus *et al.*, Phys. Rev. **C 64** 054908 (2001).

[22] H. Appelshauser *et al.* (NA49 Collaboration), Phys. Lett. **B 459**, 679 (1999).

[23] T. Anticic *et al.* (NA49 Collaboration), Phys. Rev. **C 70**, 034902 (2004).

[24] T. Anticic *et al.* (NA49 Collaboration), Phys. Rev. **C 79**, 044904 (2009).

[25] D. Adamova *et al.* (CERES Collaboration), Nucl. Phys. **A 727**. 97 (2003).

[26] K. Adcox et al. (PHENIX Collaboration), Phys. Rev. **C 66**, 024901 (2002).

[27] J. Adams, et al. (STAR Collaboration), Phys. Rev. **C 71**, 064906 (2005).

[28] J. Adams, et al. (STAR Collaboration), Phys. Rev. **C 72**, 044902 (2005).

[29] L. Adamczyk *et al.* (STAR Collaboration), Phys. Rev. C **87**, 064902 (2013).

[30] M.J. Tannenbaum, arXiv:nucl-ex/0512004.

[31] M.J. Tannenbaum, Phys. Lett. **B 498**, 29 (2001);

[32] Z.-W. Lin, C.M. Ko, B.-A. Li, B. Zhang, S. Pal, Phys. Rev. **C 72**, 064901 (2005).

[33] A. Bazavov, T. Bhattacharya, M. Cheng, *et al.*, Phys. Rev. **D 80**, 014504 (2009).

[34] S. Borsnyi, Z. Fodor, C. Hoelbling, *et al.*, Jour. High. Ener. Phys. **1009**, 73 (2010).

[35] S. Borsanyi, Z. Fodor, S. D. Katz, S. Krieg, C. Ratti, and K. Szabo, Jour. High. Ener. Phys. **1201**, 138 (2012).

[36] K.A. Olive et al. (Particle Data Group), Chin. Phys. **C 38**, 090001 (2014).

[37] L.D. Landau.and E.M. Lifshitz, STATISTICAL PHYSICS, (Course of Theoretical Physics, v. 5, 3rd, rev. and enlarged ed.) Pergamon Press (1980).

[38] A. Mazeliauskas and D. Teaney, arXiv:1509.07492 [nucl-th].

[39] R.S. Bhalerao, J.-Y. Ollitrault, S. Pal and D. Teaney, Phy. Rev Lett. **114** 152301 (2015).

[40] L. Pang, Q. Wang and X-N Wang, Phys. rev. **C 86**, 024911 (2012).

[41] E.V. Shuryak, Phys. Rev. **C 88**, 044915 (2013).

[42] F. Retiere and M. Lisa, Phys. Rev. **C 70**, 044907 (2004).

[43] S. Chatterjee *et al.*, Advances in High Energy Physics **2015**, Article ID 349013.

[44] B.I. Abelev *et al.* (STAR Collaboration), Phys. Rev. **C 79**, 034909 (2009).

[45] B, Abelev *et al.* (ALICE Collaboration), Phys. Rev. **C 88**, 044910 (2013).

[46] J. Cleymans, H. Oeschler, K. Redlich and S. Wheaton, Phys. Rev. **C 73**, 034905 (2006).

[47] A. Andronic, P. Braun-Munzinger and J. Stachel, Phys. Lett. **B 673**, 142 (2009).

[48] B, Abelev *et al.* (ALICE Collaboration), Eur. Phys. J. **C 74**, 3077 (2014).

[49] S.S. Adler *et al.* (PHENIX Collaboration), Phys. Rev. **C 71**, 034908 (2005).

[50] B. Alver *et al.* (PHOBOS Collaboration), Phys. Rev. **C 83** 024913 (2011).

Chapter 5

ALICE Experiment

ALICE (1; 2; 3) (A Large Ion Collider Experiment) is a major experiment at the Large Hadron Collider (LHC), Geneva, which is a collider facility used for the study of QCD matter created in high-energy collisions between lead nuclei. QCD (quantum chromodynamics) calculations predict the existence of a state of deconfined quarks and gluons at energy densities above 1 GeV/fm^3. The transition to this state is accompanied by chiral symmetry restoration, in which the quarks assume their current masses. This state of matter occurred in the early universe after the electroweak phase transition, i.e. at the age of 10^{-12}–10^{-5} s (for a recent review see Ref. BraunMunzinger:2009zz.) High-energy nuclear collisions allow such energy densities to be reached, albeit in a small volume and for a limited duration. Assessing the properties of the created matter requires a sound understanding of the underlying collision dynamics. For this, the heavy-ion (AA) collision studies in the new energy regime accessible at the LHC have to be complemented by proton-proton () and proton-nucleus (pA) collision experiments. These control measurements, besides being interesting in themselves, are needed to separate the genuine QCD-matter signals from the cold-matter initial- and final-state effects. The physics goals of ALICE are described in detail in Refs. Carminati:2004fp,Alessandro:2006yt; the results obtained to date are accessible at Ref. alicepub. The ALICE apparatus (Fig. 5.1)

5.1 ALICE detectors set-up:

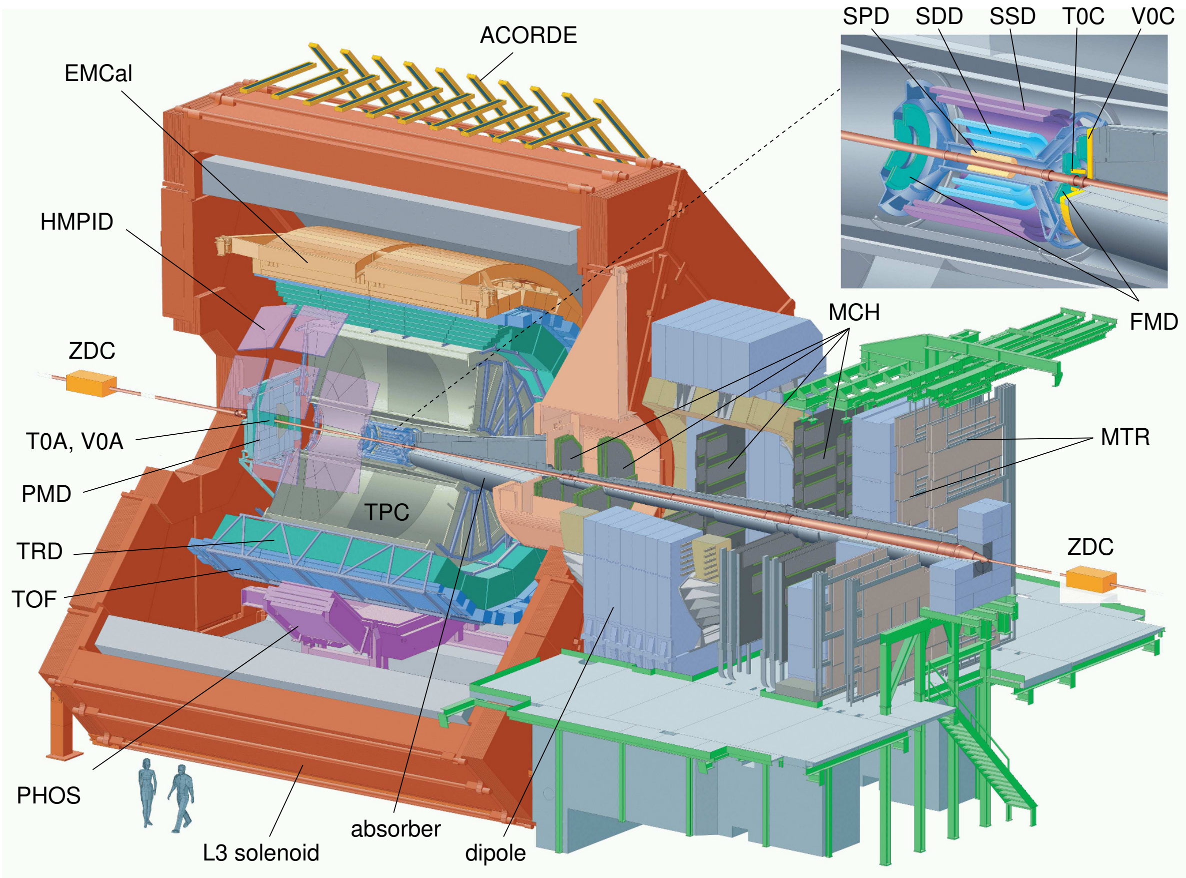

Figure 5.1: The ALICE experiment at the CERN LHC. The central-barrel detectors (ITS, TPC, TRD, TOF, PHOS, EMCal, and HMPID) are embedded in a solenoid with magnetic field $B = 0.5$ T and address particle production at midrapidity. The cosmic-ray trigger detector ACORDE is positioned on top of the magnet. Forward detectors (PMD, FMD, V0, T0, and ZDC) are used for triggering, event characterization, and multiplicity studies. The MUON spectrometer covers $-4.0 < \eta < -2.5$, $\eta = -\ln\tan(\theta/2)$.

has overall dimensions of $16\times16\times26$ m^3 and a total weight of ~10 000 t. It was designed to cope with the particle densities expected in central collisions at the LHC. The experiment has a high detector granularity, a low transverse momentum threshold $p_T{}^{min} \approx 0.15$, and good particle identification capabilities up to 20. The seventeen ALICE detector systems, listed in Table 5.1, fall into three categories: central-barrel detectors, forward detectors, and the MUON

Table 5.1: The ALICE detectors: The detectors marked with an asterisk (*) are used for triggering. The central-barrel detectors – Inner Tracking System (ITS), Time Projection Chamber (TPC), Transition Radiation Detector (TRD), Time Of Flight (TOF), Photon Spectrometer (PHOS), Electromagnetic Calorimeter (EMCal), and High Momentum Particle Identification Detector (HMPID) – are embedded in the L3 solenoid magnet which has B=0.5 T.

Detector	Acceptance Polar	Acceptance Azimuthal	Technology	Main purpose
SPD*	$\|\eta\| < 2.0$	full	Si pixel	tracking, vertex
	$\|\eta\| < 1.4$	full	Si pixel	tracking, vertex
SDD	$\|\eta\| < 0.9$	full	Si drift	tracking, PID
	$\|\eta\| < 0.9$	full	Si drift	tracking, PID
SSD	$\|\eta\| < 1.0$	full	Si strip	tracking, PID
	$\|\eta\| < 1.0$	full	Si strip	tracking, PID
TPC	$\|\eta\| < 0.9$	full	Ne drift+MWPC	tracking, PID
TRD*	$\|\eta\| < 0.8$	full	TR+Xe drift+MWPC	tracking, $e^{\pm}$ id
TOF*	$\|\eta\| < 0.9$	full	MRPC	PID
PHOS*	$\|\eta\| < 0.12$	$220 < \phi < 320$	$PbWO_4$	photons
EMCal*	$\|\eta\| < 0.7$	$80 < \phi < 187$	Pb+scint.	photons and jets
HMPID	$\|\eta\| < 0.6$	$1 < \phi < 59$	C_6F_{14} RICH+MWPC	PID
ACORDE*	$\|\eta\| < 1.3$	$30 < \phi < 150$	scint.	cosmics
PMD	$2.3 < \eta < 3.9$	full	Pb+PC	photons
FMD	$3.6 < \eta < 5.0$	full	Si strip	charged particles
	$1.7 < \eta < 3.7$	full	Si strip	charged particles
	$-3.4 < \eta < -1.7$	full	Si strip	charged particles
V0*	$2.8 < \eta < 5.1$	full	scint.	charged particles
	$-3.7 < \eta < -1.7$	full	scint.	charged particles
T0*	$4.6 < \eta < 4.9$	full	quartz	time, vertex
	$-3.3 < \eta < -3.0$	full	quartz	time, vertex
ZDC*	$\|\eta\| > 8.8$	full	W+quartz	forward neutrons
	$6.5 < \|\eta\| < 7.5$	$\|\phi\| < 10$	brass+quartz	forward protons
	$4.8 < \eta < 5.7$	$\|2\phi\| < 32$	Pb+quartz	photons
MCH	$-4.0 < \eta < -2.5$	full	MWPC	muon tracking
MTR*	$-4.0 < \eta < -2.5$	full	RPC	muon trigger

spectrometer. In this section, a brief outline of their features is given. Specifications and a more detailed description can be found in Ref. Aamodt:2008zz.

5.2 ALICE Coordinate Systems and detectors classifications:

The collision systems and energies inspected by ALICE are summarized in Table 5.1 in Section **??**. In the following, we start from a description of the running conditions, data taking and calibration, and then review the performance of the experiment in terms of various physics observables.

The ALICE Coordinate System, used in Table 5.1 and throughout the paper, is a right-handed orthogonal Cartesian system defined as follows (7).

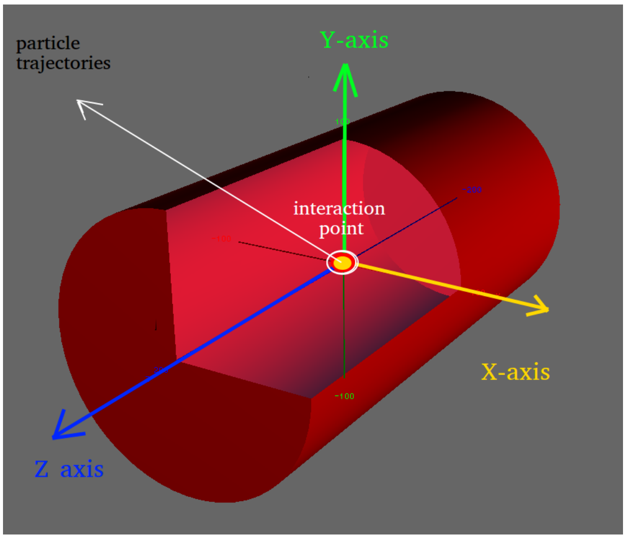

Figure 5.2: schematic diagram of ALICE coordinate system

The origin is at the LHC Interaction Point 2 (IP2). The z axis is parallel to the mean beam direction at IP2 and points along the LHC Beam 2 (i.e. LHC anticlockwise). The x axis is horizontal and points approximately towards the center of the LHC. The y axis, consequently, is approximately vertical and points upwards.

- **The central-barrel detectors** – Inner Tracking System (ITS), Time Projection Chamber (TPC), Transition Radiation Detector (TRD), Time Of Flight (TOF), Photon Spectrometer (PHOS), Electromagnetic Calorimeter (EMCal), and High Momentum Particle Identification Detector (HMPID) – are embedded in the L3 solenoid magnet which has B=0.5 T. The first four cover the full azimuth, with a segmentation of 20, at midrapidity ($|\eta| \lesssim 0.9$). The ITS and the TPC are the main charged-particle tracking detectors of ALICE.

- **The forward detectors** – Include the preshower/gas-counter Photon Multiplicity Detector (PMD) and the silicon Forward Multiplicity Detector (FMD), which are dedicated to the measurement of photons and charged particles around $|\eta| \approx 3$, respectively. The quartz Cherenkov detector T0 delivers the time and the longitudinal position of the interaction. The plastic scintillator detector VZERO measures charged particles at $-3.7 < \eta < -1.7$ and $2.8 < \eta < 5.1$, and is mainly used for triggering and for the determination of centrality and event plane angle in collisions (6). The centrality can also be measured with the Zero Degree Calorimeter (ZDC).

- **The MUON spectrometer** – With a hadron absorber of $\sim$10 λ_{int}, a dipole magnet of 3 Tm, and five tracking stations with two pad chambers each (Muon Chambers, MCH), is used to measure quarkonium and light vector meson production in a region of $-4.0 < y < -2.5$. The measurement of high-p_{T}muons, which predominantly come from the decay of charm and beauty, also falls within the scope of the spectrometer. Single-muon and muon-pair triggers with an adjustable transverse-momentum threshold are provided by two further stations (Muon Trigger, MTR) placed behind an additional $7\lambda_{\text{int}}$ absorber.

Below we discuss few main detectors which is most imporant for this analysis in detailed. It can also be classified in terms of:

- (a) Hadron identification detectors (e.g. ITS, TPC etc.)

- (b) Tracking and vertexing detectors (e.g. ITS, V0 etc.)

- (c) centrality estimator detectors (e.g. V0, ZNA etc.)
- (d) Special purpose detectors (e.g. PMD, Muon spectrometer etc.)

As this thesis is mainly dealing with precise measurement of particle idetification and their transverse momentum spectrum, so mainly (a) Hadron identification detectors are useful, keeping in mind thier idetification range capabilities which is listed below.

The ALICE detector has a number of different subsystems for identifying charged hadrons and electrons. The following subsystems are used for hadron identification:

- *ITS:* The outer four layers of the Inner Tracking System have an analog readout to measure the deposited charge, thereby providing a measurement. This is mainly useful for low-p_{T}tracks ($\mathrm{p_T} \lesssim 0.7$), specifically at very low p_{T}, where the ITS is used for standalone tracking.
- *TPC:* The Time Projection Chamber measures the charge deposited on up to 159 padrows. A truncated mean (40% highest-charge clusters discarded) is calculated and used for a wide range of momenta. The largest separation is achieved at low p_{T}($\mathrm{p_T} \lesssim 0.7$) but a good separation is also present in the relativistic rise region ($\mathrm{p_T} \gtrsim 2$) up to ∼20.
- *TOF:* The Time-Of-Flight detector is a dedicated detector for particle identification that measures the arrival time of particles with a resolution of ∼80 ps. This provides a good separation of kaons and protons up to $\mathrm{p_T} \simeq 4$.
- *HMPID:* The High Momentum Particle Identification Detector is a ring-imaging Cherenkov detector that covers $|\eta| < 0.6$ in pseudorapidity and 57.6 in azimuth, corresponding to 5% acceptance of the central barrel, and provides proton/kaon separation up to $\mathrm{p_T} \simeq 5$.

The measurements in the different particle identification detector systems are then combined to further improve the separation between particle species. This is discussed in details below.

The particle identification (PID) capabilities of these detectors are used for a wide range of physics analyses, including transverse momentum spectra for pions, kaons, and protons (9;

10), (11); heavy-flavor decays (8); Bose-Einstein correlations for pions (12; 13**?**) and kaons (14; 15); and resonance studies (16). The hadron identification systems is also used to identify electrons. In addition, the calorimeters (PHOS and EMCal) and the Transition Radiation Detector (TRD) provide dedicated electron identification.

5.3 Inner Tracking System -ITS

Location-wise being the closest detector to the beam pipe, the Inner Tracking System (ITS) (17) is used for the determination of the primary interaction vertex. Along with precise vertex measurement, ITS is also used for the tracking and particle identification of low momentum tracks that fail to reach TPC. Consisting of six concentric layers of silicon detectors around the beam-pipe, it cover 0.9 units in pseudorapidity and 2π in azimuth. As shown in the Fig. 5.3, moving radially outward from the interaction point, the six layered ITS has 2 layers each of SPD, SSD and SDD respectively.

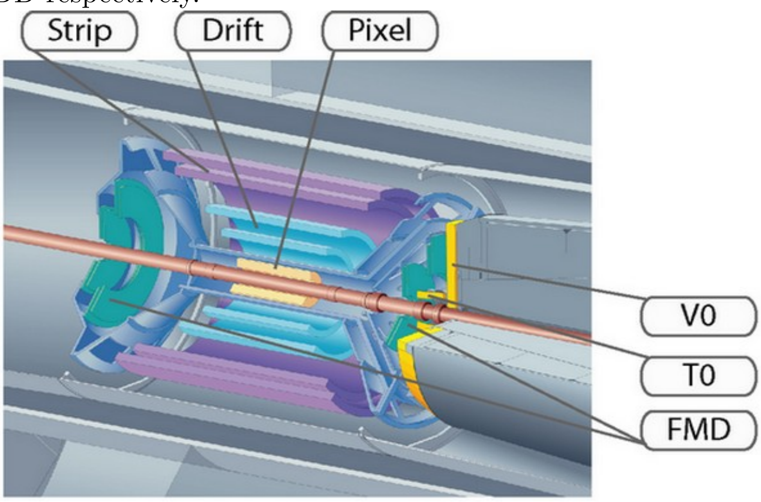

A schematic view of ALICE-Inner Tracking Chamber. Also shown different sub-layers: SPD, SDD and SSD.

Silicon Pixel Detector : The two inner-most layers of ITS consist pixel based silicon detectors, the SPD. Made of 2-dimensional array of 256 $\times$ 160 finely segmented silicon pixels. Fine granularity of SPD detectors allow them to localize tracks in the z-direction. SPD contributes significantly towards precise vertex measurement and impact-parameter measurement. **Silicon Drift Detector:** The two intermediate layers of the ITS are SDDs, are particularly used for particle identification using specific energy loss (dE/dx) of the tracks passing through the active volume of the detectors. These are finely granulated in one direction and coarse along the other. The position of the track hits in the transverse direction is obtained from the drift-time of electrons to the electrode with respect trigger-time and the z-position of the hits are determined from the centroid of the charge accumulated in the anodes. A precise knowledge of drift-time is extremely necessary for the accurate reconstruction of the tracks in SDD. **Silicon Strip Detectors:** The last two (fifth and sixth) layers of ITS are made of double-sided silicon strips. Like SDD, SPDs are also used for low momentum particle identification exploiting the energy loss (dE/dx) information in the detector volume. The outer two layer are also crucial for ITS-TPC track matching.

Overall, ITS can improve tracking and angular resolution of the tracks. Most of the low momentum tracks (tracklets) that fail to reach TPC are reconstructed in ITS thereby allowing physics measurements at low p_T below 200 MeV. Use of silicon based detectors also facilitates maintaining a low material budget.

Particle identification in the ITS

The inner tracking system (ITS) of ALICE consists of six layers of silicon detectors. The outer four layers provide a measurement of the ionization energy loss of particles as they pass through the detector. The measured cluster charge is normalized to the path length, which is calculated from the reconstructed track parameters to obtain a value for each layer. For each track, the is calculated using a truncated mean: the average of the lowest two points if four points are measured, or a weighted sum of the lowest (weight 1) and the second-lowest points (weight 1/2), if only three points are measured. An example distribution of measured truncated mean energy loss values as a function of momentum in the ITS is shown in Fig. 5.3.

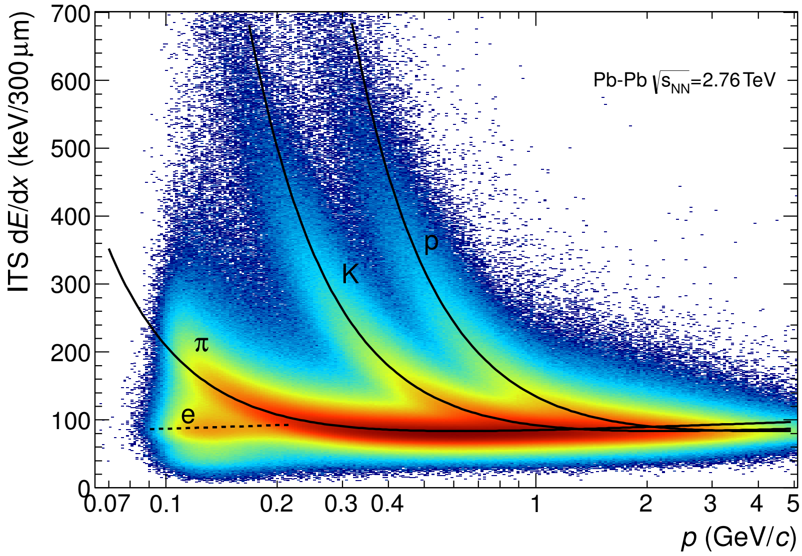

Figure 5.3: Distribution of the energy-loss signal in the ITS as a function of momentum. Both the energy loss and momentum were measured by the ITS alone.

5.3.1 Time Projection Chamber -TPC

The Time Projection Chamber or TPC (18) is a gas detector and at the center of ALICE central-barrel detectors, dedicated towards tracking and particle identification. It is most important detector in the ALICE, placed coaxially with beam-pipe and ITS, whose inner radius located at 80 cm and the outer radius at approx 250 cm from the beam pipe. The length of the chamber is about 510 cm along the beam pipe. The TPC covers a phase space of $|\eta| < 0.9$ and full range of azimuth. Till 2010 June, TPC was used with Ne:CO_2:N_2 = 85.7%:9.5%:4.8%) gas mixture but later(2011), a new gas-mixture Ne:CO_2 = 90%:10% was introduced to decrease the gas-gain and prevent frequent detector-breakdown during high luminosity runs. The choice of this gas mixtures and detector configuration has been optimised further to minimize low electron diffusion, small space charge effect and low material budget in order to ensure good momentum resolution, high rate handling capacity, minimal re-scattering and secondary particle generation.

Particle identification in the TPC

The TPC (20) is the main tracking detector in ALICE. In addition it provides information for particle identification over a wide momentum range. Particle identification is performed by simultaneously measuring the specific energy loss (), charge, and momentum of each particle traversing the detector gas. The energy loss, described by the Bethe-Bloch formula, is parametrized by a function originally proposed by the ALEPH collaboration (21),

$$f(\beta\gamma) = \frac{P_1}{\beta^{P_4}}\Big(P_2 - \beta^{P_4} - \ln(P_3 + \frac{1}{(\beta\gamma)^{P_5}})\Big) \,, \tag{5.1}$$

where β is the particle velocity, γ is the Lorentz factor, and P_{1-5} are fit parameters. Figure 5.4 shows the measured vs. particle momentum in the TPC, demonstrating the clear separation between the different particle species. The lines correspond to the parametrization. While at low momenta ($p \lesssim 1$) particles can be identified on a track-by-track basis, at higher momenta particles can still be separated on a statistical basis via multi-Gaussian fits. Indeed, with long tracks ($\gtrsim$ 130 samples) and with the truncated-mean method the resulting peak shape is Gaussian down to at least 3 orders of magnitude.

In the relativistic rise region, the exhibits a nearly constant separation for the different particle species over a wide momentum range. Due to a resolution of about 5.2 % in collisions and 6.5 % in the 0–5% most central collisions[1], particle ratios can be measured at a $p_{\mathrm{T}}$of up to 20 (22). The main limitation at the moment is statistical precision, so it is expected that the measurement can be extended up to $\sim$ 50in the future.

As an example, distributions for charged particles with $\mathrm{p_T}\approx$ 10are shown in Fig. 5.5 for and the 0–5% most central collisions. Note that, for this analysis, a specific η range was selected in order to achieve the best possible resolution. The curves show Gaussian fits where the mean and width were fixed to the values obtained using clean samples of identified pions and protons from, respectively, and Λ decays, and assuming that the response at high p_{T}depends only on

[1]The deterioration of the energy-loss resolution in high-multiplicity events is caused by clusters overlapping in z and/or sitting on top of a signal tail from an earlier cluster.

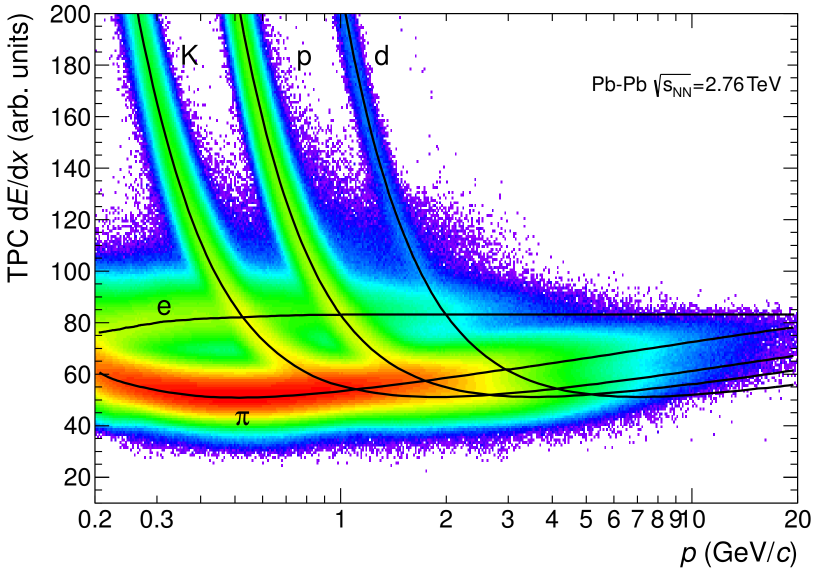

Figure 5.4: Specific energy loss () in the TPC vs. particle momentum in collisions at = 2.76 TeV. The lines show the parametrizations of the expected mean energy loss.

$\beta\gamma$.

5.4 Time of Flight -TOF

The Time-Of-Flight (TOF) detector (23) of ALICE is a large area array of Multigap Resistive Plate Chambers (MRPC), positioned at 370–399 cm from the beam axis and covering the full azimuth and the pseudorapidity range $|\eta| < 0.9$. In collisions, in the centrality range 0–70% the overall TOF resolution is 80 ps for pions with a momentum around 1. This value includes the intrinsic detector resolution, the contribution from electronics and calibration, the uncertainty on the start time of the event, and the tracking and momentum resolution (24).

The active area of the detector is filled with a gas mixture of Freon:SF_6:Iso-butane=90%:5%:5%. These MRPCs achieve an efficiency of 99.9% and time resolution better than 40 ps. The start time for the TOF measurement is provided by the T0 detector, which consists of two arrays of Cherenkov counters T0C and T0A, positioned at opposite sides of the interaction point (IP) at $-3.28 < \eta < -2.97$ and $4.61 < \eta < 4.92$, respectively. Each array has 12 cylindrical counters

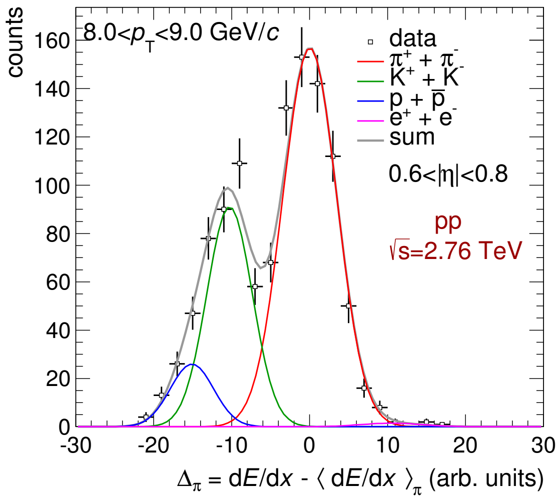

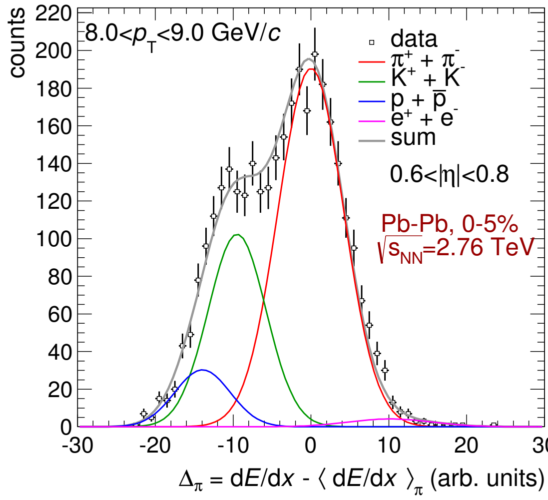

Figure 5.5: Ionization energy loss () distributions in the TPC in (left) and collisions (right) at = 2.76 TeV. The lines represent Gaussian fits as described in the main text.

equipped with a quartz radiator and photomultiplier tube (**?**). Thus the overall time resolution of ALICE-TOF is given by: $\sigma_{TOF} = \sqrt{\sigma^2_{intrinsic} + \sigma^2_{t0}}$

In Pb-Pb collisions, σ_{TOF} was found to be 86 ps. Hence a maximum separation of 2σ between protons and kaons could be reached at a momentum of 5 GeV/c. Combined with TPC and ITS, TOF can facilitate event by event identification of pure samples of $\pi^{\pm}$,K and protons upto a momentum range of 4 GeV/c (31).TOF provides PID in the intermediate momentum range, up to 2.5for pions and kaons, and up to 4for protons.

5.4.1 Particle identification in TOF

the start time (interaction time of the collision) as measured by the sum of the time signals from the T0A and T0C detectors in collisions at = 2.76 TeV with respect to the nominal LHC clock value. The width of the distribution is indicative of how much the collision time can jitter with respect to its nominal value (the LHC clock edge). This is due to the finite size of the bunches and the clock-phase shift during a fill. The time resolution of the detector, estimated by the time difference registered in T0A and T0C, is 20–25 ps in collisions and ∼40 ps in collisions. The efficiency of T0 is 100% for the 60% most central collisions at = 2.76 TeV, dropping to about

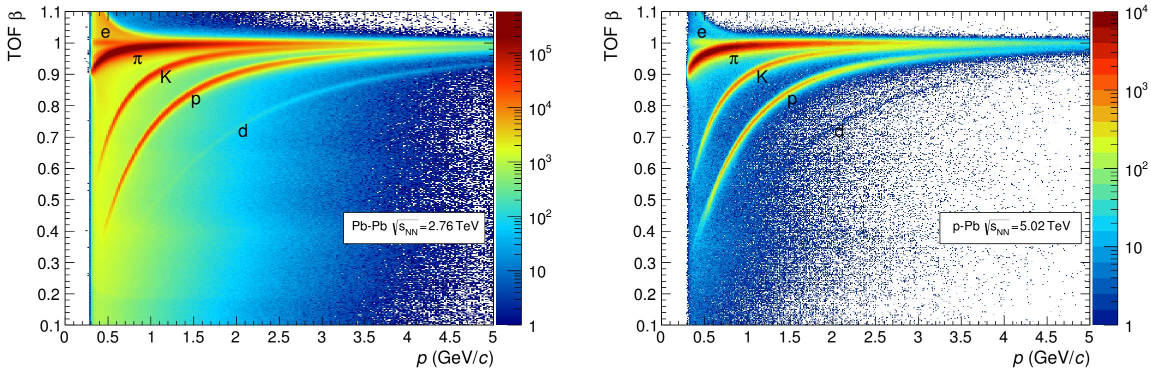

Figure 5.6: Distribution of β as measured by the TOF detector as a function of momentum for particles reaching the TOF in & interactions.

50% for events with centrality around 90%. For collisions at = 7 TeV, the efficiency is about 50% for a T0 coincidence signal (T0A-AND-T0C) and 70% if only one of the T0 detectors is requested (T0A-OR-T0C).

The start time of the event $t_{\rm ev}$ is also estimated using the particle arrival times at the TOF detector. A combinatorial algorithm based on a χ^2 minimization between all the possible mass hypotheses is used in the latter case. It can be invoked when at least three particles reach the TOF detector, to provide increased resolution and efficiency at larger multiplicity. With 30 tracks, the resolution on $t_{\rm ev}$ reaches 30 ps (24). This method is particularly useful for events in which the T0 signal is not present. If neither of these two methods is available, an average TOF start time for the run is used instead.

At $p_{\rm T} < 0.7GeV/c$, the matching efficiency is dominated by energy loss and the rigidity cutoff generated by the magnetic field. At higher transverse momenta it reflects the geometrical acceptance (dead space between sectors), the inactive modules, and the finite efficiency of the MRPCs (98.5% on average).

Figure 5.6 illustrates the performance of the TOF detector by showing the measured velocity β distribution as a function of momentum (measured by the TPC). The background is due to tracks that are incorrectly matched to TOF hits in high-multiplicity collisions. The distribution is cleaner in collisions (Fig. **??**), showing that the background is not related to the resolution of the TOF detector, but is rather an effect of track density and the fraction of mismatched tracks.

Fig. 5.7 shows, for tracks with $1.5 < p_{\mathrm{T}} < 1.6$ GeV/c, the difference between the measured time of flight and the expectation for kaons, together with a template fit to the pion, kaon, and proton peaks and the combinatorial background from mismatched tracks.

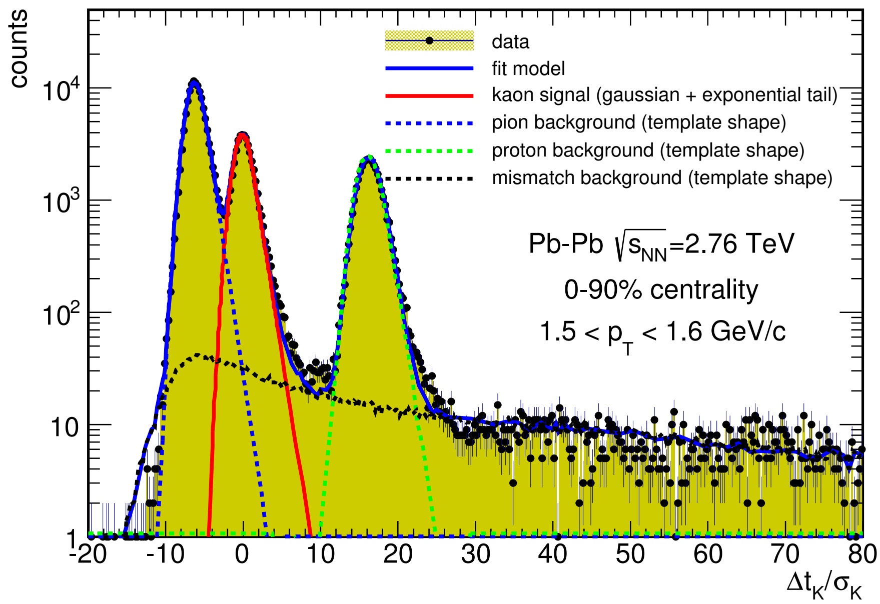

Figure 5.7: TOF measured in collisions at = 2.76 TeV. The expected time of flight for kaons is subtracted and the result is divided by the expected resolution.

5.5 The Forward Detectors

The Forward detectors in ALICE comprise of pre-shower Photon Multiplicity Detector (PMD), silicon-based Forward Multiplicity Detector (FMD) quartz Cherenkov detector T0, plastic scintilltor based V0 and Zero Degree Calorimeter (ZDC).

The main objective of the ALICE Forward Multiplicity Detector or FMD (33) is to allow determination of charged particle multiplicity at forward rapidity. The FMD consists of 5 rings of silicon strip detectors placed around the beam-pipe. 3 inner rings (FMD1i, FMD2i and FMD3i) contain 10 hexagonal silicon cells while, 2 outer rings (FMD2o and FMD3o) have 20 such silicon sensors segemented into 2 sectors. Each sector is further cut into strips at constant radius. Beside extending multiplicity measurement at large forward rapidity, it also caters the need for independent and reliable measurement of event plane inclination. The pseudorapidity coverage of the detector on either side of the interaction point is -3.4 $\leq \eta \leq$ -1.7 and -1.7 $\leq \eta \leq$ 5.0, respectively. Combination of FMD and ITS allow charged particle counting over an extraordinarily large pseudorapidity range (-3.4 $\leq \eta \leq$ 5.0).

The Photon Multiplicity Detector or PMD (35; 36) was installed with an aim to measure photons at the forward rapidity. Located at 3.67 m from the interaction point towards the A side of the ALICE it covers pseudo-rapidity 2.3 $< \eta <$ 3.9 and full azimuth. It consists of two planes, Charged Particle Veto (CPV) and Pre-Shower (PRE). A Pb-converter is sandwiched between these two planes. The thickness of the Pb-converter has been optimised to deliver high photon-conversion efficiency but low transverse shower spread. The working principle of the detector is similar to a proportional counter. The active volume of the detector is filled with Ar-CO_2 gas mixture in a proportion of 70:30 by weight. Each PMD plane has 24 modules and each module has 4608 honeycomb cells.

The T0 (33) detector consists of two arrays (T0A and T0C) of Cherenkov counter placed assymetrically with respect to the interaction point (IP). The T0A is positioned 3.75 m from the IP on the A-side of the ALICE and T0C is located 7.27 m from the IP towards the C-side of the ALICE. T0 detectors provide the start time of the collision with a precision of 25 ps. This time is also used as a start time by the TOF detector for the time-of-flight measurement of the particles.

VZERO (V0)

Similar to T0, plastic scintillator based two arrays of VZERO(V0) detectors (V0A nd V0C) (33; 40) (see Fig. 5.8) are also placed asymetrically on the either side of the IP. Located at a distance of 340 cm towards the A side of the IP, V0A measures the charged particles in the pseudo-rapidity window of 2.8 $\leq \eta \leq$ 5.1. This detector is particularly used for triggering,

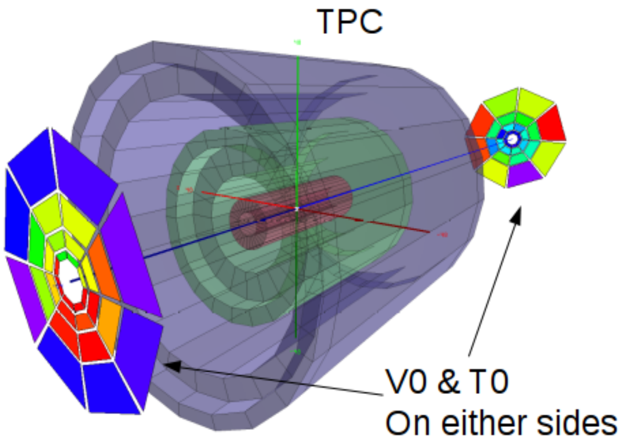

Figure 5.8: V0 detector modules (34)

centrality estimation and backgrounds rejection. Triggering logics are designed using the timing information from V0A and V0C detectors to reject backgrounds originating from the interactions other than beam-beam. Furthermore, the energy deposited in the V0 scintillators can be used to extract charged particle multiplicity in the detector coverage. The V0C is located on the other side of IP at a distance of 90 cm and measures charged particle multiplicity in $-3.7 \leq \eta \leq -1.7$. Each detector has 4 rings and each ring is segmented into 8 sectors, making an overall 32 segmented counters. The information from The calibrated V0 signal amplitudes (V0A + V0C) has been used for centrality estimation. It allows centrality estimation with a resolution of $\approx$ 0.5% and 2% (32) in most central and peripheral event classes, respectively.

Another important detector is Zero Degree Calorimeter (ZDC) (37), located at 114m on either side of the interaction point IP, measures the energy deposited by the spectator nucleons. Amount of energy deposited in ZDCs is directly related to the spectator nucleon number which are not involved in the interaction. This information can also be utilized for centrality estimation in nuclear collisions (32). Since the spectator protons are deflected by the magnetic elements along the beam-line, ZP is placed outside the beam-line on the side where positive particles are deflected.

5.5.1 The Muon Spectrometers

The purpose of the MUON spectrometer is a RPC based detector used to measure all states of quarkonia and ϕ-mesons in forward rapidity. The spectrometer is located on the C side of the IP and designed to track muons in the pseudorapidity range -4 < η < -2.5 with full azimuthal acceptance.

It is a conical shaped front end absorber made of carbon,concrete and steel to stop hadrons and photons and allow muon with momentum > 4 GeV/c to pass through. A large dipole magnet (magnetic field of 3Tm) installed perpendicular to beam-pipe outside the L3 magnet, that allows tracking and momentum reconstruction of the muon candidates.

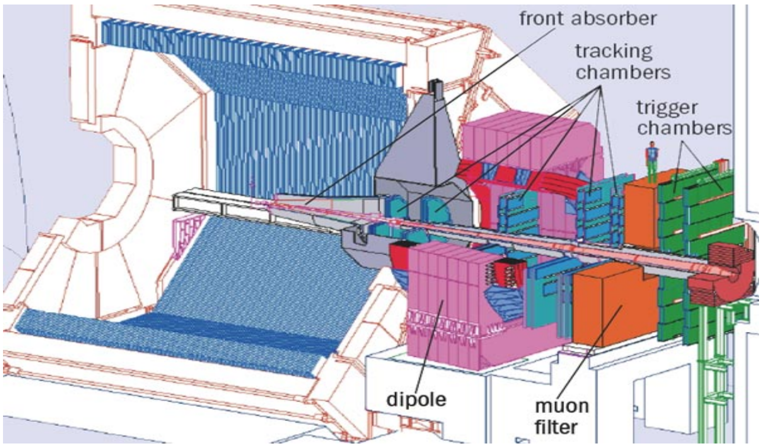

Figure 5.9: A schematic diagram of Muon Spectrometer & its position in ALICE detector system(38; 39)

5.6 Event simulation and reconstruction

The ALICE off-line analysis framework, AliRoot (46), is described in detail in Ref. (47). This framework, based on the Object Oriented / C++ environment of ROOT (48), allows to reconstruct and analyze physics data coming from simulations and real interactions. The role of the framework can be graphically represented as shown in Fig. 5.10. Events are generated via Monte Carlo simulation programs, generators and detector simulation, and are then transformed into the format produced by the detector (*raw data*). Here we have a minimum of the physics information. At this point, the reconstruction and analysis chain is used to evaluate the detector and the physics performance, and most of the initial information on the generated event can be retrieved (e.g. particle ID and kinematics, event topology). In the next paragraphs we will follow from the left to the right the parabola in Fig. 5.10 and detail the aspects which are relevant to the studies reported in this thesis. The Monte Carlo event generators that were used for the simulation of $Pb-Pb$ collisions (HIJING) at LHC energies, is mainly HIJING (26) (Heavy Ion Jet INteraction Generator) combines a QCD-inspired model of jet production with the Lund string model (**?**) for jet fragmentation. Binary scaling with Glauber geometry is used to extrapolate to proton–nucleus and nucleus–nucleus collisions.

sectionTrack reconstruction

The event reconstruction procedure includes:

1. cluster finding;

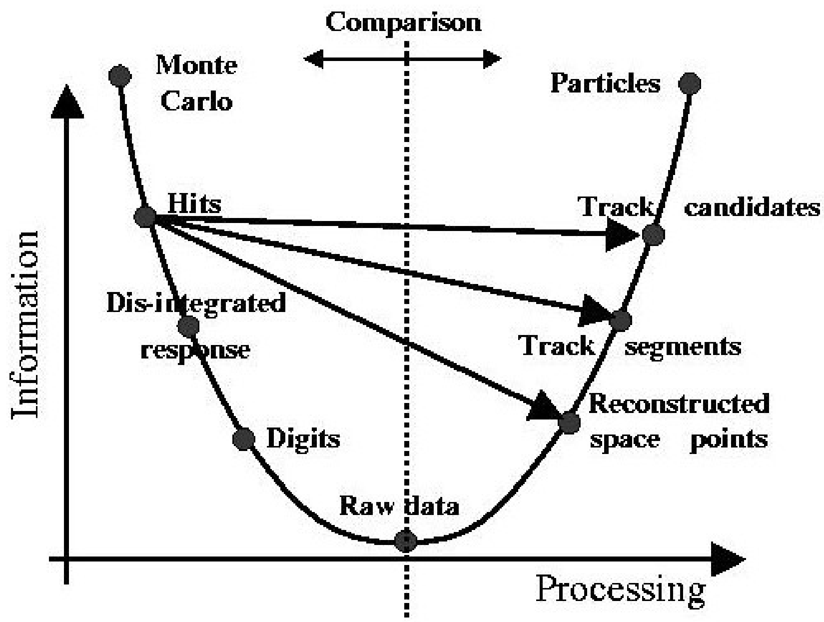

Figure 5.10: Schematic representation of the data processing chain.

2. track reconstruction;

3. reconstruction of the position of the interaction vertex.

Next part is on the cluster finding, reconstruction of the interaction (or primary) vertex determination and track reconstruction.

Cluster finding

During cluster finding, the information given by the detector electronics (*digits*) is converted to space points, interpreted as (a) the crossing points between the tracks and the centres of the pad rows in the readout chambers, in the case of the TPC, and (b) the crossing points between the tracks and the silicon sensitive volumes, in the case of the ITS. Another important piece of information provided by the cluster finder, is the estimate of the errors of the reconstructed space points. At present, a procedure for parallel clustering and tracking in the TPC is being tested. In the high-multiplicity scenario of $Pb - Pb$ collisions clusters from different tracks may overlap and a preliminary knowledge of the track parameters is very helpful in the cluster deconvolution.

The possibility to use a fast simulation of the detector response is implemented for many sub-systems of ALICE. The clusters are obtained directly from the hits via a parameterization of the response, in terms of efficiency and spatial resolution. The dramatic reduction in computing time (e.g. a factor $\simeq 25$ in the case of the ITS) allows the use of very high statistics in simulation studies. The clusters obtained via the fast simulation are called *fast points*, while those obtained from the detailed detector response are called *slow points*.

Track reconstruction in TPC–ITS

Due to the expected charged particle multiplicity, track finding in ALICE is a very challenging task. In the most pessimistic case, the occupancy (defined as the ratio of the number of read-out channels over threshold to the total number of channels) in the inner part of the TPC may reach 40%.

The track finding procedure developed for the barrel (ITS, TPC, TRD, TOF) is based on the Kalman filtering algorithm (43), widely used in high-energy physics experiments. The Kalman filter is a method for simultaneous track recognition and reconstruction (or, in other words, track finding and fitting) and its main property is that, being a local method, at any given point along the track it provides the optimal estimate of the track geometrical parameters at that point. For this reason it is a natural way to find the extrapolation of a track from a detector to another (for example from the TPC to the ITS or TRD). As we will explain, in the Kalman filter energy loss and multiple scattering are accounted for in a direct and simple way.

The first step in tracking starts with clustering of the in each of the detectors. Each cluster is loaded with information regarding its spatial location with respect to a pre-defined origin, signal strength, signal time and their corressponding errors. The clusters from first two layer in ITS are used to determine the location of preliminary priminary vertex followed by tracking in TPC using *Kalman Filter* (52) technique and track-matching with other central-barrel detectors.

- **Vertex Determination** After applying a three-level trigger system, the primary vertex determination in ALICE is performed by using the cluster information from first two layers in ITS (SPD). Each tracklet, (pair of space points in first two layers are connected by a line) is propagated to the nominal interaction point (IP) and made to converge. A primary vertex is defined as a point close to IP where most of the tracklets converge. In case of pile-up, this process is repeated and at each iteration, clusters which have been already assigned to a vertex are discarded. However, for final vertexing, global tracks from ITS and TPC after final reconstruction instead of tracklets are extrapolated and made to converge around the IP.

- **Tracking** ALICE tracking strategy based on inward-outward-inward scheme (44; 45). Tracking starts from the two outer-layers of TPC and the parameters from the outer most space-points are considered as *seeds* for the track-finding algorithm. *Seeds* are now propagated in-ward and at each step, nearest clusters are assigned depending on their proximity with the previous *seed* prolongated to the recent layer. Whenever such clusters are found track parameters and covariance matrices are updated. Tracks with less than 20 clusters are rejected. Accepted tracks are then propagated to the inner radius of TPC. Tracks reconstructed in the TPC are then extrapolated to the outer layer of the ITS which tries to extend the tracks close to the primary vertex. Once the track reconstruction in TPC-ITS is performed, a stand-alone track reconstruction in the ITS is carried out for those tracks (tracklets) which fail to reach TPC.

In the second tracking stage, tracks are refitted using Kalmann Filter in the outward direction (vertex to TPC) taking the clusters obtained in the previous stage. At this stage, track-length integrals and expected flight-time of different particles are calculated and updated for particle identification with TOF. Tracks that could reach TOF are matched with TOF-clusters and propagated further for track matching in EMCAL, PHOS and HMPID.

At the final stage, again Kalman fitting is done in outward-inward approach, starting from the TRD. Position, direction, track-curvature and their respective covariance matrices are re-evaluated and updated.

ALICE Offline Analysis

The Offline analysis procedure mainly of two ways:

- Common User Analysis Task
- Analysis Train

In both ways, Event Summary Data (ESD) or Analysis Object Data (AOD) format.

Reconstructed events are stored as ESD or AOD which contain all information about an event both at event and track level like: trigger type, vertex information, centrality/multiplicity and track by track preliminary PID from various detectors. However, ESD files are bulky and not efficient to handle. The data files can be compressed to Analysis Object Data (AOD). AODs are derived from ESD through re-filtering. Tracks satisfying some pre-defined sets of cuts are kept, rest are deleted. AOD may contain some advanced level information like reconstructed jets from different algorithms. Thus, running on AODs reduce the I/O overhead. Analysis can be performed on both AODs and ESDs, while ESDs are flexible, AODs are computationally efficient.

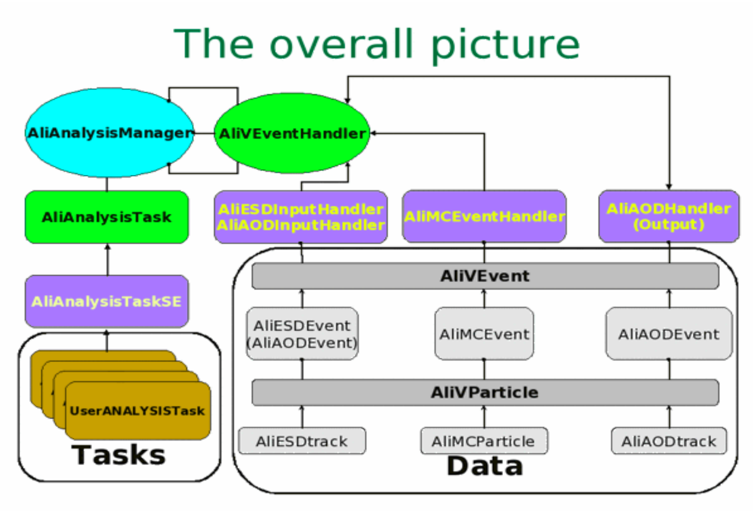

Figure 5.11: A schematic diagram of offline analysis procedure

Analyses are generally performed on a distributed computing facility called GRID. The ALICE environment software AliEn acts as an interface with the GRID. The job schedular in AliEn divides a job into multiple sub-jobs and process them parallely in short time. ALICE has also developed Light weight Environment for Grid Operation (LEGO) framework which allows simultaneous execution of jobs from different users intending to run their analyses on same sets of events. Thus data from the storage devices are read just once. This increases CPU efficiency as multiple users can run their jobs using the same computing resources. Additionally, end users are not exposed to grid complexity and hassles of job submission, resubmission, end-of run report, as these are done automatically and designated support personnels handle issues related to bug fixing of the grid environment.

In Analysis Train same procedure has been followed with a common analysis manager as engine and different analysis task as wagon. The analysis train is the way to run analysis in the most efficient way over a large part or the full dataset. It is using the AliAnalysisManager framework to optimize CPU/IO ratio, accessing data via a common interface and making use of PROOF and GRID infrastructures. The train is assembled from a list of modules that are sequentially executed by the common AliAnalysisManager object. All tasks will process the same dataset of input events, share the same event loop and possibly extend the same output AOD with their own information produced in the event loop.

Bibliography

[1] ALICE Collaboration, F. Carminati *et al.*, *ALICE: Physics performance report, volume I*, J. Phys. **G 30**, 1517 (2004), doi:10.1088/0954-3899/30/11/001.

[2] ALICE Collaboration, B. Alessandro *et al.*, *ALICE: Physics performance report, volume II*, J. Phys. **G 32**, 1295 (2006), doi:10.1088/0954-3899/32/10/001.

[3] ALICE Collaboration, K. Aamodt *et al.*, *The ALICE experiment at the CERN LHC*, JINST **3**, S08002 (2008), doi:10.1088/1748-0221/3/08/S08002.

[4] P. Braun-Munzinger and J. Wambach, *The Phase Diagram of Strongly-Interacting Matter*, Rev. Mod. Phys. **81**, 1031 (2009), arXiv:0801.4256, doi:10.1103/RevModPhys.81.1031.

[5] http://aliceinfo.cern.ch/ArtSubmission/publications.

[6] ALICE Collaboration, E. Abbas *et al.*, *Performance of the ALICE VZERO system*, JINST **8**, P10016 (2013), arXiv:1306.3130, doi:10.1088/1748-0221/8/10/P10016.

[7] L. Betev *et al.*, *Definition of the ALICE coordinate system and basic rules for sub-detector components numbering*, ALICE-INT-2003-038, http://edms.cern.ch/document/406391.

[8] ALICE Collaboration, B. Abelev *et al.*, *Suppression of high transverse momentum D mesons in central Pb-Pb collisions at* $\sqrt{s_{NN}} = 2.76$ *TeV*, JHEP **9**, 112 (2012), arXiv:1203.2160, doi:10.1007/JHEP09(2012)112.

[9] ALICE Collaboration, K. Aamodt *et al.*, *Production of pions, kaons and protons in pp collisions at $\sqrt{s} = 900$ GeV with ALICE at the LHC*, Eur. Phys. J. **C 71**, 1655 (2011), arXiv:1101.4110, doi:10.1140/epjc/s10052-011-1655-9.

[10] ALICE Collaboration, B. Abelev *et al.*, *Pion, Kaon, and Proton Production in Central Pb–Pb Collisions at $\sqrt{s_{NN}} = 2.76$ TeV*, Phys. Rev. Lett. **109**, 252301 (2012), arXiv:1208.1974, doi:10.1103/PhysRevLett.109.252301.

[11] ALICE Collaboration, B. Abelev *et al.*, *Centrality dependence of π, K, p production in Pb-Pb collisions at $\sqrt{s_{NN}} = 2.76$ TeV*, Phys. Rev. **C 88**, 044910 (2013), arXiv:1303.0737, doi:10.1103/PhysRevC.88.044910.

[12] ALICE Collaboration, K. Aamodt *et al.*, *Two-pion Bose-Einstein correlations in pp collisions at $\sqrt{s} = 900$ GeV*, Phys. Rev. **D 82**, 052001 (2010), arXiv:1007.0516, doi:10.1103/PhysRevD.82.052001.

[13] ALICE Collaboration, K. Aamodt *et al.*, *Femtoscopy of pp collisions at $\sqrt{s} = 0.9$ and 7 TeV at the LHC with two-pion Bose-Einstein correlations*, Phys. Rev. **D 84**, 112004 (2011), arXiv:1101.3665, doi:10.1103/PhysRevD.84.112004.

[14] ALICE Collaboration, B. Abelev *et al.*, *$K^0_s - K^0_s$ correlations in pp collisions at $\sqrt{s} = 7$ TeV from the LHC ALICE experiment*, Phys. Lett. **B 717**, 151 (2012), arXiv:1206.2056, doi:10.1016/j.physletb.2012.09.013.

[15] ALICE Collaboration, B. Abelev *et al.*, *Charged kaon femtoscopic correlations in pp collisions at $\sqrt{s} = 7$ TeV*, Phys. Rev. **D 87**, 052016 (2013), doi:10.1103/PhysRevD.87.052016.

[16] ALICE Collaboration, B. Abelev *et al.*, *Production of K*(892) and ϕ(1020) in pp collisions at $\sqrt{s} = 7$ TeV*, Eur. Phys. J. **C 72**, 2183 (2012), doi:10.1140/epjc/s10052-012-2183-y.

[17] ALICE Inner Tracking System (ITS): Technical Design Report, CERN-LHCC-99-012, http://edms.cern.ch/file/398932/1.

[18] ALICE Time Projection Chamber: Technical Design Report, CERN-LHCC-2000-001, http://cdsweb.cern.ch/record/451098.

[19] Saikat Biswas (for the ALICE Collaboration), arXiv:1511.04988, 2015.

[20] J. Alme *et al.*, *The ALICE TPC, a large 3-dimensional tracking device with fast readout for ultra-high multiplicity events*, Nucl. Instr. and Meth. **A 622**, 316 (2010), `arXiv:1001.1950`, `doi:10.1016/j.nima.2010.04.042`.

[21] W. Blum, W. Riegler and L. Rolandi, *Particle Detection with Drift Chambers*, 2nd ed. (Springer-Verlag, 2008), `http://www.springer.com/physics/elementary/book/978-3-540-76683-4`.

[22] ALICE Collaboration, A. Ortiz Velasquez, *Production of pions, kaons and protons at high* p_T *in* $\sqrt{s_{NN}} = 2.76$ *TeV Pb-Pb collisions*, Nucl. Phys. **A 904-905**, 763c (2013), `arXiv:1210.6995`, `doi:10.1016/j.nuclphysa.2013.02.129`.

[23] A. Akindinov *et al.*, *The ALICE Time-Of-Flight system: Construction, assembly and quality tests*, Nuovo Cimento **B 124**, 235 (2009).

[24] A. Akindinov *et al.*, *Performance of the ALICE Time-Of-Flight detector at the LHC*, Eur. Phys. J. Plus **128**, 44 (2013), `doi:dx.doi.org/10.1140/epjp/i2013-13044-x`.

[25] H. Bethe. Zur Theorie des Durchgangs schneller Korpuskularstrahlen durch Materie. Annalen der Physik, 397(3):325400, (1930).

[26] F. Bloch. Zur Bremsung rasch bewegter Teilchen beim Durchgang durch Ma- terie. Annalen der Physik, 408(3):285320, (1933).

[27] ALICE Collaboration: "Performance of the ALICE Experiment at the CERN LHC" Int. J. Mod. Phys. A 29, 1430044 (2014) .

[28] ALICE Time-Of-Flight system (TOF): Technical Design Re- port, CERN-LHCC-2000-012, http://cdsweb.cern.ch/record/430132.

[29] ALICE Time-Of-Flight system (TOF): addendum to the technical design report, CERN-LHCC- 2002-016, http://cdsweb.cern.ch/record/545834.

[30] Roberto Preghenella thesis, CERN-THESIS-2009-206.

[31] C. Lippmann, Nuclear Instruments and Methods in Physics Research A 666, 148172 (2012).

[32] B. Abelev et al. (ALICE Collaboration), Phys. Rev. C 88, 044909 (2013).

[33] ALICE forward detectors: FMD, T0 and V0: Technical Design Report, CERN-LHCC-2004-025, http://cdsweb.cern.ch/record/781854.

[34] Chiara Bianchin thesis, CERN-THESIS-2012-033.

[35] ALICE Photon Multiplicity Detector (PMD): Technical Design Report, CERNLHCC-99-032, http://cdsweb.cern.ch/record/451099.

[36] ALICE Photon Multiplicity Detector (PMD): addendum to the technical design report, CERN-LHCC-2003-038, http://cdsweb.cern.ch/record/642177.

[37] ALICE Zero-Degree Calorimeter (ZDC): Technical Design Report, CERN-LHCC-99-005, http://cdsweb.cern.ch/record/381433.

[38] ALICE dimuon forward spectrometer: Technical Design Report, CERN-LHCC-99-022, http://cdsweb.cern.ch/record/401974.

[39] ALICE dimuon forward spectrometer: addendum to the Technical Design Re- port, CERN-LHCC- 2000-046, http://cdsweb.cern.ch/record/494265

[40] E. Abbas et al. (ALICE Collaboration), JINST 8, P10016 (2013), arXiv:1306.3130.

[41] CTP Preliminary Design Review, http://www.ep.ph.bham.ac.uk/user/pedja/alice.

[42] J. Conrad , J. G. Contreras, and C. E. Jørgensen, Minimum Bias Triggers in ProtonProton Collisions with the VZERO and Silicon Pixel Detectors ALICE-INT-2005-025 version 1.0.

[43] P. Bilior, Nucl. Instrum. Methods **225** (1984) 352;
M. Regler and R. Frühwirth, Reconstruction of Charged Tracks, in Proc. of the Advanced Study Institute on Techniques and Concepts in High Energy Physics, Plenum Publ. Corp., 1989;
R. Frühwirth, Application of the Filter Methods to the Reconstruction of Tracks and Vertices in Events of Experimental High Energy Physics, HEPHY-PUB 516/88, Vienna (1988);
B. Batyunya, Yu. Belikov, K. Šafařík, ALICE Internal Note, ALICE-INT-97-24 (1997).

[44] M. Ivanov, I. Belikov, P. Hristov, T. Kuhr and K. Safarik, Nucl. Instr. and Meth. A 566, 70 (2006).

[45] Y. Belikov, M. Ivanov, K. Safarik and J. Bracinik, eConf C0303241, TULT011 (2003), arXiv:physics/0306108.

[46] `http://aliweb.cern.ch/offline`

[47] ALICE Physics Performance Report, *in preparation*;
F. Carminati *et al.*, ALICE Internal Note, ALICE-INT-2002-033 (2002).

[48] `http://root.cern.ch`

[49] Yellow Report CERN 2000-004.

[50] M. Gyulassy and X.N. Wang, Phys. Rev. **D44** (1991) 3501;
M. Gyulassy and X.N. Wang, Comput. Phys. Commun. **83** (1994) 307-331;
The code can be found in `http://www-nsdth.lbl.gov/~xnwang/hijing/`

[51] `http://wwwinfo.cern.ch/asdoc/geantold/GEANTMAIN.html`

[52] R. Frühwirth, Nucl. Instrum. Meth. A 262, 444 450 (1987).

Chapter 6

Data Analysis in ALICE and Results

In this chapter, the analysis tools used for the temperature fluctuation studies in Pb-Pb collisions at the ALICE energies have been discussed in details. Alongwith the data-sets and track-cuts used for the analysis, the centrality selection, particle identification, detector effect, efficiency correction, statistical error estimation, and data clean-up have been discussed in the following sections. The technical challenges encountered in course of the analysis and the techniques developed to deal with them, have been described also.

6.1 Selection of data-sets and track-cuts

The data taken by ALICE at LHC in 2010 has been analyzed for Pb-Pb collisions at $\sqrt{s}_{\rm NN}$ = 2.76 TeV has been analyzed. 14 million events have been analyzed for Pb-Pb collisions. Later on in 2011 another set of data has been taken for increase the sample size and decrease the statistical uncertainity. In Table 6.1, the colliding systems, vertex cuts, data-sets used, number of events, triggers used and the event generators used in the analysis have been listed.

6.1.1 Data Sample used for analysis

For Pb-Pb analysis :

Period/Production/pass : LHC 10h pass 2 AOD086 & AOD160;

Colliding systems	Pb+Pb
Collision energy	$\sqrt{s}_{\mathrm{NN}} = 2.76$ TeV
Vertex-cuts	$-10 < V_{\mathrm{z}} < 10$ cm, $-0.3 < V_{\mathrm{x}}, V_{\mathrm{y}} < 0.3$ cm
Data sets used	LHC 10h pass 2 AOD086 and AOD160
Simulation data sets	LHC 11a10a_bis AOD090 and AOD162, anchored to LHC 10h pass2
Number of events analyzed	$\approx$ 14 million (data), 2 million (Simulation)
Triggers used	kMB
Event generators	HIJING & AMPT

Table 6.1: Data sets used for the analysis

Run Numbers: 136851, 136854, 136879, 137042, 137045, 137124, 137125, 137132, 137133, 137135, 137136, 137137, 137161, 137162, 137163, 137165, 137230, 137231, 137232, 137235, 137236, 137243, 137365, 137366, 137370, 137430, 137431, 137432, 137434, 137439, 137440, 137441, 137443, 137530, 137531, 137539, 137541, 137544, 137546, 137549, 137595, 137608, 137609, 137638, 137639, 137685, 137686, 137689, 137691, 137692, 137693, 137704, 137718, 137722, 137724, 137748, 137751, 137752, 137843, 137844, 137847, 137848, 138125, 138126, 138150, 138151, 138153, 138154, 138190, 138192, 138197, 138200, 138201, 138225, 138275, 138359, 138364, 138396, 138438, 138439, 138442, 138469, 138533, 138534, 138578, 138579, 138582, 138583, 138620, 138621, 138624, 138637, 138638, 138652, 138653, 138662, 138666, 138730, 138731, 138732, 138736, 138737, 138740, 138742, 138795, 138796, 138826, 138828, 138830, 138831, 138836, 138837, 138870, 138871, 138872, 138924, 138965, 138972, 138973, 138976, 138977, 138978, 138979, 138980, 138982, 138983, 139024, 139025, 139028, 139029, 139030, 139031, 139034, 139036, 139037, 139038, 139042, 139104, 139105, 139107, 139110, 139172, 139173, 139308, 139309, 139310, 139311, 139314, 139316, 139328, 139329, 139360, 139437, 139438, 139439, 139440, 139441, 139465, 139466, 139467, 139470, 139471, 139503, 139504, 139505, 139507, 139510, 139511, 139513, 139514, 139517

6.1.2 For this analysis: Choice of Detectors

In general, any analysis associated with following points:
Event selection(Vertexing and Tracking)→Centrality determination→Track selection and Particle Identification→Analysis.
The dectecors used for particular analysis are selected on basis of these points. In the analysis, ITS (mainly SPD) (1) detectors have been used for the selection of the vertex and tracking.V0-detectors (3) have been used for the selection of centrality. TPC & TOF (2) has been also used for tracking and particle idetification.

6.1.3 Trigger Selection:

The Central Trigger Processor (CTP, the low-level hardware trigger) combines the trigger signals from the different detectors to decide whether an event is accepted. The information from the V0-detector and SPD detector are combined to form the minimum-bias triggers. This trigger (i.e, the trigger denoted by kMB for Pb-Pb) has been used for this analysis. After this selection other physics trigger used as per needed for this analysis.

6.1.4 Event QA: Vertex-cuts

For analyzing Pb-Pb collisions at $\sqrt{s}_{\mathrm{NN}} = 2.76$ TeV, one has to ensure that only those tracks are selected that are coming from the primary vertex. The vertex-cuts used for Pb-Pb data analysis at $\sqrt{s_{NN}} = 2.76$ TeV for the cleaned events, after trigger selection, have been shown in Fig. 6.1 as an example. Additional vertex-cut used is :($|V_{\mathrm{z}_{\mathrm{track}}}| - |V_{\mathrm{z}_{\mathrm{SPD}}}| < 5\ mm$).

The vertex-cuts used for Pb-Pb data analysis at $\sqrt{s_{NN}} = 2.76$ TeV for the cleaned events, after trigger selection, have been shown in Fig. 6.1 as an example.
Additional vertex-cut used for Pb-Pb :($|V_{\mathrm{z}_{\mathrm{track}}}| - |V_{\mathrm{z}_{\mathrm{SPD}}}| < 5\ mm$), to ensure that only those tracks are selected that are coming from the primary vertex.
For p-Pb analysis at $\sqrt{s_{NN}} = 5.02$ TeV, $-10 < V_{\mathrm{z}} < 10$ cm has been used as listed in Table 6.1.

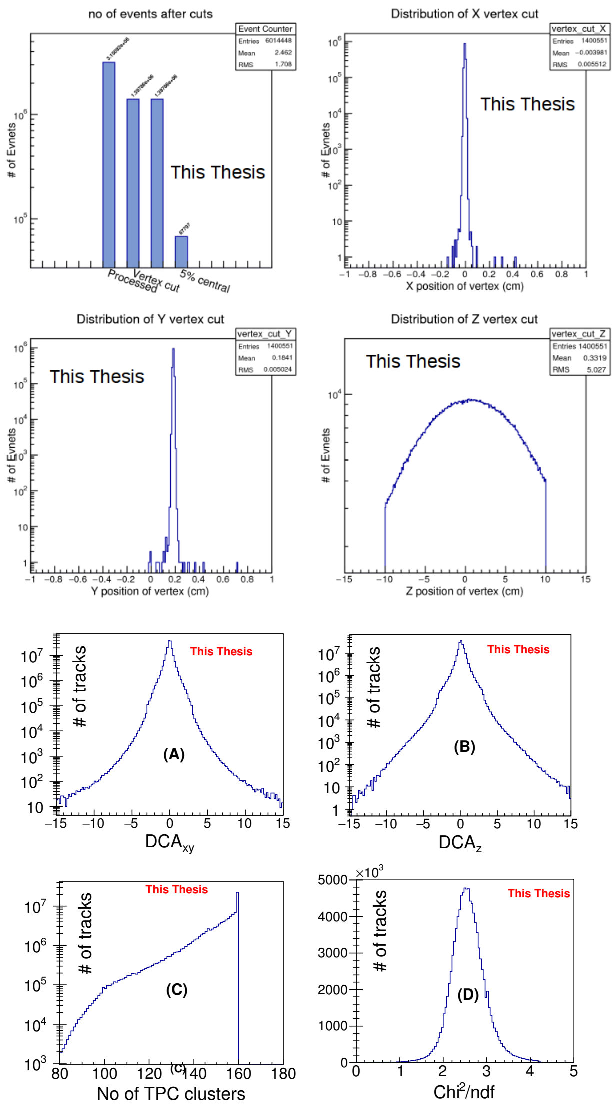

Figure 6.1: Upper pannel shows the events analyzed, Vertex-cuts used for Pb-Pb data analysis at $\sqrt{s_{NN}}$ = 2.76 TeV. Lower pannel shows the different track cuts (DCA) used, and also the fitting quality of data

6.1.5 Track-cuts

In 2010, some of the SPD channels were off during data taking which was the main cause behind the holes in the phi-distribution. Acceptance plays an important role in fluctuation studies. Therefore, the track-cut should be chosen in such a way so that the huge phi-holes can be taken care of. Hybrid tracks are used for the temperature fluctuation analysis. Although other cuts associated with different filter bit are also used for checking the purity of the sample. Hybrid track-cuts are global tracks which are basically a combination of three tracks and the resultant distribution has no phi-holes within it. Fig. 6.2 shows how the phi-holes have been taken care

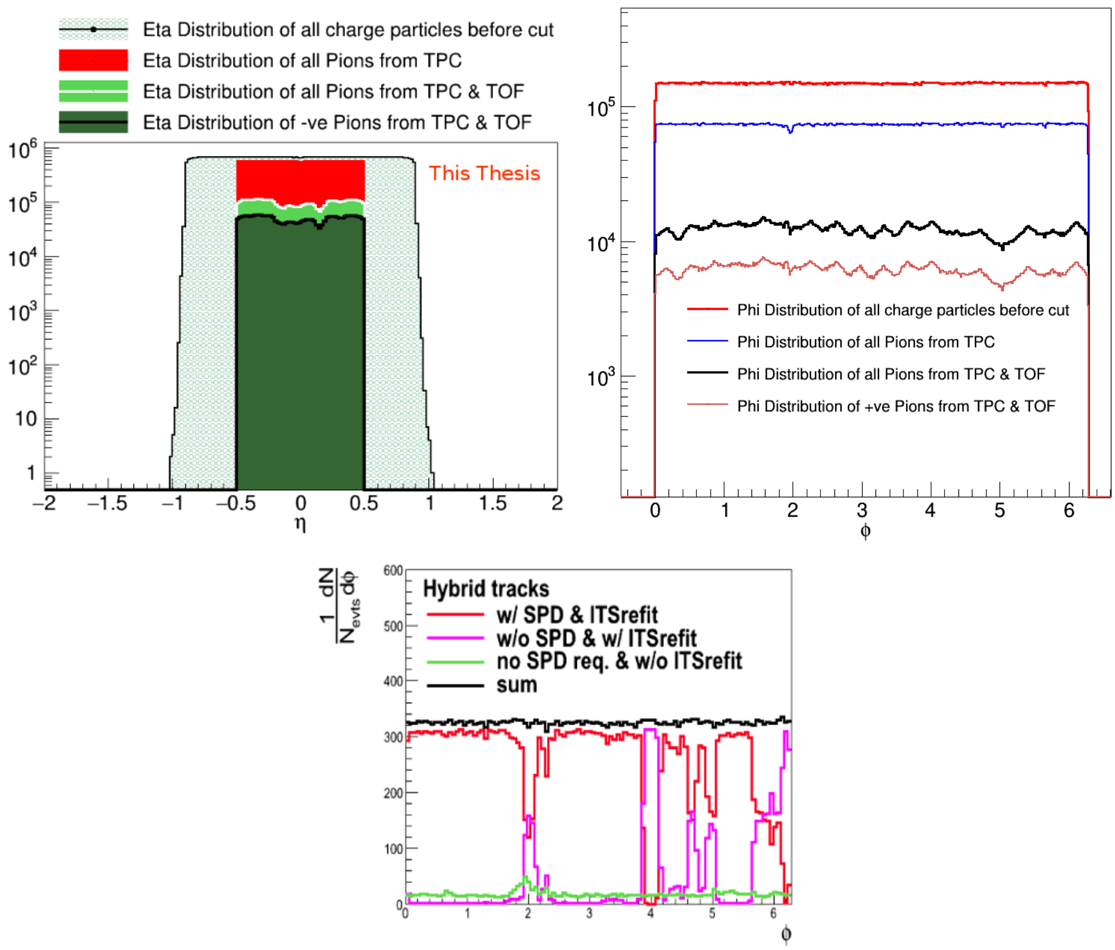

Figure 6.2: (a)η distribution (b) ϕ distribution after events and track cuts and (c) Hybrid Track-cuts

of using the hybrid-track cuts. These are basically sum of three kind of tracks : these are the global tracks with SPD hit(s) and an ITS refit, global tracks without SPD hit(s) and with an ITS refit constrained to the primary vertex, and global tracks without ITS refit constrained to primary vertex.

Another track-cut has been used for the analysis, which is the TPC-only track-cut. These are global tracks, possessing cuts for only Time Projection Chamber (such as TPC cuts for particle identifications etc).

Transverse momentum range	$0.15 < p_{\mathrm{T}} < 2.0$ GeV/c
Pseudorapidity range	$-0.5 < \eta < 0.5$
Distance of Closest Approach (DCA-cuts)	$DCA_{\mathrm{xy}} < 2.4\ cm, DCA_{\mathrm{z}} < 3.2\ cm.$
Number of TPC-clusters	80 (minimum)
χ^2 per number of clusters	4.0 (maximum)

Table 6.2: Kinematic cuts used for the analysis

The kinematic cuts used for Pb-Pb data analysis have been listed in Table 6.2. Transverse momentum range has been taken as $0.15 < p_{\mathrm{T}} < 2.0$ GeV/c, to ensure that in this analysis, mainly soft particles are to be dealt with. Below this range of p_{T}, the detector-efficiency is low. Also particle spectra suffered a lot from resonance decay and hence the spectra below this range are believe to be not properly thermalized. Above this moementum range also the chances of inclusion of minijets are quite high. Now, I will discuss the analysis flow charts following the details of particle idetification. For, pure spectra the particle idetification cuts need to be tightend. N-σ methods are used, where σ is the deviation from the expected Bethe-Bloch theoretical energy loss line to the experimental particle's energy loss line.

6.2 Analysis Flow-Chart

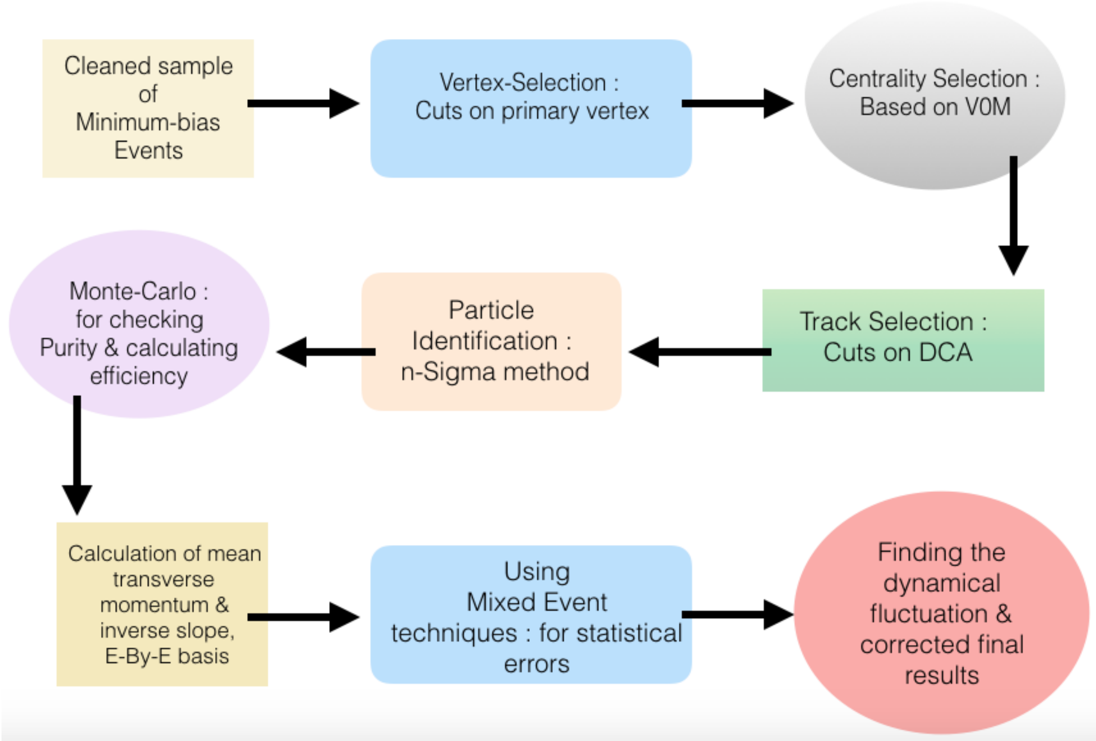

Figure 6.3: Analysis Flow Charts

6.3 Centrality determination in ALICE

In general, collision centrality is the measure of initial overlap region of the colliding nuclei and it is an important quantity to be measured correctly to study the properties of QCD matter at very high energies. Centrality determination helps in the comparison of ALICE measurements with those of other experiments as well as with theoretical calculations (4). centrality percentile can be obtained by integrating the impact parameter distribution or the number of participant distribution. In ALICE, the centrality is defined as the percentile of hadronic cross-section corresponding to multiplicity above a threshold value ($N_{\rm ch}^{\rm th}$) or energy deposited in ZDC below some given value ($E^{\rm th}_{\rm ZDC}$),i.e., as defined in (4),

$$c = \frac{1}{\sigma_{\rm AA}} \int_{N^{th}_{\rm ch}}^{\infty} \frac{d\sigma}{dN'_{\rm ch}} dN'_{\rm ch} \approx \frac{1}{\sigma_{\rm AA}} \int_{0}^{E^{\rm th}_{\rm ZDC}} \frac{d\sigma}{dE'_{\rm ZDC}} dE'_{\rm ZDC} \tag{6.1}$$

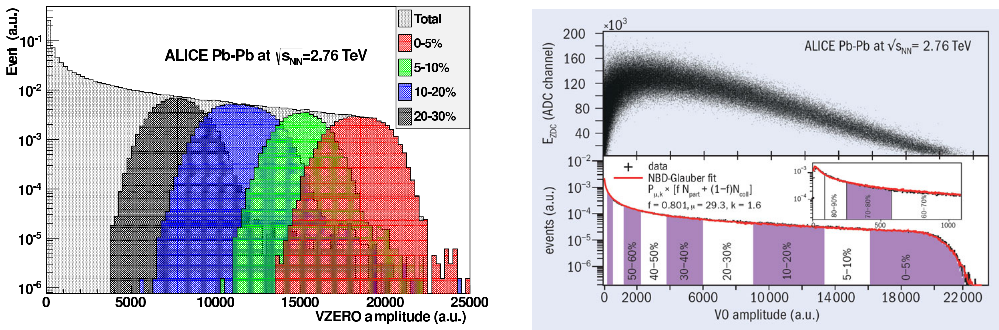

Figure 6.4: Geometric properties from Glauber MC calculation for Pb-Pb collisions at $\sqrt{s_{NN}} = 2.76$ TeV.

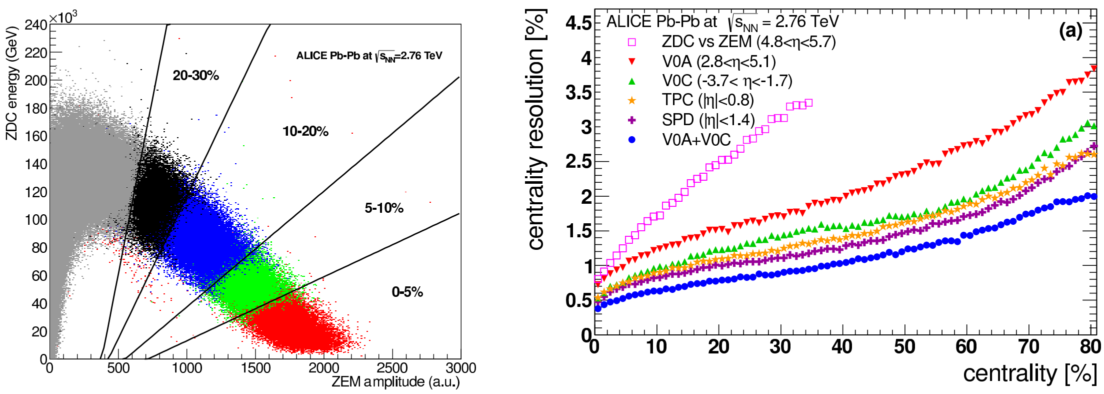

Figure 6.5: Centrality Resolution for different centrality estimators in ALICE

where, $\sigma_{\rm AA}$ is the total nuclear interaction cross-section. Cross-section may be replaced by the number of observed events after the correction for trigger efficiency. In heavy ion collision, the strong electromagnetic field generated contaminate the hadronic cross-section in the most peripheral collisions. Centrality determination is thus restricted upto which this contamination effect is negligible.

In the Ref. (4), the methods used for the centrality determination for the analysis of Pb-Pb data taken in 2010 and 2011 have been described in details. Glauber model has been implemented. The hadronic cross-section is determined mainly by using VZERO amplitude distribution fitted with the Glauber model as described in Section 6.2. In Table 1 in (4), the mean values of N_{part} and N_{coll}, RMS (the measure of dispersion) and systematic uncertainties obtained with Glauber MC calculation for each centrality class defined by the sharp-cuts in the impact parameter have been listed for Pb-Pb collisions.

In Fig. 6.4 taken from Ref. (4), the geometric properties from Glauber MC calculation has been shown. In the left panel, impact patameter distribution for hadronic cross-section percentiles has been presented and in the right panel, N_{part} distributions for corresponding centrality classes have been shown. These centrality classes have been used in the multiplicity fluctuation analysis of Pb-Pb data at $\sqrt{s_{NN}} = 2.76$ TeV.

Centrality can be determined using ZDC also. In this case, centrality classes are defined by cuts on the two-dimensional distribution of the ZDC energy as a function of the ZEM amplitude (4). The centrality selection uses the anti-correlation ZDC vs ZEM valid until the fragmentation breaks it. Thus, the centrality classes are defined within 0 *to* 35% centrality.

6.3.1 Resolution of the centrality determination

In ALICE, the centrality determination procedure uses different methods and we have different centrality estimators. Centrality can be determined using sum of amplitudes in the V0-detectors, or the number of clusters in the outer layer of SPD, or from ZDC. The resolution of the centrality classes is measured on an event-by-event basis. This is basically the RMS of the distribution of the differences between the centrality determined by different estimators and the average value of the centrality for each event (4).

Fig. 6.5 shows the centrality resolution for different centrality estimators. It is evident that the resolution depends on the rapidity range of the detector. The centrality estimator combining

V0A and V0C provides the best centrality resolution as shown in Fig. 6.5. Therefore, for Pb-Pb data analysis, V0M has been used as the centrality estimator.

6.4 Particle Identification in ALICE

Particle identification in this analysis are done via TPC and TOF. In TPC, detector responses are represented by the specific energy loss of the particle passing through TPC, expressed as $\frac{dE}{dx}$. For this the theoretical baseline followed is Bathe-Bloch. The deviation from the theoretical to actual is denoted in terms of detector resolution σ. The number of this, represented as nσ is known as nσ method of particle identification. Basically, it is defined as the deviation of the measured signal from that of the expected signal for a particular particle type π, k or p, in terms of the detector resolution (σ):

$$n\sigma_{\pi,k,p}{}^{TPC} = \frac{\frac{dE}{dx}^{\pi,k,p}_{measured} - \frac{dE}{dx}^{\pi,k,p}_{expected}}{\sigma^{\pi,k,p}} \tag{6.2}$$

In TOF, this nσ method of particle identification works like time-of-flight information from the TOF depending upon the mass of the particle species.

$$n\sigma_{\pi,k,p}{}^{TOF} = \frac{t^{\pi,k,p}_{measured} - t^{\pi,k,p}_{expected}}{\sigma^{\pi,k,p}} \tag{6.3}$$

The analysis for temperature fluctuation based on (a) only TPC, like left pannel of Fig. 6.6 (b) only TOF like right pannel of Fig. 6.6 and (c) TPC-TOF combined method of idetification.

For a analysis in the thermal low p_{T}region like mine, TPC-TOF combined cuts are used. Where then, only TPC covers low p_{T}region upto 0.6 GeV and above that TPC and TOF combined cuts are used upto typically 2.2 GeV for getting a pure idetification of π,k and p. Where the resolution parameter, σ depend on the track properties like: track- length, momentum, and other parameters used in the reconstruction algorithm.

This determined the purity of the sample. Based on the combined TPC-TOF response, a

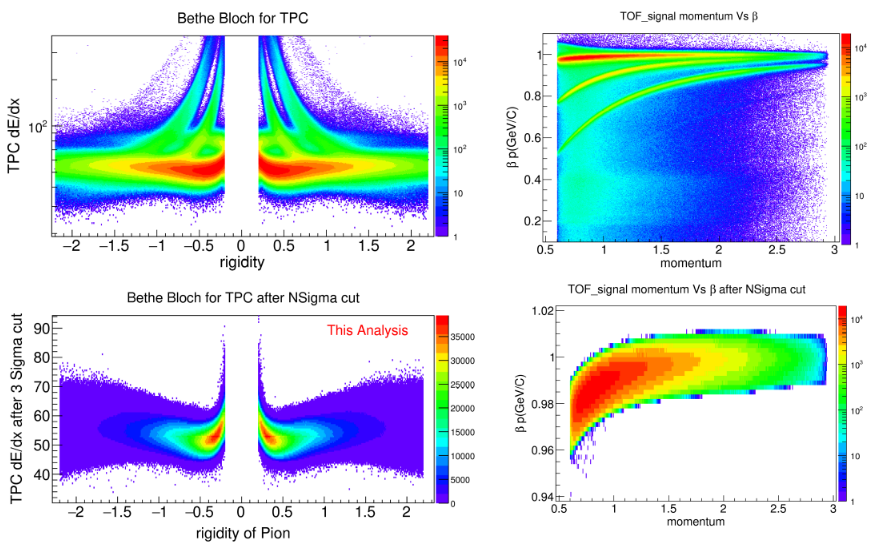

Figure 6.6: Left side represents energy-loss, $\frac{dE}{dx}$ versus rigidity in the TPC active volume. For each particle there is a distinctly separated band below p_{T}< 0.8 GeV which merges at higher $p_{\mathrm{T}} > 1.0$ GeV. similarly right side shows TOF identification cannot be done p_{T}< 0.5 Gev and upto 2.5 GeV. Both the side, upper pannel is before any nσ cut and lower paner is after n$\sigma > 3$ cut.

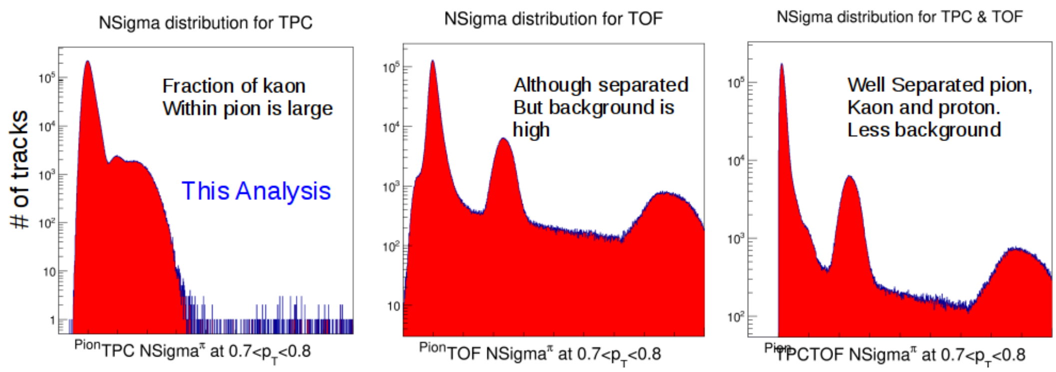

Figure 6.7: By slicing in p_{T}window with 0.1 GeV resolution the identification of π,k,p from TPC only, TOF only and TPC-TOF combined. The first peak is for π, second is for kaon and third is for protons. Clearly TPC-TOF combined separation is way-better.

track-by-track particle identification is performed by calculating $n\sigma^2_{TPC-TOF} = n\sigma^2_{TPC} + n\sigma^2_{TOF}$. For a given species, tracks within the 3σ circular cut in the 2D nσ TPC-TOF plane are taken as pure species. This cut can be varied like reducing the radius from 3 to 2.5, 2.0. Also this cut may be used as ellipsoidal cut for better particle identification as sometimes TPC identification is better than TOF and in some p_{T} region it is the reverse. Depending upon the sceneario, one can tightend the cuts in TPC and loose at TOF or vice-versa. An example of this is illustrated in Fig. 6.11, which shows the combined PID signals of pions, kaons and protons in a 2-D plot in different intervals of p_{T} . Clearly, the separation is seen to decrease with the increase in p_{T}range. To minimise the contamination due to mis-identification, strict cuts are imposed at

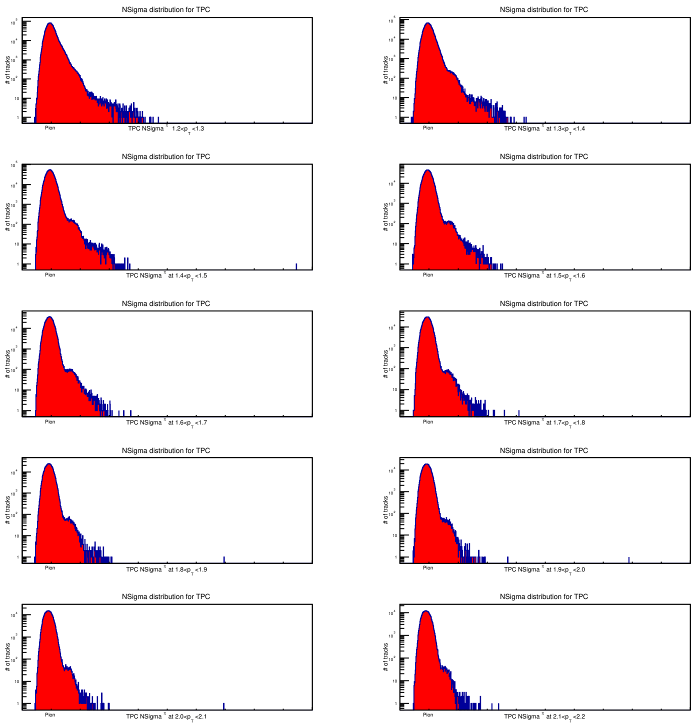

Figure 6.8: Identification of π,k,p from TPC only For slicing in p_{T}window with 0.1 GeV resolution

higher values of p_{T} , where two species have overlapping areas, sometimes it may be three.

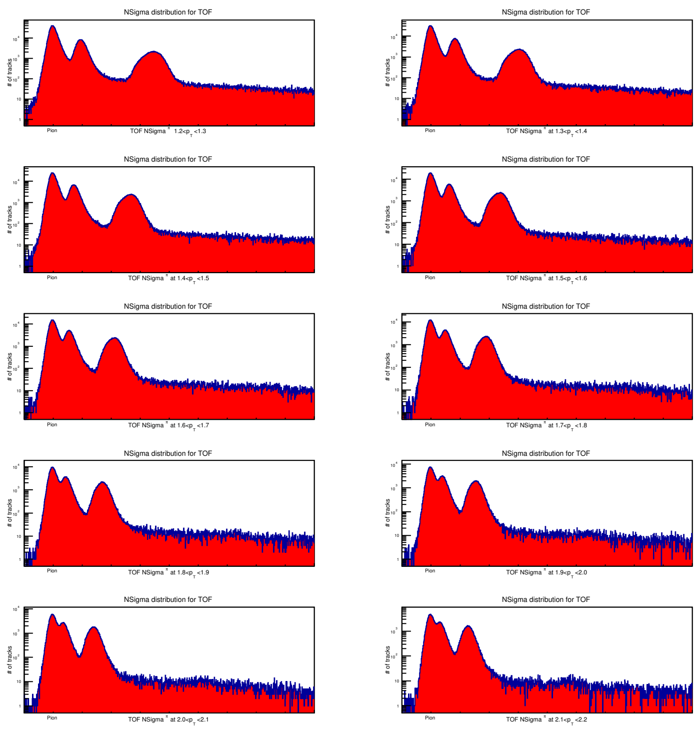

Figure 6.9: Identification of π,k,p from TOF only For slicing in p_{T}window with 0.1 GeV resolution

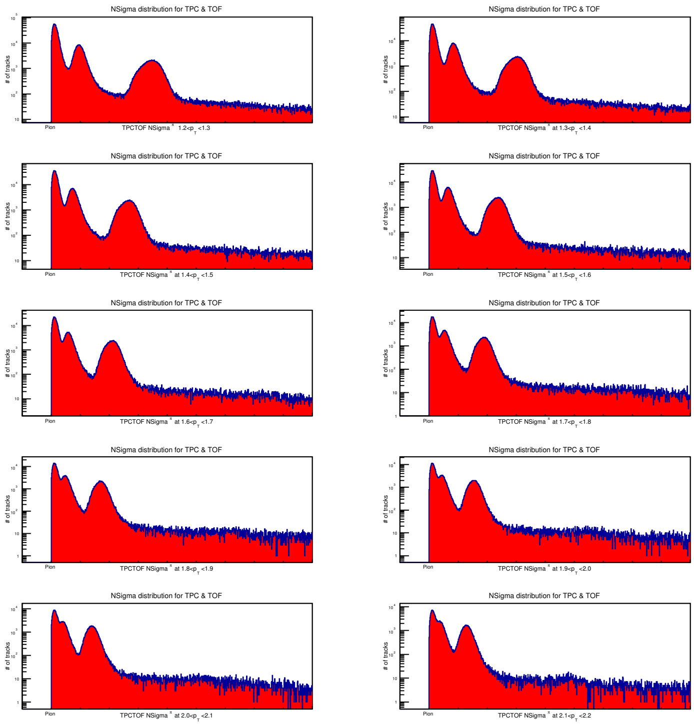

Figure 6.10: Identification of π,k,p from TPC-TOF combination For slicing in p_{T}window with 0.1 GeV resolution.

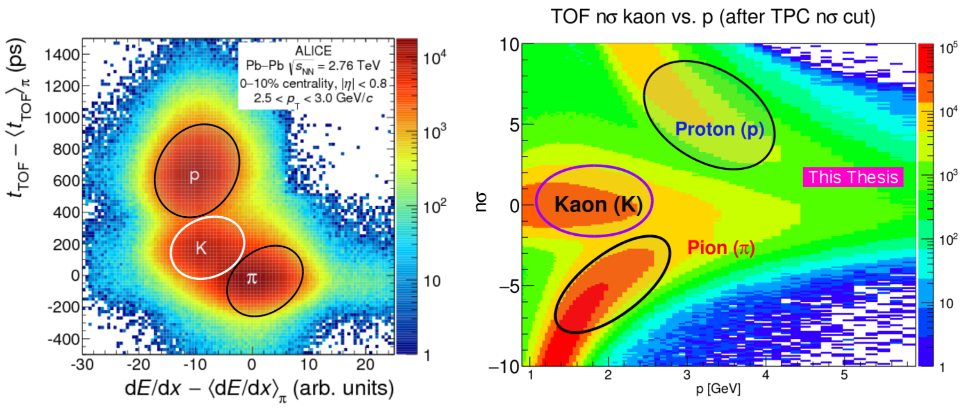

Figure 6.11: Left side represents particle species separation after TPC-TOF 3σ combined cut. Right side shows TOF nσ of Kaon after TPC 3σ cut with p_{T} centering at Kaon.

6.5 Efficiency Calculations and Corrections

The efficiency calculation is important to get the corrected spectra. In order to get a efficiency estimation species wise and for charged hadrons for different primary vertex, centrality, kinematic cuts LHC11a10a_bis Monte Carlo (MC) data set has been used, which is basically HIJING tuned for ALICE. This MC in the generator level called as MC Truth and when it passes through Geant ALICE detector labeled as MC reconstructed. Ratio of which with respect to p_T in primary particles gives the efficiency x acceptance (ϵ). The detailed study for secondary particle from weak decay, material and mis identification has been performed to obtain the contamination factor(c). Now the raw uncorrected spectra from the data has been corrected by dividing the correction factor $G = \frac{1-c}{\epsilon}$. In the data we calculate all the centrality dependendent efficiency in

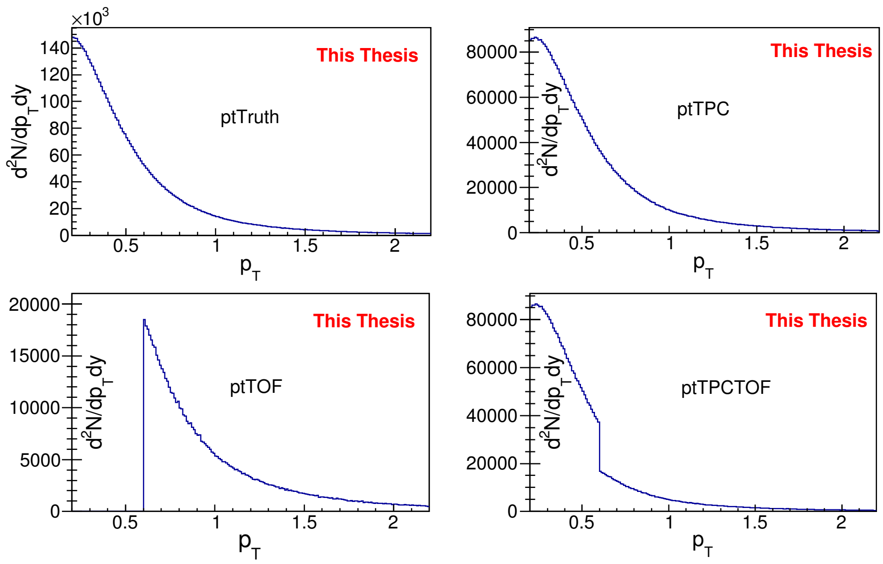

Figure 6.12: Transverse momentum spectra of pions from MC-truth, raw TPC only, raw TOF only and raw TPC-TOF combined are shown.

order to get the correct spectra. The uncorrected spectra from different detector and from Monte-Carlo are shown in Fig 6.12. Now from different kinematic and trackcuts one can calculate the efficiency factor and corresponding correction factor $p_T$and centrality wise as shown in Fig 6.13

and Fig. 6.14. Fig 6.13 shows the $p_T$dependent efficiency for all particle species while Fig. 6.14 shows the efficiency for π at all centrality. This also suggest the efficiency not varies much with centrality but mostly very much dependent on species. Also, the TPC efficiency is much higher than TOF efficiency, while purity is less.

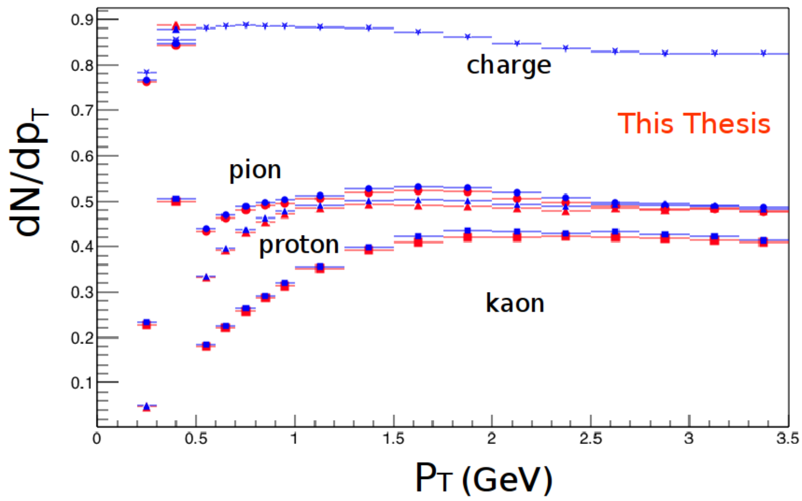

Figure 6.13: Efficiency for π, k, p from TPC-TOF combined cut for 0-5% are shown.

6.6 Results

After geting the efficiency factor and correction factor G one can calculate the corrected spectra for a given species at a given centrality. Here in this thesis I calculate the corrected spectra of π for all centrality and for both TPC only and TPC-TOF combined case. Fig 6.15, shows the corrected spectra, published data and raw spectra comparison for both TPC and TPC-TOF combined case. Ratio plot suggest that the TPC-TOF spectra of π shows a close agreement with published data.

Once the final corrected spectra is produce, the event-by-event Mean $p_T$is calculated and from there one can get the mean $p_T$distribution as shown in Fig 6.16. Here all centrality wise π mean $p_T$distribution are shown for 0.15 to 2.0 GeV $p_T$range. If one change the $p_T$window

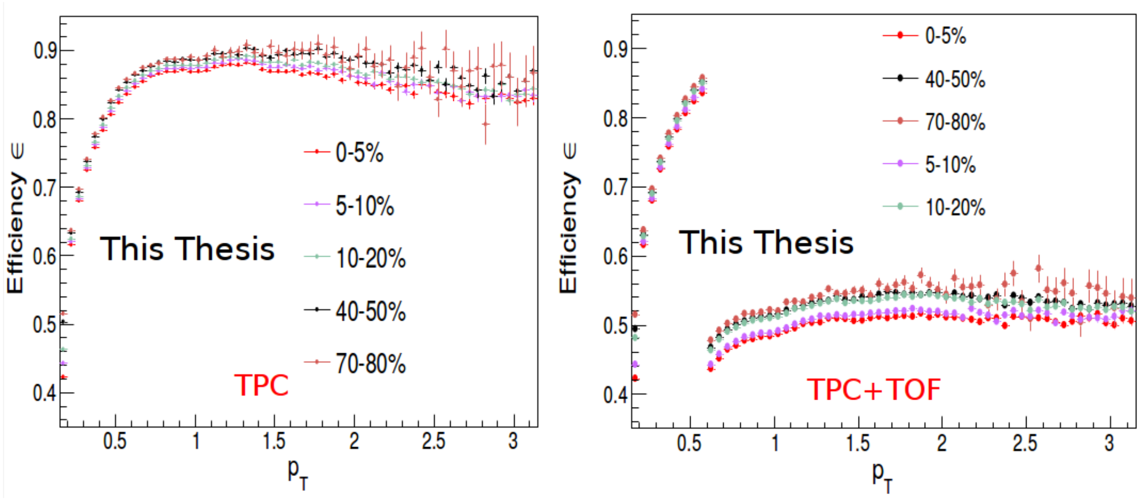

Figure 6.14: Efficiency for π for all centrality from TPC-TOF combined are shown

the distribution shape can be affected and this Choice comes from the physics motivation of the thermal range of the spectra as shown in Fig 6.17.

Also a event-by-event inverse slope parameter known as effectife temperature T_{eff} as motivated by Boltzmann statistics (discuss in Chapter 3 and Chapter 4) are shown in Fig 6.18. As, in this thesis, the mixed event techniques are not properly done, results are not upto the mark and hence not shown. The mixed event techniques are mainly used to get the dynamical fluctuation part of the T_{eff} distribution. This work are still going on and kept as future work. In future, the results are explored in terms of different species and centrality for Pb+Pb 2.76 TeV and 5.02 TeV data set.

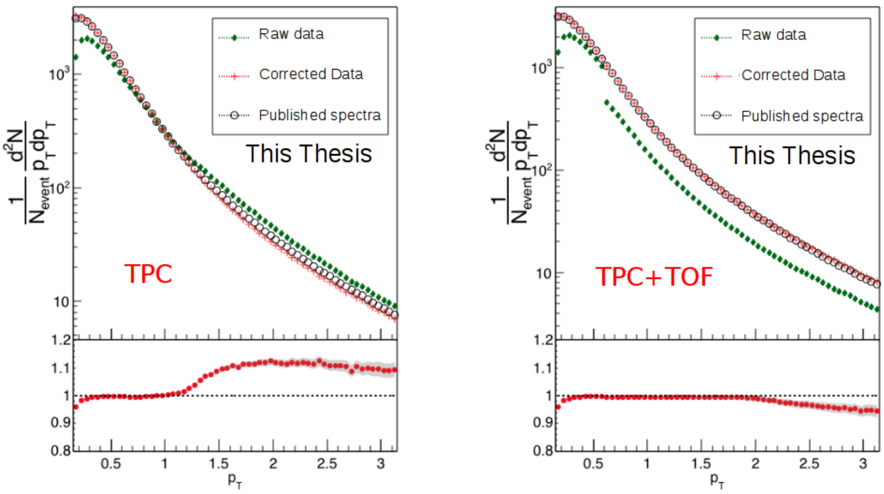

Figure 6.15: Efficiency corrected transverse momentum spectra of pions from TPC only and TPC-TOF combined are shown.

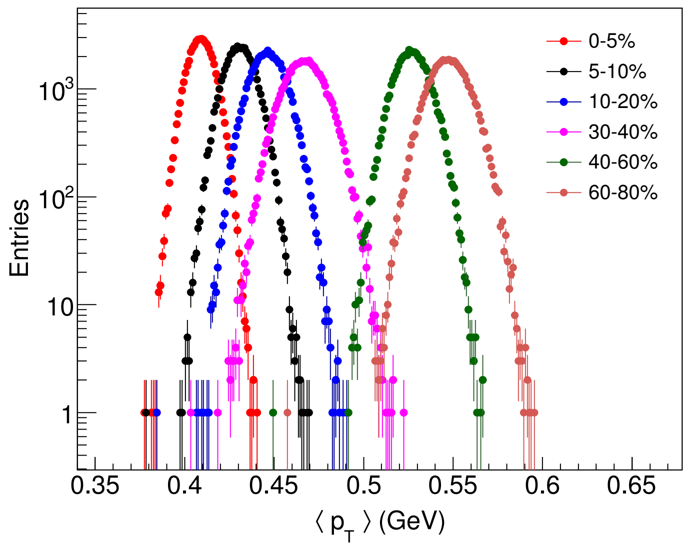

Figure 6.16: Centrality wise the distribution of mean transverse momentum of pions, (TPC-TOF combined) efficiency corrected are shown.

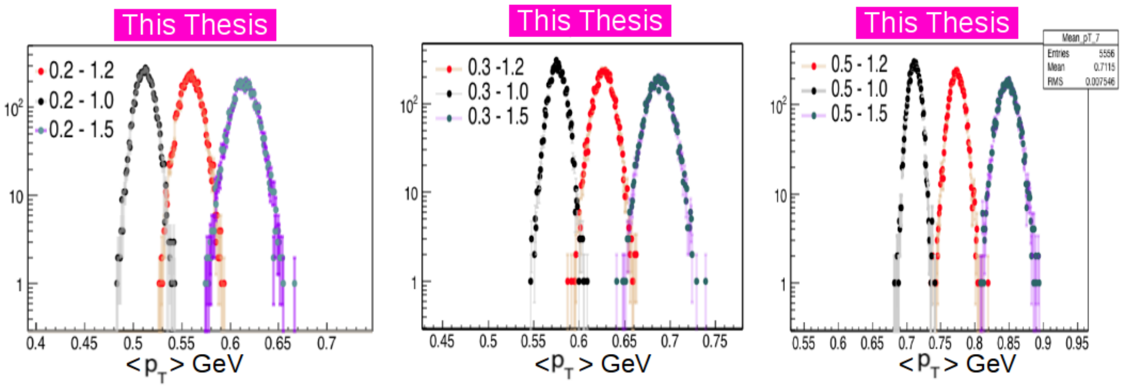

Figure 6.17: Centrality and momentum window variation of the distribution of mean transverse momentum of pions, (TPC-TOF combined) efficiency corrected are shown.

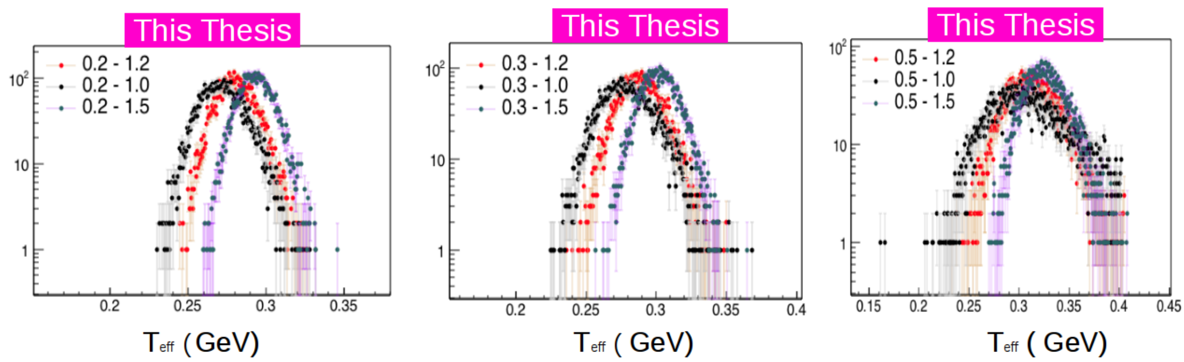

Figure 6.18: Centrality and momentum wise the distribution of effectife temperature from mean transverse momentum of pions, (TPC-TOF combined) efficiency un-corrected are shown.

Bibliography

[1] ALICE Collaboration, ALICE Inner Tracking System (ITS): Technical Design Report, CERN-LHCC-99-012, http://edms.cern.ch/file/398932/1.

[2] ALICE Collaboration, ALICE time projection chamber: Technical Design Report, CERN-LHCC-2000-001, http://cdsweb.cern.ch/record/451098.

[3] ALICE Collaboration, ALICE forward detectors: FMD, TO and VO: Technical Design Report, CERN-LHCC-2004-025, http://cdsweb.cern.ch/record/781854.

[4] B. Abelev *et al.* (ALICE Collaboration), Phys. Rev. **C 88**, 044909 (2013), arXiv:1301.4361 [nucl-ex] (2013).

[5] K. Aamodt *et al.* (ALICE Collaboration), Phys.Rev.Lett.**106**:032301, 2011.

[6] https://twiki.cern.ch/twiki/bin/viewauth/ALICE/PACentStudies.

[7] https://twiki.cern.ch/twiki/bin/viewauth/ALICE/PACentStudies.

[8] ALICE Collaboration, ALICE time projection chamber: Technical Design Re- port, CERN-LHCC-2000-001, http://cdsweb.cern.ch/record/451098.

[9] ALICE Collaboration, ALICE time projection chamber: Technical Design Re- port, CERN-LHCC-2000-001, http://cdsweb.cern.ch/record/451098.

Chapter 7

Photon Multiplicity Detector in ALICE

In this chapter I will discuss about the Photon Multiplicity Detector (PMD) in detail and also our analysis associated with PMD with its gain calibration. The measurements of spatial inclusive photon multiplicity in ALICE experiment is done by Photon Multiplicity Detector (PMD). It consists of two planes (PRE and CPV) of detectors and a lead (Pb) converter between them. PMD is situated at 367 cm away from the interaction point and covers $2.3 \leq \eta \leq\ 3.9$ with full azimuthal coverage [64].

7.1 PMD design overview

PMD consists of two identical planes with a 3X 0 thick Pb plane sandwiched between them. The plane which faces the IP is called Charged Particle Veto (CPV) and the other plane is called Preshower (PRE) plane. A schematic view of the PMD from the IP is shown in the Fig. 3.1. Each of the planes consist of 24 modules and each of the modules consist of 4608 numbers of honeycomb cells. In the latest configuration four modules has been taken out from each of the plane. So the total number of existing modules are 40. Each module is an independent gas-tight rectangular unit. The modules can be handled individually. There are two types of modules. The modules containing 48 rows and 96 column are called short modules and the modules containing 96 rows and 48 columns are called long modules. The basic unit of PMD is hexagonal or honeycomb cells having 5 mm depth and 0.23 cm 2 cross section.

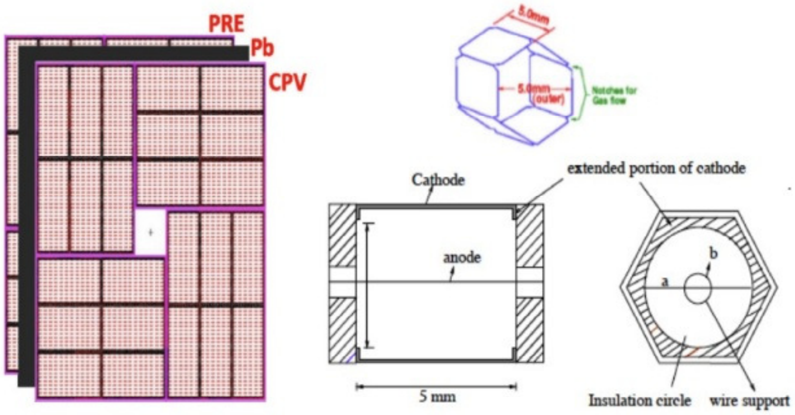

Figure 7.1: A schematic view of PMD, consists of two planes and Pb converter from the interaction point.

A matrix of 48 96 or 96 48 cells is made using thin copper sheet, which is known as honeycomb chamber. The honeycomb chamber is placed between two gold plated Printed Circuit Boards (PCB). There are 4608 number of cells in a module and gold plated tungsten wires of diameter 20 are inserted through the centre of each cell and a proper tension is applied in the wire during soldering. The top PCB has the solder islands at the centre corresponding to each cell. There are 32 connectors to extract the signal from the 32 cells in the top PCB. There are 72 connectors in a module. The bottom PCB has only soldering islands without signal tracks, serving as anchor points. The inner part of the PCBs are gold plated, with circular islands near the anode wire. Together with the honeycomb wall they form part of an extended cathode going very close to the anode wire. A proper alignment is needed to put the honeycomb plane between the two PCBs. One of the alignment pin is used to provide the high voltage to the honeycomb chamber which is used as a cathode plane. The gold plated tungsten wires are used as anodes. The modules are kept inside air-tight containers, which are made of 2 mm thick stainless steel (SS) containing the nozzles for gas inflow and outflow. A mixture of Ar and CO 2 with a ratio of 70:30 by weight flows through the modules. The rectangular Pb converter is situated between the two planes of PMD. There are 40 Pb plates corresponding to 40 modules. There are two types of Pb plates as modules. The long type lead plate is of the size 49.05 cm 21.7 cm while the short type is 42.5 cm 25.15 cm. The thickness of the Pb plates are 1.5 cm, which is equivalent to 3X 0 radiation length. PMD has two parts on both sides of beam pipe. SS plate of 5 mm thick is used to support the lead converter plates and the modules in each half of the PMD. The SS plate has tapped holes for screws corresponding to hole position in the lead converter plates. There are two different slots on the SS plate for placing two different types of modules. Each SS plate contains 10 modules. Each half of the PMD has independent gas supply, electronic accessories and cooling systems. The PMD is supported from a SS girder in such a way that the two halves can be moved on the girder to bring them together for data taking operation or separated for servicing.

A schematic diagram of the front end electronics is shown in the Fig. 3.5. The signals from the PMD are taken from the anode wires.

7.2 Electronics

Front End Electronic Boards (FEE boards), connected to the detector with the help of flexible kapton cables, collect the signals. After processing and digitizing, the signals are then sent to the Translator Board (TB) via back plane. These signals are then sent to the Cluster Readout Concentrator Unit System (CROCUS) with the help of Patch Bus cables. From the CROCUS these signals are transferred further to the Data Acquisition System (DAQ) with the help of Detector Data Link (DDL).

7.2.1 FEE boards and Translator boards (TB)

Each Front End Electronics (FEE) board of PMD consists of four Multiplexed ANAlog Signal Processor (MANAS) chips, two inverting buffer amplifiers, two serial 12 bit ADCs (AD7476) and a custom built ASIC called Muon Arm Readout Chip (MARC). The MANAS chip has sixteen input channels and one output channel. A group of 64 cells are connected to two 32-pin connectors by a flexible cable which connects to the FEE board at the other end. The signals are processed by the MANAS chips which provide the analog outputs. ADCs convert the analog signal coming from MANAS. The digitized output signal is sent to the MARC. MARC controls 4 MANAS chips and 2 serial 12-bit ADCs and performs zero suppression on data. The Low Voltage Transistor Transistor Logic (LVTTL) type signals are delivered to TB from FEE boards. The TB converts all LVTTL signals to Low Voltage

Differential (LVDS) signals before sending CROCUS and translates all the LVDS signals from CROCUS to LVTTL. Readout chain: Patch bus A flexible flat cable known as patch bus cable is designed to transfer the LVDS signals from TB to CROCUS and vise versa. To minimize the electromagnetic disturbances the cable is shielded with aluminum tape. There are 200 patch bus cables of length around 8.5 m are used for the readout of PMD.

7.2.2 CROCUS

The Cluster Read Out Concentrator Unit System (CROCUS) is one of the im- portant readout electronic component of the PMD. It gathers the signals from the FEE via patch bus cable and transfers to the DAQ. It also provide the trigger signal to the detector and allow the calibration. One CROCUS consists of one Concentra- tor Board (CRT) and five Frontal Boards (FRTs). The FRTs mange the FEEs via patch bus cable. These concentrate Level-I data, which is coming from FEESs and transfer the data to Level-II data concentration crocus system. FRTs also send the calibration signal to the detectors. The main objectives of the CRT are the data acquisition from the FRTs and distribution of the trigger signal to them.

7.3 Working principle of PMD

As mentioned earlier PMD consists of two identical planes and a Pb converter be- Pb converter and finally face the preshower plane. The photons do not produce any signal in the CPV plane. These produce electromagnetic shower in the Pb converter by pair production and bremsstrahlung radiation. The thickness of the converter is chosen such a way that conversion probability of photons is high and transverse shower spread is small to minimize shower overlap.

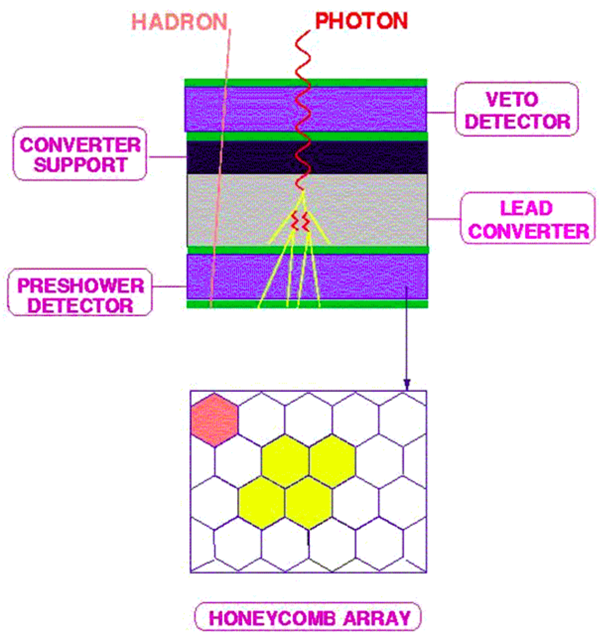

Figure 7.2: A schematic view of working principal of PMD

The shower particles give signal in the honeycomb cells of the preshower plane. So, the photon affects several cells and deposit large amount of energy in the preshower plane. On the other hand, the charged hadrons behave like Minimum Ionizing Particles (MIP) and produce signal in both CPV and preshower plane. Since the interaction cross-section of the charged hadrons with the Pb converter is very low, they deposit very small energy in the preshower plane and the signals are confined within one or two cells. The different response of the photon and the charged hadron to the detector helps us to discriminate charged particles from the photon sample.

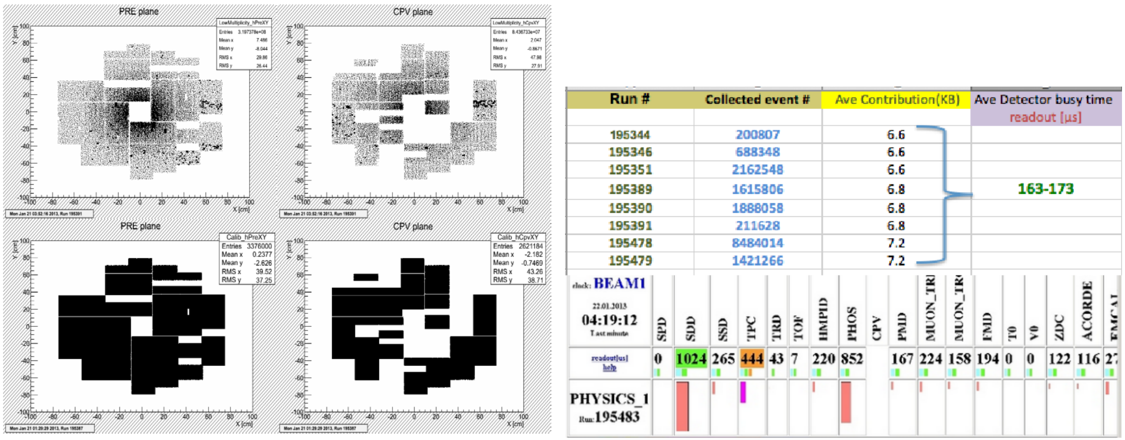

Run #	Collected event #	Ave Contribution(KB)	Ave Detector busy time readout [µs]
195344	200807	6.6	
195346	688348	6.6	
195351	2162548	6.6	
195389	1615806	6.8	163-173
195390	1888058	6.8	
195391	211628	6.8	
195478	8484014	7.2	
195479	1421266	7.2	

clock: BEAM1 22.01.2013 04:19:12 Last minute	SPD	SDD	SSD	TPC	TRD	TOF	HMPID	PHOS	CPV	PMD	MUON_TRK	MUON_TRG	FMD	T0	V0	ZDC	ACORDE	EMCAL
readout[us] help	0	1024	265	444	43	7	220	852		167	224	158	194	0	0	122	116	27
PHYSICS_1 Run: 195483																		

Figure 7.3: Detector geometry, busy time and run condition table of PMD at the time of data taking p-Pb 5.02TeV

7.4 Hot Cell Removal and Data cleaning

a minimum energy, whereas the electrons aect a large number of cells depending on their energy. The distribution of energy deposition of pions called the minimum ionizing particles (called MIPs) can be described by a Landau distribution. The Fig. **??** pictorially shows isolated cell in PMD, where a cell having non-zero energy deposited surrounded by cells having no energy deposited. The isolated cell are assumed to be formed by MIPs. The Fig **??** shows the ADC distribution of such

isolated cells in pp collisions at $\sqrt{s} = 0.9$ TeV, which forms a Landau distribution with a Most Probable Value (MPV) of 71 ADC. Since the electrons deposits a large amount of energy and hits more than one cell, we take this advantage of diferent response of the detector towards hadrons and electro-magnetic particles (photons and electrons) to discriminate them.

So one can discriminate photon and hadrons by applying a threshold on the cluster ADC and number of cells (N_{cell}). The number of clusters which pass the dis- crimination threshold are termed as γ_{like} clusters (N$\gamma - like$).

The number of clusters which pass the dis- crimination threshold are termed as γ-like clusters (N$\gamma - like$). The number of identified photons in the $N_{\gamma-like}$ sample are called $N_{\gamma-detected}$. So,

$$Efficiency = \frac{N_{\gamma-detected}}{N_{\gamma-incident}} \tag{7.1}$$

and

$$Purity = \frac{N_{\gamma-detected}}{N_{\gamma-like}} \tag{7.2}$$

7.5 Calibration and Gain calculations

I analyzed this data in the ALICE grid to obtain the variation in cell to cell mean ADC count in one super module(SM) hence for all 20(out of 24 SMs 4 SMs were not functioning during the runs,they are SM6,0,13,19) SMs.

Data Set: Energy: CM p-p@7 TeV

Data: 2010/LHC10d/pass2 ESD

Run Number: 126090,126088,126158,126160

Number of Events: 25M

The ADC distribution of each isolated cell has been obtained for both pre-shower and CPV detector SMs. The means of the ADC distributions for each isolated cells of a particular SM plotted in a 1-d histogram .(The mean calculation for isolated cell ADC distribution is restricted up to the channel number 1200 to avoid over estimation of the mean due to an enhancement in ADC count around the channel number 1400 following the saturation in the MANAS chip.)

The plots for the module by module mean of the ADC distribution of all isolated cells of all(20) pre-shower SMs are only presented here since most of the CPV detectors have no entries or just not have enough entries to be considered for any reliable calculation. A separate plot has also been done taking mean ADC counts of all isolated cells of the entire detector(pre-showers only). The plots for each supermodule has been shown here.

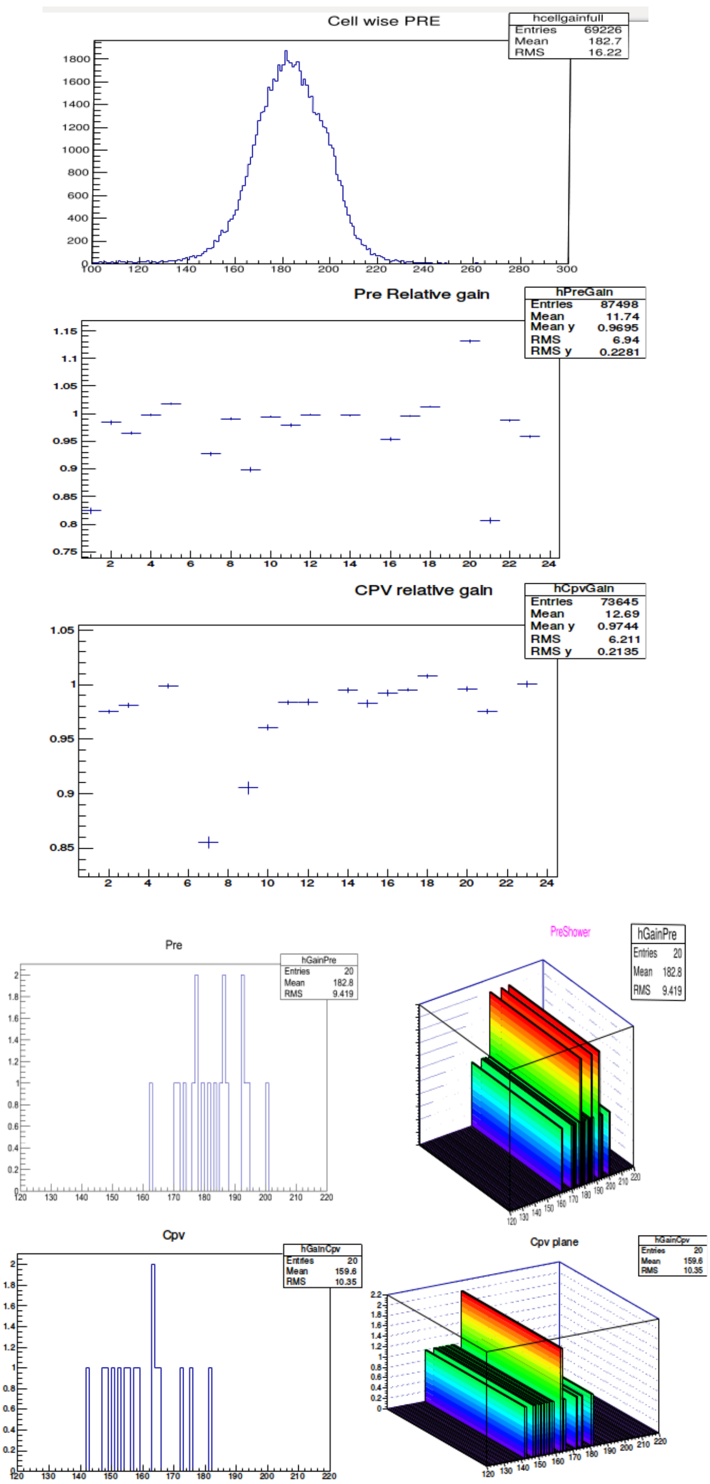

Figure 7.4: Calibration and gain calculations: (a) Cell to cell and (b) PMD super modules (PRE and CPV planes) wise

Results: The observed variation in mean ADC distribution within a module is within 10% and module to module is of the same order .

This results are already included in analysis note.

The entire process is repeated over all 20SMs . We have plotted the means of the mean ADC distributions in another 1-D histogram to study module-to-module variation in mean.

Cell to cell, module to module gain response varies reasons :

- High voltage may differ from module to module
- Wire electronics gain may vary for different cells
- Cell dimensions may vary
- Unequal cleaning of cells
- Possible variation in the effective length of the anode Normalizing the gain, cell wise and module wise (detector calibration)

Bibliography

[1] P. K. Netrakanti, Ph.D. Thesis, Jadhavpur University 2008;

[2] D. Das, Ph.D. Thesis, Jadhavpur University 2008;

[3] M. Sharma, Ph.D. Thesis, Panjab University 2008;

[4] N. Gupta, Ph.D. Thesis, Jammu University 2008;

[5] S. M. Dogra, Ph.D. Thesis, Jammu University 2009; http://drupal.star.bnl.gov/STAR/thesis

[6] S. C. Phatak Clustering Algorithm For PMD Data. http://www.iopb.res.in/phatak/cluster/clusters.html.

[7] Subhash Singha, Ph.D. Thesis, HBNI, 2014;

[8] Sudipan De, Ph.D. Thesis, HBNI, 2014;

Chapter 8

Particle production and Flow in HI collisions

The primary goal of colliding heavy-ions at ultra-relativistic energies is to study nuclear matter under extreme conditions, in which hadronic matter is expected to undergo a phase transition to a new state of matter, the Quark-Gluon Plasma (QGP) (1; 2). Quantum Chromodynamics (QCD), the theory of strong interactions, suggests that at high temperatures and energy densities, nuclear matter melts down to this new phase of deconfined quarks and gluons. Recent Lattice QCD calculations (3; 4) indicate that transition from hadronic matter to QGP occurs at a critical temperature of $T_C \sim 155$ MeV and critical energy density of $\epsilon_C \sim 0.7 - 1.9$ GeV/fm^3. The QGP research programs at the Relativistic Heavy Ion Collider (RHIC) at Brookhaven National Laboratory and the Large Hadron Collider (LHC) at CERN are on a quest to unearth the physics of deconfinement and vacuum, and to understand how matter behaved within a few microseconds after the birth of our Universe. With the first phase of the beam energy scan program at RHIC during 2010 and 2011, data for Au+Au collisions at a nucleon-nucleon (NN) center-of-mass energy ($\sqrt{s_{NN}}$) from 7.7 GeV to 200 GeV are available. The main aim of this program is to probe the onset of deconfinement and to locate the QCD Critical Point (5). The LHC has collided Pb+Pb beams at $\sqrt{s_{NN}} = 2.76$ TeV during the first phase of its operation

(2010 and 2011). During the first year of the second phase of LHC operation in 2015, data for Pb+Pb collisions at $\sqrt{s_{NN}} = 5.02$ TeV are collected. Thus with the combination of RHIC and LHC, high quality data for heavy-ion collisions have now been available over quite a broad energy range. At the same time a large number of models have emerged which attempt to analyze and explain the data and extract physical parameters (6; 7; 8; 9; 10).

Global observables such as charged particle multiplicity distributions, pseudorapidity (η) distributions, momentum spectra, particle ratios, size of the fireball, and azimuthal anisotropy provide majority of the valuable information for thermal and chemical analysis of the freeze-out conditions (11; 12). The η-distribution of charged particles is one of the most basic and most important observables to characterize the colliding system and to understand the phase transition. It has been almost 20 years of relativistic heavy-ion(A-A) and baseline(p-p) collisions data has been taken by several experiments. All the history of these data is shown in 8.1. All the observables in heavy-ion collisions scale with the number of particles. So the knowledge of the particle density is essential for validating any measurement. The pseudorapidity particle density at mid-rapidity, along with transverse energy per particle provides the energy density of the fireball using the Bjorken estimation (13). The pseudorapidity distributions are intimately connected to the energy density of the emitting source and provide an important test-bed for validating theoretical models, which attempt to describe the conditions in the early phases of the collision.

Experimental data for η-distributions have been reported for all the collider energies at RHIC (14; 15) and LHC (16; 17; 18; 19; 20). In this article, we make a compilation of some of the available data in terms of the variation of pseudorapidity distributions of charged particles with beam energy and collision centrality. We make a similar study using the string melting mode of the A Multi-Phase Transport (AMPT) model and make a comparison with the available data. In this model, different values of parton cross sections are used to explain the data at LHC. The pseudorapidity distributions, both from data and the AMPT model, of charged particles from $\sqrt{s_{NN}}$ =7.7 GeV to 2.76 TeV are fitted by a double Gaussian function. These parameters show

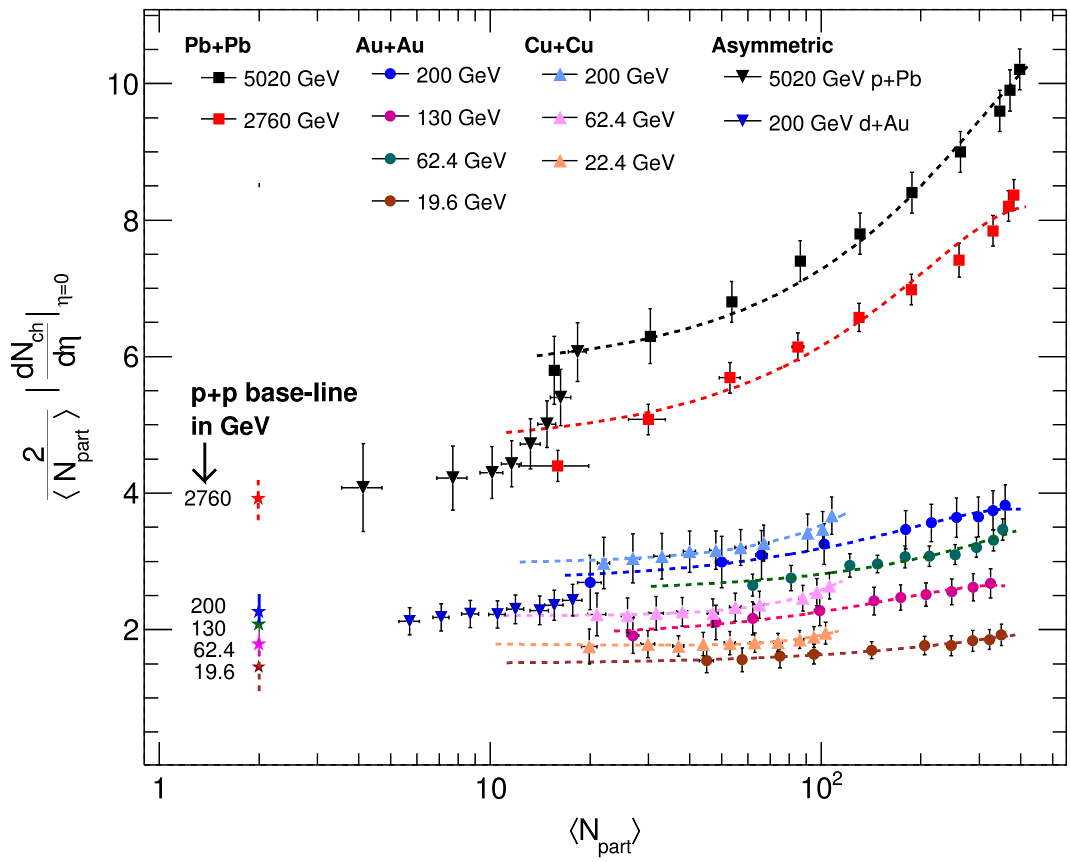

Figure 8.1: multiplicity density or $\frac{dN_{ch}}{d\eta}$ at $\eta = 0$ per participant pair obtained from various experiments at different energies for central to peripheral collisions are shown as a function of N$_{part}$

interesting trends as a function of beam energy. Extrapolating the parameters to higher energies, we obtain the η-distribution for $\sqrt{s_{NN}} = 5.02$ TeV. It is observed that the pseudorapidity density at mid-rapidity matches well with the recently reported data from ALICE (21). Furthermore, we extract the value of initial energy density for collisions at $\sqrt{s_{NN}} = 5.02$ TeV.

The paper is organized as follows. In Section II, we discuss the AMPT model which is used to compare the data results. In Section III, we present the compilation of pseudorapidity distributions for data and AMPT. In Section IV, we make an analysis of the shapes of the pseudorapidity distributions and present the results of the fit parameters. Energy dependence of charged particle multiplicity densities, pseudorapidity distributions and energy densities are presented. We conclude the paper with a summary in Section VI.

8.1 AMPT settings

The AMPT model (22) provides a framework to study relativistic heavy-ion collisions. It incorporates essential stages of heavy ion collisions from the initial condition to final observables on an event-by-event basis, including the parton cascade, hadronization and the hadron cascade (23; 24; 25). The model can generate events in two different modes: (a) default, and (b) string melting (SM). Initial conditions for both the modes are taken from HIJING (26), where two Wood-Saxon type radial density profile are taken for colliding nuclei. The multiple scattering among the nucleons of two heavy ion nuclei are governed by the eikonal formalism. The particle production has two distinct sources, from hard and soft processes, depending on the momentum transfer among partons. In the default mode, energetic partons cascade through Zhang's Parton Cascade (ZPC) before the strings and partons are recombined and the strings are fragmented via the Lund string fragmentation function,

$$f(z) \propto \; z^{-1}(1-z)^{a} exp(-bm_T^2/z), \tag{8.1}$$

where a and b are the Lund string fragmentation function parameters, taken to be 0.2 and 2.2. ART (A Relativistic Transport model for hadrons) (27) is used to describe how the produced hadrons will interact. In the String Melting mode, the strings produced from HIJING are decomposed into partons which are fed into the parton cascade along with the minijet partons. The partonic matter is then turned into hadrons through the coalescence model (28; 29) and the hadronic interactions are subsequently modeled using ART. The Default mode describes the evolution of collision in terms of strings and minijets followed by string fragmentation, and the String Melting mode includes a fully partonic QGP phase that hadronizes through quark coalescence.

In both the modes of AMPT, Boltzmann equations are solved using ZPC with total parton elastic scattering cross section,

$$\sigma_{gg} = \frac{9\pi\alpha_s^2}{2\mu^2}\frac{1}{1+\mu^2/s} \approx \frac{9\pi\alpha_s^2}{2\mu^2}, \tag{8.2}$$

where α_s is the strong coupling constant, s, t are the Mandelstam variables and μ is the Debye screening mass. Here, α_s and μ are the key deciding factors for multiplicity yield at a particular centrality of given energy, and they are taken as 0.47 and 3.22, corresponding to $\sigma_{gg} = 10$ mb. For a beam energy range 7.7 GeV to 2.76 TeV we found global observables like pseudorapidity density (16), transverse momentum distribution (30), particle ratio (22), higher harmonic anisotropic flow (30) like v2, v3 are within the range of experimental error. We have carried out a comparison study for different observables by varying a, b, α_s and μ corresponding to 1.5 mb, 3 mb, 6 mb and 10 mb cross sections. The model therefore provides a convenient way to investigate expectations for a variety of observables with and without a QGP phase.

8.2 Pseudorapidity Distributions - Data and AMPT

Pseudorapidity distributions of charged particles have been reported by fixed target as well as collider experiments. In this article, we concentrate on the results of collider experiments at

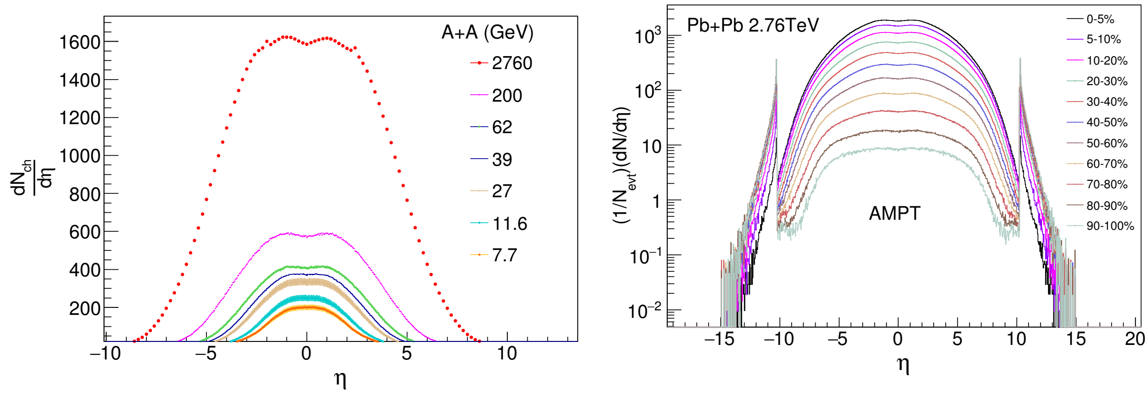

Figure 8.2: left: Beam energy dependence of charged particle pseudorapidity distributions, right: Centrality dependence of charged particle pseudorapidity distributions for $\sqrt{s_{NN}}$ = 2.76TeV, from the string melting mode of AMPT model.

RHIC and LHC. In Fig. 8.3, we present the experimental results from the PHOBOS experiment (14) at RHIC for central Au+Au collisions at $\sqrt{s_{NN}}$ = 19.6, 62.4 and 200 GeV, and from the ALICE experiment (16) at LHC for Pb+Pb collisions at $\sqrt{s_{NN}}$ = 2.76 TeV. It is observed that the distributions are symmetric around the mid-rapidity as they should be, but the dip structure at $\eta = 0$ gets more prominent with the increase of collision energy. For the LHC energy, the dip increases in going from peripheral to central collisions. The magnitude of the dip depends on the particle composition of the charged particles as the dip is more prominent for heavier particles like protons and anti-protons compared to pions.

In the present study, we have generated AMPT events with SM mode for different collision energies and collision centralities. The total parton elastic scattering cross section from 7.7 GeV to 200 GeV at RHIC energies is taken as σ_{gg} = 10 mb and for 2.76 TeV at LHC energy, it is chosen to be 1.5 mb. It is observed that with these settings AMPT can describe the data for transverse momentum spectra and flow (30). The results of AMPT model calculations for η-distributions are superimposed on Fig. 8.3. The AMPT distributions describe the data at RHIC energy well. For $\sqrt{s_{NN}}$ = 2.76 TeV, the data at mid-rapidity are well described by AMPT, but discrepancies are observed at other η-ranges especially at the peaks.

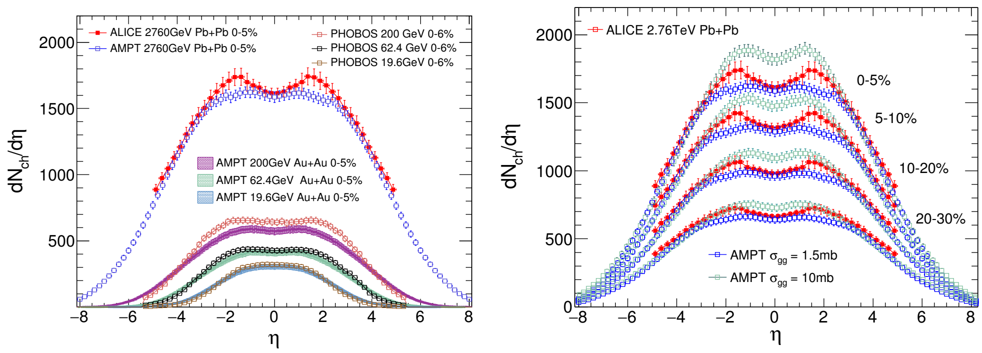

Figure 8.3: Left: Beam energy dependence of charged particle pseudorapidity distributions. Results from PHOBOS (14) and ALICE (16; 17) for central collisions are shown along with calculations from the string melting mode of AMPT model.
Right:Centrality dependence of η-distributions for Pb+Pb collisions at $\sqrt{s_{NN}}$ = 2.76 TeV with the data from ALICE experiment (16; 17) and those from the AMPT model for two settings of total parton scattering cross section (σ_{gg}).

In Fig. 8.3 (right) we show the η-distributions for LHC data at $\sqrt{s_{NN}}$ = 2.76 TeV for four centralities along with AMPT model data for two different parton scattering cross sections (1.5 mb and 10 mb). It is seen that the AMPT distributions with 1.5 mb matches the mid-rapidity value quite well. The distributions with 10 mb, match the shape of the data distribution very well, but miss the value at mid-rapidity. For further calculations in case of LHC energies, the parton cross section is kept at 1.5 mb.

8.3 Shapes of pseudorapidity distributions

A further study has been performed to investigate the centrality-wise variation of shape of the η-distributions for heavy-ion collisions, ranging from 7.7 GeV to 2.76 TeV. For central Au+Au collisions at RHIC energies, the distributions can be fitted by (32):

$$\frac{dN_{ch}}{d\eta} = \frac{c\sqrt{1 - 1/(\alpha \cosh \eta)^2}}{1 + e^{(|\eta| - \beta)/a}}, \tag{8.3}$$

where a, c, α, and β are fit parameters. As seen from Figures 8.3(left) and 8.3(right), at higher energies, the η-distributions exhibit double Gaussian nature, which can be fit using the form (16;

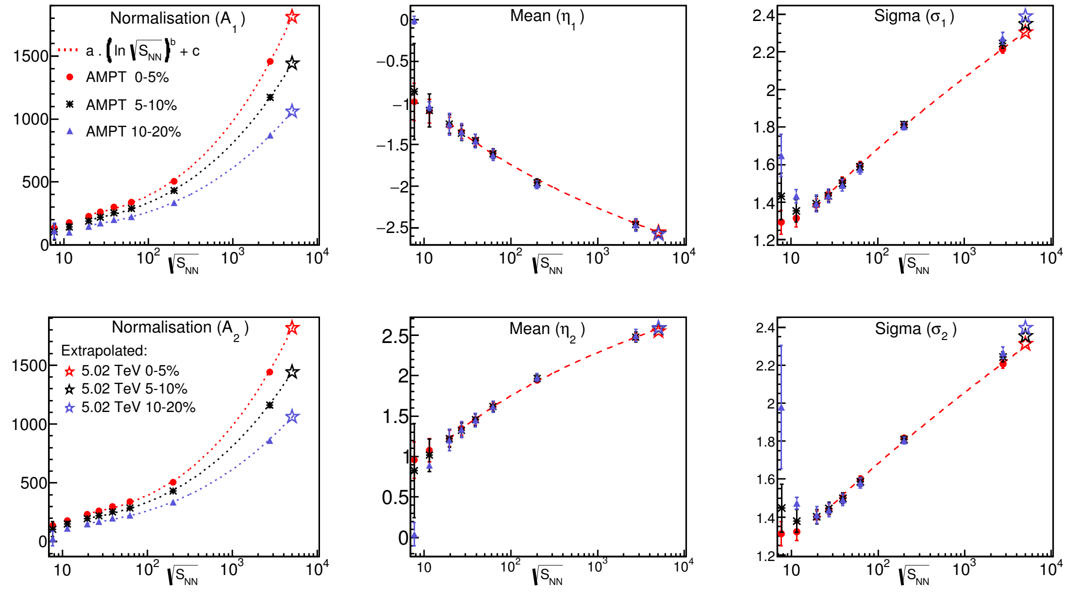

Figure 8.4: Fit parameters of the double Gaussian fit to the η-distributions obtained from the AMPT model for Au+Au collisions from $\sqrt{s_{NN}}$ = 7.7 GeV to 200 GeV and Pb+Pb collision at $\sqrt{s_{NN}}$ = 2.76 TeV. Extrapolated values of the parameters for $\sqrt{s_{NN}}$ = 5.02 TeV are also plotted in the figures.

17),

$$A_1 e^{-(\eta^2/2\sigma_1^2)} - A_2 e^{-(\eta^2/2\sigma_2^2)}, \tag{8.4}$$

where A_1, A_2 are the amplitudes and σ_1, σ_2 are the widths of the distributions. This expression gives the difference of two Gaussians centered at $\eta = 0$.

The η-distributions obtained from the AMPT model for all the energies describe the data reasonably well. The distributions are fitted with a double Gaussian function and the parameters are extracted. The Gaussian parameters are presented in Fig. 8.4, as a function of collision energy. The parameters are shown for three centralities for clarity of presentation. Results for other centralities show similar trends. The figures reveal the following trends:

(i) the normalization parameters, A_1 and A_2 increase with the increase of beam energy as per expectation,

Table 8.1: Parameters of Double Gaussian fits to the η-distributions of Au+Au collisions from $\sqrt{s_{NN}}$ = 7.7 GeV to 200 GeV, and Pb+Pb collisions at 2.76 TeV. Extrapolated parameters for $\sqrt{s_{NN}}$ = 5.02 TeV are presented.

$\sqrt{s_{NN}}$ (GeV)	Centrality (%)	A_1	η_1	σ_1	A_2	η_2	σ_2
7.7	0-5	134.93	-0.987	1.294	139.120	0.225	1.312
	5-10	102.46	-0.862	1.432	106.84	0.825	1.446
	10-20	112.36	-0.004	1.648	26.63	0.042	1.980
11.5	0-5	178.72	-1.097	1.314	180.78	0.143	1.323
	5-10	142.25	-1.091	1.354	150.42	1.016	1.380
	10-20	100.56	-1.037	1.433	114.22	0.892	1.473
19.6	0-5	226.70	-1.269	1.383	232.85	1.223	1.399
	5-10	190.92	-1.255	1.392	194.42	1.224	1.402
	10-20	147.38	-1.254	1.393	151.82	1.203	1.411
27	0-5	260.45	-1.344	1.441	260.59	1.345	1.441
	5-10	218.19	-1.361	1.433	221.92	1.326	1.446
	10-20	171.77	-1.346	1.432	172.96	1.333	1.437
39	0-5	299.95	-1.444	1.508	297.48	1.457	1.502
	5-10	254.58	-1.450	1.501	253.57	1.455	1.499
	10-20	199.13	-1.455	1.490	199.39	1.450	1.490
62.4	0-5	341.36	-1.605	1.595	340.53	1.670	1.594
	5-10	288.93	-1.608	1.589	287.59	1.619	1.587
	10-20	225.61	-1.625	1.576	225.71	1.615	1.580
200	0-5	507.18	-1.947	1.812	506.93	1.940	1.816
	5-10	430.61	-1.958	1.813	429.01	1.965	1.809
	10-20	334.48	-1.982	1.804	334.30	1.979	1.803
2760	0-5	1458.69	-2.442	2.215	1439.93	2.471	2.207
	5-10	1174.33	-2.462	2.245	1159.96	2.475	2.244
	10-20	872.77	-2.465	2.274	859.07	2.493	2.266
5020	0-5	1814.52	-2.554	2.304	1815.19	2.549	2.311
(extrapolated)	5-10	1441.13	-2.573	2.348	1442.23	2.579	2.352
	10-20	1059.63	-2.575	2.389	1061.73	2.585	2.395

(ii) the mean values, η_1 and η_2, represent the peak positions in the η distribution. The values of η_1 and η_2 show opposite trends with the increase of the beam energy. This means that the peak positions in η spread out more with the increase of beam energy,
(iii) the widths (σ_1 and σ_2) of the η-distributions increase as a function of beam energy.
The parameter sets provide a way to compute the η-distribution at any collision energy and centrality. In Fig. 8.4, the fit parameters are extended up to higher energy, *viz.*, $\sqrt{s_{NN}} = 5.02$ TeV. The fit parameters, along with the extrapolated values for $\sqrt{s_{NN}} = 5.02$ TeV are given in Table 8.1.

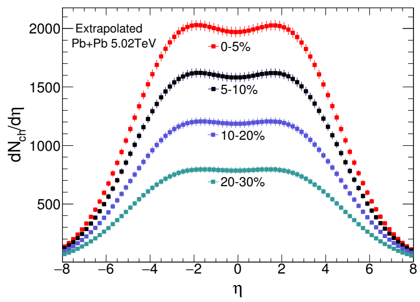

Figure 8.5: η-distributions for Pb+Pb collisions at $\sqrt{s_{NN}} = 5.02$ TeV for different centralities. The distributions are obtained from the extrapolated AMPT parameters from lower energies.

With the extrapolated parameter set for Pb+Pb collisions at $\sqrt{s_{NN}} = 5.02$ TeV, we can obtain the η-distributions at different collision energies. The results are shown in Fig. 8.5, which could be verified once the LHC results are published.

8.4 Energy dependence of global parameters

Parameterisation of η-distributions of charged particles from the AMPT model can be used to obtain energy dependence of other related global observables. Here we discuss the collision energy dependence of charged particle multiplicity density at mid-rapidity, centrality dependence of charged particle multiplicity density for LHC energies and the collision energy dependence of Bjorken energy density.

The quantity, $\frac{2}{\langle N_{\rm part}\rangle}(dN_{\rm ch}/d\eta)$, gives the charged particle multiplicity density at η=0 scaled

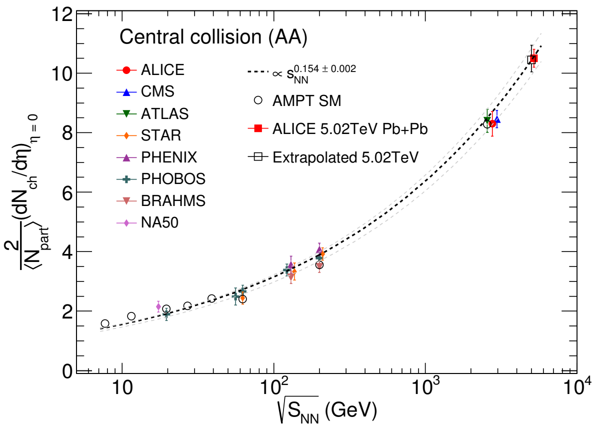

Figure 8.6: Pseudorapidity density of charged particles, normalized to number of participant pairs ($\frac{2}{\langle N_{\rm part}\rangle}(dN_{\rm ch}/d\eta)$), plotted as a function of collision energy for central Au+Au or Pb+Pb collisions from experimental data and AMPT model. Some of the data points are shifted along x-axis for clarity of presentation.

by the average number of participant pairs ($\langle N_{\rm part}\rangle/2$). Figure 8.6 shows the variation of this quantity as a function of $\sqrt{s_{NN}}$ for central (top 5% cross section) collisions. The plot shows an increase in the multiplicity density with the increase of the collision energy. The data points are taken from PHOBOS, BRAHMS, STAR, and PHENIX experiments of RHIC and ALICE, CMS and ATLAS experiment at LHC. The results from AMPT model are shown by solid red points. For Pb+Pb data at 5.02 TeV, the extrapolated results from Fig. 8.5 have been plotted. The AMPT results explain the data quite well. A power law fit to the AMPT model data gives the fit value as $(0.77\pm0.04)\times s_{\rm NN}^{0.154\pm0.002}$. This matches the fit given in Ref. (21). As shown in the figure, the extrapolated value at $\sqrt{s_{NN}}$ = 5.02 TeV is close to the recently published data from the ALICE experiment (21). The beam energy dependence of charged particle multiplicity density has been studied for other centralities. Power law fit to each of the curves give the $s_{\rm NN}$ dependence as $s_{\rm NN}^{0.154}$ to $s_{\rm NN}^{0.109}$ from top central (0-5%) to peripheral (70-80%) collisions. This is consistent with the conclusion that the particle multiplicity increases faster for central collisions compared to peripheral collisions.

The centrality dependences of charged particle multiplicity density have been reported for Pb+Pb collisions at $\sqrt{s_{NN}}$ = 2.76 TeV (16) and 5.02 TeV (21). As discussed earlier, the

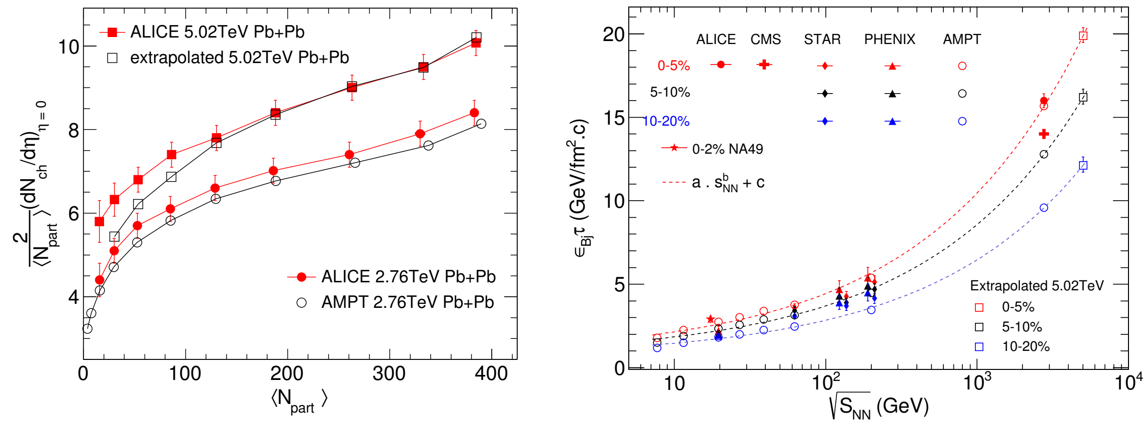

Figure 8.7: Left side: Centrality dependence of $\frac{2}{\langle N_{\rm part}\rangle}(dN_{\rm ch}/d\eta)$ for Pb+Pb collisions at $\sqrt{s_{NN}}$ = 2.76 and 5.02 TeV. AMPT model calculations for $\sqrt{s_{NN}}$ = 2.76 TeV and extrapolations for $\sqrt{s_{NN}}$ = 5.02 TeV reasonably explain the ALICE data (16; 21). Right Side: Energy density () as a function of $\sqrt{s_{NN}}$ for experimental data (15; 31; 32; 33; 34; 35; 36; 37; 38) and AMPT model, shown for three centralities. Power law fits to the results from AMPT model are extrapolated to $\sqrt{s_{NN}}$ = 5.02 TeV. Some of the data points are shifted along x-axis for clarity of presentation.

AMPT model calculations describe the data well at $\sqrt{s_{NN}}$ = 2.76 TeV. By extrapolating the fit parameters from the AMPT model to higher energies of $\sqrt{s_{NN}}$ = 5.02 TeV, we obtain the centrality dependence of charged particle multiplicity density at this energy. For central (0-5%) collisions, the multiplicity density comes out to be 1964 ± 30. The results from the experimental data and AMPT calculations for both $\sqrt{s_{NN}}$ = 2.76 and 5.02 TeV are shown in Fig. 8.4. The AMPT model results and extrapolations explain the ALICE data reasonably well.

The data on the charged particle multiplicity density is used to get an estimation of the initial energy density, an important quantity governing the evolution of the fireball. The Bjorken estimation of the initial energy density (13) is given as:

$$\epsilon_{\rm Bj} = \frac{1}{\pi R^2 \tau}\frac{dE_{\rm T}}{dy}, \tag{8.5}$$

where τ is the formation time, πR^2 is the effective area of the fireball or the oeverlap area of the colliding nuclei, and $dE_{\rm T}$ is the total initial energy within a rapidity window dy, which can

Table 8.2: Fit parameters of fitting function for energy density for three centralities. The last column gives the values of $\epsilon_{\mathrm{Bj}}\tau$ for $\sqrt{s_{NN}}$ = 5.02 TeV in GeV/fm^{2}c.

Cent. (%)	a	b	c	$\epsilon_{\mathrm{Bj}}\,\tau$ (GeV/fm^{2}c) (5.02 TeV)
0-5	0.44±0.12	0.221±0.015	0.97±0.32	19.98
5-10	0.39±0.11	0.216±0.016	0.81±0.29	16.28
10-20	0.32±0.10	0.209±0.017	0.61±0.25	11.88

be approximated as (15):

$$\frac{dE_{\mathrm{T}}}{dy} \approx \frac{3}{2}\left(\langle m_{\mathrm{T}}\rangle \frac{dN}{dy}\right)_{\pi^{\pm}} + 2\left(\langle m_{\mathrm{T}}\rangle \frac{dN}{dy}\right)_{K^{\pm},p,\bar{p}}. \tag{8.6}$$

$\langle m_{\mathrm{T}}\rangle$ is the mean transverse mass of identified particles ($\pi^{\pm}$, $K^{\pm}$, p or $\bar{p}$). The value of τ is typically taken as 1 fm. But in the absence of experimental knowledge of τ, the energy density is expressed in terms of . In Fig. 8.4, we present as a function of $\sqrt{s_{NN}}$ for three centralities. Experimental results from NA49 (31), STAR (15; 33), PHENIX (32; 34; 35), ALICE (36; 37) and CMS (38) are presented. Results at corresponding energies from the AMPT model are superimposed. It is observed that the AMPT results reasonably describe the experimental data.

The AMPT results of are fitted by power law for the three centralities. The fit parameters are shown in Table 8.2. We extrapolate these fits to $\sqrt{s_{NN}}$ = 5.02 TeV to obtain the values of , shown in the table. The variation of as a function of $\sqrt{s_{NN}}$ for all centralities has been studied. Fitting each of these distributions using power law, gives the value of the exponent, which vary from $s_{\mathrm{NN}}^{0.22}$ to $s_{\mathrm{NN}}^{0.10}$ for central (0-5%) to peripheral (70-80%) collisions, respectively. is a combination of $dN_{\mathrm{ch}}/d\eta$ and $\langle m_{\mathrm{T}}\rangle$, both of which vary as power law with respect to collision energy. That may explain the origin of the power law behaviour of energy density. As a function of collision energy, the energy density increases much faster for central collisions compared to peripheral collisions.

8.5 outlook for pseudorapidity distribution study

We have studied the η-distributions of produced charged particles for Au+Au collisions at $\sqrt{s_{NN}}$ = 7.7 to 200 GeV, corresponding to the collisions at RHIC and for Pb+Pb collisions at $\sqrt{s_{NN}}$ = 2.76 TeV, corresponding to the collisions at LHC. We have employed the string melting mode of the AMPT model to describe the experimental data. We observe that using the total parton elastic cross section, $\sigma_{gg} = 10$ mb, the AMPT model can explain the RHIC data, whereas $\sigma_{gg} = 1.5$ mb is needed for explaining the data at LHC. AMPT model, with these settings are used to further study the η-distributions and initial energy densities. The shapes of the η-distributions could be explained by using double Gaussian functions with a set of parameters comprising of the amplitude, the position of the peaks in η, and the widths of the distributions. As expected, with the increase of the beam energy, the amplitudes increase, the peak positions move farther apart, and the widths of the distributions increase. The parameters are fitted well by power law fits, using which the pseudorapidity distributions can be obtained for any beam energy and collision centrality. We obtain initial energy density as a function of collision energy and collision centrality using Bjorken formalism. Power law fits to the multiplicity density at mid-rapidity give the $s_{\rm NN}$ dependence as $s_{\rm NN}^{0.154}$ to $s_{\rm NN}^{0.109}$ from top central (0-5%) to peripheral (70-80%) collisions. Similarly, power law fits to the energy density yield the $s_{\rm NN}$ dependence as $s_{\rm NN}^{0.22}$ to $s_{\rm NN}^{0.10}$ for the same centrality ranges. As a function of collision energy, the particle multiplicity and energy density increase much faster for central collisions compared to the peripheral collisions. Extrapolating the parameters to collisions at $\sqrt{s_{NN}}$ = 5.02 TeV, we are able to explain the recently published results on centrality dependence of charged particle multiplicity and energy density. At this energy, the pseudorapidity density of charged particles for central (0-5%) collisions is 1964 ± 30 and energy density, is 19.98 GeV/fm^{2}c. Furthermore, we note that the results obtained in the present study can be interpolated for intermediate energies to obtain η-distributions and energy densities for heavy-ion collisions in the Facility for Antiproton and Ion Research (FAIR). For laboratory energy of 11 GeV at FAIR, the energy density would be 1.8 GeV/fm^3 for $\tau = 1$ fm, which is an interesting region to study the deconfined matter at high net-baryon density.

8.6 Anisotropic higher harmonics of flow co-efficients: Elliptic(v2) and Triangular(v3) flow

Ultrarelativistic heavy-ion collisions enable the study of matter at high temperature and pressure where quantum chromodynamics predicts the existence of the quark-gluon plasma (QGP) (40), a state of matter where quarks and gluons move freely over distances that are large in comparison to the typical size of a hadron. Anisitropic flow, which is caused by the initial asymmetries in the geometry of the system produced in a non-central collision, provides experimental information about the equation of state and the transport properties of the created QGP (41; 42). Since the transition from normal nuclear matter to the QGP state is expected to occur at extreme values of energy density, elliptic flow has been intensively investigated in some large heavy ion experimental accelerators like Alternating Gradient Synchrotron(AGS) (43), Relativistic Heavy Ion Collider(RHIC) (44; 45), and Large Hadron Collider(LHC) (46; 47; 48; 49), which lately injected Pb+Pb $\sqrt{s_{NN}}$=5.02 TeV beam energy. From the previous studies, azimuthal anisotropy of particle production have contributed significantly to the c haracterization of the system created in heavy-ion collisions because it is sensitive to the properties of the system at an early time of its evolution. We compare th e AMPT string melting simulate results with the STAR and ALICE published data, and try to investigate the azimuthal distribution of particles production for different dependencies with increasing beam energies.

Anisotropic Flow is characterized by coefficients in the Fourier expansion of the azimuthal dependence of the invariant yield of particles relative to the reaction plane (50; 51):

$$E\frac{d^3N}{d^3p} = \frac{d^2N}{2\pi p_T dp_T dy}\left\{1 + \sum_{n=1}^{\infty} 2v_n \cos\left[n(\phi - \Psi_R)\right]\right\} \tag{8.7}$$

Here $v_n = \langle \cos\left[n\left(\phi - \Psi_R\right)\right]\rangle$ are coefficients to quantify anisotropic flow. The first coefficient, v_1, is usually called directed flow, and the second coefficient, v_2, is called elliptic flow. In this analysis, we use Q-cumulant method to obtain the anisotropic flow coefficients. Multi-particle correlations can be expressed in terms of flow vector Q_n:

$$Q_n \equiv \sum_{i=1}^{M} e^{in\phi_i} \tag{8.8}$$

where M is the number of particles. Then 2-particle and 4-particle azimuthal correlations in one event can be expressed as (52; 53):

$$\langle 2\rangle = \frac{\left|Q_n\right|^2 - M}{M\left(M-1\right)} \tag{8.9}$$

$$\langle 4\rangle = \frac{\left|Q_n\right|^4 + \left|Q_{2n}\right|^2 - 2\cdot \mathrm{Re}\left[Q_{2n}Q_n^*Q_n^*\right]}{M\left(M-1\right)\left(M-2\right)\left(M-3\right)} \tag{8.10}$$

$$-2\frac{2\left(M-2\right)\cdot\left|Q_n\right|^2 - M\left(M-3\right)}{M\left(M-1\right)\left(M-2\right)\left(M-3\right)} \tag{8.11}$$

For detectors with uniform acceptance, the 2^{nd} order cumulant and 4^{th} order cumulant are obtained with:

$$c_n\left\{2\right\} = \langle\langle 2\rangle\rangle \tag{8.12}$$

$$c_n\left\{4\right\} = \langle\langle 4\rangle\rangle - 2\cdot\langle\langle 2\rangle\rangle^2 \tag{8.13}$$

Reference flow v_n estimated from the 2^{nd} order cumulant and 4^{th} order cumulant are:

$$v_n\left\{2\right\} = \sqrt{c_n\left\{2\right\}} \tag{8.14}$$

$$v_n\{4\} = \sqrt[4]{-c_n\{4\}} \tag{8.15}$$

In this analysis, we use the events simulated from a multiphase transport(AMPT) model (55) to obtain anisotropic flow coefficient. The AMPT model is constructed to describe nuclear collisions ranging from p+A to A+A systems at center-of-mass energies from about $\sqrt{s_{NN}} = 5$ GeV up to 5500 GeV at LHC, where strings and minijets dominate the initial energy production and effects from final-state interactions are important. It consists of four main components: the initial conditions, partonic interactions, the conversion from the partonic to the hadronic matter, and hadronic interactions. The initial conditions are generated by the heavy-ion jet interaction generator (HIJING) model, the strings are converted into partons and the next stage, which models the interactions between all the partons, is based on ZPC(Zhang's parton cascade (56)). In ZPC, the default value of the cross section is 3 mb. The transition from partonic to hadronic matter is modeled by a simple coalescence model, which combines two quarks into mesons and three quarks into baryons. And the dynamics of the subsequent hadronic matter is described by a hadronic cascade, which is based on the ART model.

In the kinetic theory, the shear viscosity is given by Ref (39).

$$\eta_s = \frac{4 < p >}{15\sigma_t} \tag{8.16}$$

where $\langle p \rangle$ is mean momentum of partons and $_{tr}$ is the viscosity cross section and is defined as

$$\sigma_t = \int dt \frac{d\sigma}{dt}(1 - cos^2\theta) \tag{8.17}$$

where t is the standard Mandelstam variable for four-momentum transfer and

$$\frac{d\sigma}{dt} \approx \frac{9\pi\alpha_s^2}{[2(t-\mu^2)^2]} \tag{8.18}$$

is the differential cross section used in the AMPT model. By assumming that the partonic matter only consists of non-interacting massless up and down quarks as in the AMPT model, we have $< p > = 3$T and the entropy density s = (ϵ+ P)/T = $4\epsilon/3$T = $96T^3/\pi^2$ with T being the temperature of the partonic matter. The specific viscocity, i.e. the ratio between the shear viscosity and the entropy density is given by

$$\eta_s/s \approx \frac{3\pi}{40\alpha_s^2} \frac{1}{(9 + \frac{\mu^2}{T^2}) ln(\frac{18+\mu^2/T^2}{\mu^2/T^2})} \tag{8.19}$$

where μ is the screening mass of a gluon in the QGP and α_s is the QCD coupling constant. Both are input parameters for the AMPT model. In Ref. (73), it is shown that parameter set B ($\mu = 3.2$ fm^{-1} and $\alpha_s = 0.33$) provides a good description of the v_2 and v_3 data at $\sqrt{s_{NN}} =$ 200 GeV and 2.76 TeV. These parameters and equation 8.19 then yield the $\eta_s/s(T)$ as shown in figure 8.8 with the label Set B. For the estimated initial temperatures (378 MeV) at top RHIC energy, η_s/s=0.38, far above the ADS/CFT or quantum lower bound of $1/4\pi$ (87; 88) and also above most estimates from hydrodynamic models. The AMPT model provides two modes: Default and String Melting (74). AMPT in default mode is essentially a string and minijets model (without a QGP phase) where initial strings and minijets are produced with the HIJING event generator (75) as discussed earlier in this chapter.

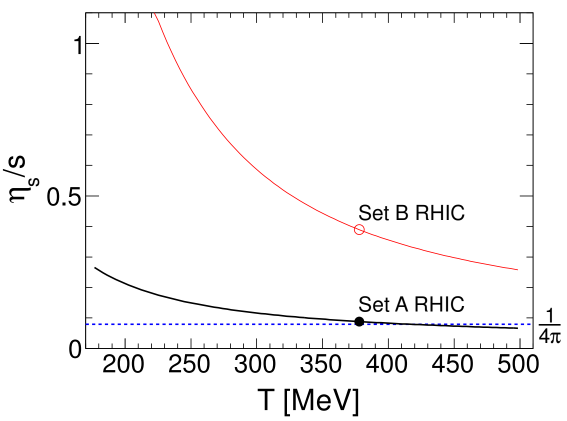

Figure 8.8: The temperature dependence of η_s/s according to eq. 8.19 for two parameter sets.

Several parameters need to be specified in the model including parameters a and b for Lund string fragmentation, the QCD coupling constant α_s (which the model treats as a constant), and the screening mass for gluons in the QGP phase μ. A recent study found that a good description of the multiplicity density, v_2 and v_3 could be achieved with the parameter set: a=0.5, b=0.9 (GeV^{-2}), α_s=0.33 and μ=3.2 (fm^{-1}) (73). In this study, we found that we can acheive a good desciption of the multiplicity density at all energies from $\sqrt{s_{NN}}$= 7.7 GeV to 2.76 TeV by using parameter set: a=2.2, b=0.5 (GeV^{-2}), α_s=0.47 and μ=1.8 (fm^{-1}) and turning off initial and final state radiation in HIJING. In this case, the initial cutoff for minijets p_0 does not need to be adjusted with $\sqrt{s}$ in order to match the LHC multiplicity densities (76). We leave p_0 and all other parameters fixed for all energies. Figure 8.9 shows the charged particle multiplicity density scaled by $N_{\mathrm{part}}/2$ for 0-5% central Au+Au or Pb+Pb collisions from AMPT String Melting and Default vs $\sqrt{s_{NN}}$. The line shows the parameterization of the experimental data from Ref. (77). Both the SM and Default calculations are in good agreement with the experimental data throughout the entire energy range.

AMPT SM and Default calculations for v_2 and v_3 has been done as a part of thesis work and to understand the various effects of anisotropy. The primary purpose of these calculations is to provide a reference for measurements of the beam energy dependence of v_2 and v_3. We found that we can describe RHIC and LHC data on multiplicity, v_2 and v_3 by turning off initial and final state radiation in HIJING (reducing the initial entropy) but keeping relatively large cross-sections in the QGP phase. These settings give a good description of event multiplicities from $\sqrt{s_{NN}}$ =7.7 GeV up to 2.76 TeV. Whereas a previous study found a good description of data using a much smaller cross-section implying a much larger value for η_s/s, our studies with a larger cross-section implies a ratio of viscosity to entropy much closer to the ADS/CFT conjectured lower bound. We have also studied how $v_2(p_T)$ changes from 7.7 GeV to 2.76 TeV. We find that within this model, $v_2(p_T)$ changes very little across the whole energy range studied, consistent with what is observed in data. We also find that AMPT reproduces the experimental observation that $v_3/\varepsilon_3 \propto \sqrt{N_{\mathrm{part}}}$. These experimental observations therefore seem to be understandable without major changes to our description of heavy ion collisions and a subsequentx nearly perfect liquid QGP phase. Our studies of the centrality and beam energy dependence of v_2 and v_3 with SM and Default settings provide a comparitive base-line for studies of v_2 and v_3 in the RHIC beam energy scan. In this study, we have used parameter set A ($\mu = 1.8$ fm^{-1} and $\alpha_s = 0.47$) corresponding to a larger partonic scattering cross section of 10 mb rather than 1.5 mb for set B. We find a good description of the data with set A by turning of initial and final state radiation in HIJING. This reduces the initial entropy production and multiplicity but in a way that matches the multiplicity at all the energies studied without varying any other parameters. The smaller initial multiplicity compensates for the larger cross sections so that the data are still well described. The $\eta_s/s(T)$ estimated from this parameter set is labeled Set A in figure 8.8. For set A, η_s/s at 378 MeV is 0.088 which is very close to the ADS/CFT conjectured lower bound. We conclude therefore that the AMPT model can give a good description of the v_2 and v_3 data with a wide range of η_s/s values and that it's crucial to understand the initial entropy production in order to extract the correct value of η_s/s in the QGP phase.

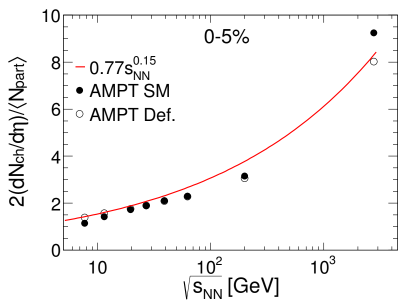

Figure 8.9: The charged particle multiplicity density scaled by $N_{\text{part}}/2$ in the AMPT model for String Melting and Default modes. The red line shows the parameterization of experimental data presented in Ref (77).

The motivation for colliding heavy ions at facilities like the Relativistic Heavy Ion Collider (RHIC) at Brookhaven National Laboratory and the Large Hadron Collider (LHC) at CERN is to form a state of matter called the Quark Gluon Plasma (QGP) (59). Each of these collisions creates a region so hot and dense that quarks and gluons become the relevant degrees of freedom instead of hadrons (60). Studying the conversion of coordinate space anisotropies into momentum space anisotropies gives insight into the nature of the matter created in these collisions (61). For decades, elliptic flow ($v_2 = \langle \cos 2(\phi - \Psi_{\mathrm{RP}}) \rangle$) has been studied to probe the conversion of the elliptic shape of the initial overlap zone into azimuthal anisotropy in momentum space (62) over a broad range of colliding beam energies. Measuring the strength of that conversion as a function of beam energy to search for evidence of the onset of deconfinement or a softening of the equation-of-state is one of the goals of the RHIC Beam Energy Scan program. In 2007 Mishra et. al. (63) proposed the analysis of v_n^2 for all values of n and argued that density inhomogeneities in the initial state would lead to non-zero v_n^2 values for higher harmonics including v_3. Although they proposed that v_n vs. n could be used to search for superhorizon fluctuations, it was later noted that higher harmonics of v_n would be washed out by viscous effects and that the shape of v_n vs. n would provide a valuable tool for studying η/s (64). It was also subsequently pointed out that information on v_n^2 was to a large extent contained within already existing two-particle correlations data (65), and that v_n and v_n fluctuations would provide a natural explanation for the novel features seen in those correlations, such as the ridge like (66) and mach-cone like (67) structures. That the ridge could be related to flux-tube like structures in the initial state was already argued by Voloshin in 2006 (68). Calculations carried out within the NEXSPHERIO model showed that in a hydrodynamic model fluctuations in the initial conditions lead to a near-side ridge correlation and a mach-cone like structure on the away-side (69). In 2010, Alver and Roland used a generalization of participant eccentricity ($\varepsilon_{n,\mathrm{part}}$) to arbitrary values of n as in Ref. (70) and showed that within the AMPT model, the final momentum space anisotropy for v_3 was proportional to the initial $\varepsilon_{3,\mathrm{part}}$ (71).

This explained the previous observation that the AMPT model produced correlations similar to those seen in the data (albeit with smaller amplitudes) (72). Later studies showed that with changes to the input parameters, AMPT could quantitatively describe the centrality dependence of v_2 and v_3 at 200 GeV and 2.76 TeV (73).

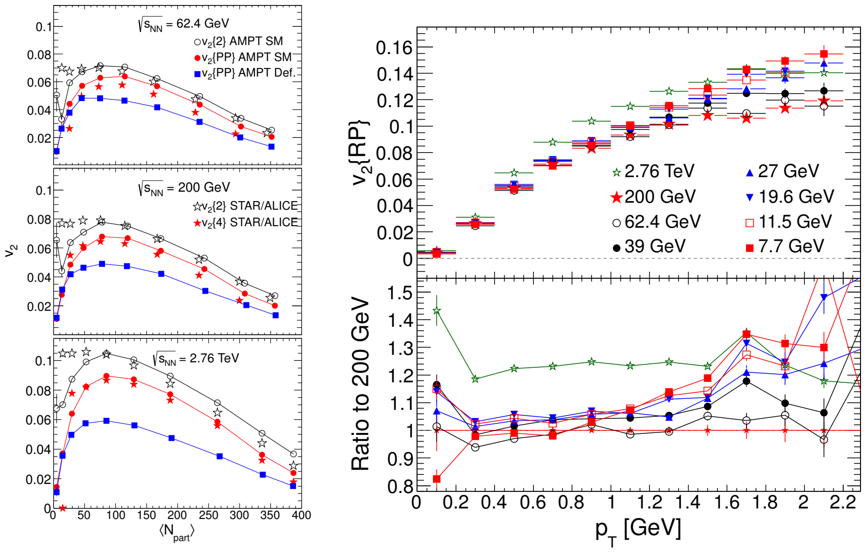

Figure 8.10: Elliptic flow data from AMPT and experiments at $\sqrt{s_{NN}}$=62.4 GeV, 200 GeV [STAR], and 2.76 TeV [ALICE]. For the String Melting calculation we show v_2 calculated relative to the participant plane $v_2\{\mathrm{PP}\}$ defined by the positions of the nucleons and using the two particle cumulant $v_2\{2\} = \langle \cos 2(\phi_i - \phi_j) \rangle$. Experimental results are shown for the two-particle $v_2\{2\}$ and four-particle $v_2\{4\}$ cumulants.

In this section we use the AMPT model to study the beam energy dependence of v_2 and v_3. We study collisions ranging from $\sqrt{s_{NN}}$ = 7.7 GeV to 2.76 TeV. We compare AMPT in the string melting and the default setting.

In Figure 8.10, the AMPT model results are compared to experimental data at $\sqrt{s_{NN}}$ =62.4 GeV, 200 GeV, and 2.76 TeV. For the SM calculations, we show (i) v_2 relative to the participant plane ($v_2\{PP\}$) calculated from the initial conditions of AMPT and (ii) the two-particle cumulant results $v_2\{2\}$. While $v_2\{2\} = \sqrt{\langle v_2^2 \rangle} + \delta$ where δ is a term to account for correlations not related to the participant plane (non-flow), $v_2\{P.P.\}$ is the true mean v_2 relative to the participant plane. The difference between those results therefore reflects both the effect of fluctuations $\sqrt{\langle v_2^2 \rangle} - \langle v_2 \rangle^2$ and non-flow correlations present in the model. All the model calculations have a similar centrality dependence but the Default results are well below the SM results. The data generally agree well with the SM calculations. In the case that the v_2 fluctuations are dominated by eccentricity fluctuations and those eccentricity fluctuations follow a Gaussian distribution in

x and y, $v_2\{4\}$ should be equal to v_2 with respect to the reaction plane (78). The fact that the experimental $v_2\{4\}$ results are slightly below the model results calculated with respect to the participant plane does not therefore signify a discrepancy between data and model. We consider the agreement between the model and the data to be satisfactory.

STAR has shown that for $p_T < 1$ GeV, $v_2\{4\}(p_T)$ increases with $\sqrt{s_{NN}}$, for $p_T > 1$ GeV $v_2\{4\}(p_T)$ is roughly independent of collision energy in the range 7.7 GeV to 2.76 TeV (79). It is surprising for a measurement that is supposed to be sensitive to viscosity and collective effects in the expansion to not depend on $\sqrt{s_{NN}}$ over such a wide range of energies where the initial conditions and properties of the fireball should be changing quite significantly. Given this surprising experimental result, it is interesting to see if the same trend is reproduced in the AMPT model. In Figure 8.10, we show $v_2(p_T)$ calculated with respect to the reaction plane for collisions with center of mass energies ranging from 7.7 GeV to 2.76 TeV. Although the statistics in our study were not sufficient to calculate $v_2\{4\}(p_T)$, it has been shown that as long as v_2 fluctuations are dominated by eccentricity fluctuations and those eccentricity fluctuations are Gaussian distributed along the x and y axis, then $v_2\{4\}$ is equivalent to $v_2\{\mathrm{RP}\}$ (78). We therefore check to see if $v_2\{\mathrm{RP}\}(p_T)$ is independent of $\sqrt{s_{NN}}$ for $p_T > 1$ GeV in the AMPT model. We find that the variation of $v_2\{\mathrm{RP}\}$ is not large in AMPT throughout the energy range studied. For $p_T < 1$ GeV, $v_2\{\mathrm{RP}\}$ varies by about 5% from 7.7 GeV up to 200 GeV. Going from 200 GeV to 2.76 TeV, $v_2\{\mathrm{RP}\}$ increases by 20%, independent of p_T. In the RHIC range, the AMPT $v_2\{\mathrm{RP}\}$ results for $p_T > 1$ GeV are actually increasing as the energy is decreased with $v_2\{\mathrm{RP}\}$ at $p_T = 1.5$ GeV for 7.7 GeV being 20% larger than for 200 GeV. This likely reflects the softening of the spectrum which allows flow effects that push low momentum particles to higher momentum, to have a larger influence at intermediate p_T. The same trends hold when studying $v_2\{\mathrm{PP}\}(p_T)$ (not shown). Although there are differences between the trends seen in AMPT and in the data, one can conclude that even in the AMPT model, the changes in $v_2\{\mathrm{RP}\}(p_T)$ or $v_2\{\mathrm{PP}\}(p_T)$ when increasing $\sqrt{s_{NN}}$ from 7.7 GeV to 2.76 TeV are not large. In this case, it is not necessarily surprising that the data also does not change drastically. Since based on the AMPT model, we would not expect a large variation of $v_2\{\mathrm{RP}\}(p_T)$ with $\sqrt{s_{NN}}$, as long as one assumes that a string melting or QGP phase exists throughout the energy range under study, the fact that the data seem to change very little no longer appears to be so difficult to understand.

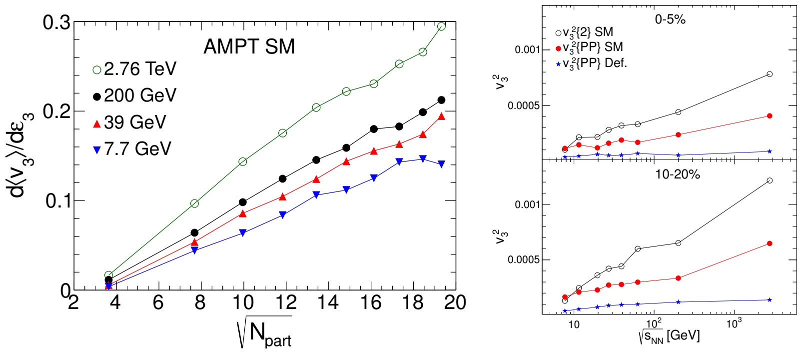

Figure 8.11: The slope of $\langle v_3 \rangle$ vs. ε_3 as a function of the square root of the number of participants for four different colliding energies.

8.7 The Third Harmonic

Having shown that our parameter selection provides a good description of the charged particle multiplicity densities and the elliptic flow, we now turn to investigate v_3 and its energy dependence. We first study the relationship of v_3 to the third harmonic participant eccentricity. In Ref. (71) the AMPT model is used to show that v_2 and v_3 have a linear dependendence on ε_2 and ε_3. At Quark Matter 2011, STAR showed that v_3/ε_3 scales with $1/\sqrt{N_{\mathrm{part}}}$ (80). Here we check to see if this phenomenological observation is also reproduced in the AMPT model.

In Figure 8.11 we investigate the dependence of the slope of $\langle v_3 \rangle$ vs. ε_3 on N_{part}. The figure shows $d\langle v_3 \rangle / d\varepsilon_3$ vs. $\sqrt{N_{\mathrm{part}}}$ for $\sqrt{s_{NN}}$ = 7.7 GeV, 39 GeV, 200 GeV, and 2.76 TeV. We find that for all the energies investigated (including those not shown in the figure), $d\langle v_3 \rangle / d\varepsilon_3$ increases linearly with $\sqrt{N_{\mathrm{part}}}$. The AMPT model therefore correctly describes the phenomenological observation made by STAR. This also indicates that according to the string melting version of AMPT, even at energies as low as $\sqrt{s_{NN}}$=7.7 GeV, v_3 reflects the fluctuations in the initial

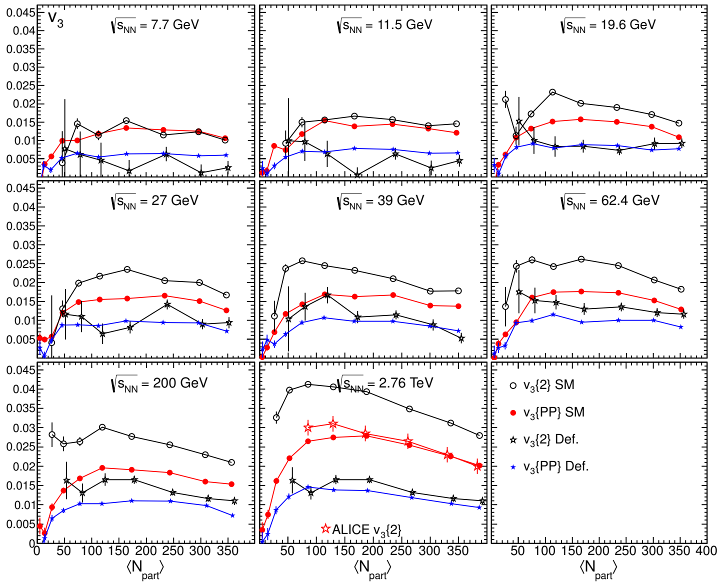

Figure 8.12: $v_3\{2\}$ and $v_3\{\mathrm{PP}\}$ from AMPT SM and Default calcualtions for $\sqrt{s_{NN}}$ = from 7.7 GeV to 2.76 TeV. Experimental results are shown at 2.76 TeV (82).

geometry of the collisions and that the centrality dependence will remain similar at all energies although the magnitude will change. At the lowest energies investigated here, the contributions from jets and minijets should be negligible so they will not contribute significantly to the centrality dependence of v_3. The experimental observation of a similar centrality dependence for v_3 at 7.7 and 200 GeV (80), therefore strongly contradicts assertions that v_3 is dominated by jet-like correlations (81).

In Figure 8.12, AMPT SM and Default calculations of $v_3\{2\}$ and $v_3\{\mathrm{PP}\}$ are shown for 7.7, 11.5, 19.6, 27, 39, 62.4, 200 GeV and 2.76 TeV. While $v_3\{\mathrm{PP}\}$ reflects the true correlation of particles with the initial participant plane, $v_3\{2\}$ includes non-flow and fluctuation effects. The difference between $v_3\{2\}$ and $v_3\{\mathrm{PP}\}$ is large at 200 and 39 GeV while at 7.7 GeV $v_3\{2\}$ and $v_3\{\mathrm{PP}\}$ are equivalent. This indicates that indeed, according to AMPT SM, non-flow does not make an appreciable contribution to $v_3\{2\}$ at 7.7 GeV. We compare the model results to ALICE data at 2.76 TeV and find that $v_3\{\mathrm{PP}\}$ for AMPT SM matches the ALICE data on $v_3\{2\}$. The $v_3\{2\}$ AMPT SM results over predict the ALICE data and the $v_3\{\mathrm{PP}\}$ AMPT Default results underpredict the ALICE data. The $v_3\{2\}$ Default results also underpredict the ALICE data for $N_{\text{part}} > 100$. The correspondence of $v_3\{\text{PP}\}$ from AMPT SM with $v_3\{2\}$ from ALICE data means that either non-flow and fluctuations are overpredicted in AMPT or v_3 is underpredicted. The 200 GeV data is also in good agreement with preliminary STAR data (80) (not shown) in the same centrality range. In more peripheral collisions, the STAR data in Ref. (80) tends to increase as seen with the AMPT $v_3\{2\}$ results. This suggests that while $v_3\{2\}$ measurements for $N_{\text{part}} > 100$ are dominated by the correlation of particles with the participant plane, in more peripheral collisions $v_3\{2\}$ begins to reflect correlations related to mini-jet structure similar to that in $p + p$ collisions.

In figure 8.11 we show the AMPT results for the variation of $v_3^2\{2\}$ and $v_3^2\{\text{PP}\}$ with $\sqrt{s_{NN}}$ from 7.7 GeV to 2.76 TeV for two centrality intervals. The results on $v_3^2\{\text{PP}\}$ using the default setting for AMPT are very small and well below the preliminary data presented by STAR. The $v_3^2\{\text{PP}\}$ SM results decrease rather smoothly with decreasing energy but still have an appreciable value down to 7.7 GeV. The calculations for $v_3^2\{2\}$ SM have the same value as the $v_3^2\{\text{PP}\}$ SM at 7.7 and 11.5 GeV. This again indicates that within this model, non-flow from minijets has a negligible impact on two-particle correlations at the lowest energies measured in the RHIC beam energy scan. Above those energies, the difference between $v_3^2\{2\}$ and $v_3^2\{\text{PP}\}$ grows substantially. It will be interesting to see if the experimental data on v_3 follows the same trend as AMPT SM all the way down to 7.7 GeV where non-flow from minijets can be neglected. It will be most interesting to see if data eventually drops down to the values predicted by the AMPT Default model. Estimates of the Bjorken energy density (83) compared to the Lattice QCD estimates for the critical energy density (84) suggest that this may not happen until below 7.7 GeV (85). The calculations presented here for higher harmonics of flow provide a base-line with which to compare future experimental data.

Bibliography

[1] J.W. Harris, B. Muller, Ann. Rev. Nucl. Part. Sci. **46**, 71 (1996).

[2] P. Braun-Munzinger and J. Stachel, Nature **448**, 302 (2007).

[3] A. Bazavov *et al.* Phys. Rev. **D90**, 094503 (2014).

[4] Y. Aoki *et al.* J. High Ene. Phys. **06**, 088 (2009).

[5] M.M. Aggarwal *et al.* (STAR Collaboration) arXiv:1007.2613 [nucl-ex].

[6] S. Ozonder, R.J. Fries, Phys. Rev. **C89**, 034902 (2014).

[7] J. Dias de Deus and R. Ugoccioni, Phys. Lett. **B494** 53 (2000).

[8] J. Zhi-jin and S. Yu-Fen, Chin. Phys. Lett. **29** 022502 (2012).

[9] L. Zhou and G. Stephans, Phys. Rev. **C90**, 014902 (2014).

[10] F.I. Shao, T. Yao and Q. Xie, Phys. Rev. **75**, 034904 (2007).

[11] M. Kliemant, R. Sahoo, T. Schuster and R. Stock, The Physics of the Quark-Gluon Plasma, Vol. 785 of the series Lecture Notes in Physics pp 23-103, Springer Publication.

[12] R. Sahoo, A.N. Mishra, N.K. Behera, B.K. Nandi, Adv. in High Ener. Phys., **2015** (2015).

[13] J.D. Bjorken, Phys. Rev. **D27**, 140 (1983).

[14] B. Alver *et al.* (PHOBOS Collaboration), Phys. Rev. **C83**, 024913 (2011).

[15] B.Abelev *et al.* (STAR Collaboration), Phys. Rev. C **79**, 034909 (2009).

[16] E. Abbas *et al.* (ALICE Collaboration), Phys. Lett. **B726**, 610 (2013).

[17] J. Adam *et al.* (ALICE Collaboration), arXiv:1509.07299 [nucl-ex].

[18] Y. Chen *et al.* (ATLAS Collaboration), J. Phys. **G38**, 124042 (2011).

[19] G. Aad *et al.* (ATLAS Collaboration), Phys. Lett. **B710**, 363 (2012).

[20] S. Chatrchyan *et al.* (CMS Collaboration), Jour. High Ene. Phys. **1108**, 141 (2011).

[21] J. Adam *et al.* (ALICE Collaboration), arXiv:1512.06104 [nucl-ex].

[22] Z.W. Lin, C.M. Ko, B.A. Li, B. Zhang, S. Pal, Phys. Rev. **C72**, 064901 (2005).

[23] Z.W. Lin, arXiv:1403.1854 [nucl-th].

[24] S. Pal and M. Bleicher, Phys. Lett. **B709**, 82 (2012).

[25] J. Xu and C.M. Ko, Phys. Rev. **C84**, 014903 (2011).

[26] X.-N. Wang, M. Gyulassy, Phys. Rev. **D44**, 3501 (1991).

[27] B. Li, A. T. Sustich, B. Zhang and C. M. Ko, Int. J. Mod. Phys. **E10**, 267 (2001)

[28] R.J. Fries, V. Greco, P. Sorensen, Ann. Rev. Nucl. Part. Sci. **58**, 177 (2008)

[29] R. J. Fries, B. Muller, C. Nonaka, S.A. Bass, Phys. Rev. Lett. **90**, 202303 (2003)

[30] D. Solanki, P. Sorensen, S. Basu, R. Raniwala, and T.K. Nayak, Phys. Lett. **B720**, 352 (2013).

[31] T. Alber *et al.*, Phys. Rev. Lett. **75**, 3814 (1995).

[32] K. Adcox *et al.* (PHENIX Collaboration), Phys. Rev. Lett. **87**, 052301 (2001).

[33] J. Adam *et al.* (STAR Collaboration), Phys. Rev. C **70**, 054907 (2004).

[34] S.S. Adler *et al.*, (PHENIX Collaboration), Phys. Rev. **C71**, 034908 (2005).

[35] J.T. Mitchell *et al.*, (PHENIX Collaboration), arXiv:1601.00904 [nucl-ex].

[36] C. Loizides *et al.* (ALICE Collaboration), Jour. Phys. **G38**, 124040 (2011).

[37] A. Toia *et al.* (ALICE Collaboration), Jour. Phys. **G38**, 124007 (2011).

[38] S. Chatrchyan *et al.* (CMS Collaboration), Phys. Rev. Lett. **109**, 152303 (2012).

[39] J. Xu and C.M. Ko, Phys. Rev. **C84**, 014903 (2011).

[40] S. A. Bass, M. Gyulassy, H. Stoecker and W. Greiner, J. Phys. G **25** R1 (1999)

[41] J. Barrette *et al.* (E877 Collaboration), Phys. Rev. C **55**:1420 (1997)

[42] Z. Xu, C. Greiner, and H. Stocker, Phys. Rev. Lett. **101**:082302 (2008)

[43] L. Adamczyk *et al.* (STAR Collaboration), Phys. Rev. C **88**:014902 (2013)

[44] B. I. Abelev *et al.* (STAR Collaboration), Phys. Rev. C **77**:054901 (2008)

[45] B. Abelev *et al.* (ALICE Collaboration), Physics Letters B **719**:18-28 (2013)

[46] S. Voloshin and Y. Zhang, Z. Phys. C **70**:665 (1996)

[47] K. Aamodt *et al.* (ALICE Collaboration), Phys. Rev. Lett. **105**:252302 (2010)

[48] K. Aamodt *et al.* (ALICE Collaboration), Phys. Rev. Lett. **107**:032301 (2011)

[49] J. Adam *et al.* (ALICE Collaboration), Phys. Rev. Lett. **116**:132302 (2016)

[50] K. Aamodt *et al.* (ALICE Collaboration), JINST **3**:S08002 (2008)

[51] A. M. Poskanzer and S. A. Voloshin, Phys. Rev. C **58**:1671 (1998)

[52] Ante Bilandzic, Raimond Snellings, and Sergei Voloshin, Phys. Rev. C **83**:044913 (2011)

[53] A. Bilandzic, C. H. Christensen, K. Gulbrandsen, A. Hansen and Y. Zhou, Phys. Rev. C **89**:064904 (2014)

[54] Y. Zhou, *Anisotropic Flow and Flow Fluctuations at the Large Hadron Collider*, Ph.D. Thesis(Netherlands: Utrecht University, 2015)

[55] You Zhou, Kai Xiao, Zhao Feng, Feng Liu, and Raimond Snellings, Phys. Rev. C **93**:034909 (2016)

[56] Zi-Wei Lin, Che Ming Ko, Bao-An Li, Bin Zhang, and Subrata Pal, Phys. Rev. C **72**:06490 (2005)

[57] B. Zhang, Comput. Phys. Commun. **109**:193 (1998)

[58] Guo-Liang Ma, and Zi-Wei Lin, Phys. Rev. C **93**:054911 (2016)

[59] W. Reisdorf and H. G. Ritter, Ann. Rev. Nucl. Part. Sci. **47**, 663 (1997); N. Herrmann, J. P. Wessels and T. Wienold, Ann. Rev. Nucl. Part. Sci. **49**, 581 (1999).

[60] Y. Aoki, G. Endrodi, Z. Fodor, S. D. Katz and K. K. Szabo, Nature **443**, 675 (2006). F. Karsch, PoS C **POD07** (2007) 026. PoS **LAT2007** (2007) 015.

[61] S. A. Voloshin, A. M. Poskanzer and R. Snellings, arXiv:0809.2949 [nucl-ex]; P. Sorensen, arXiv:0905.0174 [nucl-ex].

[62] J. Adams *et al.* [STAR Collaboration], Phys. Rev. C **72**, 014904 (2005); K. Aamodt *et al.* [The ALICE Collaboration], Phys. Rev. Lett. **105**, 252302 (2010).

[63] A. P. Mishra, R. K. Mohapatra, P. S. Saumia and A. M. Srivastava, Phys. Rev. C **77**, 064902 (2008) [arXiv:0711.1323 [hep-ph]].

[64] A. Mocsy and P. Sorensen, arXiv:1008.3381 [hep-ph]; [arXiv:1101.1926 [hep-ph]].

[65] P. Sorensen, arXiv:0808.0503 [nucl-ex].

[66] J. Adams et al. [STAR Collaboration] Phys. Rev. Lett. 95:152301, (2005); F. Wang [STAR Collaboration], J. Phys. G **30** (2004) S1299 [arXiv:nucl-ex/0404010]; J. Adams *et al.* [STAR Collaboration], Phys. Rev. C **73** (2006) 064907 [arXiv:nucl-ex/0411003]; J. Putschke, J. Phys. G **34** (2007) S679 [arXiv:nucl-ex/0701074]; J. Adams *et al.* [Star Collaboration], Phys. Rev. C **75** (2007) 034901 [arXiv:nucl-ex/0607003]; Brijesh Srivastava for the STAR Collaboration, Int. J. Mod. Phys. E16, 3371 (2008); Feb. 4th-10th, 2008, to be published in conference proceedings; A. Adare *et al.* [PHENIX Collaboration], Phys. Rev. C **78** (2008) 014901 [arXiv:0801.4545 [nucl-ex]]; B. Alver *et al.* [PHOBOS Collaboration], J. Phys. G **G35**, 104080 (2008).

[67] J. Adams *et al.* [STAR Collaboration], Phys. Rev. Lett. **95**, 152301 (2005) [nucl-ex/0501016].

[68] S. A. Voloshin, Nucl. Phys. A **749**, 287 (2005) [nucl-th/0410024].

[69] J. Takahashi, B. M. Tavares, W. L. Qian, R. Andrade, F. Grassi, Y. Hama, T. Kodama and N. Xu, Phys. Rev. Lett. **103**, 242301 (2009) [arXiv:0902.4870 [nucl-th]].

[70] W. Broniowski, P. Bozek and M. Rybczynski, Phys. Rev. C **76**, 054905 (2007) [arXiv:0706.4266 [nucl-th]].

[71] B. Alver and G. Roland, Phys. Rev. C **81**, 054905 (2010) [Erratum-ibid. C **82**, 039903 (2010)] [arXiv:1003.0194 [nucl-th]].

[72] G. L. Ma, S. Zhang, Y. G. Ma, H. Z. Huang, X. Z. Cai, J. H. Chen, Z. J. He and J. L. Long *et al.*, Phys. Lett. B **641**, 362 (2006) [nucl-th/0601012].

[73] J. Xu and C. M. Ko, Phys. Rev. C **84**, 014903 (2011) [arXiv:1103.5187 [nucl-th]].

[74] Z. -W. Lin, C. M. Ko, B. -A. Li, B. Zhang and S. Pal, Phys. Rev. C **72**, 064901 (2005) [nucl-th/0411110].

[75] X. -N. Wang and M. Gyulassy, Phys. Rev. D **44**, 3501 (1991).

[76] W. -T. Deng, X. -N. Wang and R. Xu, Phys. Rev. C **83**, 014915 (2011) [arXiv:1008.1841 [hep-ph]].

[77] B. Abelev *et al.* [ALICE Collaboration], Pb-Pb collisions at $\sqrt{s_{NN}} = 2.76$ TeV," Phys. Rev. Lett. **105**, 252301 (2010) [arXiv:1011.3916 [nucl-ex]].

[78] S. A. Voloshin, A. M. Poskanzer, A. Tang and G. Wang, Phys. Lett. B **659**, 537 (2008).

[79] L. Adamczyk *et al.* [STAR Collaboration], arXiv:1206.5528 [nucl-ex].

[80] P. Sorensen [STAR Collaboration], J. Phys. G **38**, 124029 (2011) [arXiv:1110.0737 [nucl-ex]].

[81] T. A. Trainor, D. J. Prindle and R. L. Ray, arXiv:1206.5428 [hep-ph].

[82] K. Aamodt *et al.* [ALICE Collaboration], Phys. Rev. Lett. **107**, 032301 (2011) [arXiv:1105.3865 [nucl-ex]].

[83] J. D. Bjorken, Phys. Rev. D **27**, 140 (1983).

[84] P. Petreczky, Nucl. Phys. Proc. Suppl. **140**, 78 (2005) [hep-lat/0409139].

[85] See PHENIX website:
http://www.phenix.bnl.gov/WWW/plots/show_plot.php?editkeyp̄1164

[86] J. Xu and C. M. Ko, Phys. Rev. C **83**, 034904 (2011) [arXiv:1101.2231 [nucl-th]].

[87] P. Danielewicz and M. Gyulassy, Phys. Rev. D **31**, 53 (1985).

[88] P.K. Kovtun, D. T. Son and A. O. Starinets, Phys. Rev. Lett. **94**, 111601 (2005).

Chapter 9

Summary and Conclusion

My main research interest is the event-by-event temperature fluctuations for the charged hadrons and identified particles in order to obtain the estimation of specific heat of the system. Other estimations of local temperature fluctuations within the event in order to search for anisotropy pattern in temperature and hot spot in energy density had been performed. Apart from that I had been also involved with various research interests which are associated with the main dissertation topic. So, broadly my dissertation layout is following:

- Temperature fluctuations : Motivation & Theoretical background
  - 1A. Global temperature fluctuation $\Longrightarrow$ Specific Heat.
  - 1B. Local temperature fluctuation $\Longrightarrow$ Hot spots and temperature anisotropy pattern searching.
  - 1C. Theoretical model and event generator expectations : Hydro, HRG and AMPT and Lattice.
  - 1D. Estimation of specific heat at RHIC Energies from published results.
- Data Analysis in ALICE experiment : LHC10h
  - 2A. Particle identification.

  - 2B. Efficiency Calculations and Corrections.
  - 2C. p_T distributions and calculations of $\langle p_T \rangle$.
  - 2D. Mixed event Technique and estimation of statistical error.
  - 2E. Centrality−wise estimations of specific heat and temperature fluctuation map.

- Miscellaneous
  - 3A. $\Delta p_{Ti} \Delta p_{Tj}$correlations and $\langle p_T \rangle$ fluctuations.
  - 3B. Different fitting function the spectra and associated physics.
  - 3C. Particle productions and distributions in Heavy ion collisions in Beam Energy Scan.
  - 3D. Higher Harmonic flow for different energy.
  - 3E. Multiplicity fluctuations and its effect on temperature fluctuations.

- Experience with PMD-hardware
  - 4A. Hardware Experience $\Longrightarrow$ Photon Multiplicity Detector Testing and Callibration.
  - 4B. PMD : QA and gain calculation analysis.

9.1 Temperature fluctuation : Motivation & Theoretical background

My aim is to study the physics of strongly interacting matter at extreme energy densities, where the formation of a new phase of matter, the quark-gluon plasma, is expected. The existence of such a phase and its properties are key issues in QCD for the understanding of confinement and of chiral-symmetry restoration. For this purpose, I am carrying out a comprehensive study to address the following questions: How is entropy produced and behaved? Nature of the phase transition? What are the properties of the medium?

Answer to all of the above questions are lie in the theory of fluctuations. Also study of fluctuations of various quantities provides a powerful means of observing QCD phase transition as in QCD phase transition associated with a QGP and hadronic phase change. The strength of this fluctuations known as correlation also specify the strength of the collectivity of the medium produced in the heavy ion collisions. Temperature fluctuations have been discussed in the literature as a means of characterizing the evolving system. The fluctuations may have three distinct origins, first, quantum fluctuations that are initial state fluctuations, second, thermodynamical fluctuations which is my prime interest and last statistical fluctuations due to limited number of particles produced in each event due to collisions.

9.1.1 1A. Global temperature fluctuation $\Longrightarrow$ Specific Heat

I discuss a method of extracting the thermodynamic temperature from the transverse momentum spectra and mean transverse momentum of charge hadrons, identified pions, by using controllable parameters such as centrality of the system, and range of the transverse momenta and specifying pseudo-rapidity and azimuthal window. Event-by-event fluctuations in global temperature over a large phase space provide the specific heat of the system. In thermodynamics, the heat capacity (C) is defined in terms of the ratio of the event-by-event fluctuations of the energy of a part of a finite system in thermal equilibrium to the energy $(\Delta E^2) = T^2 C(T)$. This can be applied for a locally thermalized system produced during the evolution of heavy-ion collisions. But for a system at freeze-out, specific heat can expressed in terms of the event-by-event fluctuations in temperature of the system where volume is fixed: $\frac{1}{C} = \frac{(\langle T^2\rangle - \langle T\rangle^2)}{\langle T\rangle^2}$. As specific heat is define by the heat capacity per unit volume, so we define the specific heat as the heat capacity for a system with number of particles as heat capacity per particle. Like, either per charge particle in case of non-identified hadrons or per identified species like pions, kaons within the available phase space or the experimentally available window in rapidity and azimuth. As the phase space volume is equivalent to the number of interacting particles.

9.1.2 1B. Local temperature fluctuation $\Longrightarrow$ Hot spots and temperature anisotropy pattern searching

The origin of the local fluctuations has been studied within a event. Here main idea is to find some hot spot pattern in the phase space in terms of energy density and temperature, which is done via $\langle p_T \rangle$ distribution in a grid like $\eta - \phi$ zone. The correlation in multiplicity of each small of these bins are connected to the isothermal compressibility. The effect of multiplicity in local temperature had been studied for both non identified charged hadrons and identified pions. The map of this temperature fluctuation contains hot spots and cold spots. This irregularities in temperature or p_T may have their origin from the extreme regions of phase space, which existed during the early stages of the reaction. This may indicate that the observed fluctuations are remnants of the initial energy density fluctuations and are not washed out until the freeze-out stage. From this maps of temperature fluctuations and $\langle p_T \rangle$ are constructed from large number of events of similar multiplicity class could be used for making power spectrum analysis.

9.1.3 1C. Theoretical model and event generator expectations : Hydro, HRG and AMPT and Lattice

The result from different experiments are explained successfully from different school of thoughts of various theoretical models and even generators. Mainly hydrodynamics and microscopic models are used for explaining different observables to understand the properties of the matter produced due to collisions.

Hydrodynamics has been used extensively and to a large extent successfully to explain majority of these experimental results Use of a (2+1)-dimensional event-by-event ideal hydrodynamical framework developed by the Finland group with lattice-based equation of state. The formation time of the plasma is taken to be 0.14 fm in this purpose. A wounded nucleon (WN) profile is considered where the initial entropy density is distributed using a 2-dimensional Gaussian distribution function. The size of the density fluctuations is taken to be 0.4 fm. The transition temperature from the QGP to the hadronic phase is chosen to be 0.170 GeV via cooper-fry formalism and the kinetic freeze-out temperature is taken as 0.160 GeV. Both the free streaming and defining freezeout hyper surface has been used to study the fluctuation in energy density and temperature with the elapsed time.

Also, Hadron Resonance Gas (HRG) model analysis of the particle yields indicate the formation of a thermal source for the produced particles in heavy-ion collisions. Similar way lattice results are very promising at higher temperature and lower baryonic potential region. A comparison of these models has been studied in temperature fluctuations view point.

Similarly there are some heavy ion event generators which explains most of the experimental observables nicely at different collision energies, viz. HIJING, URQMD and AMPT. Some of these models are completely microscopic, some are hybrid in origin. In-spite of different origin and mechanism adopted by these event generators, most of them explains the p_T distributions for different flavour. A detailed study of AMPT model calculation for this regard is done. The AMPT model provides two modes: Default and String Melting. In both the cases these two modes taken initial condition from HIJING with two Wood-Saxon type radial density profile colliding nuclei. The multiple scattering among the nucleons of two heavy ion nuclei, are governed by the eikonal formalism. In both mode, energetic patrons cascading (Zhang's Parton Cascade) before the strings and partons are recombined. Default mode is fragmentation dominated (Lund string fragmentation function) and String Melting is quark coalescence process dominated to mimicking the realistic hadronization scenario transported from the patrons.

Global and local fluctuations in temperature had been studied by using these theoretical models and event generator. Both beam energy and centrality dependence of said fluctuations have been estimated as a model based expectations.

9.1.4 1D. Estimation of specific heat at RHIC Energies from published results

Experimental results from NA49, CERES, STAR, PHENIX, PHOBOS and ALICE are combined to obtain the specific heat as a function of beam energy for event-by-event global temperature fluctuations. In this regard, $\langle p_T \rangle$ distributions from the published results are used for charged hadrons. The distribution of $\langle p_T \rangle$ from data and mixed event helps to find out the dynamical fluctuations in $\langle p_T \rangle$ and subsequently fluctuations in temperature. These calculation gives the excitation function of specific heat over a large collisional energy. The blast-wave mechanism is used further to determine the kinetic temperature from the effective temperature decoupling the radial flow part. Results shows below 19.6 GeV energy (NA49, CERES) the temperature fluctuations dominated by the statistical fluctuations due to low multiplicity. A detailed methodology and combined results from these published data and different model expectation has been reported.

Beam Energy Scan of sp. heat from data, AMPT and HRG model prediction. For Pb-Pb collisions at the Large Hadron Collider (LHC) energies, because of the production of a large number of particles in every event, it is possible to divide the phase space into small bins and obtain local temperature for each bin. Event-by-event fluctuations in local temperature can be obtained by following a novel procedure of making fluctuation map of each event.

The origin of the local fluctuations has been studied with the help of event-by-event hydrodynamic calculations, which shows that the system exhibits fiercely large fluctuations at early times after the collision, which diminishes with the elapse of time. Any observation of non-zero local fluctuations may imply that a part of the early fluctuations might have survived till freeze-out. We discuss the hydrodynamic calculations and a feasibility study at LHC using AMPT simulated data.

9.2 Data Analysis in ALICE experiment : LHC10h

ALICE Experiments at LHC in CERN are on the quest to unearth the nature of the QCD phase transition and to get a glimpse of how matter behaves at extreme conditions of temperature and energy density. The temperature fluctuation can also be studied in heavy-ion physics at TeV energy scale in ALICE experiment as for mainly three reasons. First high temperature, secondly,a very large number of events and very large multiplicity at each event which will lead to a better control in statistical fluctuations and third it is in the cross-over region in the phase space diagram where baryonic potential is almost zero.

9.2.1 2A. Particle identification

In ALICE experiment from the slope of the p_T spectrum of charged hadrons and identified particles for every event fit with different functions such as exponential, Boltzmann Gibbs Blast Wave etc. The slope parameter can also be obtained from $\langle p_T \rangle$ of each event at mid rapidity. From there the distribution for a large number of events, heat capacity and specific heat had been calculated for charged hadrons and identified pions. For local temperature fluctuation specified phase space (η-ϕ) or (y-ϕ). For particle identification Time projection Chamber(TPC) and Time of Flight(TOF) detectors has been used. For the data sets of Pb+Pb collisions at $\sqrt{s}_{NN}$= 2760 GeV, 0.15$\langle p_T \langle$2.0 cuts are used for kinematic cut. V0 detector has been used for the centrality cuts at mid rapidity $-0.8\langle\eta\langle0.8$. Particle identification has been done via only TPC upto 0.15 $\langle p_T \langle$ 0.6 and combined TPC+TOF has been used 0.6$\langle p_T \langle$0.6 via NSigma method.

9.2.2 2B. Efficiency Calculations and Corrections

The efficiency calculation is important to get the corrected spectra. In order to get a efficiency estimation species wise and for charged hadrons for different primary vertex, centrality, kinematic cuts LHC11a10a_bis Monte Carlo (MC) data set has been used, which is basically HIJING tuned for ALICE. This MC in the generator level called as MC Truth and when it passes through Geant ALICE detector labeled as MC reconstructed. Ratio of which with respect to p_T in primary particles gives the efficiency x acceptance (ϵ). The detailed study for secondary particle from weak decay, material and mis identification has been performed to obtain the contamination factor(c). Now the raw uncorrected spectra from the data has been corrected by dividing the correction factor $G = \frac{1-c}{\epsilon}$.

9.2.3 2C. p_T distributions and calculations of $\langle p_T \rangle$

Applying the above methodology with different kinematic with different centrality once corrected spectra (p_T) is obtained for each of the event. With full azimuth and $-0.8 \langle \eta \langle 0.8$ from each event corrected p_T distribution is giving $\langle p_T \rangle$ for both identified pions, kaons and charged hadrons. From there I calculate the slope for each of the event and making distribution of both $\langle p_T \rangle$ and T_{eff}.

9.2.4 2D. Mixed event Technique and estimation of statistical error

In order to calculated the dynamical component once has to take out the statistical fluctuation from the $\langle p_T \rangle$ and T_{eff} distribution. For this mixed event technique is adopted. Here mixed event are produced by mixing the events in track level of same multiplicity class keeping other cuts similar to that of the data and then following the same techniques to produces spectra and subsequently the distribution of $\langle p_T \rangle$ and T_{eff}. By doing this one could get rid off from the statistical fluctuations due to limited number of charge particles or identified species, and also from other auto correlation and resonance effect. The effect of jet and mini jets in the fluctuations are studied via varying the window of the p_T distributions.

9.2.5 2E. Centrality−wise estimations of specific heat and temperature fluctuation map

Following the above methodology of getting corrected spectra and estimation of dynamical fluctuations of $\langle p_T \rangle$ and T_{eff} distributions the analysis divided into two main categories. First for global temperature fluctuations, I use then simultaneous Boltzmann-Gibbs Blast Wave fit to different species for estimation of kinetic temperature and radial flow velocity. Then using $\frac{1}{C} = \frac{(\Delta T_{eff}^{dun})^2}{(T_{kin})^2}$, heat capacity is calculated. Divided by the average number of charged hadron or identified particles within the available phase space, the specific heat is obtained for different centrality from most central to peripheral. Second, the available phase space η-ϕ for each of the event is subdivided into 4x4,5x5 and 6x6 grid like zone for local temperature fluctuations. This division being optimised in for constructing the p_T distributions and multiplicity. Now similar approach as global is followed to make map of $\langle p_T \rangle$ and T_{eff} in order to search for local hotspot. Repeating the same for a large event sample on similar centrality I tried find some pattern in local temperature fluctuation maps. This methodology is limited only for charged hadrons and identified pions. For kaons and protons it can not be applied as the number of production of these species for each event is very less compared to other two.

9.3 Miscellaneous

In addition of the main research work, the following detailed studies have been performed as a part thesis work:

3A. Transverse Momentum spectra for identified particles with p_T correlations: Several experiments involves with the basic observables like transverse momentum. Although it has very rich physics goal. During the detailed research work, we try to relate the p_T correlation with it. It has been observed that different experiments uses different observables for this study. A inter-relation and comparative study has been made on this basis. A system size and energy dependence helps a lot for characterizing and understanding the evolving fire ball. Also a centrality scan may address the effect of mini jets and degree of hadronizations.

3B. Spectra−fitting functions and associated physics.

Different spectra fitting functions are available for addressing the different physics aspects. Mainly these are used for calculated the particle yield, temperature and flow. Combined blast wave are used for decoupling the radial boost from the kinematic freeze-out temperature in heavy ion collisions where as Tsallis are used for non−extinsive type spectra or non thermalized spectra. An extensive study has been made for both the data and different event generators.

3C. Theoretical baseline studies using Hydro, HRG and AMPT.

To understand various sources of fluctuation related to heavy ion collision, various model simulations have been performed for the Temperature fluctuations. Those models are HIJING, AMPT and Event by event Hydro. These models are based upon certain known physics processes like, jet-interaction, transport phenomena, coalescence mechanism, thermal equilibrium etc., which are blind to the CP phenomena. These models may sever as baseline studies for the Temperature fluctuation analysis and other baseline studies.

3D. Higher harmonic anisotropic flow.

A beam energy scan from RHIC to LHC energies of anisotropic flow had been performed. The detailed study of elliptic, triangular and other higher harmonic flow are done in models and compared with different published results. These study are very important to understand for NCQ scaling, quark coalescence and other phenomena to fixing the initial conditions and also the shear viscosity of the system.

3E. Multiplicity fluctuations.

Detailed study of total charge multiplicity, η distributions and its fluctuations had been studied for having the nature of the evolution of these observable with the centrality and collision beam energy. It could also help to predict the same for the intermediate or higher energy. The event−by−event basis study of net charge, particle ratio, net baryon is related to some susceptibility as these are the conserved quantities. from there one can achieve the corresponding observable which are directly comparable with the Lattice QCD results.

9.4 Experience with PMD-hardware

Hardware and software associated with PMD is one part of my dissertation. High voltage testing, detector building is performed for part of the full detectors. The modules which had been prepare and tested now taking data in ALICE experiments at CERN. The detailed QA test for these detector data set has been performed for gain calculations and other characteristics.